UNIVERSITY OF STRATHCLYDE

Methods for the Generation

of Ultra-Short

Free-Electron Laser Pulses

David James Dunning

ASTeC, STFC Daresbury Laboratory

and the Cockcroft Institute

November 1, 2015

Declaration

This thesis is the result of the author's original research. It has been composed by the author and has not been previously submitted for examination which has led to the award of a degree.

The copyright of this thesis belongs to the author under the terms of the United Kingdom Copyright Acts as qualified by University of Strathclyde Regulation 3.50. Due acknowledgement must always be made of the use of any material contained in, or derived from, this thesis.

Signed:

Date:

Abstract

This thesis details studies to develop methods for the generation of ultra-short pulse of light to enable the study of ultra-fast phenomena. The main contents are: an overview of methods of light sources and applications; a review of the physics of the free-electron laser, and its resultant properties; a review of existing and proposed methods of generating ultra-short pulses from free-electron lasers; a study into the physics of the mode-locked amplifier FEL technique, including its use to amplify an HHG source while retaining the pulse train structure, an explanation of the role of electron beam modulation in the technique, specification of alternative modulation methods, and a simplified model to describe the behaviour; and lastly a proposal for a method to generate x-ray laser pulses with duration approaching the zeptosecond range, two orders of magnitude shorter than the current record, including detailed modelling and analytic description.

Acknowledgements

Contents

List of Figures

x

Chapter 1

Introduction

The application of sources of electromagnetic radiation, commonly referred to as light sources, has been the basis of numerous scientific breakthroughs. The wavelength of the radiation emitted by a light source dictates its spatial resolution, while the duration of the pulse of light sets its temporal resolution. Figure 1.1 shows three examples (at progressively faster timescales and smaller sizes) of short pulses of light being captured to reveal the dynamics of processes. The focus of this thesis is on concepts for generating shorter pulses of light than are presently available, thereby enabling study of processes on faster timescales.
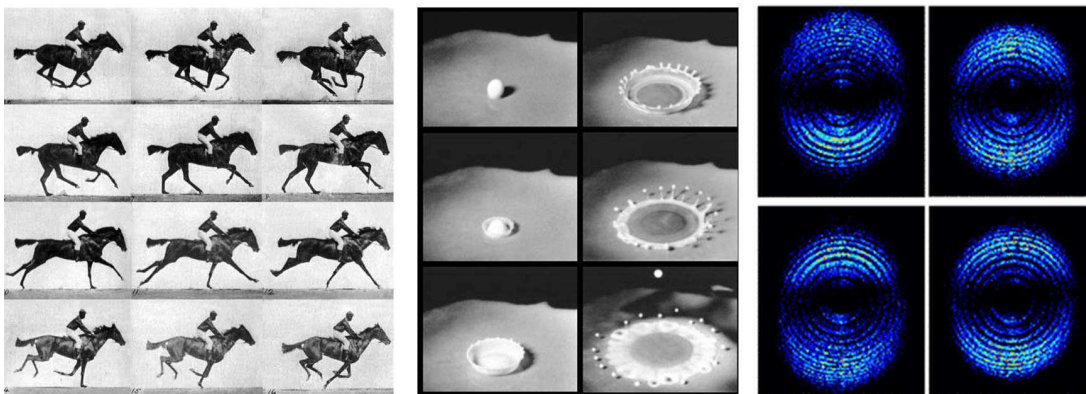
Figure 1.1: Left to right: E. Muybridge 1878, shutter time $\sim 1 \times 10^{-3}$ s to capture the dynamics of a horse in motion; H.Edgerton 1931 flashed pulse of $\sim 1 \times 10^{-6}$ s to capture fluid drop dynamics; J. Mauritsson et al. 2008, electron wave packet dynamics at hundreds of attosecond (1×10^{-18} s) scale [1].

The work focuses on the technology of free-electron lasers, and the main content of the study is to examine and develop various concepts for short pulse

generation through computer modelling. This chapter introduces the fields of short pulses and free-electron lasers, and sets out the content of the thesis.

1.1 Ultra-fast processes

Pulses of light, tens to hundreds of attoseconds in duration, have enabled the exploration and control of processes that occur at atomic time scales [2, 3]. The timescales of different processes have been described by Krausz and Ivanov [3] as shown in Figure 1.2: Atomic motion on molecular scales occurs at femtosecond (10^{-15} s) to picosecond (10^{-12} s) scales, electron motion in outer shells of atoms takes place on tens to hundreds of attoseconds, and electron motion in inner shells of atoms is expected to occur around the scale of a single attosecond (10^{-18} s). At faster scales still are nuclear dynamics, which are predicted to occur at zeptosecond (10^{-21} s) time scales.
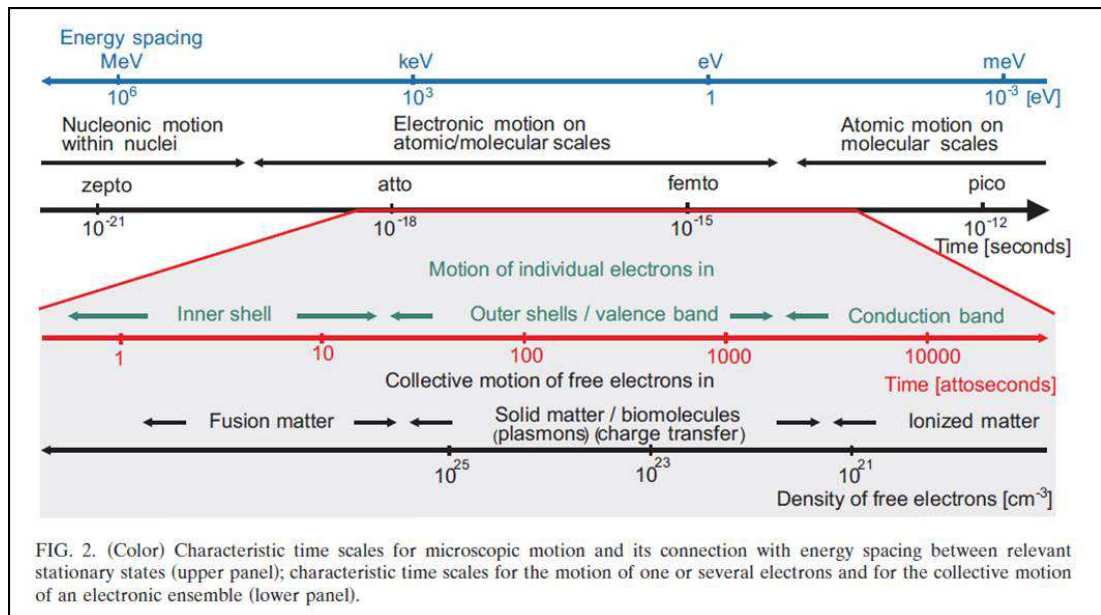
Figure 1.2: Characteristic timescales of ultra-fast processes. Figure reproduced from [3].

The extremity of such timescales can be illustrated by considering that there are approximately as many attoseconds in one second, as there have been seconds in the history of the universe!

1.2 History of short pulses

The record for the shortest pulse of light has seen a progression from approximately 10 ps in the 1960s to around 67 attoseconds generated recently by Chang et al. [4] - a development of approximately five orders of magnitude in five decades. As noted by Corkum et al. [2, 5] (see Figure 1.3), it is particularly relevant to consider the way in which this frontier progressed. The duration of a pulse of light is its wavelength, λ_r multiplied by the number of optical cycles, N, divided by the speed of light. Initially progress was made in conventional lasers operating at approximately a fixed wavelength ($\lambda_r \approx 600$ nm), by reducing the number of optical cycles. This continued until, in the mid 1980s, pulses of only a few cycles could be generated (corresponding to a few fs), then could proceed little more.
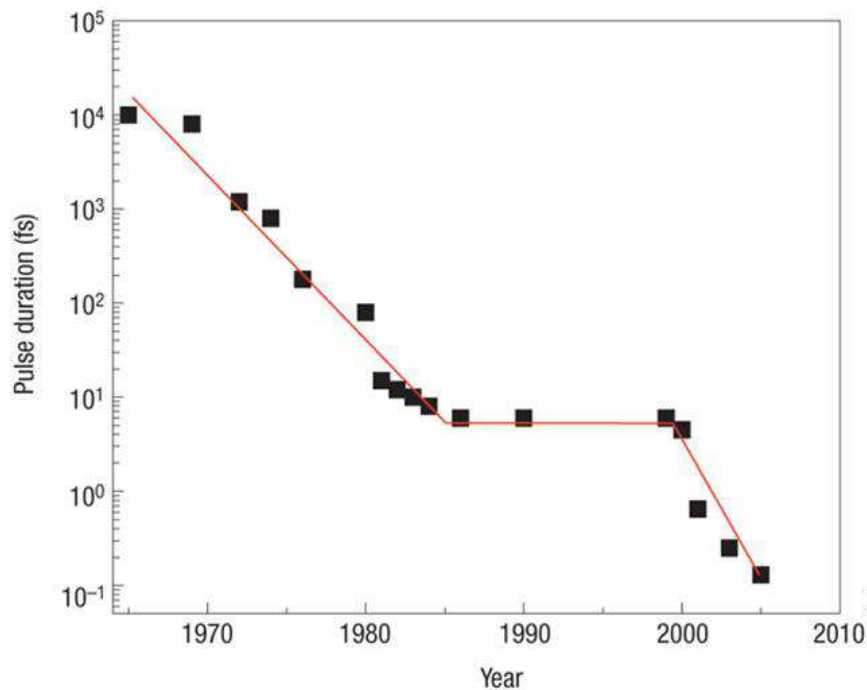
Figure 1.3: History of short pulses. The record shortest pulse of light is plotted against year. Figure reproduced from [2], with an additional point corresponding to [4] in 2012.

It took a transformative step - high harmonic generation (HHG) [2, 3, 5], for progress to continue by (in very simple terms) reducing the wavelength of the generated light. This technology allowed pulses in the attosecond scale to be generated for the first time, and now reaches just under a hundred attoseconds. Isolated pulses may be generated or, more commonly, a periodic train of pulses

which can act as an ultra-fast strobe. This fast stroboscopic property has been successfully applied to a range of experiments to image and control electron wave packet behaviour in atoms [1, 6, 7, 8, 9, 10].

It seems that a further step to shorter wavelength is now required to progress to significantly shorter pulses. Proposals are being developed outlining how future progress in HHG might achieve this [11, 12]. Alternatively, x-ray free-electron lasers (FELs) (reviewed in several papers [13, 14, 15, 16, 17]) presently surpass HHG sources in terms of shortest wavelength by approximately two orders of magnitude, and it is this property which first suggests FELs as a promising candidate for progressing to shorter radiation pulses than are available today.

Reducing pulse durations towards 1 attosecond, and beyond into the zeptosecond regime with high (GW) peak-powers may extend opportunities to directly resolve electronic behaviour within inner shells of atoms; the imaging and possible control of electronic-nuclear interactions such as Nuclear Excitation by Electron Transition/Capture (NEET/NEEC) [18]; and move towards the resolution of nuclear dynamics [19]. However, this will require a sufficient flux of photons with energies in the hard x-ray ($\gtrsim$10 keV) which are currently not available from HHG sources.

1.3   Introduction to FELs

Free-electron lasers [13, 14, 15, 16, 17], and particularly their operation to x-ray wavelengths (X-FEL), are a spectacular development in the history of tools for scientific experiments. They can be seen as both a huge advance in the line of x-ray sources to orders of magnitude higher brightness and shorter pulses, and as a similarly significant step in lasers to orders of magnitude shorter wavelength.

The difference from conventional lasers is most marked in terms of the gain medium. The term 'free-electron' refers to the fact that the electrons are not bound in atoms as in conventional lasers (where discrete energy level differences dictate the wavelength of the light), but are 'free' particles propagating from a particle accelerator. This feature leads to some of the key properties of FELs, including scaleability of the technology across an exceptionally broad range of radiation wavelengths (from THz to X-ray), as well as tunability, and high power.

The relationship of X-FELs to electron storage rings is much closer. Both rely

on particle accelerators to raise bunches of electrons to high energy, and magnetic fields to deflect and so extract energy from the electrons in the form of light. This is due to the fact that accelerated charged particles emit EM radiation, with light due to radial acceleration termed 'synchrotron radiation'. A key component of both FELs and storage rings is the undulator magnet, which is a periodic array of dipole magnetic fields, causing the electrons to take an undulating path.

The key distinction between storage ring undulator sources and the FEL is coherence. Unlike other synchrotron radiation sources, the FEL exhibits the truly remarkable property of self-organisation of the electrons ('micro-bunching') such that they emit coherently. A positive feedback mechanism leads to exponential growth of both the radiation intensity and the electron beam micro-bunching. Figure 1.4 shows the basic layout of a free-electron laser, and the micro-bunching effect that leads to coherent emission. FEL theory is described in Chapter 2.
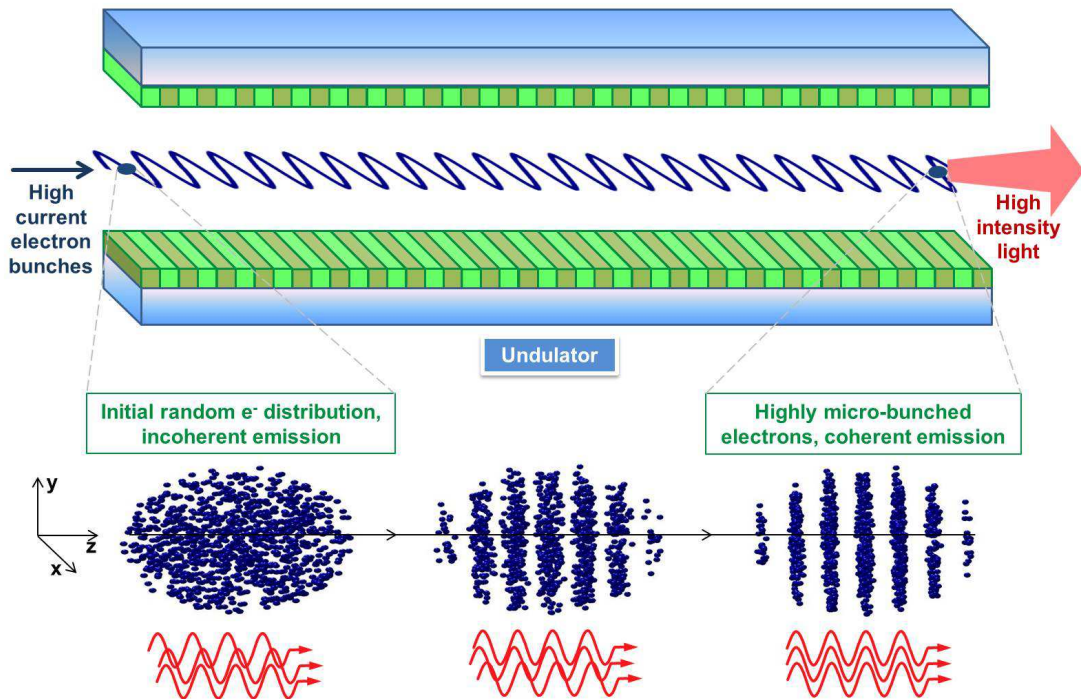
Figure 1.4: Basic layout of a free-electron laser. Bunches of electrons are generated, accelerated and then propagated in the z-direction through an undulator. The light and darker green blocks represent opposite polarity magnetic poles, such that the main field component is in the y-direction, and is periodic in z. The electron trajectory is oscillatory in x. Below shows the electrons initially randomly distributed within the bunch (therefore generating low-intensity incoherent emission), then micro-bunching occurring to give rise to coherent, high intensity emission.

1.4 Short-pulse potential of free-electron lasers

The free-electron laser has two particular advantages which give it potential for pushing the frontier of short pulse generation. The first, as described in Section 1.2, is short wavelength. Recent FEL facilities (LCLS [20] commissioned in 2009, and SACLA [21, 22] commissioned in 2011) have extended FEL operation down to approximately 0.1 nm. Assuming that pulses of only a few optical cycles could be attained, this would correspond to pulse durations of approximately a single attosecond - two orders of magnitude shorter than present HHG sources, and four orders of magnitude beyond conventional lasers.

Of course x-ray sources other than FELs have been available for many years, however the peak powers are insufficient for many applications to deliver a significant number of photons within an attosecond timescale. It is the high peak power of the free-electron laser (exceeding storage rings - the next highest intensity source of x-rays - by approximately 9 orders of magnitude) which gives it potential to push the frontier of ultra-short pulse generation. A hard x-ray FEL typically generating approximately 20 GW peak power, corresonds to 10^{25} photons/second. For a pulse duration of a single attosecond this would correspond to 10^7 photons per pulse.

The challenge for reaching the very shortest pulses from FELs will be to minimise the number of cycles per pulse (due to reasons described in Chapter 3), and addressing this challenge is the main topic of this thesis.

1.5 Thesis Outline

This thesis details studies to assess methods for the generation of ultra-short pulses of light from x-ray free-electron lasers, and to develop new concepts. The main contents are:

- An introduction to the types of light source available for ultra-fast science.

- A review of the physics of the free-electron laser, and its resultant properties.

- A review of existing and proposed methods of generating ultra-short pulses from free-electron lasers.

- A study into the physics of the mode-locked amplifier FEL technique, including:

- Its use to amplify an HHG source while retaining the pulse train structure

- An explanation of the role of electron beam modulation in the technique, and specification of alternative modulation methods.

- A simplified model to describe the behaviour.

- Development of a new method to generate x-ray free-electron laser pulses with duration approaching the zeptosecond range, two orders of magnitude shorter than currently available from any source, including detailed modelling.

Chapter 2

Free-Electron Laser Physics

2.1 Introduction

This chapter outlines a description of the free-electron laser based on a review of previous works. The major developments leading to modern x-ray FELs are outlined, and the main points of FEL theory are described. Much of the approach is based on the review of [23] as well as a number of useful texts [14, 15, 16, 24, 25, 26].

2.2 History

This section gives a brief historical overview of the developments leading to the high-gain FEL, which is the basis of modern short-wavelength FELs. A more detailed history is given in [15].

The radiation from 'fast' electron beams passing through a series of alternating polarity magnetic fields was theorised by Motz [27] and Ginzburg [28], and Motz demonstrated the first undulator in 1953 [29]. Phillips developed a device named the ubitron [30] ('undulating beam interaction') - an undulator microwave device, which had low electron beam energy compared to modern day FELs but otherwise demonstrated the key properties of density modulation (bunching) and radiation energy extracted from axial velocity (i.e. kinetic energy) of the electron beam.

The origin of the term 'free-electron laser' came from Madey - who unaware of the work of Phillips - introduced the free-electron laser concept in 1971 [31]. He used a quantum mechanical description and recognised the potential scaleability of the technique to short wavelengths. Madey and colleagues proceeded to demon-

strate an 'amplifier FEL' configuration [32] in which externally generated laser light is amplified through co-propagating with an electron beam in an undulator magnet, with single-pass gain (the radiation intensity increase in a single undulator pass) up to 7 % recorded. A second set of experiments by the same group demonstrated an 'oscillator FEL' configuration [33], in which an optical cavity was introduced such that radiation is amplified by successive electron bunches.

These experiments prompted much theoretical work on the nature of the device, and classical alternatives to the quantum theory were proposed e.g. Colson [34] and Hopf [35]. Work by a number of groups resulted in the conclusion that the FEL is classical to a very good approximation, with the quantum contribution (due to electron recoil in photon emission) being negligibly small down to short wavelengths (nowadays recognised as gamma ray wavelengths. Colson's approach is widely known today as it shows that in the 'low-gain' regime of FEL operation (typically a few percent gain per undulator pass), the FEL equations take the same form as those of a simple pendulum. This approach is described in Section 2.5.3.

Modern short-wavelength FELs work in the 'high-gain' regime, which was described theoretically in the 1970s and 80s. The pendulum model is not fully self-consistent as it assumes fixed radiation intensity during one undulator pass, so a fully self-consistent model including radiation evolution was required. The high-gain theory was a product of a number of groups [36, 37, 38, 39, 40, 41, 42, 43], and showed the possibility for exponential increase in radiation intensity during one undulator pass. Identifying the high-gain regime was hugely significant since it removed the need for optical cavities (and therefore reliance on mirror technology), and opened up the possibility of FEL operation towards x-rays.

The first high-gain FEL was demonstrated in 1985 at microwave wavelengths [44], much of the statistical properties of the output were verified against theory in an infrared experiment at UCLA [45], and a series of facilities including FLASH [46], LCLS [20], and SACLA [21, 22] have pushed the technology to successively shorter wavelengths.

2.3 Fundamentals

2.3.1 Relativity - Lorentz factor

FELs utilise relativistic electrons, i.e. electrons moving at a velocity, v, which is a significant fraction of the speed of light. The speed of an electron normalised to the speed of light is $\beta = v/c$. A relativistic electron has total energy $E = \gamma mc^2$, where γ is the Lorentz factor:

$$\gamma = \frac{E}{mc^2} = \frac{1}{\sqrt{1-\beta^2}} = \frac{E[\text{GeV}]}{0.511 \times 10^{-3}} \tag{2.1}$$

where m is the rest mass of the electron and c is the speed of light. Rearranging for β, and simplifying for the case of $\gamma \gg 1$:

$$\beta = \sqrt{1 - \frac{1}{\gamma^2}} \approx 1 - \frac{1}{2\gamma^2} \tag{2.2}$$

2.3.2 Radiation emission from relativistic electrons

Synchrotron radiation originates from radial acceleration of charged particles. The key feature for relativistic particle beams is that the particles follow very closely behind the emitted radiation such that the radiation is highly concentrated in the direction of travel. Electrons in an undulator take a sinusoidal path, so in a frame co-moving with the electron longitudinal motion the emission is the typical emission from charged particles as familiar in radio waves etc. In the laboratory frame, the emission is concentrated in the forward direction of travel into an opening angle of $\sim 1/\gamma$.

2.3.3 Undulator magnetic field

Undulators are usually either 'planar' or 'helical', meaning the electrons take either a sinusoidal or helical path respectively. Electron net propagation is along the undulator axis which is defined as the $\boldsymbol{z}$ direction.

Planar undulator

In a planar undulator, the magnetic field is perpendicular to the electron direction in either the horizontal, $\boldsymbol{x}$, or vertical, $\boldsymbol{y}$, direction, and varies sinusoidally in $\boldsymbol{z}$

with period λ_u. In this section the magnetic field is chosen to be in the vertical, $\boldsymbol{y}$, direction. The undulator magnetic field, $\boldsymbol{B}$, is thus described as:

$$B_y(z) = B_0 \sin(k_u \boldsymbol{z}) \tag{2.3}$$

where B_0 is the peak magnetic field, and $k_u = 2\pi/\lambda_u$ is the angular wavenumber of the undulator field.

It is convenient to describe an undulator parameter, K, as follows:

$$K = \frac{eB_0}{mck_u} = 93.36 B_0[T]\lambda_u[m] \tag{2.4}$$

It is also convenient, as will be seen in the following sections, to define an rms undulator parameter, a_u:

$$a_u = \frac{eB_{\text{rms}}}{m_0 ck_u} \tag{2.5}$$

where B_{rms}, the root mean square magnitude (rms) of the undulator magnetic field is used, rather than the peak field.

Helical undulator

Another common type of undulator is a helical or elliptical undulator, in which the magnetic field has components in both the vertical and horizontal directions:

$$B_x(z) = B_{x_0} \sin(k_u \boldsymbol{z} - \phi) \tag{2.6}$$
$$B_y(z) = B_{y_0} \sin(k_u \boldsymbol{z}) \tag{2.7}$$

Depending on the magnitude and phasing of the two components, different degrees of ellipticity from planar to circular are possible, though it is most common to consider the case where $B_{x_0} = B_{y_0}$ and $\phi = \pi/2$, for which it will be seen that the electrons take a circular path when viewed along the axis of propagation. The undulator K-parameter for a helical undulator can be defined in the two components:

$$K_x = \frac{eB_{x_0}}{m_0 ck_u}; \quad K_y = \frac{eB_{y_0}}{m_0 ck_u} \tag{2.8}$$

When the magnitude of the field in the two planes is equal, a single undulator parameter is defined: $K = K_x = K_y$. Since K is defined in terms of the peak magnetic field, and the deflection in a helical undulator is in two planes rather

11

than one (as in a planar undulator), the electron delay (relative to propagation in free space) for a helical undulator of parameter K is a factor of $\sqrt{2}$ higher than the equivalent K value for a planar undulator.

It is therefore often convenient to use the rms undulator parameter, a_u, given in equation 2.5, which is defined in terms of the rms magnetic field, and is $\sqrt{2}$ lower for a planar undulator than for a helical undulator with equal peak field. A helical undulator and a planar undulator with the same a_u value will introduce the same electron delay. The significance of the delay will be seen in Section 2.5.2.

2.4 Electron trajectory

2.4.1 Planar undulator

The electron path in a planar undulator is now derived. The Lorentz force equation describes the force, $\boldsymbol{F}$, on a moving charged particle in electric and magnetic fields:

$$\boldsymbol{F} = q(\boldsymbol{E} + \boldsymbol{v} \times \boldsymbol{B}) \tag{2.9}$$

where q is the electric charge of the particle (equal to the electron charge, e, in FELs), $\boldsymbol{E}$ is the electric field, $\boldsymbol{v}$ is the velocity of the particle, and $\boldsymbol{B}$ is the magnetic field given by equation 2.3.

The force on the electron can be related to an equation of motion as follows. The force is equal to the rate of change of momentum:

$$\boldsymbol{F} = \frac{d\boldsymbol{p}}{dt} \tag{2.10}$$

where the relativistic momentum is:

$$\boldsymbol{p} = m\boldsymbol{v} = \gamma m_0 \boldsymbol{v} \tag{2.11}$$

This is substituted into equation 2.10, and a change of variables from time to distance is made using $1/dt = v_z/dz$, transforming the left hand side of equation 2.9 as follows:

$$\frac{d\boldsymbol{p}}{dt} = v_z \frac{d\boldsymbol{p}}{dz} = v_z \frac{d(\gamma m_0 \boldsymbol{v})}{dz} \tag{2.12}$$

The right side of equation 2.9 is simplified by neglecting the electric field term (no radiation field), and multiplying out the cross product. Since a planar

undulator is considered, only the B_y term is present, so $\boldsymbol{v} \times \boldsymbol{B} = -v_z B_y \hat{\boldsymbol{x}} + v_x B_y \hat{\boldsymbol{z}}$. Since the longitudinal velocity far exceeds the transverse velocity, $v_z \gg v_x$, the z-component can be neglected. Substituting in the undulator field description from equation 2.3, the Lorentz force equation becomes:

$$\frac{d(\gamma m_0 \boldsymbol{v})}{dz} = -e B_0 \sin(k_u z) \hat{\boldsymbol{x}} \tag{2.13}$$

Taking only the x-component, and rearranging gives:

$$\frac{dv_x}{dz} = -\frac{e B_0}{\gamma m_0} \sin(k_u z) \tag{2.14}$$

Integrating with respect to z gives the transverse component of the velocity, which is a sinusoidal oscillation in the horizontal plane:

$$v_x = -\frac{e B_0}{\gamma m_0 k_u} \cos(k_u z) \tag{2.15}$$

The maximum transverse velocity is therefore:

$$v_{x_{\max}} = \frac{e B_0}{\gamma m_0 k_u} \tag{2.16}$$

and using the small-angle approximation $v_x/v = \sin\theta \approx \theta$ it is seen that v_x/v is equal to the deflection angle, θ, of the electron path away from the undulator axis, with the maximum deflection angle:

$$\theta_{max} = \frac{e B_0}{\gamma m_0 c k_u} = \frac{K}{\gamma} \tag{2.17}$$

The meaning of the undulator K parameter which was previously introduced in equation 2.4 is now revealed to be a measure of the deflection angle scaled by the electron beam energy:

Using the K parameter in the transverse velocity equation gives:

$$v_x = -\frac{cK}{\gamma} \cos(k_u z) \tag{2.18}$$

Average longitudinal velocity

Since the transverse component of the velocity oscillates in a planar undulator through the $\cos(k_u z)$ term, it is reasonably straightforward to appreciate that

the longitudinal velocity must oscillate at twice this frequency. This can be demonstrated as follows:

$$v_z{}^2 = v^2 - v_x{}^2 \tag{2.19}$$

$$v_z{}^2 = c^2 \left(1 - \frac{1}{\gamma^2}\right) - \frac{c^2 K^2}{\gamma^2} \cos^2(k_u z) \tag{2.20}$$

Using a trigonometric identity for the cosine term, the oscillatory term is seen to emerge at twice the transverse oscillation frequency:

$$v_z{}^2 = c^2 \left(1 - \frac{1}{\gamma^2} - \frac{K^2}{\gamma^2} \left(\frac{\cos(2k_u z) + 1}{2}\right)\right) \tag{2.21}$$

Averaging over the oscillatory term can be carried out to define an average longitudinal velocity:

$$\bar{v}_z = c\sqrt{1 - \frac{1}{\gamma^2} - \frac{K^2}{2\gamma^2}} \tag{2.22}$$

$$\bar{v}_z \simeq c \left(1 - \frac{1 + K^2/2}{2\gamma^2}\right) \tag{2.23}$$

where the approximation $(1 - x)^n \simeq 1 - nx$ is used, and is valid since $\gamma \gg 1$

2.4.2 Helical undulator

For a helical undulator configured to generated circularly polarised light, the electron beam simply takes a sinusoidal path in both transverse planes, with a phase difference of $\pi/2$ between the two components. The analysis of the trajectory is similar to that of the planar undulator above, but is simplified by the fact that the electrons maintain a constant deflection angle. The longitudinal velocity is constant, so there is no factor of $1/2$ introduced in its derivation:

$$\bar{v}_z \simeq c \left(1 - \frac{1 + K^2}{2\gamma^2}\right) \tag{2.24}$$

2.4.3 Undulator vs Wiggler

As described in Section 2.3.2, synchrotron radiation emission is into a narrow cone of angle $1/\gamma$, so for $K < 1$ the electrons will overlap with the emitted radiation cone leading to interference effects; this case is termed an undulator. For $K > 1$ the electron deflection is greater than the emitted radiation cone

such that there will be little overlap and the output will be more like a series of independent source points; this case is termed a wiggler. The distinction is in reality a gradual transition [47], and has little significance in terms of FEL physics.

2.5 Low-gain FEL

The previous section described the electron trajectory through an undulator in the absence of a radiation field. Now the interaction between the electrons and a co-propagating radiation field is considered.

2.5.1 Energy exchange

As outlined in Section 2.3.2, a radiation field will be generated by the transverse electron oscillation. Or alternatively, a field may be injected from an external source to co-propagate with the electrons. In either case the electromagnetic field is described by a travelling sinusoidal wave:

$$\boldsymbol{E} = \hat{\boldsymbol{x}} E_0 \cos(kz - \omega t + \phi) \tag{2.25}$$

where $\omega = ck = (2\pi c)/\lambda$, and λ is the radiation wavelength.

Again the Lorentz force equation (2.9) is used, and the scalar product of both sides with $\boldsymbol{v}$ is taken to give the rate of energy transfer between the radiation field and the electrons. The magnetic field term is zero since the velocity is orthogonal to the force imposed by the field. Substituting in for $\boldsymbol{E}$ from equation 2.25 and $\boldsymbol{v}$ from 2.18 gives:

$$m_0 c^2 \frac{d\gamma}{dt} = \boldsymbol{F} \cdot \boldsymbol{v} = -e\boldsymbol{E} \cdot \boldsymbol{v} = -eE_0 \cos(kz - \omega t + \phi) \frac{cK}{\gamma} \cos(k_u z) \tag{2.26}$$

The product $\boldsymbol{F} \cdot \boldsymbol{v}$ can be either positive or negative, allowing energy exchange between electrons and radiation in either direction, i.e. electrons can lose energy to the field and decelerate, or gain energy from the field and be accelerated. For an electron bunch both processes can occur simultaneously with some electrons gaining and some losing energy. FEL operation requires achieving a net transfer of energy to the radiation field (though as an aside, another application, the 'inverse FEL' is a method of electron acceleration [48, 49]).

2.5.2 Resonance condition

For a significant energy exchange there must be a sustained interaction: $\boldsymbol{F} \cdot \boldsymbol{v}$ must remain positive or negative. This is not the case in general but can be shown to hold for certain 'resonant' conditions. Multiplying out the cosine terms in the energy exchange equation:

$$
\begin{aligned}
m_0 c^2 \frac{d\gamma}{dt} &= -\frac{ecKE_0}{\gamma} \cos(kz - \omega t + \phi) \cos(k_u z) \\
&= -\frac{ecKE_0}{2\gamma} \left[\cos((k + k_u)z - \omega t + \phi) + \cos((k - k_u)z - \omega t + \phi) \right]
\end{aligned}
$$

(2.27)

where the identity: $\cos\theta \cos\varphi = (\cos(\theta + \varphi) + \cos(\theta - \varphi))/2$ is used.

The second cosine term in equation 2.27 corresponds to a phase velocity $v_{\text{ph}} = \omega/(k - k_u) > \omega/k = c$, so is neglected here. The first cosine term corresponds to the 'ponderomotive wave' which has phase velocity $< c$, such that it is possible for it to match the electron velocity and allow sustained energy exchange. The phase $\theta = ((k + k_u)z - \omega t + \phi - \pi/2)$, is termed the ponderomotive phase. Taking the rate of change of the ponderomotive phase:

$$
\frac{d\theta}{dt} = (k + k_u)v_z - ck
$$

(2.28)

and using equation 2.23 for the average longitudinal velocity:

$$
\begin{aligned}
\frac{d\theta}{dt} &= (k + k_u) \left(\left(1 - \frac{1 + K^2/2}{2\gamma^2}\right) - ck \right. \\
&= ck \left(\frac{k_u}{k} - \frac{1 + K^2/2}{2\gamma^2} \right)
\end{aligned}
$$

(2.29)

A continuous energy exchange can occur with a stationary phase, $d\theta/dt = 0$, i.e.:

$$
\frac{k_u}{k} = \frac{1 + K^2/2}{2\gamma^2}
$$

(2.30)

Using $k_u/k = \lambda/\lambda_u$, equation 2.30 can be rearranged to give an equation for the resonant radiation wavelength for given electron energy and undulator parame-

ters:

$$\lambda_r = \frac{\lambda_u}{2\gamma^2}(1 + K^2/2) \tag{2.31}$$

For a helical undulator there is no factor on $1/2$ associated with the K^2 term. The reason for using the rms undulator parameter given in equation 2.5 is now clear - it allows a resonance condition to be written that holds for both planar and helical undulators:

$$\lambda_r = \frac{\lambda_u}{2\gamma^2}(1 + {a_u}^2) \tag{2.32}$$

Figure 2.1 indicates the undulator resonance condition. The resonance condition
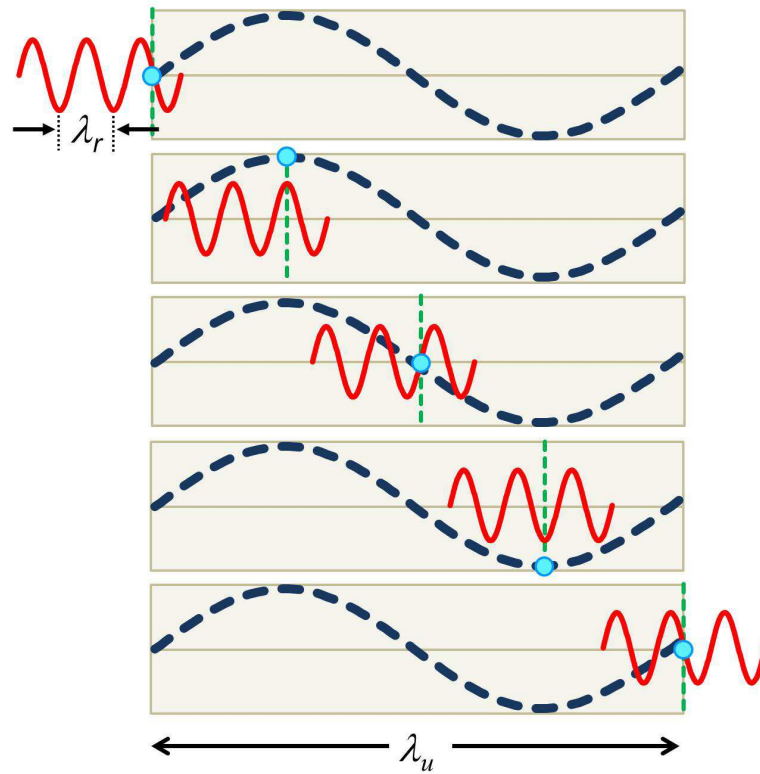
Figure 2.1: Figure to show the undulator resonance condition. Panels from top to bottom show propagation in time: as the electron (blue dot) propagates along its trajectory the transverse velocity (blue dashed line) is maintained in the same direction as the radiation electric field (red waveform)

corresponds to the case where the electrons slip back relative to the the radiation at a rate of one radiation wavelength per undulator period. As an alternative derivation it is fairly straightforward to show the following expression is equivalent

to equation 2.32:

$$\frac{\lambda_u}{v_z} = \frac{\lambda_r}{(c - v_z)} \tag{2.33}$$

The resonance condition can also be derived considering $1/\gamma$ length contraction of the undulator period in the electron frame, and a Doppler shift of the emitted radiation of $1/2\gamma$ back to the lab frame. Higher harmonics of the fundamental resonant wavelength will also be resonant.

2.5.3 Pendulum equations

The resonance condition allows a sustained energy exchange between electrons and the radiation field. The next step is to consider the effect this energy exchange has on the electrons. In this section a constant radiation field is assumed, which is a reasonable approximation for a low-gain FEL.

The electron energy, γ, is now defined as a variable with propagation through the undulator. A fixed term, γ_r, is introduced to represent the resonant energy. To simplify the phase equation, an electron energy variable, η, is introduced representing the normalised energy deviation from the resonant energy:

$$\eta = \frac{\gamma - \gamma_r}{\gamma_r} \tag{2.34}$$

Substituting in $\gamma = \gamma_r(\eta + 1)$ to the phase equation (2.29), using equation 2.30:

$$
\begin{aligned}
\frac{d\theta}{dt} &= ck \left(\frac{k_u}{k} - \frac{1 + K^2/2}{2\gamma_r{}^2(\eta + 1)^2} \right) \\
&= ck_u \left(1 - \frac{1}{(\eta + 1)^2} \right) \\
&= 2k_u c\eta
\end{aligned}
\tag{2.35}
$$

where the approximation $1/(1-x)^2 \approx 1 + 2x$ is used, and is valid for small energy deviation.

Having introduce the normalised energy deviation, η, the energy exchange equation 2.27 is put in terms of this variable:

$$\frac{d\eta}{dt} = \frac{1}{\gamma_r} \frac{d\gamma}{dt} \tag{2.36}$$

18

$$\frac{d\eta}{dt} = -\frac{1}{m_0 c^2} \frac{ecKE_0}{2\gamma\gamma_r} \sin(\theta) \qquad (2.37)$$

(note that a phase offset of $\pi/2$ was introduced in the definition of θ to aid the analogy to the pendulum equations).

Collecting together the constants in one variable, ϵ:

$$\epsilon = \frac{eE_0 K[JJ]}{2\gamma_r^2 m_0 c^2} \qquad (2.38)$$

where the [JJ] term is a difference of Bessel functions term to account for the oscillating part of the longitudinal motion:

$$K \to K[JJ], \quad [JJ] = J_0\left(\frac{K^2}{4 + 2K^2}\right) - J_1\left(\frac{K^2}{4 + 2K^2}\right) \qquad (2.39)$$

Making a change of variable from time, t, to distance through the undulator, z, leaves two simple equations to describe the electron energy and phase:

$$\frac{d\theta}{dz} = 2k_u\eta \qquad (2.40)$$

$$\frac{d\eta}{dz} = -\epsilon \sin\theta \qquad (2.41)$$

These equations are of identical form to those for describing a simple pendulum.

2.5.4 Energy-phase plot

The electron dynamics can be understood by considering a plot of the energy-phase plane (often referred to as a longitudinal phase space plot).

The electron phase is plotted on the horizontal axis and the electron energy deviation on the vertical, as shown in Figure 2.2. A phase extent of 2π, corresponds very closely to one radiation wavelength, so Figure 2.2 containing 3 ponderomotive buckets is a very short longitudinal slice of what is usually a much longer electron bunch. In this example the electrons are distributed evenly in phase, and with zero initial energy displacement.

Considering the central bucket, the system has a stable fixed point at (0,0) (corresponding to a pendulum hanging freely with no initial velocity), and an unstable fixed point at (0,π) corresponding to a pendulum starting at vertical. The dashed lines shows trajectories in the phase space, with the trajectory passing
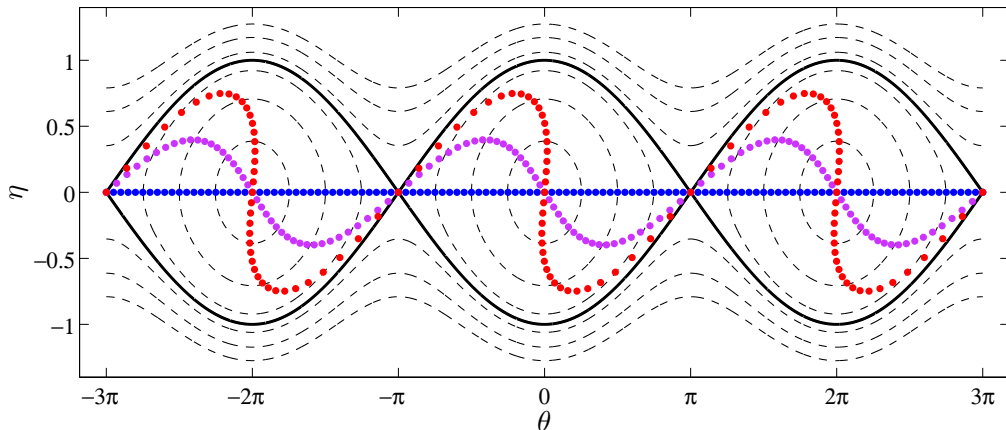
Figure 2.2: Low gain FEL electron evolution in longitudinal phase space. The dashed lines show electron trajectories in the phase space, and the black line shows the separatrix. The blue points represent the initial state of the electrons - evenly distributed in phase and with zero energy displacement. The purple points represent the electrons at an intermediate distance through the undulator when energy moduation has developed, and the red points represent a later point in the undulator when energy modulation has developed into density modulation (micro-bunching).

through the unstable fixed point termed the separatrix. The separatrix is defined by:

$$\eta = \pm\sqrt{\epsilon(1 + \cos\theta)/k_u} \qquad (2.42)$$

Electrons starting in the separatrix remain bounded within, and follow the defined trajectories such that energy modulation and then longitudinal density modulation (micro-bunching) occurs.

2.5.5 Gain/Loss

Further aspects of low-gain FELs are not considered in detail here, but can be found in a number of texts, e.g. [23]. Just one important point is made, and that is that micro-bunching alone (i.e. about $\theta = 0$) is insufficient for large energy transfer. Note that in the example shown with zero initial energy displacement (Figure 2.2), there is no net transfer of energy between the electrons and the radiation field: the system is symmetric with as many electrons gaining energy as those losing energy. An offset between the average rate of change of phase of the electrons and the ponderomotive wave is required for net energy transfer. For a low-gain amplifier FEL this means offsetting the electron beam energy from reso-

nance with the 'seed' radiation field (to positive values such that a greater number of electrons fall into the 0-π region losing energy). In an oscillator starting from noise, it is more intuitive to consider that gain occurs for radiation wavelengths offset from resonance. These two interpretations are shown in Figure 2.3.
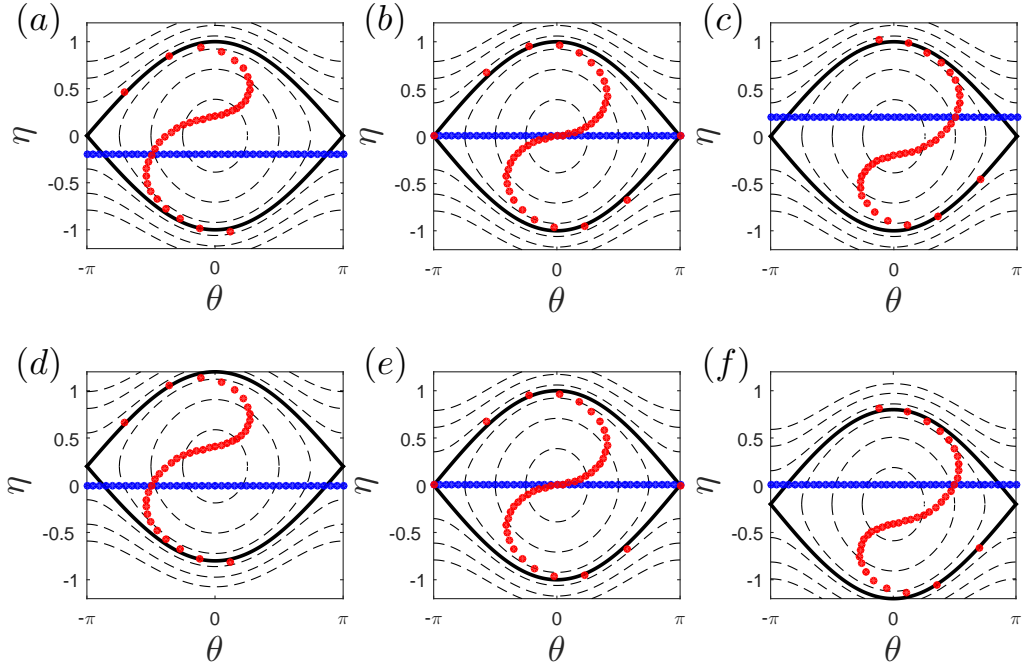
Figure 2.3: Low-gain FEL detuning. The plots show the longitudinal phase space of a low-gain FEL for various starting conditions. The blue points represent the initial state of the electrons - evenly distributed in phase and with zero energy displacement, and the red points represent a later point in the undulator. Plot (a) shows the electrons detuned to low energy relative to resonance with an external radiation field: the electrons have a net energy gain. Plot (b) shows zero detuning with zero net energy transfer, and plot (c) shows positive detuning with net energy loss - i.e. gain in the radiation field. Plots (d)-(f) represent a low gain FEL starting up from noise: it is more intuitive in this case to see the initial electron beam energy as fixed, and see that radiation gain occurs at wavelengths detuned from resonance - e.g. plot (f), while other wavelengths experience loss - e.g. plot (d), or no net change - plot (e).

2.6 Deriving the high-gain FEL equations

Though suitable for low-gain FELs, the pendulum model of the previous section is not fully self-consistent in that it assumes the radiation is kept constant during one undulator pass. A fully self-consistent model is required to describe the high-gain regime. In this section, the high-gain FEL equations are derived, starting with the introduction of the Maxwell wave equation, then a number of approximations are made to reduce the equations to a form that is simpler to solve and interpret.

2.6.1 Exponential form of the EM wave

The co-propagating electromagnetic field as described in equation 2.25 is a travelling sinusoidal wave. Using the exponential form of the cosine term:

$$\cos(x) = \frac{e^{ix} + e^{-ix}}{2};\tag{2.43}$$

and decomposing the field term into two parts: a fast oscillatory term, $e^{i(kz-\omega t)}$ (with wavenumber $k = \omega_r/c$), and a slowly varying complex envelope, $\tilde{E}(z,t) = \frac{E}{2}e^{i\phi}$ which defines the amplitude and phase, the field can now be written as:

$$E_x = \tilde{E}e^{i(kz-\omega t)} + \tilde{E}^*e^{-i(kz-\omega t)}\tag{2.44}$$

2.6.2 Maxwell wave equation

To include the effect of the electron beam on the radiation field, the Maxwell wave equation for the transverse electric field in the presence of a current source term is used:

$$\left[\frac{\partial^2}{\partial z^2} - \frac{1}{c^2}\frac{\partial^2}{\partial t^2} - \nabla_\perp^2\right]E_x = \frac{1}{\epsilon_0 c^2}\left[\frac{\partial J_x}{\partial t} + c^2\frac{\partial \rho_e}{\partial x}\right]\tag{2.45}$$

where $\nabla_\perp^2$ is the transverse Laplacian, ϵ_0 is the permittivity of free space, J_x is the transverse current density term, and ρ_e is the charge density. The transverse current density term is defined as:

$$J_x = -ecK\cos(k_u z)\sum_{j=1}^{N_e}\frac{1}{\gamma_j}\delta(\boldsymbol{x} - \boldsymbol{x}_j(t))\delta(z - z_j(t))\tag{2.46}$$

The charge density term in equation 2.45 can normally be dropped, on the basis that the effect is small relative to the transverse current effect [23].

2.6.3   Slowly varying envelope approximation

The slowly varying envelope approximation (SVEA) is a common approximation in FEL physics. By requiring the complex radiation envelope to vary slowly with respect to the radiation wavelength in both time and space, it allows the second order differential equations of the Maxwell wave equation to be reduced to first order.

Starting from the 3D Maxwell equation 2.45, the t and z operators are decomposed as follows:

$$\left(\frac{1}{c}\frac{\partial}{\partial t}\right)^2 - \left(\frac{\partial}{\partial z}\right)^2 = D_+ D_-$$
(2.47)

where:

$$D_+ = \frac{1}{c}\frac{\partial}{\partial t} + \frac{\partial}{\partial z}; \quad D_- = \frac{1}{c}\frac{\partial}{\partial t} - \frac{\partial}{\partial z}$$
(2.48)

The wave equation is therefore:

$$\left[D_+ D_- - \nabla_\perp^2\right] E_x = \frac{1}{\epsilon_0 c^2}\left[\frac{\partial J_x}{\partial t}\right]$$
(2.49)

Substituting in $E_x = \tilde{E}e^{i(kz-\omega t)} + \tilde{E}^*e^{-i(kz-\omega t)}$, and multiplying out the LHS gives:

$$
\begin{aligned}
&= \left[D_+ D_- - \nabla_\perp^2\right] E_x \\
&= \left[D_+ D_- - \nabla_\perp^2\right]\left(\tilde{E}e^{i(kz-\omega t)} + \tilde{E}^*e^{-i(kz-\omega t)}\right) \\
&= D_+ D_- \tilde{E}e^{i(kz-\omega t)} - \nabla_\perp^2 \tilde{E}e^{i(kz-\omega t)} + D_+ D_- \tilde{E}^*e^{-i(kz-\omega t)} - \nabla_\perp^2 \tilde{E}^*e^{-i(kz-\omega t)}
\end{aligned}
$$

The fundamental step of the SVEA is to show:

$$D_-[\tilde{E}e^{i(kz-\omega t)}] = \tilde{E}\underbrace{D_-[e^{i(kz-\omega t)}]}+e^{i(kz-\omega t)}D_-[\tilde{E}]$$

$$\underbrace{\frac{1}{c}\frac{\partial}{\partial t}e^{i(kz-\omega t)} - \frac{\partial}{\partial z}e^{i(kz-\omega t)}}$$

$$\underbrace{\frac{-i\omega}{c}e^{i(kz-\omega t)} - ike^{i(kz-\omega t)}}$$

$$- 2ike^{i(kz-\omega t)} \qquad \left(\text{using } \frac{\omega}{c} = k\right)$$

$$= -2ik\tilde{E}e^{i(kz-\omega t)} + e^{i(kz-\omega t)}D_-[\tilde{E}]$$

$$\approx -2ik\tilde{E}e^{i(kz-\omega t)} \tag{2.50}$$

where in the final step the second term is neglected on the basis that the change of the field envelope is small over one wavelength:

$$|D_-\tilde{E}| \ll k|\tilde{E}|$$

$$\left|\left(\frac{1}{c}\frac{\partial}{\partial t} - \frac{\partial}{\partial z}\right)\tilde{E}\right| \ll \frac{2\pi}{\lambda}|\tilde{E}| \tag{2.51}$$

This is the essence of the SVEA: it allows a second order expression to be reduced to first order. Further analysis of the expression shows that another term drops out in expanding the D_+ part:

$$D_+[\tilde{E}e^{i(kz-\omega t)}] = \tilde{E}\underbrace{D_+[e^{i(kz-\omega t)}]}+e^{i(kz-\omega t)}D_+[\tilde{E}]$$

$$\underbrace{\frac{1}{c}\frac{\partial}{\partial t}e^{i(kz-\omega t)} + \frac{\partial}{\partial z}e^{i(kz-\omega t)}}$$

$$\underbrace{\frac{-i\omega}{c}e^{i(kz-\omega t)} + ike^{i(kz-\omega t)}}$$

$$0 \qquad \left(\text{using } \frac{\omega}{c} = k\right)$$

$$= e^{i(kz-\omega t)}D_+[\tilde{E}] \tag{2.52}$$

such that the Maxwell equation simplifies to:

$$e^{i(kz-\omega t)}\left(-2ikD_+ - \nabla_\perp^2\right)\tilde{E} + e^{-i(kz-\omega t)}\left(2ikD_+ - \nabla_\perp^2\right)\tilde{E}^* = \frac{1}{\epsilon_0 c^2}\frac{\partial J_x}{\partial t} \tag{2.53}$$

Both sides are integrated using:

$$\frac{1}{\Delta t}\int_t^{t+\Delta t} dt e^{-i(kz-\omega t)}\bigg|_{\text{fixed z}} \tag{2.54}$$

The second term on the left hand side of 2.53 is a fast oscillating term which drops out [23], then using integration by parts:

$$\int u(x)v'(x) = u(x)v(x) - \int u'(x)v(x)dx \tag{2.55}$$

the RHS of equation 2.53 becomes:

$$\left(\frac{\frac{1}{\epsilon_0 c^2}}{\Delta t}\right)\left[e^{-i(kz-\omega t)}J_x - \int_t^{t+\Delta t} i\omega e^{-i(kz-\omega t)}J_x dt\right] \tag{2.56}$$

The first term in the square bracket drops out [23] leaving the RHS of equation 2.53 as:

$$-\frac{i\omega\frac{1}{\epsilon_0 c^2}}{\Delta t}\int_t^{t+\Delta t} e^{-i(kz-\omega t)}J_x dt \tag{2.57}$$

Substituting in for J_x:

$$-\frac{i\omega}{\epsilon_0 c^2}\frac{1}{\Delta t}\int_t^{t+\Delta t} e^{-i(kz-\omega t)}ecK\cos(k_u z)\sum_{j=1}^{N_e}\frac{1}{\gamma_j}\delta(\boldsymbol{x}-\boldsymbol{x}_j(t))\delta(z-z_j(t))dt \tag{2.58}$$

changing the variable of the delta function in z to t, and evaluating the integral to pick out a slice of the electron beam within $c\Delta t$ of the plane at z, equation 2.53 becomes:

$$(2ikD_+ + \nabla_\perp^2)\tilde{E} = \frac{i\omega}{\epsilon_0 c^2}\frac{1}{\Delta t}\frac{cK}{\gamma}\sum_{j\in[z,\Delta t]} e^{-i(kz-\omega t_j)}\cos(k_u z)\delta(\mathbf{x}-\mathbf{x_j}) \tag{2.59}$$

The exponential $(e^{-i(kz-\omega t_j)})$ and cosine $(\cos(k_u z))$ terms can be combined in terms of $\theta_j(z) = (k+k_u)z - ck\bar{t}_j(z)$ - the ponderomotive phase of the jth electron, and the average electron volume density, n_e, is introduced:

$$n_e(z - \bar{v}_z t, \mathbf{x}) = \frac{1}{\bar{v}_z\Delta t}\sum_{j\in[z,\Delta t]}\delta(\mathbf{x}-\mathbf{x_j}) \tag{2.60}$$

which results in a simple form of the Maxwell equation in the SVEA:

$$\left(\frac{\partial}{\partial z} + \frac{1}{c}\frac{\partial}{\partial t} + \frac{\nabla_\perp^2}{2ik} \right) \tilde{E} = \chi_2 \langle e^{-i\theta_j} \rangle_\Delta \tag{2.61}$$

where:

$$\chi_2 = \frac{eK[JJ]}{4\epsilon_0 \gamma} n_e(z - \bar{v}_z t, \boldsymbol{x}) \tag{2.62}$$

again using $K \to K[JJ]$, as per equation 2.39. The exponential term in equation 2.61 is the bunching parameter, b, a measure of the degree of micro-bunching in a slice, with magnitude varying between 0 (uniformly distributed) and 1 (fully bunched - all particles in a slice have the same phase):

$$\langle e^{-i\theta_j} \rangle_\Delta = b \tag{2.63}$$

Change of variables

The variables z and t are not ideal for describing an electron bunch propagating in a FEL, since they are coupled. To describe an electron at the head of the bunch relative to the centre can either be described as it being further progressed in z or that having reached a fixed point in z at an earlier time. It is therefore convenient to decouple these variables and work with one co-ordinate which describes the distance through the undulator, and another that is co-moving with the electron bunch and can therefore be used to describe distance and variations along the bunch. The electron energy equation is also written in terms of $\tilde{E}$ to reach a 'final' form of the FEL equations (before introducing universal scaling in the next section).

The change of variables is made from (z,t) to (z,θ), where $\theta = (k+k_u)(z-\bar{v}_z t)$ (which is the same as the ponderomotive phase defined previously.

$$\begin{aligned} \frac{\partial}{\partial z} &= \frac{\partial z}{\partial z}\frac{\partial}{\partial z} + \frac{\partial \theta}{\partial z}\frac{\partial}{\partial \theta} \\ &= \frac{\partial}{\partial z} + (k + k_u)\frac{\partial}{\partial \theta} \\ \frac{\partial}{\partial t} &= \frac{\partial \theta}{\partial t}\frac{\partial}{\partial \theta} \\ &= -(k + k_u)\bar{v}_z\frac{\partial}{\partial \theta} \end{aligned} \tag{2.64}$$

26

Collecting terms:

$$\frac{\partial}{\partial z} + \frac{1}{c}\frac{\partial}{\partial t} = \frac{\partial}{\partial z} + (k + k_u)\frac{\partial}{\partial \theta} - (k + k_u)\frac{\bar{v}_z}{c}\frac{\partial}{\partial \theta}$$
$$= \frac{\partial}{\partial z} + (k + k_u)\left(1 - \frac{\bar{v}_z}{c}\right)\frac{\partial}{\partial \theta}$$
$$= \frac{\partial}{\partial z} + k_u\frac{\partial}{\partial \theta} \tag{2.65}$$

using $v_z = ck/(k + k_u)$ to give $(k + k_u)(1 - \frac{\bar{v}_z}{c}) = k_u$ in the final step.

The Maxwell wave equation in SVEA becomes:

$$\left(\frac{\partial}{\partial z} + k_u\frac{\partial}{\partial \theta} + \frac{\nabla_\perp^2}{2ik}\right)\tilde{E} = \chi_2\langle e^{-i\theta_j}\rangle_\Delta \tag{2.66}$$

and the pendulum equations (2.40, 2.41) are re-stated with the energy equation given in exponential form and in terms of $\tilde{E}$:

$$\frac{d\theta}{dz} = 2k_u\eta \tag{2.67}$$

$$\frac{d\eta}{dz} = -\chi_1\left(\tilde{E}e^{i\theta} + \tilde{E}^*e^{-i\theta}\right) \tag{2.68}$$

where the parameter χ_1 is defined as:

$$\chi_1 = \frac{eK[JJ]}{2\gamma_0^2 mc^2} \tag{2.69}$$

Equations 2.66, 2.67, and 2.68 are the final 'non-scaled' form of the FEL equations before undertaking the universal scaling in the following section. The pendulum equations introduced in Section 2.5.3 (which didn't allow for field variation), are now coupled with the wave equation which describes how the field varies due to the electrons: the set of equations is now self-consistent.

2.6.4   Universal scaling

This section introduces a commonly used scaling of the FEL parameters, known as the universal scaling, developed by Bonifacio et al. [43]. This is a hugely useful approach that relates many of the properties of a high-gain FEL to a single parameter, ρ (called the FEL, Pierce, or simply ρ-parameter), which is a function of electron beam density and energy, undulator parameter and period, and fundamental constants. Fundamentally this introduces a scaling relative to the rate of amplification in the FEL. Doing this allows quick estimates of FEL performance over a wide range of operating parameters.

Scaled distance through the undulator

The distance through the undulator, z, is scaled as follows:

$$\bar{z} = \frac{4\pi\rho}{\lambda_u} z \tag{2.70}$$

where ρ, the fundamental FEL parameter is defined as:

$$\rho = \frac{1}{\gamma_r} \left(\frac{\bar{a}_u \omega_p}{4 c k_u} \right)^{\frac{2}{3}} \tag{2.71}$$

where the plasma frequency, ω_p is defined as:

$$\omega_p = \sqrt{\frac{e^2 n_p}{\epsilon_0 m}} \tag{2.72}$$

and n_p is the peak electron number density of the electron bunch.

Scaled co-moving co-ordinate

In Section 2.6.3 the co-ordinate system was changed from (z,t) to (z,θ), where θ is the ponderomotive phase. It is also useful to define a co-moving distance, z_1. First a non-scaled version is defined as follows:

$$z_1 = z - \bar{v}_z t \tag{2.73}$$

This z_1 parameter is then scaled relative to the wavelength of the ponderomotive field, $\lambda = \bar{\beta}_z \lambda_r$, which is very close to λ_r for typical FEL parameters:

$$\bar{z}_1 = \frac{4\pi\rho}{\bar{\beta}_z \lambda_r} z_1 \approx \frac{4\pi\rho}{\lambda_r} z_1 \qquad (2.74)$$

Hence the scaled distance along the bunch $\bar{z}_1$ takes a similar form to the scaled distance along the undulator $\bar{z}$. It is also useful to express a relation between $\bar{z}_1$ and the ponderomotive phase):

$$\theta = \frac{\bar{z}_1}{2\rho} \qquad (2.75)$$

Scaled phase equation

The change of variables $z \to \bar{z}$ is now made in the equation for the rate of change of phase (2.67):

$$\frac{d\theta}{dz} = \frac{d\bar{z}}{dz}\frac{d\theta}{d\bar{z}} = 2k_u\rho\frac{d\theta}{d\bar{z}} = 2\eta k_u$$

to give the scaled form of the rate of change of phase equation:

$$\frac{d\theta}{d\bar{z}} = p \qquad (2.76)$$

where p is the normalised electron energy deviation from the resonant energy scaled by the FEL parameter:

$$p = \frac{\eta}{\rho} \qquad (2.77)$$

Scaled energy exchange equation

The change of variables $z \to \bar{z} = 2k_u\rho z$ and $\eta \to p = \eta/\rho$ are made in the energy exchange equation (2.68) as follows:

$$\frac{d\eta}{dz} = \frac{dp}{d\bar{z}}\frac{d\eta}{dp}\frac{d\bar{z}}{dz}$$

which, using $\dfrac{d\eta}{dp} = \rho$ and $\dfrac{d\bar{z}}{dz} = 2k_u\rho$, gives:

$$\frac{d\eta}{dz} = 2k_u\rho^2\frac{dp}{d\bar{z}} \qquad (2.78)$$

and so yields the scaled form of the energy exchange equation:

$$
\begin{aligned}
\frac{dp}{d\bar{z}} &= -\frac{\chi_1}{2k_u\rho^2}\left(\tilde{E}e^{i\theta} + \tilde{E}^*e^{-i\theta}\right) \\
&= -Ae^{i\theta} - A^*e^{-i\theta}
\end{aligned}
\tag{2.79}
$$

where the complex scaled field amplitude is defined as:

$$
A = \frac{\chi_1}{2k_u\rho^2}\tilde{E}
\tag{2.80}
$$

Scaled wave equation

The final equation to be converted to the scaled units is the wave equation (2.66). The variable change is from $z \to \bar{z} = 2k_u\rho z$ and $\theta \to \bar{z}_1 = 2\rho\theta$. The partial derivatives convert as follows:

$$
\begin{aligned}
\frac{\partial}{\partial z} &= \frac{\partial \bar{z}}{\partial z}\frac{\partial}{\partial \bar{z}} = 2k_u\rho\frac{\partial}{\partial \bar{z}} \\
\frac{\partial}{\partial \theta} &= \frac{\partial \bar{z}_1}{\partial \theta}\frac{\partial}{\partial \bar{z}_1} = 2\rho\frac{\partial}{\partial \bar{z}_1}
\end{aligned}
$$

The wave equation becomes:

$$
\left(2k_u\rho\frac{\partial}{\partial \bar{z}} + 2k_u\rho\frac{\partial}{\partial \bar{z}_1} + \frac{\nabla_\perp^2}{2ik}\right)\tilde{E} = \chi_2\langle e^{-i\theta_j}\rangle_\Delta
\tag{2.81}
$$

Substituting in for $\tilde{E} = (2k_u\rho^2/\chi_1)A$ and rearranging gives the scaled form of the wave equation:

$$
\begin{aligned}
\left(\frac{\partial}{\partial \bar{z}} + \frac{\partial}{\partial \bar{z}_1} + \frac{\nabla_\perp^2}{4ikk_u\rho}\right)A &= \frac{\chi_1\chi_2}{4k_u^2\rho^3}\langle e^{-i\theta_j}\rangle_\Delta \\
&= \langle e^{-i\theta_j}\rangle_\Delta
\end{aligned}
\tag{2.82}
$$

Where the collection of constants on the RHS is set to 1 through the choice of definition of the ρ-parameter.

Definition of the ρ-parameter

The dimensionless ρ-parameter is therefore:

$$
\rho = \left[\frac{\chi_1\chi_2}{(2k_u)^2}\right]^{\frac{1}{3}}
\tag{2.83}
$$

As well as the two forms of the ρ parameter given in equation 2.71, and equation 2.83 other forms are often used, and can be shown to be equivalent:

$$\rho = \left(\frac{e^2 K^2 [JJ]^2 n_e}{32\epsilon_0 \gamma^3 mc^2 k_u^2} \right)^{\frac{1}{3}} \tag{2.84}$$

$$= \left[\frac{1}{8\pi} \frac{I}{I_A} \left(\frac{K[JJ]}{1 + K^2/2} \right)^2 \frac{\gamma \lambda^2}{\sum_A} \right]^{\frac{1}{3}} \tag{2.85}$$

$$= \left[\left(\frac{I}{I_A} \right) \left(\frac{\lambda_u K[JJ]}{2\pi \sigma_x} \right)^2 \left(\frac{1}{2\gamma} \right)^3 \right]^{\frac{1}{3}} \tag{2.86}$$

where $I_A = ec/r_e = 17.045 kA$ is the Alfven current, and $\sum_A = 2\pi \sigma_x^2$ is the cross sectional area of the beam. The ρ-parameter is typically in the range $10^{-4} - 10^{-3}$ for short wavelength high-gain FELs.

Summary of the scaled FEL equations

The scaled FEL equations (2.76, 2.79, 2.82) derived over the course of the previous sections are now collected together for convenience. Note that j-subscripts are included to denote individual electrons in the electron equations.

$$\frac{d\theta_j}{d\bar{z}} = p_j \tag{2.87}$$

$$\frac{dp_j}{d\bar{z}} = -Ae^{i\theta_j} - A^* e^{-i\theta_j} \tag{2.88}$$

$$\left(\frac{\partial}{\partial \bar{z}} + \frac{\partial}{\partial \bar{z}_1} + \frac{\nabla_\perp^2}{4ikk_u\rho} \right) A = \langle e^{-i\theta_j} \rangle_\Delta \tag{2.89}$$

2.7 Solving the FEL equations

The FEL equations derived in the previous section have been reduced from second-order to first-order, but still involve non-linear terms.There are $2N_e + 1$ coupled equations, where N_e, the number of electrons for a real bunch is very large! $N_e \approx 10^9$). Solving such a large set of non-linear equations is not open to analytic solution, so must be solved numerically using simulation codes. However, for certain conditions the FEL equations can be solved analytically. In this section the the FEL equations are solved via linearising in terms of a significantly reduced number of 'collective' variables as introduced by Bonifacio et al. [43], and following the approaches of [24] and [25]. Solutions are found via Laplace transforms and other methods to yield both qualitative insights into the high-gain FEL physics (i.e. that exponential amplification can occur), as well as quantitative information on the growth rate etc.

2.7.1 From 3D to 1D

To simplify matters, transverse effects are neglected here, thereby converting the problem from 3D to 1D. The 1D high gain theory [43] provides a useful picture of the FEL process, and the basic FEL process does not change, though growth rates etc. must be modified to account for 3D effects [50].

2.7.2 From time-dependent to steady-state

Another simplification is to assume that there is no variation in any parameters along the bunch. This assumption allows the derivative of A with respective to $\bar{z}_1$ to be neglected [51]. This condition is referred to as the 'steady-state'. The more complete picture including variations along the bunch is referred to as the time-dependent case, and is covered in Section 2.10.

2.7.3 Steady-state 1D FEL equations

The scaled FEL equations (2.87, 2.88, 2.89) are converted from 3D to 1D by neglecting the $\frac{\nabla_\perp^2}{4ikk_u\rho}$ term and removing $\bar{z}_1$ dependence in equation 2.89:

$$\frac{d\theta_j}{d\bar{z}} = p_j \tag{2.90}$$

$$\frac{dp_j}{d\bar{z}} = -Ae^{i\theta_j} - A^*e^{-i\theta_j} \tag{2.91}$$

$$\frac{dA}{d\bar{z}} = \langle e^{-i\theta_j}\rangle_\Delta \tag{2.92}$$

2.7.4 Linear Analysis

In this section linear analysis is performed by examining the behaviour of the equations in the presence of a small perturbation to their initial conditions. A function $f(x)$, is considered to be composed on a fixed initial value, f_0, and a small perturbation, $f_1(x) \ll 1$:

$$f(x) = f_0 + f_1(x) \tag{2.93}$$

In this way, the initial values of the scaled radiation field, electron energy and phase to be A_0, $p_{0j} = \delta$, and $\theta_{0j} + \delta\bar{z}$ respectively, and small perturbations, $p_{1j}(\bar{z})$ and $\theta_{1j}(\bar{z})$ are applied to the electron variables, such that the following values for $A(\bar{z})$, $p_j(\bar{z})$ and $\theta_j(\bar{z})$ are used in the linearisation:

$$A(\bar{z}) = A_0 \tag{2.94}$$

$$p_j(\bar{z}) = \delta \qquad\qquad + p_{1j}(\bar{z}) \tag{2.95}$$

$$\theta_j(\bar{z}) = \underbrace{\theta_{0j} + \delta\bar{z}}_{\text{initial values}} \quad \underbrace{+\theta_{1j}(\bar{z})}_{\text{perturbation}} \tag{2.96}$$

where the detuning parameter δ is introduced, which describes the energy offset of the electron beam relative to the resonant wavelength of the radiation field (and the consequent effect on the phase via the $\delta\bar{z}$ term). The detuning parameter is important for giving an understanding of FEL behaviour and is defined as follows:

$$\delta = \frac{1}{2\rho}\frac{\langle\gamma\rangle_0^2 - \gamma_r^2}{\gamma_r^2} \approx \frac{1}{\rho}\frac{\langle\gamma\rangle_0 - \gamma_r}{\gamma_r} \tag{2.97}$$

with the approximate relation is valid where $(\langle\gamma\rangle_0 + \gamma_r) \approx 2\gamma_r$, i.e. a narrow wavelength range: $(\langle\gamma\rangle_0 - \gamma_r)/\gamma_r \ll 1$.

At this stage dot notation is introduced for derivatives with respect to $\bar{z}$, e.g. $\dot{A} = \dfrac{dA}{d\bar{z}}$.

Linearisation of $\dot{A}$

The field equation is analysed by substituting equation 2.96 for $\theta_j(\bar{z})$ into equation 2.92:

$$
\begin{aligned}
\dot{A} &= \langle e^{-i(\theta_0 + \delta\bar{z} + \theta_1)} \rangle \\
&= \langle e^{-i(\theta_0 + \delta\bar{z})} e^{-i\theta_1} \rangle \\
&= \langle e^{-i(\theta_0 + \delta\bar{z})} (1 - i\theta_1) \rangle \\
&= \underbrace{\langle e^{-i(\theta_0 + \delta\bar{z})} \rangle}_{=\,0} \underbrace{-\langle i\theta_1 e^{-i(\theta_0 + \delta\bar{z})} \rangle}_{=\,b}
\end{aligned}
\tag{2.98}
$$

where the approximation $e^{-i\theta_1} \approx 1 - i\theta_1$ is used, and is valid since $\theta_1 \ll 1$. The first term on the RHS of equation 2.98 is equal to zero since (before the perturbation) the electrons are assumed to be uniformly distributed in phase. The second term on the RHS is defined as a collective variable representing the electron beam bunching, as in equation 2.63. Here the bunching parameter is:

$$
b \equiv -\langle i\theta_1 e^{-i(\theta_0 + \delta\bar{z})} \rangle
\tag{2.99}
$$

and the equation for $\dot{A}$ is now:

$$
\dot{A} = b
\tag{2.100}
$$

34

Linearisation of $\dot{p}$

The energy equation is analysed by substituting the perturbed value of θ_j (equation 2.96) into the $\dot{p}$ equation (2.91):

$$
\begin{aligned}
\dot{p}_j &= -Ae^{i\theta_j} - A^* e^{-i\theta_j} \\
&= -Ae^{i(\theta_0 + \delta\bar{z} + \theta_1)} - A^* e^{-i(\theta_0 + \delta\bar{z} + \theta_1)} \\
&= -Ae^{i(\theta_0 + \delta\bar{z})} \underbrace{-iA\theta_1 e^{i(\theta_0 + \delta\bar{z})}}_{\text{second order}} - A^* e^{-i(\theta_0 + \delta\bar{z})} \underbrace{+iA^*\theta_1 e^{-i(\theta_0 + \delta\bar{z})}}_{\text{second order}}
\end{aligned}
$$

where the 'second order' terms can be ignored since θ_1 is small. Noting that $\dot{p}_j = \dot{p}_1$, and multiplying both sides by $e^{-i(\theta_{0j} + \delta\bar{z})}$ gives:

$$
e^{-i(\theta_{0j} + \delta\bar{z})}\dot{p}_1 = -A - A^* e^{-2i(\theta_{0j} + \delta\bar{z})} \tag{2.101}
$$

Averaging over all electrons, the second term on the RHS again disappears to zero due to the initial uniform distribution of electrons in phase:

$$
\langle e^{-i(\theta_{0j} + \delta\bar{z})}\dot{p}_1 \rangle = -A \tag{2.102}
$$

A second collective variable, P, a phase-momentum average, is introduced in order to simplify further:

$$
P \equiv \langle p_1 e^{-i(\theta_0 + \delta\bar{z})} \rangle \tag{2.103}
$$

which is of similar form to the bunching collective variable previously defined. Equation 2.102 is simplified by differentiating and rearranging P as follows:

$$
\begin{aligned}
\dot{P} &= \langle \dot{p}_1 e^{-i(\theta_0 + \delta\bar{z})} \rangle - \langle i\delta p_1 e^{-i(\theta_0 + \delta\bar{z})} \rangle \\
\dot{P} &= -A - i\delta P \tag{2.104}
\end{aligned}
$$

which is the second of the linearised equations.

Linearisation of $\dot{\theta}$

Finally the $\dot{\theta}$ equation (2.90) is linearised. Substituting in for the perturbed values:

$$\dot{\theta} = p_j$$

$$\frac{d}{d\bar{z}}(\theta_0 + \delta\bar{z} + \theta_1) = \delta + p_1$$

which gives:

$$\dot{\theta}_1 = p_1 \tag{2.105}$$

This result is then used in differentiating b, in order to give an expression in terms of the collective variables already defined:

$$\dot{b} = -\langle i\dot{\theta}_1 e^{-i(\theta_0 + \delta\bar{z})}\rangle - \langle \delta\theta_1 e^{-i(\theta_0 + \delta\bar{z})}\rangle$$
$$\dot{b} = -\langle ip_1 e^{-i(\theta_0 + \delta\bar{z})}\rangle - i\delta b$$
$$\dot{b} = -iP - i\delta b \tag{2.106}$$

Summary of the linearised equations

The linearised equations are collected here for ease of reference:

$$\dot{A} = b \tag{2.107}$$
$$\dot{P} = -A - i\delta P \tag{2.108}$$
$$\dot{b} = -iP - i\delta b \tag{2.109}$$

2.7.5 Solution of the linear equations for $\delta = 0$

As a first case, the equations are analysed for the case of $\delta = 0$. The linear equations reduce to:

$$\dot{A} = b \tag{2.110}$$

$$\dot{P} = -A \tag{2.111}$$

$$\dot{b} = -iP \tag{2.112}$$

These three first order equations can be collected into one third order equation in terms of A by differentiating equation (2.110) twice, substituting in equation (2.112) differentiated, and then substituting in equation (2.111):

$$\dddot{A} = \ddot{b} = -i\dot{P}$$
$$\dddot{A} = iA \tag{2.113}$$

Inserting a trial solution of the form:

$$A(\bar{z}) = A_0 e^{i\lambda\bar{z}} \tag{2.114}$$

the derivatives of A are as follows:

$$\dot{A} = i\lambda A_0 e^{i\lambda\bar{z}} = i\lambda A \tag{2.115}$$

$$\ddot{A} = -\lambda^2 A_0 e^{i\lambda\bar{z}} = -\lambda^2 A \tag{2.116}$$

$$\dddot{A} = -i\lambda^3 A_0 e^{i\lambda\bar{z}} = -i\lambda^3 A \tag{2.117}$$

Equating equations (2.113) and (2.117) yields the cubic dispersion relation:

$$\lambda^3 + 1 = 0 \tag{2.118}$$

There are three solutions for λ - one real and two complex, each with magnitude equal to one, and evenly distributed angularly in the complex plane:

$$\lambda_1 = -1 \tag{2.119}$$

$$\lambda_2 = \frac{1}{2} + \frac{i\sqrt{3}}{2} \tag{2.120}$$

$$\lambda_3 = \frac{1}{2} - \frac{i\sqrt{3}}{2} \tag{2.121}$$

Inserted back into the trial solution:

$$A_0 e^{i\lambda_1 \bar{z}} = A_0 e^{-i\bar{z}} \tag{2.122}$$

$$A_0 e^{i\lambda_2 \bar{z}} = A_0 e^{\frac{i\bar{z}}{2}} e^{-\frac{\sqrt{3}\bar{z}}{2}} \tag{2.123}$$

$$A_0 e^{i\lambda_3 \bar{z}} = A_0 e^{\frac{i\bar{z}}{2}} e^{\frac{\sqrt{3}\bar{z}}{2}} \tag{2.124}$$

it is seen that λ_1 corresponds to an oscillatory mode with constant magnitude. The second solution, λ_2 exhibits exponential decay, and the third solution, λ_3 exhibits exponential growth - the key feature of the high-gain FEL. Note that it is the negative imaginary component of λ_3 which leads to exponential growth.

The general solution is a linear combination of the three independent solutions:

$$A(\bar{z}) = A_0 \sum_k c_k e^{i\lambda_k \bar{z}} \tag{2.125}$$

Solving the system via Fourier-Laplace transforms [25], shows that for initial conditions $A \neq 0$, $b_0 = 0$ and $P_0 = 0$ the coefficients c_k all equal $1/3$, so the power is distributed evenly between the modes. Figure 2.4 shows the radiation
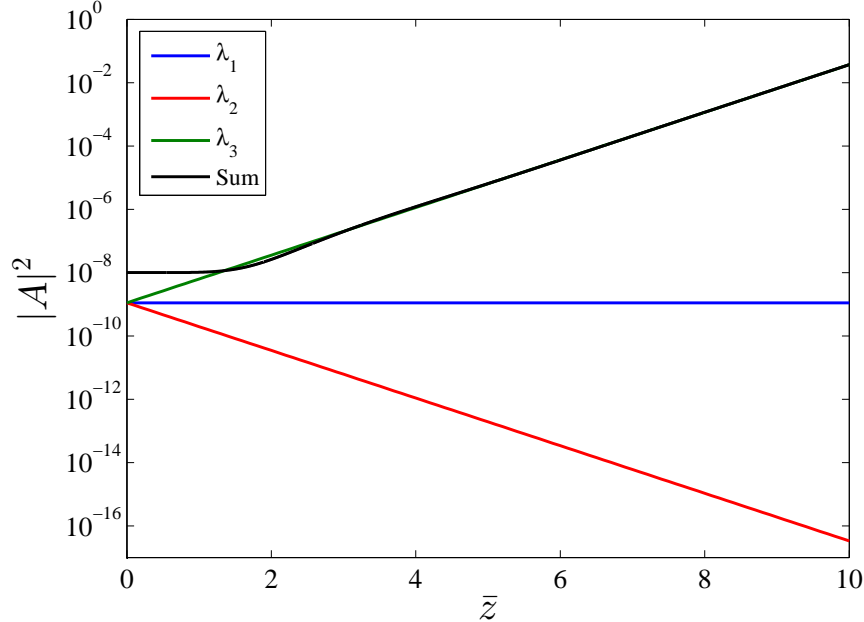
Figure 2.4: Radiation intensity ($|A|^2$) evolution with scaled distance through the undulator $\bar{z}$, for the three solutions of the cubic dispersion equation for $\delta = 0$, and their sum. For $\bar{z} \gtrsim 2$ the exponential growth ($\lambda 3$) term dominates. $A_0 = 10^{-4}$ and $c_{1,2,3}=1/3$

intensity evolution for each of the three components individually, and combined. Is is seen that the total radiation intensity - the sum of the three solutions - does not grow significantly until $\bar{z} \approx 2$. This is commonly referred to as the 'lethargy' region. For $\bar{z} \gtrsim 2$ the exponential growth ($\lambda 3$) term dominates and the sum of the three components tends towards this.

Solution in terms of initial conditions

Though the general solution of equation 2.125 requires a detailed analysis to find the co-efficients $c_{1,2,3}$, some simple manipulation (following [23]) allows a solution to be found in terms of the initial conditions of the collective variables (A_0, b_0, P_0). Inserting $\bar{z} = 0$ into equation 2.125 and its derivatives yields:

$$A(0) = A_0[c_1 + c_2 + c_3] \tag{2.126}$$

$$\left. \frac{dA}{d\bar{z}} \right|_0 = \quad b(0) = iA_0[\lambda_1 c_1 + \lambda_2 c_2 + \lambda_3 c_3] \tag{2.127}$$

$$\left. \frac{d^2 A}{d\bar{z}^2} \right|_0 = -iP(0) = -A_0[\lambda_1^2 c_1 + \lambda_2^2 c_2 + \lambda_3^2 c_3] \tag{2.128}$$

and using:

$$\frac{1}{\lambda_k^2} = -\lambda_k \tag{2.129}$$

the coefficients can be expressed in terms of the initial conditions:

$$\sum_k c_k = \frac{1}{3A_0} \sum_k \left(A(0) - i\frac{b(0)}{\lambda_k} - iP(0)\lambda_k \right) \tag{2.130}$$

such that the general solution becomes:

$$A(\bar{z}) = \frac{1}{3} \sum_k \left(A(0) - i\frac{b(0)}{\lambda_k} - iP(0)\lambda_k \right) e^{i\lambda_k \bar{z}} \tag{2.131}$$

The dependence on each of the initial conditions is now considered independently. Figure 2.5 shows the radiation intensity $|A|^2$ as a function of distance through the undulator $\bar{z}$ for each of the initial conditions in turn (e.g. $A_0 = 10^{-4}$, $b_0 = P_0 = 0$), It is seen that for $\bar{z} \gtrsim 2$ the three solutions converge as the exponential growth (λ_3) term dominates. An important consequence is that exponential growth of the radiation intensity can start up from either an initial radiation field (e.g. an external seed), or from the intrinsic noise in the electron beam (electrons not
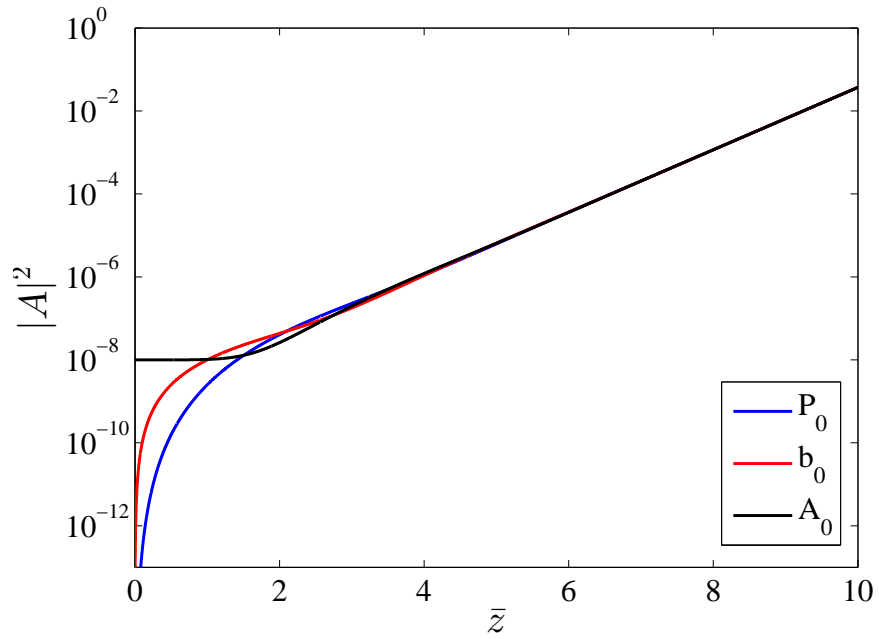
Figure 2.5: Radiation intensity ($|A|^2$) evolution with scaled distance through the undulator $\bar{z}$, for the general solution of the cubic dispersion equation for $\delta = 0$, starting from each of the initial conditions $A_0 \neq 0$, $b_0 \neq 0$, $P_0 \neq 0$. For $\bar{z} \gtrsim 2$ the three solutions converge as the exponential growth ($\lambda 3$) term dominates. The value of the initial condition is 10^{-4} in each case, with the other two terms set to zero.

uniformly distributed in phase), i.e. $b_0, P_0 \neq 0$. This so called 'shot-noise' is the mode of start-up for short wavelength FELs where no external seed field is available.

2.7.6 Solution of the linear equations for $\delta \neq 0$

The case of solving the linear FEL equations in the case that the detuning parameter, δ, is not necessarily equal to zero, is now considered. This allows the FEL behaviour to be analysed across a range of electron energies relative to the resonant radiation wavelength (or vice versa), and therefore gives a deeper insight into FEL behaviour.

Simple approach

A similar approach as in Section 2.7.5 is followed, whereby the field equation is differentiated twice. It is convenient in the case of $\delta \neq 0$ to make a further change of variables as follows:

$$\tilde{A} = A e^{i\delta\bar{z}} \tag{2.132}$$

Substituting into the linear radiation equation 2.107 gives:

$$
\begin{aligned}
\dot{A} &= b \\
\frac{d}{d\bar{z}} \tilde{A} e^{-i\delta\bar{z}} &= b \\
\dot{\tilde{A}} e^{-i\delta\bar{z}} - i\delta e^{-i\delta\bar{z}} \tilde{A} &= b \\
(\dot{\tilde{A}} - i\delta\tilde{A}) e^{-i\delta\bar{z}} &= b \\
\dot{\tilde{A}} - i\delta\tilde{A} &= b e^{i\delta\bar{z}}
\end{aligned} \tag{2.133}
$$

Differentiating again:

$$
\begin{aligned}
\ddot{\tilde{A}} - i\delta\dot{\tilde{A}} &= \dot{b} e^{i\delta\bar{z}} + i\delta b e^{i\delta\bar{z}} \\
&= (\dot{b} + i\delta b) e^{i\delta\bar{z}} \\
&= -iP e^{i\delta\bar{z}}
\end{aligned}
$$

And one more time:

$$
\begin{aligned}
\dddot{\tilde{A}} - i\delta\ddot{\tilde{A}} &= -i(\dot{P} e^{i\delta\bar{z}} + i\delta P e^{i\delta\bar{z}}) \\
&= -i(\dot{P} + i\delta P) e^{i\delta\bar{z}} \\
& \quad -i(-\tilde{A} e^{-i\delta\bar{z}}) e^{i\delta\bar{z}}
\end{aligned}
$$

Giving:

$$\dddot{\tilde{A}} - i\delta\ddot{\tilde{A}} - i\tilde{A} = 0 \tag{2.134}$$

Again inserting the trial solution (2.114), the dispersion relation is obtained:

$$\lambda^3 - \delta\lambda^2 + 1 = 0 \tag{2.135}$$

which of course reduces to the previous dispersion relation (2.118) for $\delta = 0$. The cubic dispersion relation either has three distinct real roots, in which case the general solution is a sum of oscillatory terms i.e. no exponential growth, or one real and two complex conjugate terms, in which case the complex root with negative imaginary component gives rise to an exponential increase. Mathematica was used to determine the roots of the dispersion equation (2.135) as a function of the detuning parameter. Figure 2.6 shows the real and imaginary parts of the three roots.
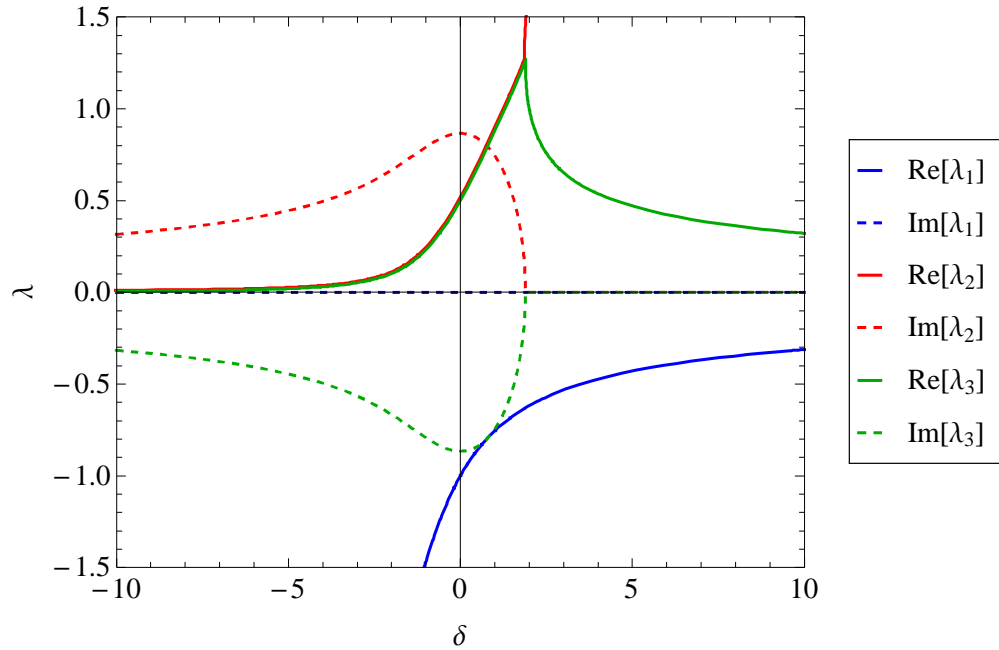
Figure 2.6: Roots of the dispersion function.

Of the three roots, λ_1 is real for all values of δ. The other two roots λ_2 and λ_3 consist of both real and imaginary parts below the threshold value $\delta_T = 1.89$, and are real above this threshold. Again the negative imaginary part of λ_3 is the critical term which gives exponential growth. Looking at the variation of this

term with δ it is seen that there is no exponential growth above $\delta_T = 1.89$, and the maximum growth rate (i.e. most negative value) is at $\delta = 0$.

Brief description of Laplace transform approach

A full solution of the linear equations may be obtained by Laplace transforms [25]. An overview of this approach is given here, and has been used to generate Figures 2.7 and 2.8. The Laplace transform, and its application to a differential is as follows:

$$
\begin{aligned}
\mathcal{L}[f(t)](s) &= \int_0^\infty f(t)e^{-st}dt \\
\mathcal{L}[f'(t)]| &= \int_0^\infty \frac{df}{dt}e^{-st}dt \\
&= e^{-st}f(t)\big|_0^\infty - \int_0^\infty [-se^{-st}]f(t)dt \\
&= \lim_{t\to\infty} \underbrace{e^{-st}f(t)} - \underbrace{e^{-s.0}f(0)} + s\underbrace{\int_0^\infty f(t)e^{-st}dt} \\
&= \qquad 0 \qquad\quad -f(0) \qquad + s\mathcal{L}[f(t)]|_s \qquad (2.136)
\end{aligned}
$$

which gives the general result for a Laplace transform of a differential:

$$
\mathcal{L}_{x\to s}\frac{df(x)}{dx} = s\acute{f}(s) - f(x_0) \qquad (2.137)
$$

Applying Laplace transforms to both sides of the linear equations (2.107-2.109):

$$
\begin{aligned}
s\acute{A} &= \acute{b} + A_0 & (2.138) \\
s\acute{P} &= -\acute{A} - i\delta\acute{P} + P_0 & (2.139) \\
s\acute{b} &= -i\acute{P} - i\delta\acute{b} + b_0 & (2.140)
\end{aligned}
$$

Putting everything in terms of $\acute{A}$, and making a change of variables from $s \to p$, where $p = \delta - is$:

$$
\acute{A} = \frac{P_0 - pb_0 - ip^2 A_0}{p^3 - \delta p^2 + 1} \qquad (2.141)
$$

where it is noted that the denominator is the same as the dispersion equation. The inverse Laplacian is:

$$
A = \frac{1}{2\pi i}\int_{\gamma-i\infty}^{\gamma+i\infty} e^{s\bar{z}}f(s)ds \qquad (2.142)
$$

43

such that the equation for A is:

$$A = \frac{1}{2\pi i} \int_{i\gamma-\infty}^{i\gamma+\infty} i e^{i(p-\delta)\bar{z}} \frac{P_0 - pb_0 - ip^2 A_0}{p^3 - \delta p^2 + 1} dp \qquad (2.143)$$

The integral can be evaluated by applying the residue integration theorem [25]:

$$A = \sum \text{Res}[i e^{i(p-\delta)\bar{z}} f(p)] \qquad (2.144)$$

The poles are simply the roots found in the previous section. Mathematica was used to evaluate the residues for the case of an initial radiation field only (i.e. $b_0 = P_0 = 0$), and this allows A to be found, and hence the intensity $|A|^2$. The gain, G, is defined as the fractional increase in radiation intensity in passing through the undulator:

$$G = \frac{|A|^2 - |A_0|^2}{|A_0|^2} \qquad (2.145)$$

The gain as a function of δ is plotted in Figure 2.8 for three different values of $\bar{z}$ corresponding to low gain ($\bar{z} = 0.5$), intermediate gain ($\bar{z} = 2$) and high gain ($\bar{z} = 10$). The transition from low to high gain is visualised in Figure 2.7.
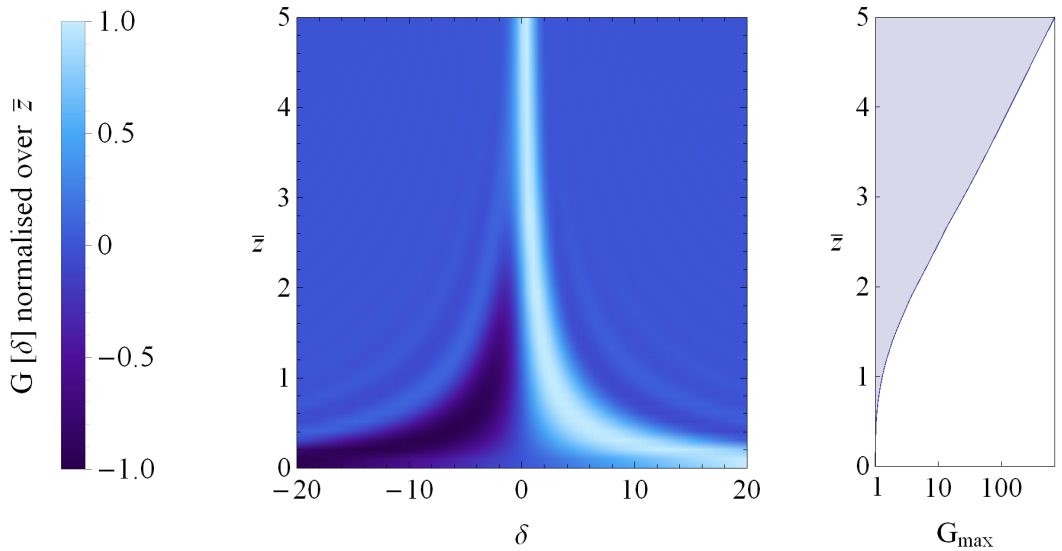
Figure 2.7: Transition of the FEL from low to high gain: the colour density plot shows gain against electron detuning for $\bar{z}$ from 0 to 5. The gain as a function of δ is normalised to its maximum value at a given $\bar{z}$. The maximum gain value as a function of $\bar{z}$ is given on the right.
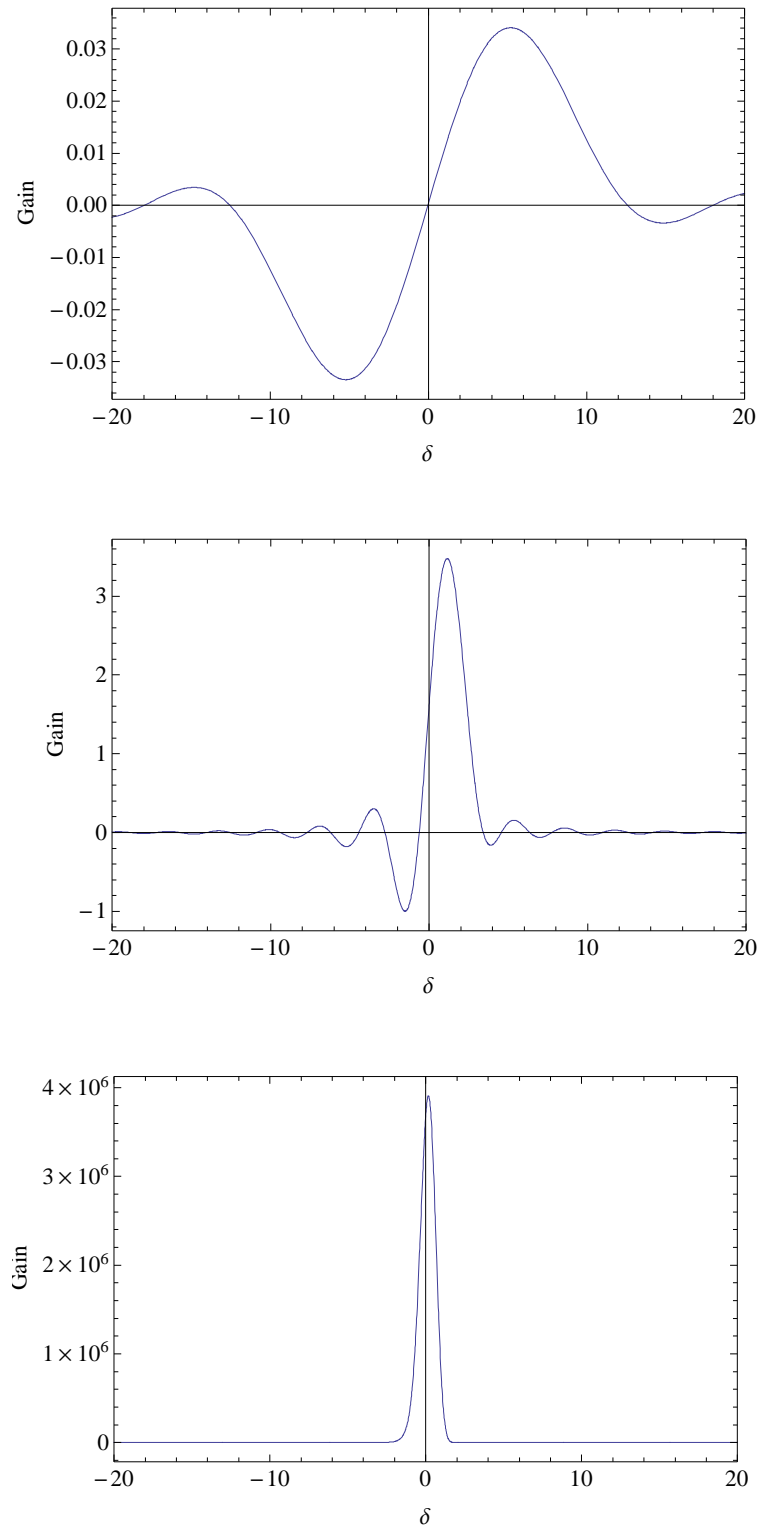
Figure 2.8: Gain versus detuning for three different values of $\bar{z}$ corresponding to low gain ($\bar{z} = 0.5$), intermediate gain ($\bar{z} = 2$) and high gain ($\bar{z} = 10$)

45

2.8 Qualitative description of the high-gain FEL

In the previous sections, the equation describing the high-gain FEL have been derived and solved. In the next section the consequent properties will be described quantitatively. Before that, this section gives a qualitative description of the high-gain process.

Figure 2.9 shows the evolution of the longitudinal phase space in a high-gain FEL. The electrons are initially approximately uniformly distributed longitudinally, as shown in Figure 2.9 (a). In practice there will also be finite energy spread as shown in the figure, though this has not been considered in the analysis. The system starts up from either a radiation ('seed') field, or from shot noise in the electron bunch. Exponential growth occurs as a three-step process in which positive feedback gives rise to a collective instability [15]:

- The interaction of the electrons with the radiation field within the undulator causes energy modulation of the beam on the scale of the radiation wavelength, λ_r.

- The energy modulation evolves into density modulation (micro-bunching) since the higher energy electrons are deflected less by the undulator field and propagate forwards relative to the lower energy electrons.

- The density modulation of the electrons leads to coherent emission, and enhanced radiation intensity.

A more subtle point to note is that by following through one loop of the 3-step process in the equations 2.110-2.112, there is a $\pi/2$ phase difference incurred. In this case the radiation drives energy modulation, which drives bunching, which then emits $\pi/2$ out of phase with the initial radiation. It can be interpreted that the additional emission causes a phase change of the radiation, which then allows gain [14]. Another way of considering this is that the phases of the three components reach an equilibrium with bunching occurring at a phase corresponding to gain, with some similarity to the required phase for gain in the low-gain FEL (Figure 2.3).

The exponential amplification cannot continue indefinitely and eventually saturates as shown in Figure 2.9 (f). The phase space at saturation is shown in Figure 2.9 (e). The electrons approach maximal bunching ($b = 1$), and the mean relative energy loss approaches ρ: a significant offset from resonance.
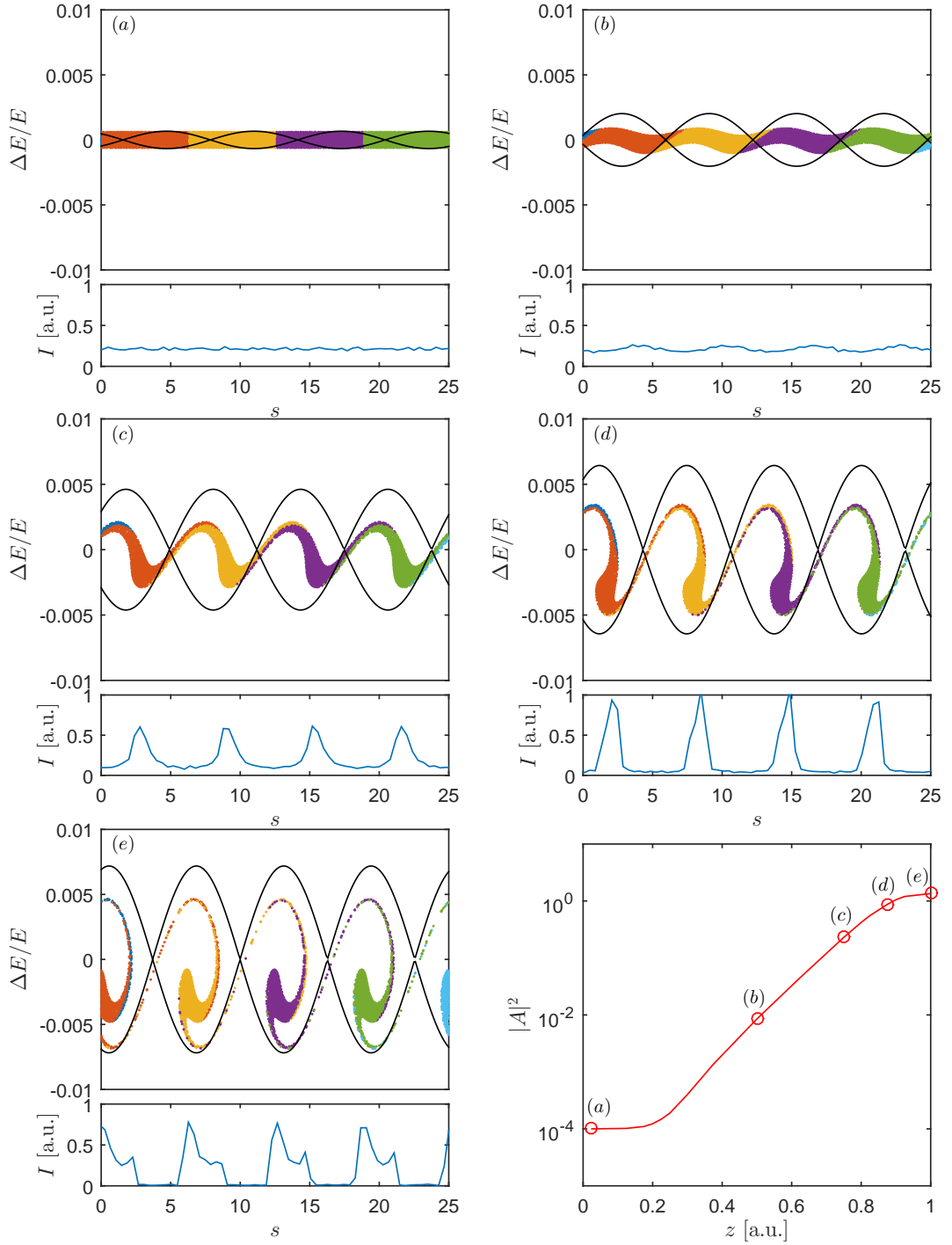
Figure 2.9: High-gain FEL longitudinal phase space evolution. Plots (a)-(e) show the longitudinal phase space (and the corresponding density modulation below) at different points in the high-gain amplification process, as indicated in the plot of radiation intensity against distance through the undulator (bottom right panel). Plot (a) is the initial condition of the electron beam, (b) and (c) are during the exponential growth phase as modulation and bunching grow, plot (d) is the start of saturation as the electrons become maximally bunched, and (e) is into saturation, as the phase space continues to evolve with little power growth. Different slices of the electron bunch are marked in different colours.

2.9 High-gain FEL properties

In this section, the properties of the FEL output radiation are described, following on from the solutions of the FEL equations.

2.9.1 Growth rate

In Section 2.7.5 the solutions of the FEL equations were found, and it was shown in equation 2.124 that there is an exponentially growing solution:

$$A = A_0 e^{\frac{i\bar{z}}{2}} e^{\frac{\sqrt{3}\bar{z}}{2}} \tag{2.146}$$

The scaled radiation intensity growth, taking into account the co-efficients, is:

$$|A(\bar{z})|^2 = \frac{1}{9}|A_0|^2 e^{\sqrt{3}\bar{z}} \tag{2.147}$$

and reverting to non-scaled units using $\bar{z} = 2k_u\rho z$, the 1D power gain length is found to be:

$$L_G = \frac{\lambda_u}{4\pi\sqrt{3}\rho} \tag{2.148}$$

such that in SI units the power grows with z as:

$$P_{\text{rad}} \propto e^{z/L_G} \tag{2.149}$$

The universal scaling of Section 2.6.4 can now be seen in context as a scaling in terms of a nominal gain length, $l_g = \sqrt{3}L_G$:

$$l_g = \frac{\lambda_u}{4\pi\rho} \tag{2.150}$$

2.9.2 Bandwidth

The bandwidth of the high-gain FEL can be obtained [51] by considering the variation of the negative imaginary part of the λ_3 root with the detuning, δ, in Figure 2.6:

$$\text{Im}(\lambda) \simeq \frac{\sqrt{3}}{2}\left(1 - \frac{\delta^2}{9}\right) \tag{2.151}$$

The power in terms of $\bar{z}$ and δ can be expressed:

$$|A(\bar{z}, \delta)|^2 \simeq \frac{|A_0|^2}{9} \exp\left[\sqrt{3}\left(1 - \frac{\delta^2}{9}\right)\bar{z}\right] \tag{2.152}$$

and the rms bandwidth, σ_λ can be calculated with distance through the undulator:

$$\sigma_\lambda \simeq \sqrt{\frac{\rho}{N_u}} \simeq 2\rho\sqrt{\frac{\pi}{\bar{z}}} \tag{2.153}$$

The system typically saturates at $\bar{z} \simeq 10$, hence the bandwidth at saturation is $\sigma_\lambda \simeq \rho$.

2.9.3 Saturation power

The FEL power can be estimated by considering the maximum bunching of the system [23]. The scaled FEL equations each have co-efficients equal to one, so A, b, and P exponentially increase together with the same magnitude. There is however, a maximum bunching that can occur, with all electrons perfectly in phase, corresponding to $b = 1$. Therefore the maximum A and P values are also ~ 1.

The scaled field amplitude (equation 2.80), $A = \tilde{E}(\chi_1/2k_u\rho^2)$, can be used to find the field energy density, U:

$$U = 2\epsilon_0 \tilde{E}\tilde{E}^* = 2\epsilon_0\rho\frac{4k_u^2\rho^3}{\chi_1^2} = 2\epsilon_0\rho\frac{\chi_2}{\chi_1} = \rho n_e mc^2\gamma \tag{2.154}$$

where $n_e mc^2\gamma$ is the electron beam energy density - hence ρ is the saturation efficiency. The power of the radiation beam is therefore:

$$P_{\text{rad}} = \rho P_{\text{beam}} = \rho I[\text{A}]E[\text{eV}] \tag{2.155}$$

The ρ-parameter (Section 2.6.4) therefore sets the efficiency, and is typically in the range $10^{-4} - 10^{-3}$ for short wavelength high-gain FELs. Tapering the undulator parameter can be used to enhance the efficiency [41].

2.10 Temporal properties - SASE

In solving the FEL equations (Section 2.7), the steady-state assumption was made, that there is no variation in any parameters along the bunch. This assumption allowed the derivative of A with respective to $\bar{z}_1$ to be neglected in equation 2.89. This thesis is concerned with the longitudinal properties of the FEL output - i.e. the pulse duration. In order to study this, the more complete picture including variations along the bunch is required. This is referred to as the time-dependent case.

Key to understanding the temporal properties is the slippage effect, introduced in Section 2.5.2. In the undulator, a resonant radiation wavefront propagates forward relative to the electrons at a rate of one radiation wavelength, λ_r per undulator period, λ_u. This relative propagation, or slippage in one nominal gain length l_g is called the 'co-operation length' [52]:

$$l_c = \lambda_r/4\pi\rho \tag{2.156}$$

The default operating mode of high-gain amplifier FELs is self-amplified spontaneous emission (SASE) (as described by Bonifacio et al. [43]). In this mode the FEL starts up from random density fluctuations in the electron beam, so initially has a very spiky temporal profile with very limited temporal coherence, as shown in Figure 2.10 (a). The slippage of the radiation through the electron bunch has the effect of increasing the range of the temporal coherence. However, since exponential amplification takes place as slippage occurs, the forward-propagating radiation only has a limited range of influence, dictated by $\sim l_c$. The electron bunch is typically relatively long with respect to $\sim l_c$, so the temporal profile of the SASE radiation consists of a series of spikes of duration $\sim l_c$, with phase coherence within a spike but random phase relation from one spike to the next, as shown in Figure 2.10 (b). More detailed analysis shows the maximum peak to peak distance of SASE spikes is $2\pi l_c$ [53], and that the coherence length of the system, $l_{coh} \simeq 3.2 l_c$ [24].

The co-operation length is an important characteristic of the high-gain FEL. The implications for generating ultra-short pulses of light from FELs are considered in more depth is Chapter 3. The temporal properties of the FEL can be improved by use of an external seed field at a higher level than the shot noise

power. However it will be seen that the co-operation length still dictates the minimum pulse duration from the system (Figure 6.1).
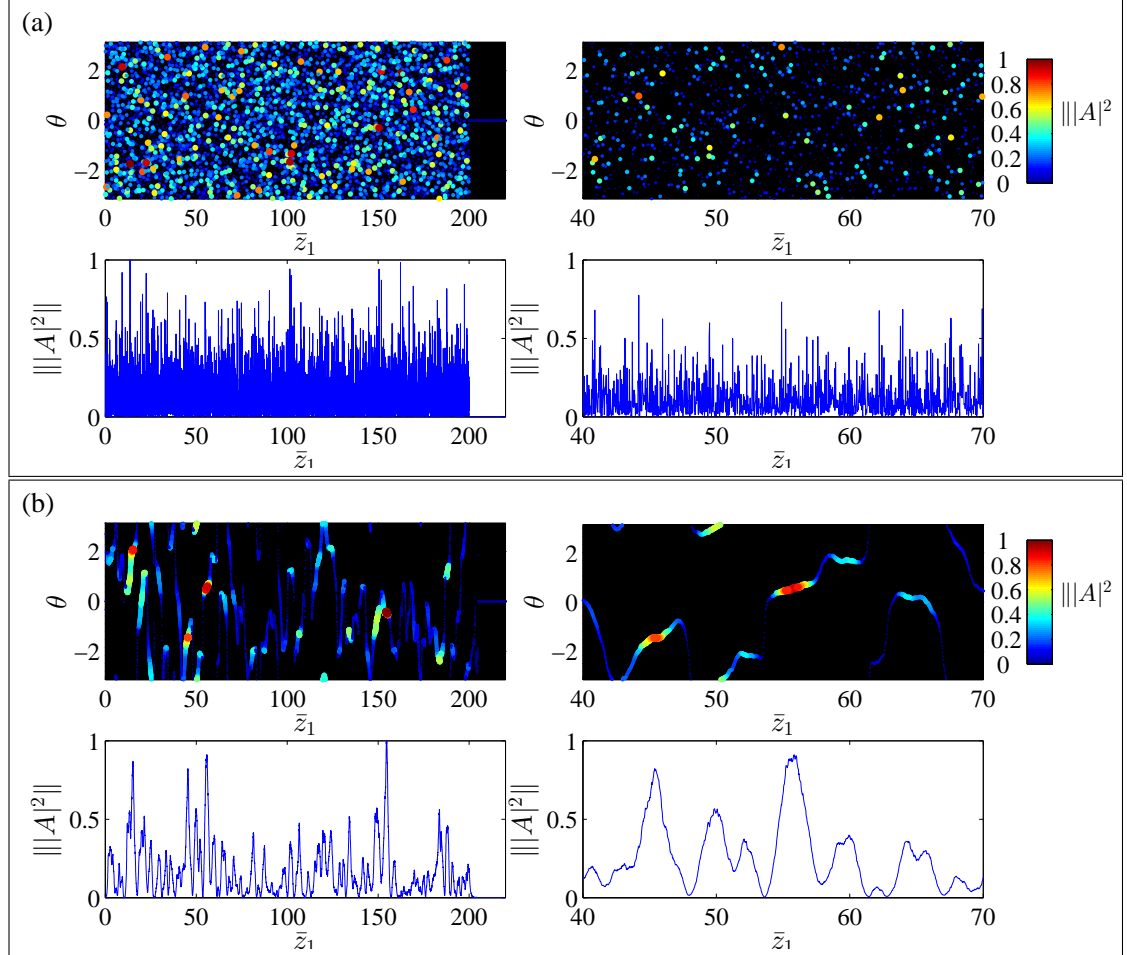
Figure 2.10: Radiation phase (top) and normalised intensity (bottom) after (a) 10 undulator periods and (b) 200 undulator periods ($\bar{z} = 5$) for simulations of a SASE FEL with FEL parameter $\rho = 2 \times 10^{-3}$. A sequence of autonomous regions of length $\approx 2\pi l_c$ develop. In the phase plots, the size and colour of the plotted points are related to the radiation intensity to ease identification of the peaks. The plots on the left show the full temporal window of the simulation, and the plots on the right show an inset of this.

2.10.1   Symmetry between radiation and electron beam

The temporal profile of the electron beam properties is also notable. Whereas in conventional lasers it seems a distinction is often made when discussing the radiation and the gain medium, in the FEL the two are a combined system with approximately symmetric temporal properties. For example the phase and intensity profiles of the radiation are mirrored in the bunching phase and magnitude

profiles of the electron beam. Note that an example of this is shown later in Figure 6.1. The fact that there are two similar copies of the temporal information has significance for FEL techniques involving multiple stages since it means that either radiation or electron beam can be used to transmit information between stages. The two copies can also be offset and overlapped to improve the temporal coherence [54].

In Chapters 8 and 9, it will be shown that this symmetry can be broken to generate ultra-short regions of electron bunching, which can subsequently be used to generate ultra-short pulses of radiation.

2.11   FEL modelling

Computer modelling is the main tool for much of the work reported in this thesis. There are numerous FEL codes available. In general they work by solving the wave equation 2.66 and the pendulum equations 2.67, and 2.68, usually using 'macro-particles' to represent typically thousands of electrons. Different codes make various approximations to meet different requirements, e.g. in some cases steady-state modelling is sufficient. However, for the work in this thesis - concerned with pulse duration - time-dependent modelling is required, and two main codes have been used for this: 'mlsase', and 'Genesis 1.3'.

The 'mlsase' code is a one-dimensional model, meaning 3D effects are disregarded allowing it to be relatively quick to run. It is an adapted version of the code 'FELO' [55] which was originally written to model oscillator FELs. The code solves the scaled FEL equations (2.87, 2.88, 2.89) (neglecting the transverse dependence). It subdivides the system into a series of slices corresponding to ponderomotive buckets and numerically integrates the system with a standard 4th order Runge-Kutta method. The radiation field is shifted forward in z_1 by one radiation wavelength per undulator period by a simple array shift. The code can also model chicanes inserted within break sections in the undulator by use of additional shifts of the radiation field relative to the electrons, together with the application of the appropriate longitudinal dispersive effect (energy dependent phase change). A Matlab version of the code (originally written in Fortran 90) was developed in the course of the thesis, and was used for some of the results.

Genesis 1.3 [56] is a widely used 3D FEL code, which has been extensively

benchmarked against experiments. It works in a similar way to the 1D mlsase code described above, but with the inclusion of 3D effects such as radiation diffraction, and transverse electron beam extent (and consequently the necessary quadrupole focusing etc.). It works in SI units, rather than the scaled units of the 1D code.

The 1D code is typically used for initial investigations since it is quicker to run, while Genesis is used to test the impact of 3D effects for the final results.

Chapter 3

Existing Concepts for Short Pulses from FELs

3.1 Introduction

In Section 1.4 it was outlined how the short wavelength and high peak power of FELs give them the potential to generate ultra-short pulses of light - conceivably orders of magnitude shorter than from existing sources. A number of schemes have been devised to deliver short pulses from FELs, some of which have been tested in experiments and many which have not.

This chapter gives an overview of the field. The aim is to classify concepts into several broad groups and examine the potential of each, with some of the methods highlighted. In Section 3.3, particular attention is given to one particular scheme - the mode-locked amplifier FEL [57], which serves as the starting point for much of the work in this thesis. Some of the content of this chapter has been published in [58].

3.1.1 Pulse duration in cycles

The first point to note when discussing short pulses in the context of FELs is wavelength dependence. This issue was also highlighted in Section 1.2 with regard to the history of short pulse development. The duration of a pulse of light is its wavelength, λ_r multiplied by the number of optical cycles, N, divided by the speed of light. FELs operate over a very large wavelength range, and attaining a pulse of N cycles clearly corresponds to a shorter absolute pulse duration at a

shorter wavelength facility than a longer wavelength one.

The shortest wavelength FEL facilities (down to $\sim$ 0.1 nm) are dedicated 'user' facilities, which limits the available time for testing new concepts. Longer wavelength machines, by virtue of requiring lower electron beam energy, are less costly and more appropriate for acting as dedicated facilities for testing new concepts. For example, the UK FEL test facility CLARA [59] - currently under development - will focus on such experiments, and will operate down to $\sim$ 100 nm.

The vast wavelength range of FELs means it is difficult to compare FEL schemes in terms of absolute pulse duration without consideration of wavelength. For this reason it is a more meaningful comparison to consider short pulses relative to the FEL co-operation length, l_c (equation 2.156), where $\sim 2\pi l_c$ typically sets the shortest possible pulse from the system, and in terms of optical cycles.

3.2 FEL short pulse methods

In FELs, there are several scales of what is meant by 'short pulses', and many methods proposed to generate them. This section examines some of the present methods, and challenges in progessing to shorter pulse durations.

3.2.1 SASE

The default operating mode of the high-gain FEL is self-amplified spontaneous emission (SASE), as described in Section 2.10. The electron bunch length effectively sets the overall radiation pulse duration, and the radiation pulse consists of many radiation spikes, each of length $\sim 2\pi l_c$.

In an example of pushing this technique to very short pulses, the LCLS facility has delivered few-fs radiation pulses, through the use of few-fs electron bunches [60]. However, this is still long in terms of optical cycles ($\sim$ 5000), and relative to $2\pi l_c$ (typically a few hundred cycles), hence the output still consists of multiple phase-uncorrelated spikes. A schematic example of SASE output is shown in Figure 3.1 (a), compared to other short pulse methods.

3.2.2 Slicing a Single SASE Spike

Since each SASE spike can be considered to act independently, it has been proposed by a number of groups e.g. [53, 61, 62, 63, 64] that only one spike can be

made to occur, either by reducing the bunch length (so called 'single-spike SASE') or by slicing the electron beam quality. Experimental progress has been made for a few of these methods, including reducing the electron bunch length [60], and by slicing part of the beam via emittance spoiling [63, 65]. A short-pulse technique using 'chirped' electron beams (variation of electron beam energy along the bunch) and a tapered undulator has been demonstrated at visible wavelengths [66, 67] and could be extended to x-ray.

A number of such proposals (e.g. by Saldin et al. [61]) suggest using a few-cycle conventional laser pulse to pick out part of the electron beam, as shown in Figure 3.1 (b), which has the advantage of generating a radiation pulse synchronised to the external source.

Picking out one SASE spike for present hard x-ray FEL parameters corresponds to a few hundred optical cycles or $\sim$100 as, which would be close to the frontier presently set by HHG, and at shorter wavelength and higher photon flux (methods are predicted to reach normal SASE saturation power levels or even higher). This class of techniques therefore has exceptional promise, however in terms of shortest pulse duration there is still potential for a further two orders of magnitude reduction by reducing the number of cycles per pulse. Possible methods of doing this are considered in the following sections.

3.2.3 Issues in generating few-cycle pulses from FEL amplifiers

Exponential amplification of the radiation power in an FEL amplifier requires a sustained interaction between the radiation field and the electron bunch. This presents a difficulty for generating few-cycle radiation pulses from FELs, since the slippage of the radiation relative to the electrons means that a few-cycle radiation pulse can only interact with a fixed point in the electron beam for a few undulator periods before slipping ahead of it.

For example if we were to use one of the methods described in the previous section, but were to slice a high quality section of the electron beam much shorter than one SASE spike (e.g. a few cycles) then the rapid slippage of the generated radiation ahead of the high quality region would significantly inhibit FEL amplification [53, 68].

(a) SASE:

P

Many radiation spikes each with
duration ≈ few hundred × λ_r

S

The electron bunch is relatively long, e.g. ~few fs = ~10000 × λ_r (not to scale)

(b) Slicing:

P

Region of higher quality electron beam
selected by e.g. interaction with a few-
cycle conventional laser pulse

Isolated radiation pulse with
duration ≈ few hundred × λ_r

S

(c) Mode-locked:

P

Multiple few-cycle regions of
higher quality electron beam

Train of radiation pulses each
with duration ≈ few × λ_r

S

Figure 3.1: Figure to illustrate different concepts for FEL operation (not to scale): (a) Typical hard x-ray SASE FEL output consists of a number of radiation spikes, each of length $\sim 2\pi l_c$ (a few hundred optical cycles); (b) Example of proposals to 'slice' the electron bunch such that a single pulse of length $\sim 2\pi l_c$ (a few hundred optical cycles) is generated; (c) The mode-locked FEL concepts work by slicing the electron bunch into regions $\ll 2\pi l_c$, and periodically shifting the radiation to generate a pulse train with pulses on a similarly short scale.

3.2.4 Superradiant regime

Another route to pulses shorter than $\sim 2\pi l_c$ may be the superradiant regime in a seeded FEL amplifier, which has been addressed in theory [69, 70], and in experiment, with short pulses generation observed in both direct seeding [71, 72] and harmonic cascade [73, 74] configurations. In such techniques a short section of an electron bunch is seeded such that it reaches saturation before the rest of

the bunch (which starts up from noise). Beyond saturation the FEL interaction proceeds into the superradiant regime in which the radiation intensity continues to increase (though quadratically with distance through the undulator, z, rather than exponentially), and the pulse length reduces as $z^{-1/2}$.

Compared to the exponential regime, where the 'centre-of-mass' of a radiation spike is kept close to the electron longitudinal velocity due to amplification, in this mode the radiation pulse propagates closer to the speed of light, i.e. forward relative to the electrons. Consequently it propagates into 'fresh' electrons, provided the rest of the bunch starting from noise has not reached saturation.

The superradiant technique has been demonstrated at longer wavelengths [71, 72, 73, 74], however its scalability to hard x-ray wavelengths still requires significant development. Few-cycle pulses have been attained via superradiance in FEL oscillators, however FEL oscillators operating at x-ray wavelengths are still under development [75, 76], and present ideas for suitable mirror cavities have very narrow bandwidth which would seem incompatible with the broad-band operation required for few-cycle pulses.

3.2.5 Externally imposed microbunching

An alternative might be to disregard FEL amplification to establish microbunching, and instead use external light sources with longer pulse duration (though this itself may be a FEL) and electron bunch manipulation in order to induce microbunching (or a single sharp current spike) over a region only a few cycles in length and then make it radiate in an undulator, as shown in Figure 3.2. There are several proposals to do this, such as by Zholents and Fawley [77] or by Xiang et al. [78], though again the slippage has a limiting effect.

A significant point to note is that if the number of undulator periods in the radiator is greater than the number of cycles in the microbunched region, then the slippage effect dominates and lengthens the pulse. The undulator must therefore be similarly short - also a few periods - otherwise slippage of the radiation relative to the electrons broadens the pulse. As a consequence proposals for this class of technique typically predict relatively low power compared to FEL saturation. There also remains significant technical challenges in imposing microbunching to the shortest wavelengths of FELs.
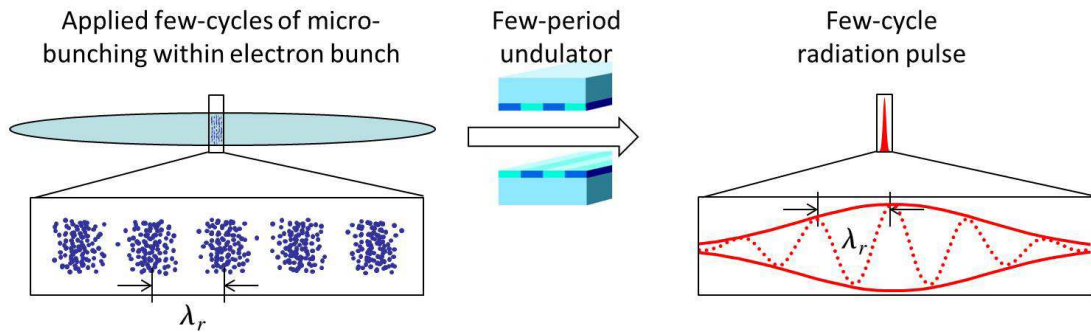
Figure 3.2: Figure to illustrate a concept to generate an isolated few-cycle pulse from an electron bunch. Instead of using the FEL interaction, an external light source and electron bunch manipulation are used to induce microbunching over a region only a few cycles in length, followed by a few-period undulator to emit a few-cycle pulse.

3.2.6 Trade-off between power and pulse duration?

The slippage of the radiation ahead of the electrons seems to imply a trade-off between maximising the emitted power (requiring a long interaction), and minimising the pulse duration (requiring a short interaction). It will be seen that the concepts considered in the next section and the remainder of the thesis could allow both high power and few-cycle pulses.

59

3.3 A route to few-cycle pulses - mode-locked amplifier

In the final section of this chapter another route towards few-cycle pulses from FELs is introduced - the mode-locked amplifier FEL [57], which is the starting point for much of the work in this thesis.

3.3.1 Mode-locked amplifier FEL concept

The mode-locked amplifier FEL [57] (ML-FEL) is a proposed technique that applies concepts from mode-locked cavity lasers, in order to generate a train of pulses with lengths less than the co-operation length, l_c. In this technique, a series of spatio-temporal shifts are introduced between the radiation and the co-propagating electron bunch that define a set of axial radiation modes. The modes are 'locked' by modulating the electron beam energy to deliver a clean series of pulses. Figure 3.3 shows both the schematic layout and expected output for a conventional SASE FEL, a case where only the spatio-temporal shifts are introduced (termed 'mode-coupled') and the mode-locked case.
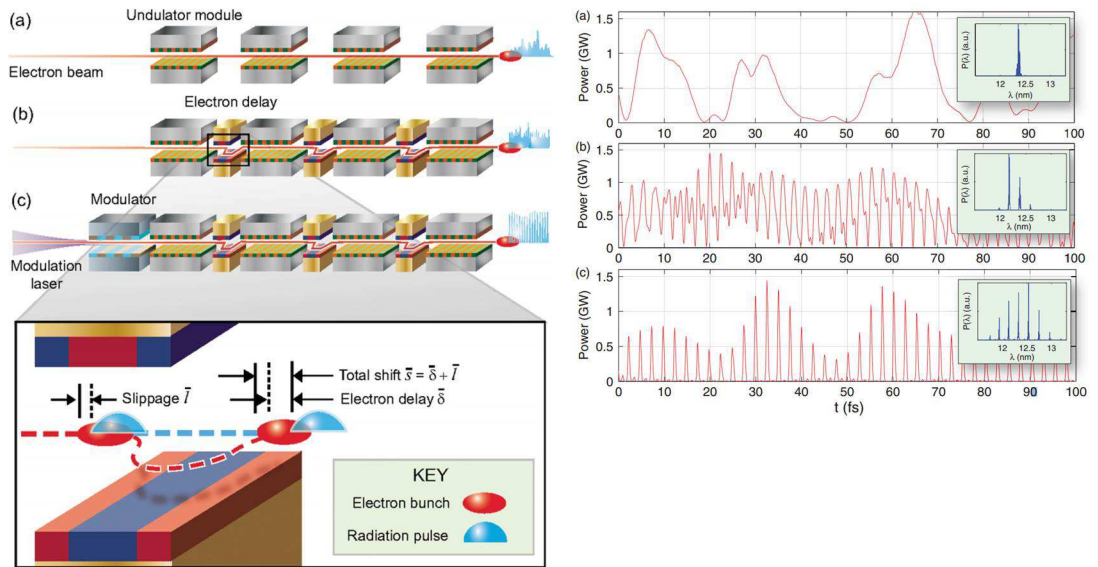
Figure 3.3: Schematic (left) and example output (right) of three modes of FEL interaction: (a) SASE (b) mode-coupled SASE and (c) mode-locked SASE. The inset in the bottom left of the figure shows details of the electron delay. The plots on the right show the temporal profile of the radiation power near to saturation and the radiation power spectrum as a function of wavelength (inset) for each of the three cases, for a soft x-ray example. Figure reproduced from [57].

The spatio-temporal shifts that generate the equally spaced modal structure in the amplifier spectrum are achieved by periodically delaying the electron bunch using magnetic chicanes between undulator modules [57], as shown schematically in Fig. 3.3. It is noted that the dispersive effect of the chicances enhances the micro-bunching, thereby reducing the distance to saturation by the so-called 'optical klystron' effect.

3.3.2 Notation

The notation used to describe the mode-locked amplifier FEL is set out in [57]. The total slippage of the radiation with respect to the electron bunch per module in units of the scaled electron bunch co-ordinate, $\bar{z}_1$, is:

$$\bar{s} = \bar{l} + \bar{\delta} \tag{3.1}$$

where $\bar{l}$ is the slippage occurring in the undulator and $\bar{\delta}$ is the slippage within the chicane. The scaled resonant FEL frequency is:

$$\bar{\omega} = \frac{(\omega - \omega_r)}{2\rho\omega_r} \tag{3.2}$$

where ω_r is the resonant FEL frequency. The slippage enhancement factor is defined as:

$$S_e = \frac{\bar{s}}{\bar{l}} \tag{3.3}$$

In [57], a solution is obtained for the one dimensional wave equation describing the field evolution of a small, constant electron source term for a series of N undulator-chicane modules.

For $S_e > 1$ the spectrum takes the form of a sinc-function envelope (the single undulator module spectrum) modulated by a frequency comb centered at the scaled resonant frequency $\bar{\omega}$, with mode separation:

$$\Delta\bar{\omega} = \frac{2\pi}{\bar{s}} \tag{3.4}$$

corresponding to:

$$\Delta\omega = \frac{2\pi}{T_s} \tag{3.5}$$

where $T_s = s/c = \bar{s}l_c/c$ is the time taken for radiation to travel the slippage length.

The number of modes under the central peak of the spectrum is shown to be:

$$N_0 = 2S_e - 1 \qquad (3.6)$$

3.3.3   Mode-locked amplifier FEL pulse durations

The key point of the mode-locked amplifier technique is that the bandwidth envelope of the emitted radiation is much broader than the usual FEL bandwith, and is in fact increased up to that of a single undulator module (equation 3.4. The significance is that pulse durations less than the co-operation length can be supported. Indeed the number of cycles per pulse will be approximately equal to the number of periods per undulator - which could potentially be made very short indeed!

In [57], two examples of the mode-locked amplifier FEL are simulated. A hard x-ray example ($\lambda_r = 0.15$ nm) is predicted to generate a train of pulses with duration ~ 23 as. This corresponds to ~ 46 optical cycles. The other example, in the soft x-ray ($\lambda_r = 12.4$ nm) is predicted to generate a train of pulses with duration ~ 400 as, which is shorter in terms of number of optical cycles (~ 10). This is a consequence of there being fewer periods per undulator module in the soft x-ray example (12) than in the the hard x-ray case (72). Significantly shorter pulses could be attained by reducing the number of undulator periods per module in the x-ray case, though this would constitute a significantly different undulator configuration than available at present FEL facilities.

Chapter 4

Amplification of HHG: Seeded Mode-Locked Amplifier FEL

4.1 Introduction

This chapter details the first main study of the thesis: a series of investigations to assess the feasibility of seeding the mode-locked amplifier FEL [57] (Section 3.3) with an HHG source (described in Chapter 1). This combination potentially offers the benefit to HHG sources of amplification to higher power, while it offers the benefit to the ML-FEL concept of controlling and stabilising the output, which retains random fluctuations in the envelope upon starting up from noise.

This study also reveals much about the role of electron beam energy modulation in the ML-FEL, which is considered in Section 4.5, and followed up in Chapter 5. Some of the content of this chapter has been published in [79] and [80].

4.2 Context

The initial idea for this study was proposed by Brian McNeil and Neil Thompson, directly following the publication of their initial paper on the mode-locked amplifier FEL [57]. Up to this point, modelling of the ML-FEL concept had been for the case of start-up from noise in the electron beam (SASE). With no energy modulation (mode-coupled), the pulse separation and duration is irregular, and it requires energy modulation to generate a regular pulse structure.

Even with energy modulation the envelope of the train still shows SASE-like

noise. Seeding the ML-FEL would be expected to give a predictable temporal profile (and also phase, though this was not considered in detail up until this point). Seeding FELs is a well established concept to overcome the noisy properties of SASE, as described in Section 2.10.

It was also anticipated that the well-defined pulse train structure of the HHG seed might itself introduce mode-locking and therefore remove the need for energy modulation: the first part of this chapter (Section 4.4) deals with this case. It will be seen that while the seeding 'works' in terms of giving a clean pulse train, it does not fully 'work' in terms of mode-locking to retain the shortest pulses. Hence the latter part of this chapter (Section 4.5) deals with HHG seeding in combination with energy modulation.

This work is also relevant from the perspective of the HHG community, as it potentially offers the benefit of amplification of these sources to higher power, while retaining the short-pulse features. As described in Chapter 1, HHG sources are important sources for experiments in their own right, consisting of a train of ultra-short pulses, but their peak power is typically orders of magnitude lower than that of FELs

The case of seeding a conventional high-gain FEL amplifier with an HHG source has been considered in experiments and modelling [81]. Amplification results in the pulse train structure washing out due to the bandwidth of the FEL being narrower that that of the HHG source. Figure 4.1 shows simulations results I contributed to prior to the work in this thesis.
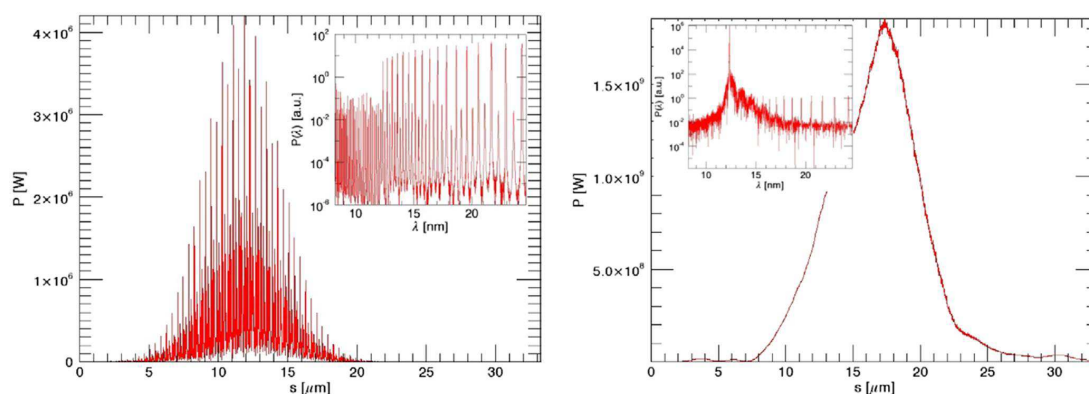
Figure 4.1: Amplification in FEL amplifier washing out HHG structure. The left plot shows the temporal profile of an HHG seed and its corresponding spectrum (inset). The right plot shows the temporal profile and spectrum after amplification in a conventional FEL amplifier. The effect of FEL amplification is to wash out the pulse train structure of the HHG seed due to the narrower bandwidth of the FEL. Figure reproduced from [81]

The mode-locked amplifier FEL concept exhibits temporal/spectral properties more closely matched to HHG sources, raising the prospect of retaining the pulse structure. The spectrum generated by the XUV mode-coupled SASE system of [57] has a modal structure with mode-spacing $\Delta\omega$ similar to the spacing of harmonics in a HHG source. Equivalently, the temporal structure of the two systems are a comb of attosecond pulses. By matching the spectral/temporal structures of a mode-coupled FEL amplifier to an HHG seed, it may therefore be possible to amplify the HHG seed to saturation while retaining its attosecond train structure.
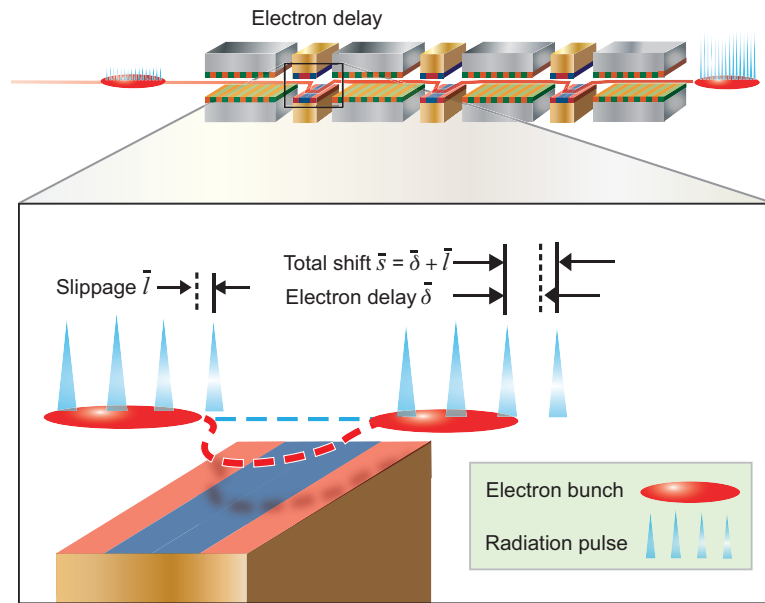
Figure 4.2: Schematic of the mode-coupled amplifier FEL interaction operating with an HHG seed. The inset shows detail of the electron delay.

4.3 Structure of the HHG source

The model of the HHG source follows that of previous work [81]. The source was modelled as a set of in-phase odd harmonics of a fundamental drive laser, hence it consists of a train of equally spaced pulses in the temporal domain. A drive laser wavelength of 800 nm was used, with the resonant wavelength to be used in FEL modelling chosen to be the 65th harmonic of the drive laser, i.e. $\lambda_r = \lambda_d/65 = 12.4$ nm. The temporal comb is separated by half the wavelength of the drive laser, $\lambda_d/2 = 400$ nm, and modulated by the drive laser power envelope.

The seed model was used as input to the 1D FEL code (Section 2.11), in which the Nyquist theorem limits the frequencies that can be modelled [81] to harmonics 33 to 97. The temporal and modal structure of the seed is shown in Figure 4.3, in the scaled units of the 1D code. Because the maximum width of the spectral content is utilised, the pulse duration of the seed is at the limit of the shortest pulse that can be represented in the 1D code, i.e. ∼1 optical cycle. The following work utilises a simple method for calculating the pulse widths in the FEL code, by integrating the area under the pulse and dividing by the peak height. By this method the seed pulse width ≈ 0.045 FWHM in terms of $\bar{z}_1$, corresponding to 1.8 optical cycles. In SI units, this equates to 74 as which is close to the shortest duration demonstrated from HHG sources, hence this seems a reasonable idealised approximation of the source. The HHG power level was set a factor of ∼ 400 below FEL saturation following [81]. The assumption that the modes are perfectly in phase represents an ideal case with minimum initial pulse duration. Non-ideal cases have also been studied but are not presented here.
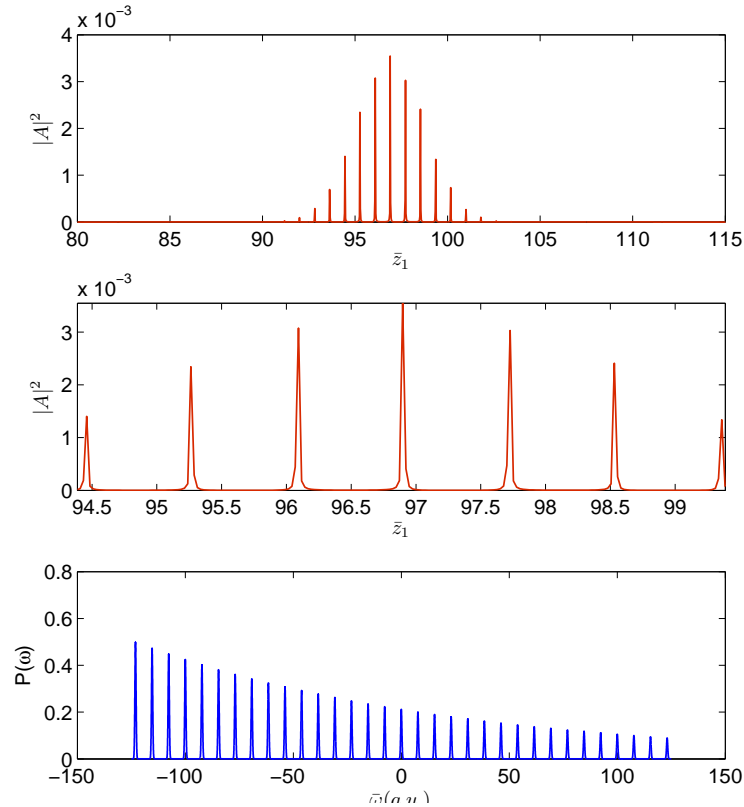
Figure 4.3: Scaled longitudinal intensity profile (top and middle) and scaled spectral power distribution for the HHG seed (bottom).

4.4 Amplification of HHG without energy modulation

4.4.1 System parameters

As described in Chapter 3, the spectrum of the ML-FEL output takes the form of a sinc-function envelope (the single undulator module spectrum) modulated by a frequency comb centered at the scaled resonant frequency. In order to increase the bandwidth of the system (and hence amplify as much of the HHG spectrum), short undulators of only 8 periods were chosen initially for this study. This is slightly fewer than the XUV example of [57] where 12 periods/module were used, and significantly fewer than the hard x-ray case (72 periods/module).

For a typical HHG drive laser wavelength of $\lambda_d = 805$ nm (e.g. Ti:sapphire) and an FEL parameter of $\rho = 2 \times 10^{-3}$ similar to that for an FEL operating in the XUV, then for undulator modules of 8 periods, the scaled module length is $\bar{l} = 0.201$. The value of the scaled slippage generated by the chicanes was chosen to be $\bar{\delta} = 0.616$ so that $\bar{s} = \bar{\lambda}_d/2$, matching the undulator-chicane system to the spectral and temporal structure of the HHG seed. This results in a slippage enhancement factor of $S_e = 4.0625$.

For speed and simplicity, the system was primarily modelled using the 1D code based on [55] (Section 2.11), with the 3D code Genesis [56] also used to cross-check the results. Initially the modelling was carried out with a fully 'cold' electron beam (no energy spread as well as no energy moduation); the effects of energy spread are introduced in Section 4.4.4, and energy modulation is covered in Section 4.5. The effects of chicane dispersion are included in the model [24].

4.4.2 Modelling results

The amplified scaled radiation power and spectrum after 22 undulator-chicane modules are shown in Figure 4.4. At this point the scaled intensity is 0.4, which is approaching the FEL saturation level of 1, and two orders of magnitude above the seed intensity in this case. Notably, the output consists of a train of pulses in the temporal domain, and discrete modes in the spectrum, indicating that the mode-coupled amplifier FEL configuration is capable of retaining these characteristics of the seed to some extent - unlike conventional FEL amplifiers which wash out the structure entirely. However, it is evident that a significant broadening of the individual pulses within the train occurs - from 0.045 ($\sim$1.8 cycles) to 0.35 ($\sim$14

67

cycles) - a factor of ∼8 with associated narrowing of the spectral envelope. It is significant to note that the pulses are not only broader than the seed pulses, but also broader than the pulse duration anticipated from the single undulator bandwidth (∼8 cycles).
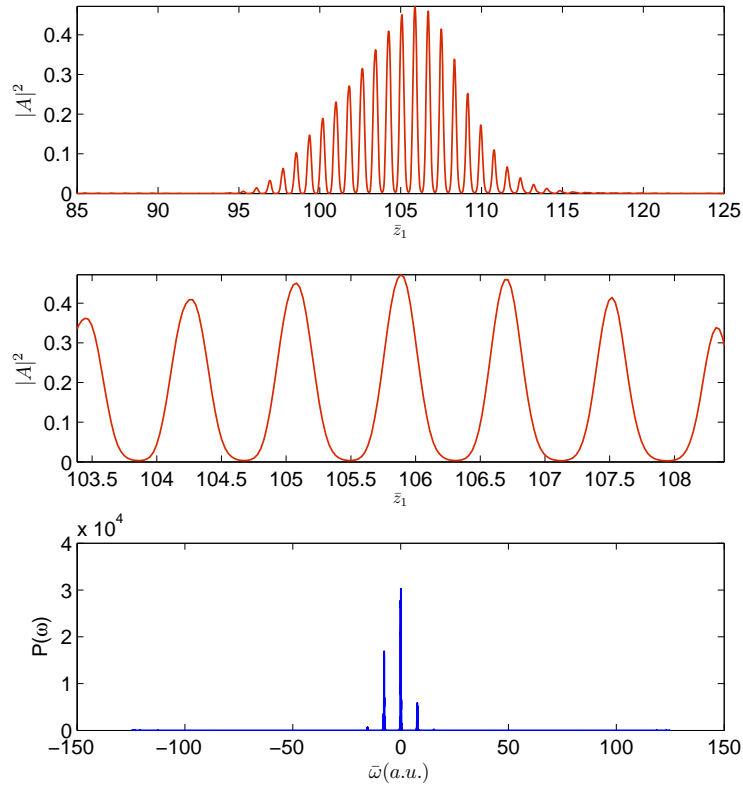
Figure 4.4: Scaled longitudinal intensity profile (top and middle) and scaled spectral power distribution of the amplified HHG radiation for $\bar{l} = 0.201$ ($S_e = 4.0625$), after 22 undulator-chicane modules.

The number of undulator modules corresponds to a scaled FEL interaction length of $22 \times \bar{l} \approx 4.4$. Note that the dispersive strength of the chicanes $D = R_{56}/2l_c \approx 10\bar{\delta}/6$ reduces the gain length as discussed in [57]. The scaled power does reach normal FEL levels of $|A|^2 \approx 1$ upon further amplification, however the temporal structure of the pulses begins to break up.

68

4.4.3 Optimising for shortest pulses

Since with 8 periods per undulator module the amplified pulses broadened significantly compared to the HHG seed, the system was modified. In order to attain narrower amplified HHG pulses, the bandwidth of the system (and hence number of modes amplified) was increased by reducing the number of undulator periods per module. To reduce $\bar{l}$ while continuing to satisfy the condition $\bar{s} = \bar{\lambda}_d/2$, the value of $\bar{\delta}$ was increased to keep $\bar{s}$ constant. The system was simulated for a case with the number of undulator periods per module set to 4. The corresponding value of the slippage enhancement factor is $S_e = 8.125$.

The amplified scaled radiation power and spectrum is as shown in Figure 4.5, after 34 4-period undulator modules. Again the HHG seed is amplified and
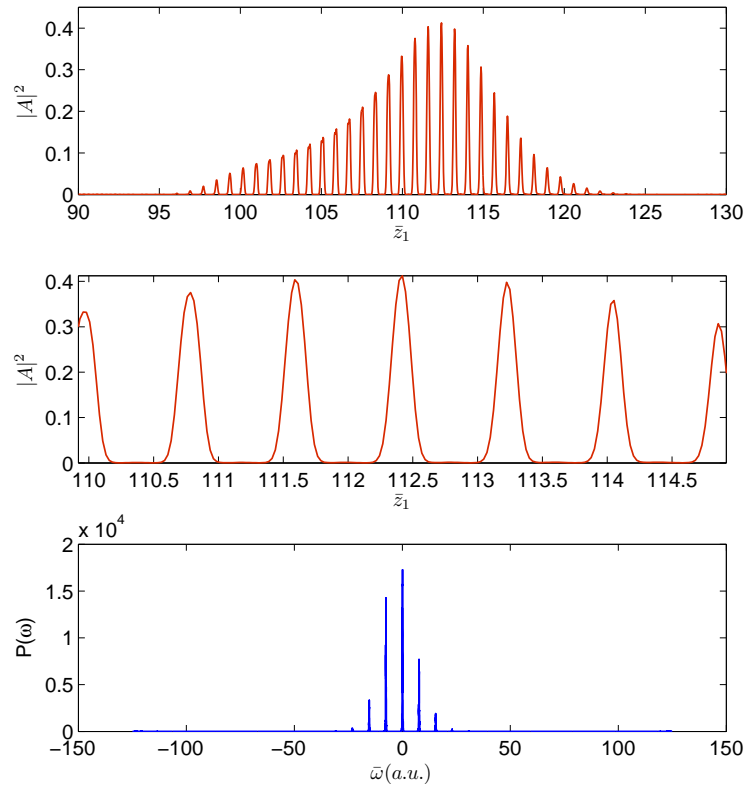
Figure 4.5: Scaled longitudinal intensity profile (top and middle) and scaled spectral power distribution of the amplified HHG radiation for $\bar{l} = 0.101$ ($S_e = 8.125$), after 34 undulator-chicane modules.

the comb of temporal spikes is retained. There still occurs a broadening of the individual pulses, however the pulses are now significantly shorter - at 0.2 (~ 8

cycles) than in the case with 8-period modules. However the pulse durations are still longer than the minimum of 4 cycles implied by the single undulator bandwidth.

The variation of the peak intensity and pulse width with scaled distance through the undulator are plotted in Figure 4.6 for the two cases $S_e = 4.0625$ ($\bar{l} = 0.201$) and $S_e = 8.125$ ($\bar{l} = 0.101$). For both cases there is a rapid initial broadening tending towards the pulse duration implied by the single undulator spectrum ($0.2 \equiv 8$ cycles and $0.1 \equiv 4$ cycles respectively). This occurs since only the modal content that falls under the envelope of the single undulator spectrum is amplified. The pulse durations then continue to increase, but at a slower rate
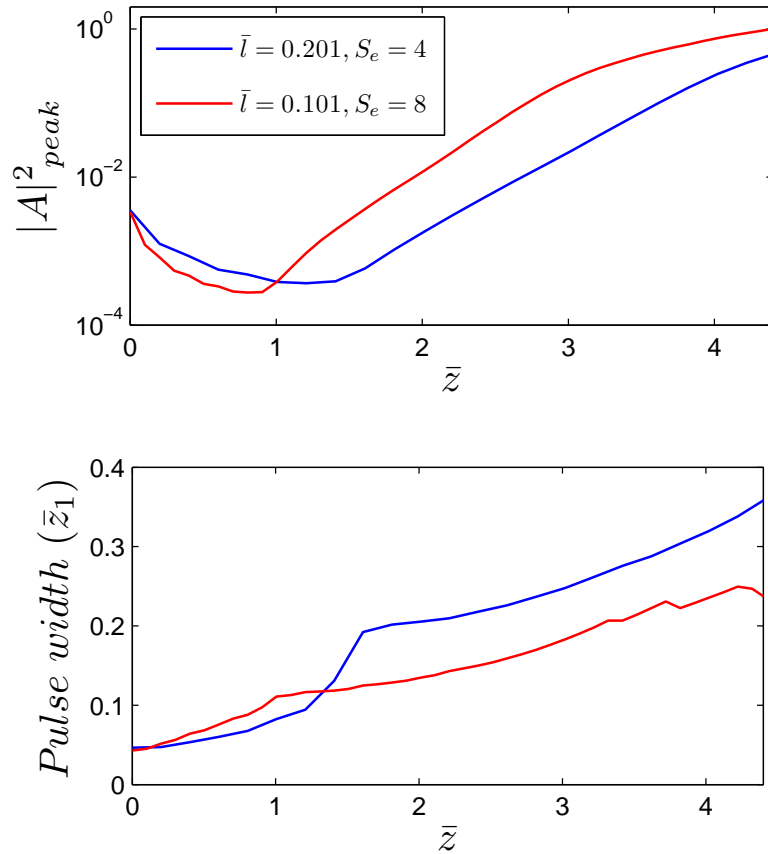
Figure 4.6: Peak intensity (top) and pulse width (bottom) plotted against the scaled undulator distance, $\bar{z}$ [57], for the two cases $S_e = 4.0625$ ($\bar{l} = 0.201$) and $S_e = 8.125$ ($\bar{l} = 0.101$). By reducing the number of undulator periods per module the pulse duration and the gain length are both reduced.

during further amplification. This slow pulse broadening effect is attributed to

slippage in the undulators, and is described in depth in Chapter 6.

For $S_e = 8.125$, 34 undulator-chicane modules are required to produce the same amplification of the 22 module $S_e = 4.0625$ case. This corresponds to a reduction in the total undulator length from 4.4 to 3.4, which can be attributed to more effective seeding since a broader spectral range of the seed is amplified, and reduced gain length due to an increased number of chicanes.For larger values of S_e, modelling the broadening of the modal sinc-function envelope becomes restricted by the Nyquist limit for the code used.

4.4.4 Effect of energy spread

The effects of energy spread on the interaction have been investigated using the 1D model by introducing a relative Gaussian energy spread of width $\sigma_\gamma/\gamma = \rho/10 = 0.02\%$ for the case $S_e = 8.125$. While the cold beam case took 34 undulator-chicane modules, the case with energy spread took 42 modules. Note that the temporal and spectral structure of the radiation power remains largely unaffected by the energy spread (not shown). Larger energy spreads have also been simulated with the main effect being a larger number of modules to saturation.

4.4.5 3D simulations

The system has also been modelled using the three-dimensional code Genesis 1.3 [56]. The main results of the 1D simulations are reproduced using the 3D code and show amplification of an HHG seed pulse retaining its pulse train structure.

Similar parameters as for the XUV mode-coupled FEL amplifier of [57] were used (i.e. without electron beam modulation) including an energy spread of width $\sigma_\gamma/\gamma = 0.01\%$. The seed power and spectrum show the attosecond pulse train structure and frequency comb, as seen in Figure 4.7. The peak power of the seed was set to 3 MW with FWHM duration 25 fs. It was assumed that the wavelength of the Ti:Sapphire drive laser was $\lambda_d = 780$ nm and the FEL was then tuned to be resonant with the 63rd harmonic of the drive laser with $\lambda_r = 12.4$ nm.

Each undulator module had 4 periods of 3.1 cm and each chicane had a delay of 28 radiation wavelengths corresponding to a slippage enhancement $S_e = 8$. These parameters for the undulator-chicane modules then match the mode spacing of the HHG seed. The amplified seed approaching saturation, after 47 modules, is plotted in Figure 4.7 and the pulse temporal and spectral properties agree well
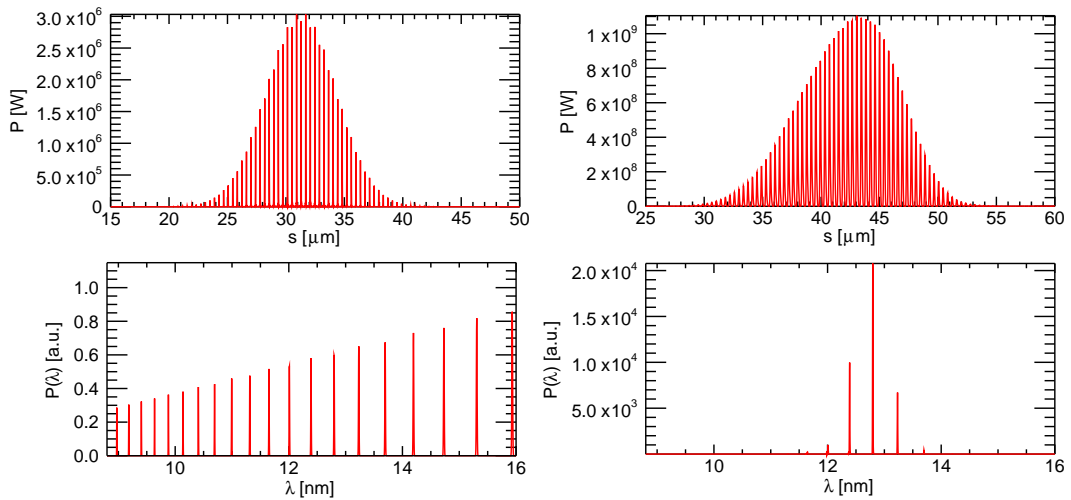
Figure 4.7: Longitudinal intensity profile (top) and spectral power distribution (bottom) of the HHG seed (left), and of the amplified radiation (right) in 3D simulations, with $S_e = 8$. The agreement with the equivalent 1D simulations shown in Figure 4.5 is very good.

with the equivalent one-dimensional $S_e = 8.125$ case of Figure 4.5. The FWHM length of each pulse in the amplified train is 300 as. Further 3D simulations (not shown) with $S_e = 4$ agreed well with the $S_e = 4.0625$ case of Figure 4.4.

4.4.6 Amplification of a single-frequency seed

To further understand the behaviour of the mode-coupled FEL configuration, it is instructive to consider the case where it is used to amplify a single-frequency seed. The simulation is exactly the same as that shown in Figure 4.5, except that the HHG seed is filtered to retain only the central harmonic - resulting in a long-scale temporal structure to the seed, rather than a pulse train. The seed structure, together with the amplified scaled radiation power and spectrum after 42 4-period undulator modules are shown in Figure 4.8.

The figure shows that the mode-coupled FEL system amplifies the single-frequency seed without a significant modal structure developing. There is a ripple in the temporal profile, and corresponding spectral spikes - but at a low level. This is similar to conventional FEL seeding - while both systems have a 'natural' temporal/spectral structure, they are both capable of amplifying a narrow bandwidth, single-frequency source, if such a seed is available. The conclusion is that the mode-coupled FEL is capable of amplifying both narrow-frequency, long pulses, or broad frequency, short-pulse trains, with a seeming tendency for the
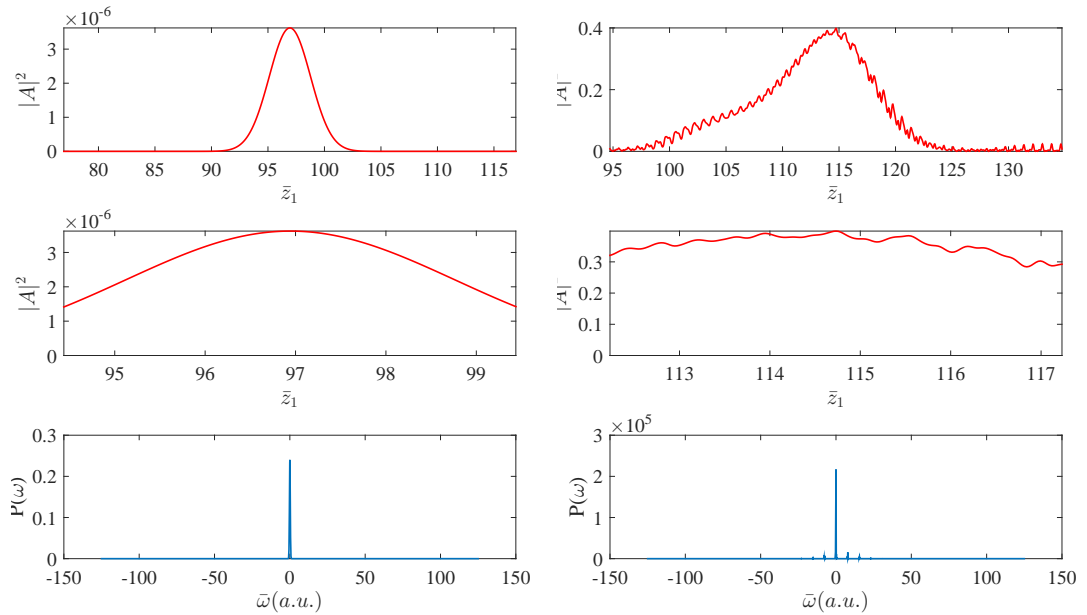
Figure 4.8: Scaled longitudinal intensity profile (top and middle) and scaled spectral power distribution (bottom) of the single frequency seed (left) and the amplified HHG radiation (right) for $\bar{l} = 0.101$ ($S_e = 8.125$), after 42 undulator-chicane modules.

pulse durations to slowly broaden.

4.4.7 Summary of HHG amplification without energy modulation

The investigation of seeding the mode-coupled FEL is concluded by noting the main findings as follows:

1. An HHG seed can be amplified to FEL saturation in the mode-coupled FEL configuration (no energy modulation) while retaining a pulse train structure. Increase in peak intensity of two orders of magnitude is predicted, given the seed properties of [81].

2. The duration of individual pulses broadens during the amplification process, and the bandwidth narrows. There is a rapid initial broadening towards the pulse duration implied by the natural undulator bandwidth, followed by a slower subsequent broadening.

3. Selecting the maximum bandwidth of the system (i.e. through minimising the number of undulator periods per module) is key to minimising the am-

plified pulses durations. Bandwidth narrowing occurs regardless but from a wider initial bandwidth.

4. The mode-coupled FEL configuration also supports amplification of a seed with much narrower bandwidth than a single module - similar to a normal FEL configuration that will amplify a seed with much narrower bandwidth than the FEL bandwidth.

4.5 Amplification of an HHG seed with energy modulation

Section 4.4 showed that the pulse train structure of an HHG source can be retained to some extent during amplification to saturation in the mode-locked FEL without any modulation of the electron beam, however the radiation pulses broaden as the FEL interaction progresses. In this section the effects of introducing electron beam energy modulation are considered, and are shown to restrict the pulse broadening effect. A novel method for seeding the mode-locked configuration is also developed in Section 4.5.4.

4.5.1 Method: pulse alignment and modulation amplitude

The modelling method follows that of Section 4.4.1, using the 1D code, the HHG seed model (Figure 4.3), and with 8 periods per undulator module. Again, the FEL parameter was set to $\rho = 2 \times 10^{-3}$, the scaled slippage to $\bar{l} = 0.201$, and the chicane slippage was $\bar{\delta} = 0.616$. The key difference to Section 4.4, is the introduction of an energy modulation to the electron beam.

A sinusoidal energy modulation was applied with period set equal to $\bar{s}$, to match both the HHG pulse spacing and the slippage per undulator-chicane module, such that all HHG seed pulses have the same initial longitudinal alignment relative to the beam modulation phase.
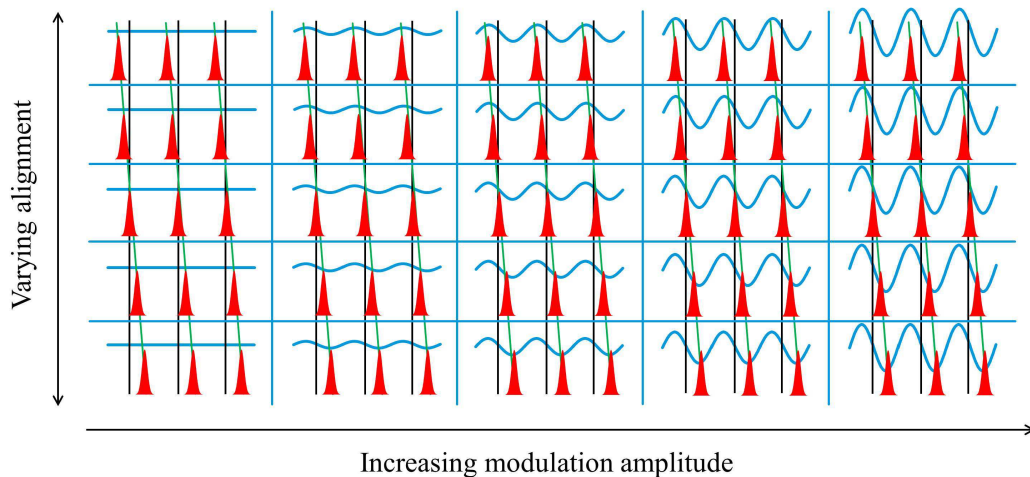
Figure 4.9: Simulations were carried out for a range of initial longitudinal alignment between radiation pulses (red) and sinusoidal electron beam energy modulation (blue). The green lines are used to highlight the offset relative to an arbitrary reference (black lines).

It is thus assumed that the radiation pulses interact with only certain parts of the electron beam: slipping forward a distance l in the undulator sections (where they interact), and a distance δ in the chicanes (where they do not). The energy variation across the interacting parts of the electron beam is therefore a function of both the initial alignment with the seed, and the modulation amplitude. Figure 4.9 outlines the method of the study: to vary the initial alignment of the seed pulses for a range of modulation amplitudes and to assess the effects.

4.5.2 Results of modelling

Energy offset

The first significant result to note is illustrated schematically in Figure 4.10. It was found that the the central energy of the modulated beam must be offset
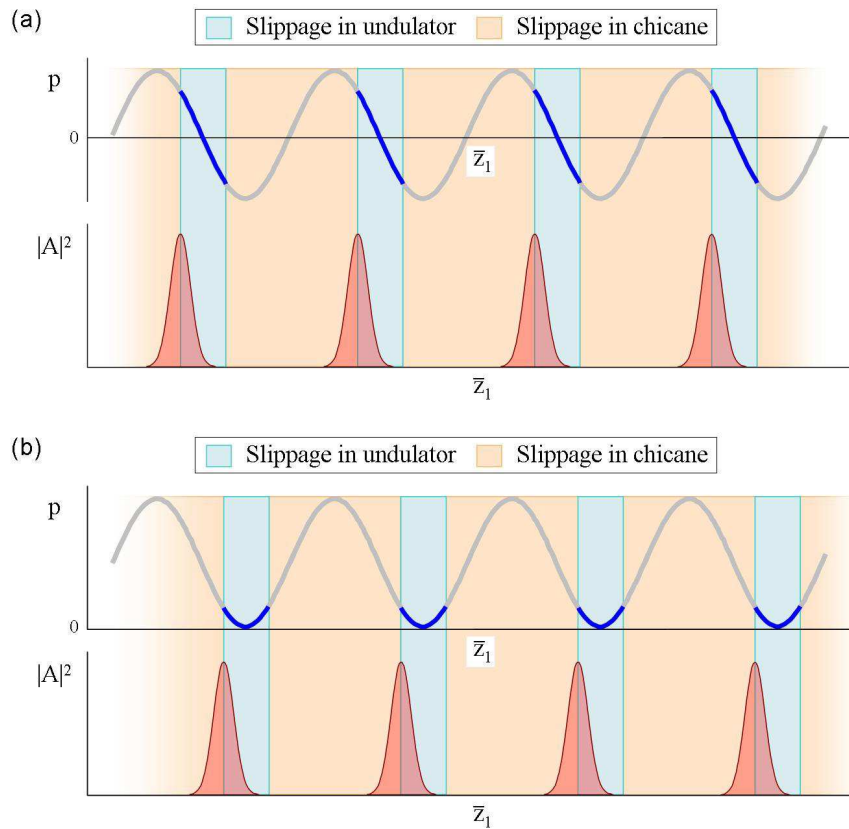
Figure 4.10: Initial alignment of the HHG seed pulses relative to the electron beam energy modulation for two cases (a) $\bar{l}/2$ behind the central energy of the modulation and (b) $\bar{l}/2$ behind the minima of the energy modulation. The energy of the electron beam is detuned such that the resonant frequency of the centre of the seeded region is matched to the seed.

such that the 'interacting regions' of the electron beam are resonant with the seed. The interacting regions are those a distance l ahead of the initial seed position. Without this matching the seeding effect is significantly reduced, or even negligible. An example of such energy offsetting is shown in Figure 4.10 for two different examples of initial conditions of the HHG pulse alignment relative to the modulation phase. This result in itself is significant as it confirms the earlier assumption that only certain parts of the electron beam are interacting with the seed.

Pulse alignment and modulation amplitude

The initial longitudinal position of the seed pulses, $\bar{z}_{1_0}$, was varied over one period of the beam modulation and the intensity of the radiation intensity recorded at a fixed undulator distance. This was repeated for varying energy modulation amplitude, with the results given in Figure 4.11.
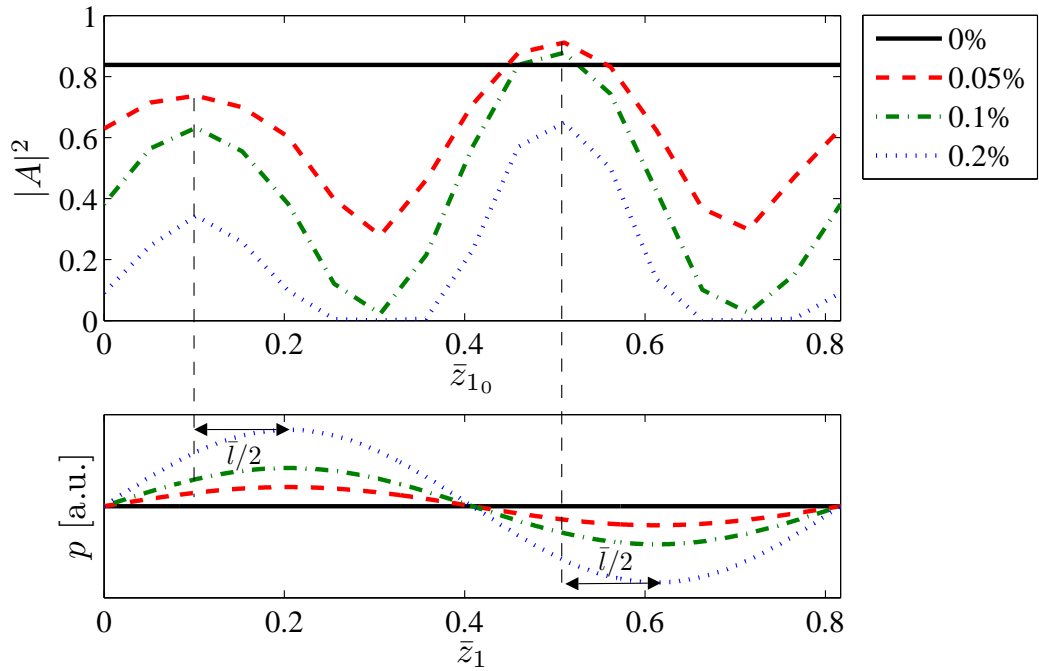
Figure 4.11: Peak radiation intensity after 40 modules against initial longitudinal position of the seed pulses (top) relative to the electron beam energy modulation (bottom), for varying energy modulation amplitude. The initial alignment of the seed becomes more significant as the energy modulation amplitude is increased. The optimum initial alignment of the seed is half the undulator slippage ($\bar{l}/2$) behind the positions of zero energy gradient.

With zero modulation amplitude there is no dependence on the alignment of the seed as would be expected. As the amplitude is increased the initial alignment of the seed becomes more significant. The optimum amplification of the seed is seen to occur with the seed pulses aligned $\bar{l}/2$ behind the positions of zero energy gradient at the beginning of the interaction, e.g. Figure 4.10 (b). This corresponds to the pulses aligning with the position of zero energy gradient at the centre of the undulator modules. It is also noted that the amplification rate is higher at the minimum energy position than at the maximum - this point is considered in more detail in Section 5.3.3.

Pulse width

The effect of energy modulation amplitude on pulse width during amplification was also investigated. The optimal longitudinal alignment of the seed was used ($\bar{z}_{1_0}$= 0.51 in Figure 4.11), and the energy modulation was varied. Figure 4.12 shows the pulse width and peak radiation intensity with scaled distance through the undulator, $\bar{z}$. With no energy modulation there occurs a continual broadening of the radiation pulses, in agreement with the previous section. An energy modulation amplitude of 0.2% is sufficient to restrict the pulse broadening. Pulse durations of $0.2 \equiv 8$ cycles were obtained - meeting the minimum implied by the single undulator bandwidth, and a factor of 2 better than the case with no energy modulation.

Increasing the modulation amplitude further does not reduce the pulse width but does reduce the growth rate. More detailed analysis of the optimum energy modulation amplitude is given in Section 5.3.

The interpretation of these results is that the effect of energy modulation is two-fold: it both defines the optimal positions within the beam for pulse train amplification, and it constrains pulse broadedning during amplification. These effects are discussed further in Chapter 5.
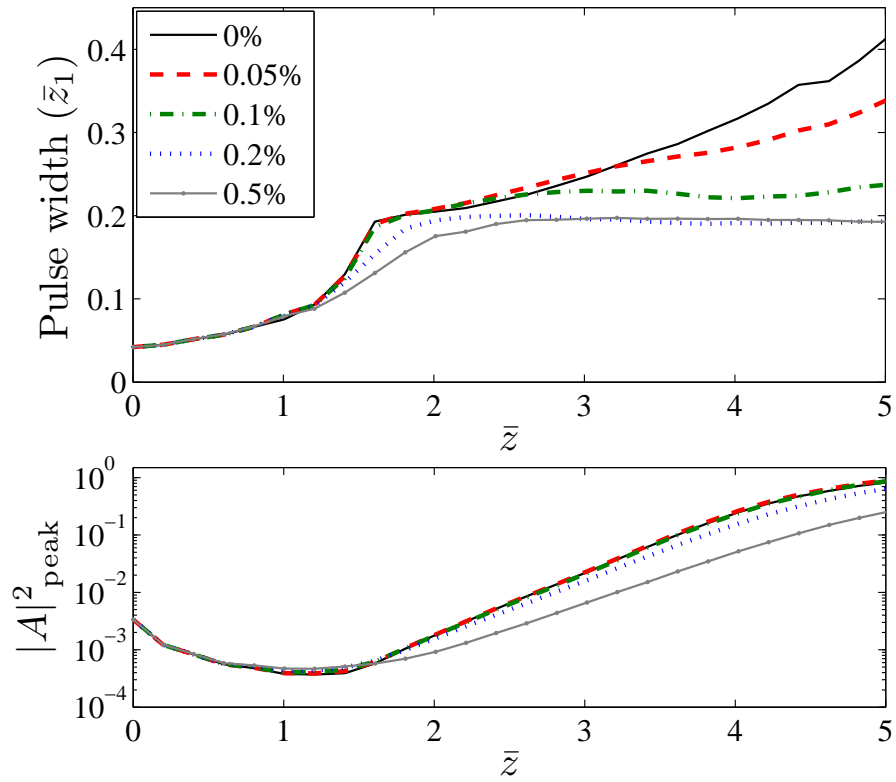
Figure 4.12: Pulse width (top) and peak intensity (bottom) plotted against distance through the undulator, $\bar{z}$, for varying energy modulation amplitude. The optimal initial seed alignment is used ($\bar{z}_{1_0} = 0.51$ in Figure 4.11). Energy modulation amplitude of 0.2% is sufficient to restrict the pulse broadening. Increasing the modulation amplitude further does not reduce the pulse width and reduces the growth rate.

4.5.3 Optimising for shortest pulses

Similarly to the case with no energy modulation, a second case was optimised for minimum pulse duration. In order to attain narrower amplified HHG pulses, the bandwidth of the system was increased by reducing the number of undulator periods per module to 4, meaning $\bar{l}$ was decreased to 0.101, the value of $\bar{\delta}$ was increased to keep $\bar{s}$ constant. The corresponding value of the slippage enhancement factor is $S_e = 8.125$.

The results are shown in Figure 4.13. Pulse durations of $0.1 \equiv 4$ cycles were obtained - meeting the minimum implied by the single undulator bandwidth.
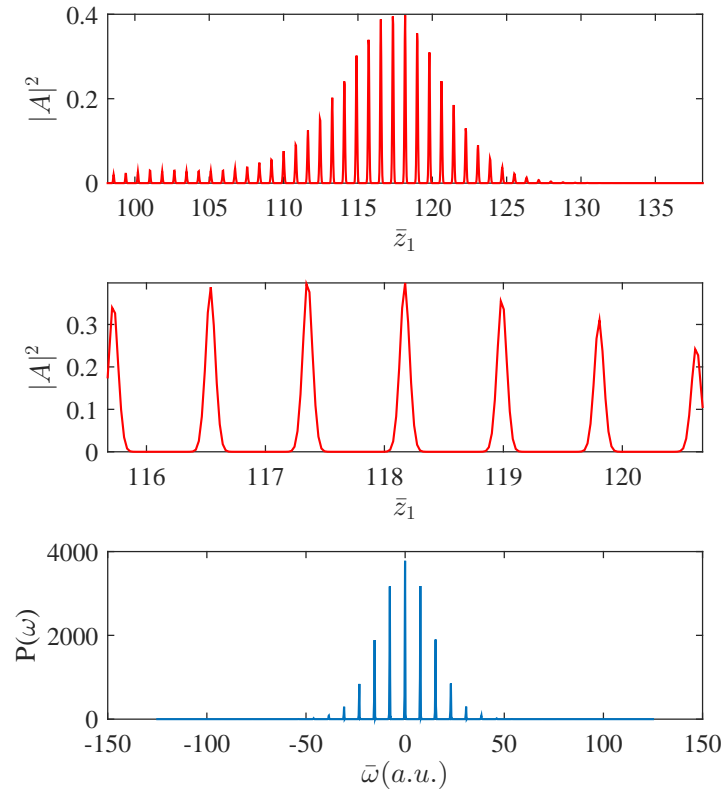
Figure 4.13: Scaled longitudinal intensity profile (top and middle) and scaled spectral power distribution of the amplified HHG radiation for $\bar{l} = 0.101$ ($S_e = 8.125$), after 40 undulator-chicane modules.

4.5.4   Amplification of a single-frequency seed

In the previous sections it has been shown that an HHG seed can be amplified without energy modulation - but with pulse broadening, and that modulation of the electron beam energy can be used to constrain this broadening effect. However, an obvious difficulty with the latter technique in practice would be the precise phase-matching of the HHG seed pulse train to the correct phase of the electron beam energy modulation. A relatively simple method is now proposed which negates this requirement for precise phase-matching, while constraining pulse broadening.

Outline of new method

The new method is to use an energy modulated beam as in the previous section, but to filter the HHG seed to remove the attosecond pulse train structure. The HHG seed field of Figure 4.3 was filtered to preserve only the central resonant mode, $\bar{\omega} = 0$, such that no attosecond structure remains and the seed has the simple Gaussian envelope of the drive laser. A beam energy modulation amplitude of 0.5% was used with the seed frequency set to the resonant frequency of the electrons at the minimum of the modulated energy.

Simulation results

Figure. 4.14 shows the evolution of the pulse shape and spectrum with amplification in the mode-locked FEL starting from a single-frequency seed. It is seen that while there is initially a broad Gaussian seed, the amplification process rapidly modifies this into a pulse train. In the frequency domain it is seen that though seeding is only initially at the central frequency, the familiar set of discrete modes quickly develops. At saturation very similar pulse widths and powers to those of Figure 4.12 are attained.

This is a useful result as it relaxes the constraints on seeding the mode-locked amplifier. It is also interesting in that it reveals more insight into the way the mode-locked FEL operates, i.e. that in the presence of appropriate energy modulation, the system cannot support a single-frequency radiation field without exciting other frequencies.
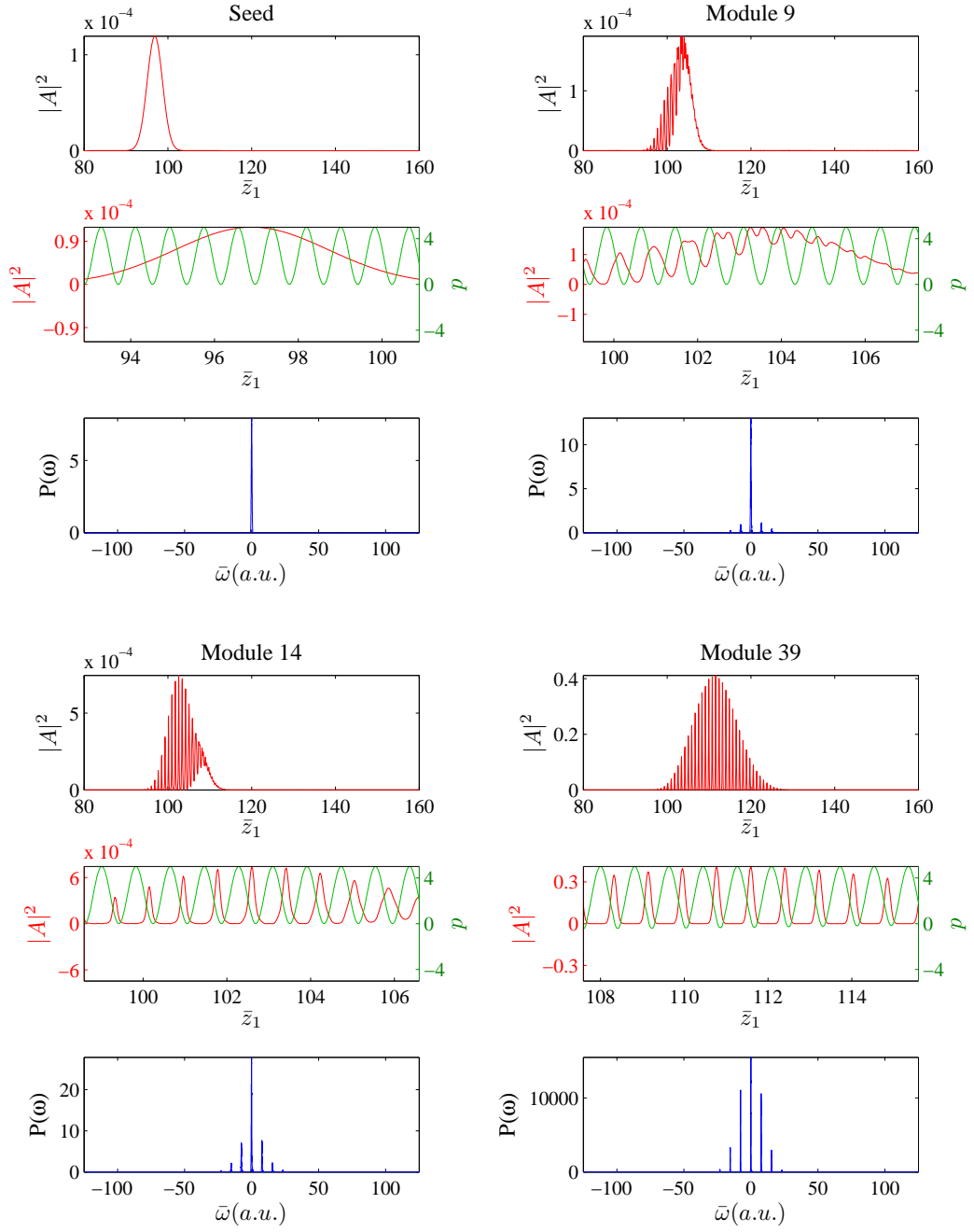
Figure 4.14: Simulation results for the mode-locked amplifier FEL with a filtered HHG seed. The four sets of plots show the properties of the seed, and the amplified radiation after 9, 14, and 39 modules (near saturation). Each set of plots show the radiation temporal profile (top), an inset of the radiation temporal profile relative to the electron energy modulation (middle), and the spectrum (bottom).

4.5.5 Summary of HHG amplification with energy modulation

The investigation of amplification of an HHG seed in the mode-locked FEL is concluded by noting the main findings as follows:

1. The introduction of energy modulation can allow the pulse broadening effect to be constrained. The full bandwidth of the single-module undulator spectrum can be retained, with the pulse duration correspondingly minimised. Seed pulses shorter than the minimum will still rapidly broaden to this value during amplification.

2. An optimum range of modulation amplitudes exists for which the pulse broadening is constrained and the amplification rate is not decreased. Lower values do not constrain pulse broadening, and higher values decrease amplification rate without a further decrease in pulse duration.

3. In addition to an optimum modulation amplitude, there is also an optimum temporal alignment of the seed pulses relative to the modulation phase. This occurs with the seed pulses aligned $\bar{l}/2$ behind the positions of zero energy gradient at the beginning of the interaction, corresponding to the pulses aligning with the position of zero energy gradient at the centre of the undulator modules. Of the two zero energy gradient postions, the minimum energy position has higher growth rate.

4. Furthermore, for optimum amplification to occur, the regions of the electron beam interacting with the seed must meet the resonance condition.

5. The temporal alignment constraints can be alleviated by using a filtered seed such that its pulse train structure is removed. The minimum pulse duration of the system can still be attained with this simplified method.

4.6 Conclusions

The study into seeding the mode-locked FEL has resulted in a number of interesting findings. It was shown that seeding the mode-coupled FEL with an HHG source has the effect of cleaning up the temporal and spectral properties of the output. The output consists of a regularly spaced set of temporal spikes, rather than the irregular output when starting up from noise. This would be expected to be beneficial in terms of its utility for experiments.

In terms of the mode-coupled FEL being judged as an amplifier for HHG sources, the verdict is mixed: the radiation can indeed be amplified while retaining a pulse train structure (by two orders of magnitude, given the seed properties of [81]). However, where the bandwidth of the HHG source exceeds that of the single undulator module bandwidth, the bandwidth of the amplified radiation quickly falls to that of the single undulator module bandwidth, and continues to fall during amplification, corresponding to temporal broadening of the pulses. By minimising the number of periods per undulator module, the amplified bandwidth can be maximised and pulse broadening minimised.

The mode-locked FEL, with correct choice of energy modulation amplitude, can avoid the secondary pulse broadening effect and so retain the full bandwidth of a single undulator module. Due to this, the pulse durations can be approximately a factor of 2 shorter than the mode-coupled case. However, this comes with the stringent requirement of matching the seed pulses to the energy modulation phase. An alternative using a single frequency of the HHG seed removes this constraint, while still resulting in optimum output.

The seeding study reveals significant insight into the role of energy modulation in the mode-locked FEL. It shows that the positions in the electron beam with minimum energy gradient are optimum for amplification, and that energy modulation constrains pulse broadening during amplification. These effects are explored further in Chapter 5.

Chapter 5

Role of Electron Beam Modulation in the Mode-Locked Amplifier FEL

5.1   Introduction

The previous chapter revealed some insights into the role of energy modulation in the seeded mode-locked FEL: it both defined the positions for optimum amplification, and constrained pulse broadening during amplification. This chapter considers the role of electron beam modulation in detail. Firstly, the electron beam modulation is considered in the case of start-up from noise - the SASE mode-locked FEL - in Section 5.2, with several new properties of the system revealed. These properties suggest that the system may perhaps be most intuitively described in the temporal domain, and this description in outlined in Section 5.2.3. The role of energy modulation is described in detail in Section 5.3. This understanding of the role of energy modulation allows potential alternative modulation techniques to be identified, and one such method is studied in Section 5.4.2. Limitations of the modelling method are considered in Section 5.5.

5.2   SASE mode-locked FEL

The first section of the chapter describes the mode-locked FEL starting from noise [57]. New aspects are considered which reveal much about the behaviour of

the system, namely:

- The phase of the radiation.

- The longitudinal location of the pulses relative to the energy modulation phase.

- The properties of the micro-bunching profile.

5.2.1   Radiation phase

The radiation phase is now considered. A comparison is made between simulation results of three cases starting from noise (SASE): the conventional FEL amplifier regime, and the mode-coupled and mode-locked regimes. One-dimensional modelling was carried out as described in Section 2.11, and the results are shown in Figure 5.1. In addition to the temporal profiles considered previously [57] (shown in Figure 3.3), the radiation phase is now plotted. This gives further insight into the behaviour of the different regimes as described in the following sections.

Conventional SASE FEL

Figure 5.1 (a) shows simulation results demonstrating the properties of typical radiation output from a conventional FEL amplifier starting from noise (SASE). The temporal output power is noisy, consisting of a series of spikes with separation $\lesssim 2\pi l_c$, while the phase plots show that there is no phase correlation from spike to spike.

Mode-coupled SASE FEL

Figure 5.1 (b) shows simulation results demonstrating the properties of typical radiation output from a mode-coupled FEL amplifier starting from noise. The temporal profile now consists of a series of spikes much shorter than in the conventional SASE case (i.e. shorter than the co-operation length), but it is not a 'clean' pulse train like in the mode-locked case (Figure 5.1 (c)). In fact it is more like a number of interleaved pulse trains.

The phase plot is particularly revealing concerning the structure of the output for two reasons. Firstly, it shows that there is phase-correlation across pulse trains. Secondly (and most significantly) it shows that the radiation output does

indeed consist of interleaved pulse trains, each of which have phase-correlation within the pulses of the train but with no phase-matching between trains. This is a significant result in terms of interpreting the behaviour, and is discussed further in section 5.2.3. The longitudinal extent of the phase correlation is increased compared to the SASE case (to $S_e \times l_c$), but as already noted the phase correlation is not continuous. Hence there are phase transitions on the scale of l, the slippage in one undulator module.

Also noted is that there is continual temporal broadening of the radiation pulses during amplification, consistent with that observed in Section 4.4. This corresponds to narrowing of the spectral envelope relative to the single undulator bandwidth in agreement with [57].

Mode-locked SASE FEL

Figure 5.1 (c) shows simulation results demonstrating the properties of typical radiation output from a mode-locked FEL amplifier starting from noise. The most obvious difference compared to the mode-coupled case (Figure 5.1 (b)) is the absence of interleaved pulse trains. The output consists of a train of pulses that are regularly spaced over the entire longitudinal extent of the output, but which are phase-correlated over only the enhanced coherence length ($S_e \times l_c$).

The phase and envelope variations of the mode-locked FEL output are very similar to the conventional SASE output of Figure 5.1 but on a longer temporal scale.
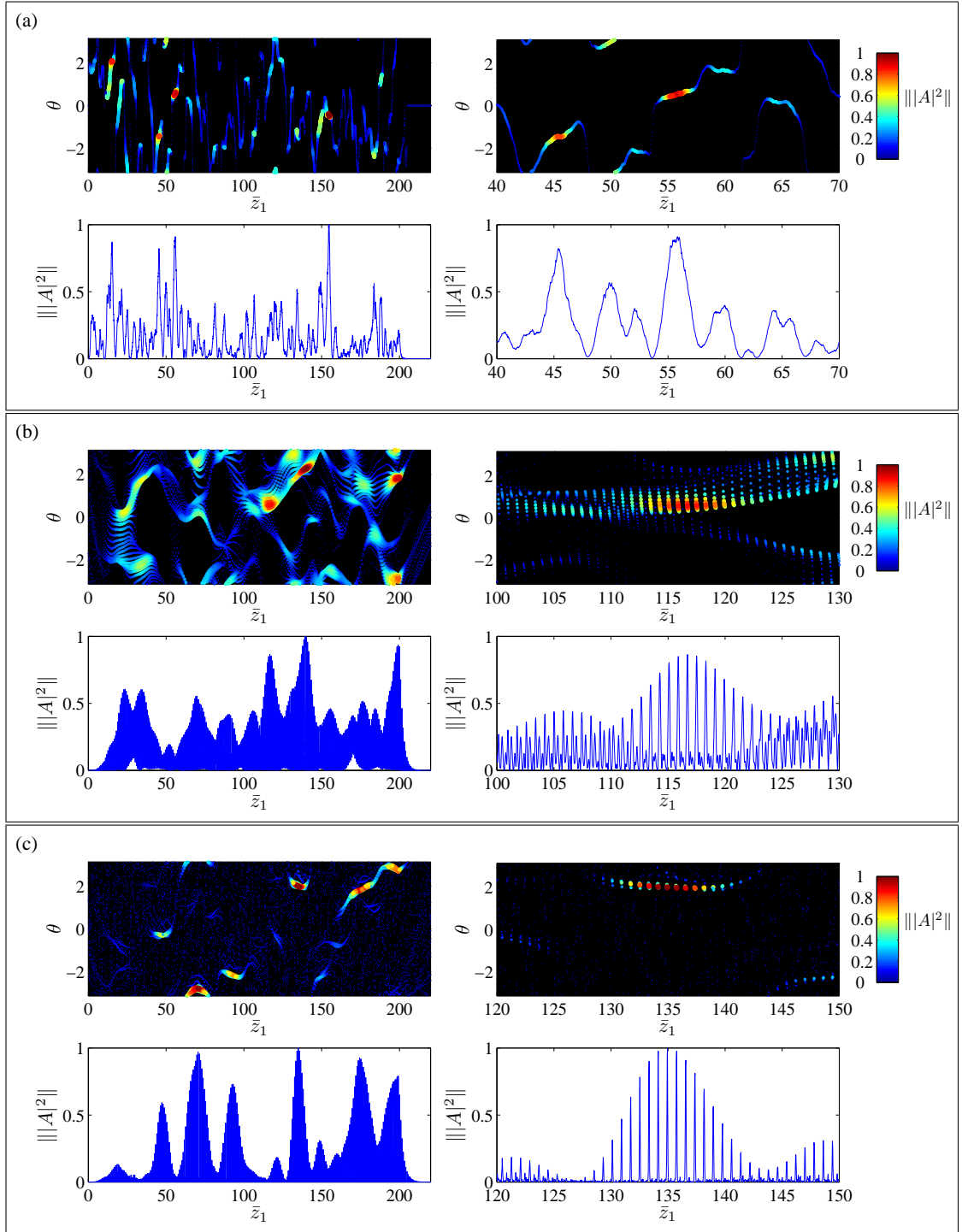
Figure 5.1:   Radiation phase and temporal profile for (a) conventional SASE, (b) mode-coupled SASE, and (c) mode-locked SASE FEL output. Each panel shows radiation phase (top) and normalised intensity (bottom) (with insets of the temporal window to the right). The results are plotted after 200 undulator periods ($\bar{z} = 5$) for simulations with FEL parameter $\rho = 2 \times 10^{-3}$. In the phase plots, the size and colour of the plotted points are related to the radiation intensity to ease identification of the peaks.

5.2.2 Pulse alignment and micro-bunching profile

Two other new characteristics of the mode-locked FEL starting from noise are identified here: the longitudinal location of the pulses relative to the energy modulation phase, and the properties of the micro-bunching profile. Figure 5.2 shows the radiation and micro-bunching profiles, and the electron beam energy modulation for a mode-locked FEL simulation. The 1D code was used for the simulation as described in Section 2.11, 8 periods per module were used, and the results are plotted mid-way through the 25th module. The results shown show typical features that have been observed across a range of parameters.
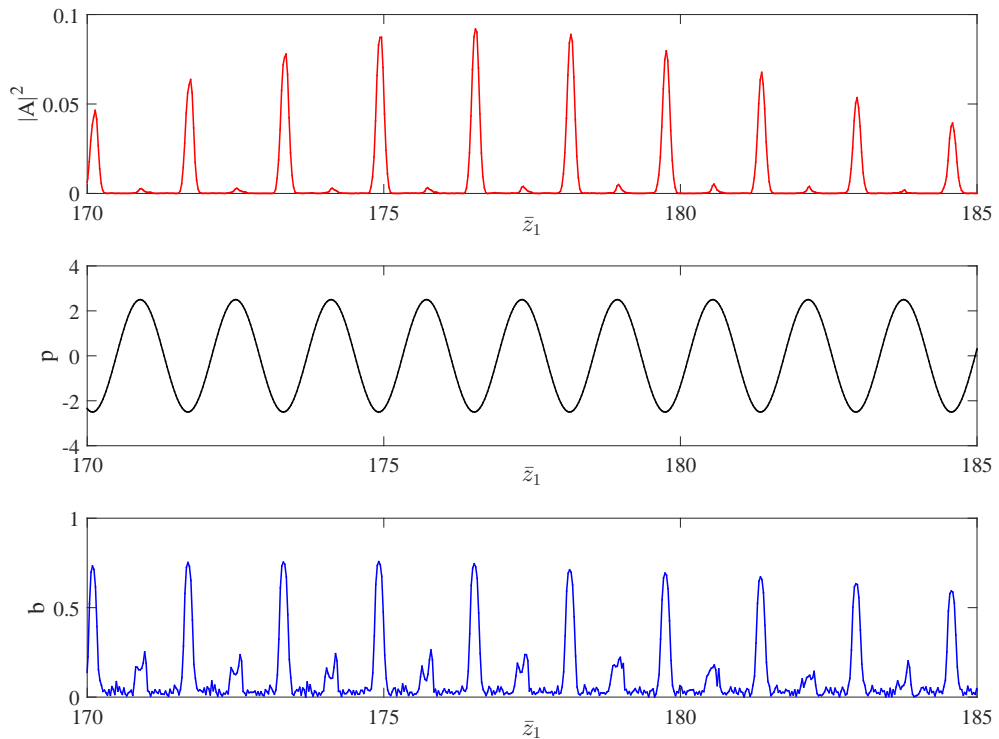
Figure 5.2: Top - temporal profile of the radiation power at the centre of the 25th undulator module; Middle - slice-averaged electron beam energy offset from the resonant energy (in terms of electron rest mass energy); Bottom - temporal profile of the electron beam bunching at the centre of the 25th undulator module. The radiation pulses align with the positions of minimum energy gradient. Differences between the pulses/bunching at the minimum/maximum energies are observed.

The radiation profile shows a higher intensity set of pulses aligned with the minimum energy positions, and a lower intensity set aligned with the maximum energy positions. This is consistent with the findings of Section 4.5, in which the positions of minimum energy gradient were found to be optimum for HHG

amplification. The maximum energy positions support amplification of radiation pulse trains, but at a lower growth rate than the minimum energy.

Also shown in Figure 5.2 is the micro-bunching profile. It is seen that the micro-bunching profile takes a similar form to the radiation profile, firstly in that it consists of a series of spikes. The bunching spikes align with the positions of minimum energy gradient, hence the radiation pulses and bunching spikes align exactly at the centre of the undulator module. Therefore, at the entrance to the undulator module, the radiation pulses are offset behind the peak of the bunching spikes by a number of radiation wavelengths equal to half the number of periods per module, and slip such that they are offset the same amount ahead by the module exit. This effect is considered further in Section 6.3.

Another significant feature of the bunching profile is the difference in shapes between the bunching spikes at the maxima and minima of the energy modulation. The bunching spikes at the minima consist of a smooth, single peak, whereas those at the maxima generally exhibit two peaks either side of the centre. This is the first indication of a difference in behaviour between the two positions, and an explanation for this effect is proposed in Section 5.3.3.

By observing the pulse alignment and bunching profiles, additional insight into the effect of energy modulation in the mode-locked FEL is gained that had not been observed previously in [57].

5.2.3 Temporal description

Simplified representation of the 3 regimes

A simplified representation of the radiation output from the three regimes is shown in Figure 5.3 to emphasise the differing temporal coherence properties. For the SASE case, a sequence of autonomous regions of length $\approx 2\pi l_c$ develop, while for the mode-coupled and mode-locked cases, the phase correlation is distributed across autonomous trains of pulses of length $\approx s \times 2\pi l_c$. In the mode-coupled regime, multiple pulse trains can occur within the enhanced coherence length, while in the mode-locked regime, one pulse train dominates within this distance.
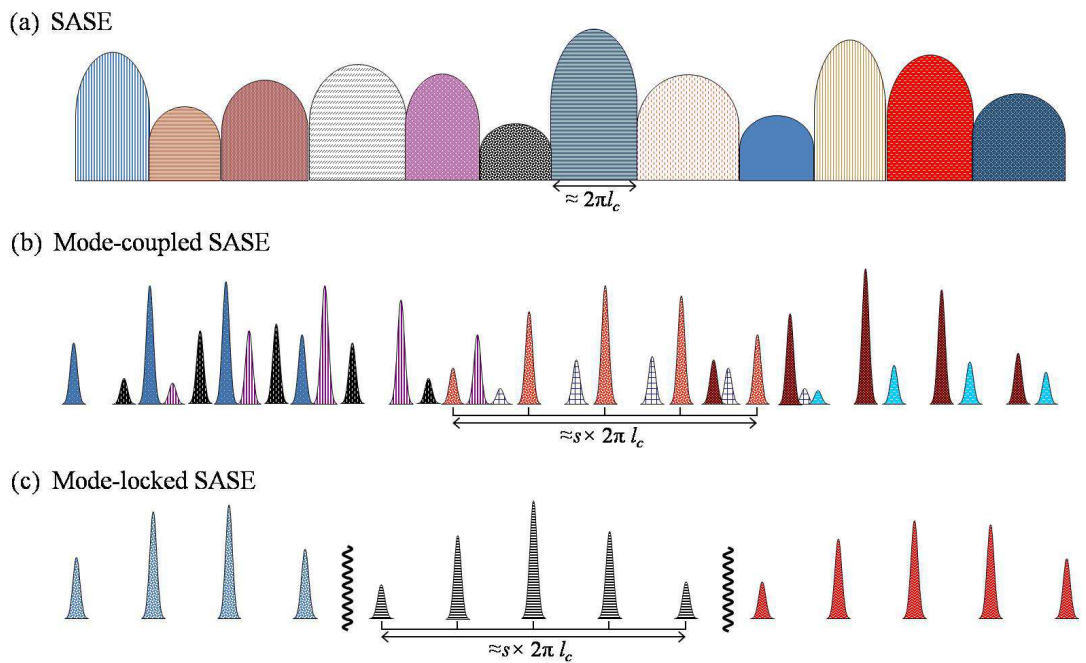
Figure 5.3: Simplified representation of the radiation output from (a) conventional SASE, (b) mode-coupled SASE and (c) mode-locked SASE regimes. Regions with the same shading are phase-correlated; for the SASE case there are a sequence of autonomous regions of length $\approx 2\pi l_c$ while for the mode-coupled and mode-locked cases, the phase correlation is distributed across autonomous trains of pulses of length $\approx s \times 2\pi l_c$.

The results shown in Figure 5.1, and illustrated schematically in Figure 5.3 are important for understanding the behaviour of the mode-locked FEL. While the output of the mode-coupled FEL exhibits some degree of periodicity, it is clearly not periodic. The phase correlation across the pulses within a train gives the periodicity. But the fact that these pulse trains are finite and interleaved

with no common start/end points ensures that the overall temporal structure is not periodic. Since the profile is not periodic it cannot be fully described by a simple combination of several discrete modes. This can be observed in simulation results as a noisy splitting effect of the modes in the spectrum.

Consequently, it is perhaps more intuitive to describe the system in the temporal domain. From this perspective, the fundamental 'unit' of the system - instead of being modes - is a finite pulse train with integrated length on the order of the co-operation length: basically equivalent to one SASE spike. Whereas in the conventional FEL the SASE spikes occur consecutively, in the mode-coupled FEL the SASE spikes are interleaved. And in the mode-locked FEL the conditioning of the electron beam means this interleaving does not occur and there are effectively a series of SASE spikes occuring consecutively again (but now with fine structure). This interpretation is developed further in a simplified model in Chapter 6.

5.3 Analysis of energy modulation effects

The results of Chapter 4 and Section 5.2 indicate three significant features of the role of energy modulation in the mode-locked FEL:

- Definition of pulse positions.

- Constraint of pulse broadening.

- Difference between maxima and minima of energy modulation.

This section assesses these effects in more detail.

5.3.1 Definition of pulse positions

The results for both the seeded and SASE mode-locked FEL indicate that introducing an electron energy modulation of sufficient amplitude has the effect of defining the positions at which optimum amplification occurs. Criteria for the energy modulation amplitude are now derived.

The energy modulation of the electron beam can be described as:

$$\gamma = \gamma_0 + \gamma_m \cos(\Delta\bar{\omega}\bar{z}_1) \tag{5.1}$$

The cosine term can be differentiated to give the gradient of the modulation, and multiplied by $\bar{l}$, to find that a radiation wavefront propagating a distance of one undulator module about the maximum of the beam energy gradient will experience a beam energy range of:

$$\Delta\gamma \approx \gamma_m \frac{2\pi\bar{l}}{\bar{s}} \approx \gamma_m \Delta\bar{\omega}\bar{l} \tag{5.2}$$

If this range is sufficiently large that $\Delta\gamma/\gamma_0 > \rho$, then the FEL interaction will be suppressed [43]. Hence, for a beam modulation period defined by the radiation mode spacing, $\Delta\bar{\omega} = 2\pi/\bar{s}$, then, for beam energy modulation amplitudes:

$$\frac{\gamma_m}{\gamma_0} > \frac{\rho S_e}{2\pi} \tag{5.3}$$

the radiation peak powers will start to become confined to grow about the extrema of the beam energy modulation where the energy gradients are smallest. For

example, given the parameters used in Figure 4.11 this corresponds to $\gamma_m/\gamma_0 > 0.13\%$, in good agreement with the simulation results. The effect can be seen in Figure 4.11 where radiation output is suppressed with increasing beam energy modulation amplitude for pulses that are phased to evolve in the regions of high energy gradient about $\bar{z}_{1_0} \approx 0.3$ and 0.7.

This pinning of the radiation pulses to these well defined positions, in both the seeded and SASE cases, is likely to be of significant benefit where the phasing of the output pulses to an external signal is important, e.g. pump-probe experiments.

5.3.2 Constraint of pulse broadening

The pulse broadening effect during amplification is dependent upon the energy modulation amplitude. The effect of energy modulation for varying amplitude is shown schematically in Figure 5.4.

For small amplitudes (Figure 5.4 (a)), the energy gradient does not significantly spoil the beam and pulse broadening occurs. There is an optimum range of amplitudes (Figure 5.4 (b)) where the energy gradient spoils all but a region of length $\sim l$ centred around the zero energy gradient position. In this case the radiation pulse duration is restricted to $\sim l$. For larger amplitudes (Figure 5.4 (c)), the unspoiled region of the beam is $< l$. This reduces the growth rate of the FEL interaction and does not further reduce the radiation pulse widths from the system. This occurs since the radiation field slips a distance l in one undulator module, hence a region of length $\sim l$ experiences the unspoiled electron beam and is amplified.

A condition for the upper limit of the energy modulation that accommodates the dual criteria of allowing sufficient growth rate while minimising the pulse duration may be obtained by considering the beam energy range a radiation pulse interacts with when propagating $\pm \bar{l}/2$ about the extrema of the modulated beam. By expanding $\cos(x) \approx 1 - x^2/2$ in the modulation term of Equation 5.1, and letting $\Delta \bar{z}_1 = \bar{l}/2$, then setting the energy range to the upper limit of ρ, the condition for the upper limit of the energy modulation is obtained:

$$\frac{\gamma_m}{\gamma_0} < \frac{2\rho S_e^2}{\pi^2} \tag{5.4}$$
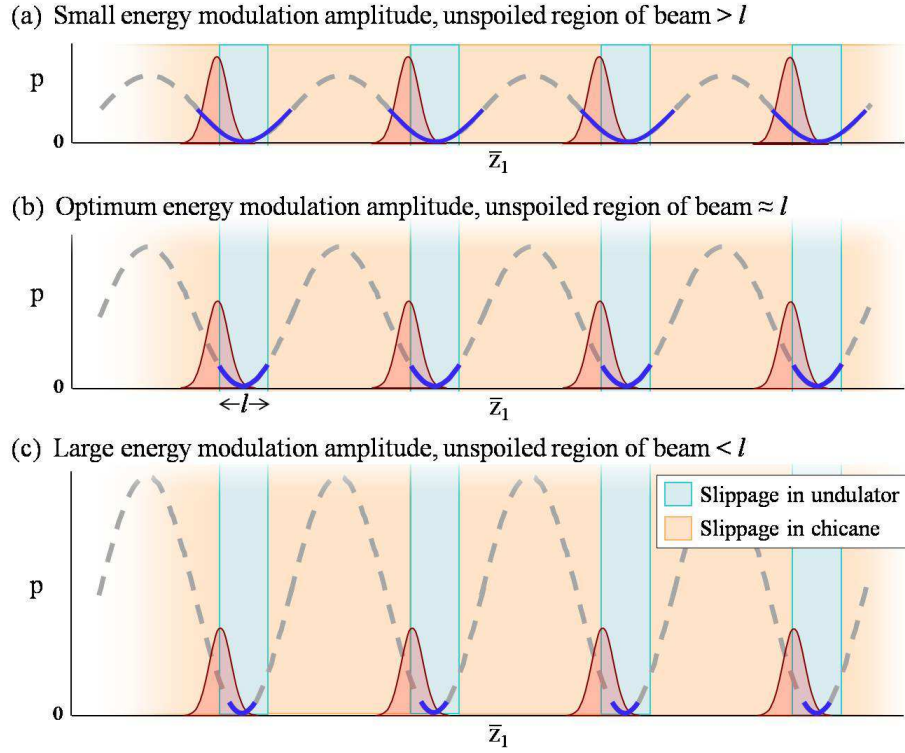
Figure 5.4: The effect of energy modulation is to spoil regions of the beam with high energy gradient. The unspoiled regions of the beam (highlighted in blue for the minimum energy positions) become narrower for increasing modulation amplitude.

For the parameters used above (as per Figure 4.11), this corresponds to a beam energy modulation of $\gamma_m/\gamma_0 < 0.68\%$.

The conditions 5.3, 5.4 may be combined to give the range of electron beam energy modulation that allow the pinning of the radiation pulses to the beam modulation extrema while allowing for a satisfactory radiation growth rate:

$$\frac{\rho S_e}{2\pi} < \frac{\gamma_m}{\gamma_0} < \frac{2\rho S_e^2}{\pi^2} \tag{5.5}$$

Results across a range of parameters suggest that the lower end of the range is often sufficient to constrain pulse broadening in addition to defining pulse positions.

Analogy with mode locking

In terms of mode-locking this effect can be understood to be analogous to the temporal domain description of mode-locking in conventional lasers. In this de-

scription the modulation effect occurs as a shutter that opens for a short period defining the pulse width, with repetition rate matched to the round-trip time of the cavity.

5.3.3 Difference between maxima and minima

It Sections 4.5.2 and 5.2.2 it was noted that differences in the behaviour of the system occur between the maximum and minimum energy positions. An explanation for this effect is proposed here.

The initial expectation was that the energy offset between the minima and maxima could potentially cause the difference in amplification rates. This could be attributed to the asymmetry of the high-gain FEL detuning curve (Figure 2.6). However, this theory was tested by applying a more complex energy modulation in which the upper half of the sinusoid was displaced to lower energy such that the maxima occurred at zero, while the lower half was displaced to higher energy such that the minima also occurred at zero. This made no significant change to the amplification rates - the minima still showed higher growth rate than the maxima.

The observation of the difference in bunching profiles between minima and maxima shown in Figure 5.2 suggested an alternative explanation for the difference in amplification rates, as follows:

The maxima and minima (as the positions of minimum energy gradient, and therefore optimum amplification) dominate the radiation emission and operate at two separate resonant wavelengths, each with an associated set of radiation pulse trains. The regions of the electron beam either side of the maxima are at low energy relative to the local resonance condition, hence on average they shift backwards relative to those at the maxima. An integral part of the high-gain FEL mechanism is that the radiation phase is continually driven backwards by the electron beam micro-bunching (see Section 2.8). It is proposed that a condition can occur where these two effects are matched such that the regions of the electron beam either side of the maxima developed enhanced bunching.

The above theory was tested by varying the energy modulation amplitude and observing the effect on the bunching profile. If a fixed longitudinal position offset from the position of maximum energy is considered, then increasing the modulation amplitude will increase the relative phase slippage experienced by the

electrons at this position. Therefore increasing the modulation amplitude should bring the positions of optimum phase drift (and therefore optimum bunching) closer in towards the maxima. Figure 5.5 shows the bunching profiles for three different modulation amplitudes. It is observed that increasing the modulation amplitude does indeed bring the peaks of the bunching profile in closer to the maxima, supporting the theory.
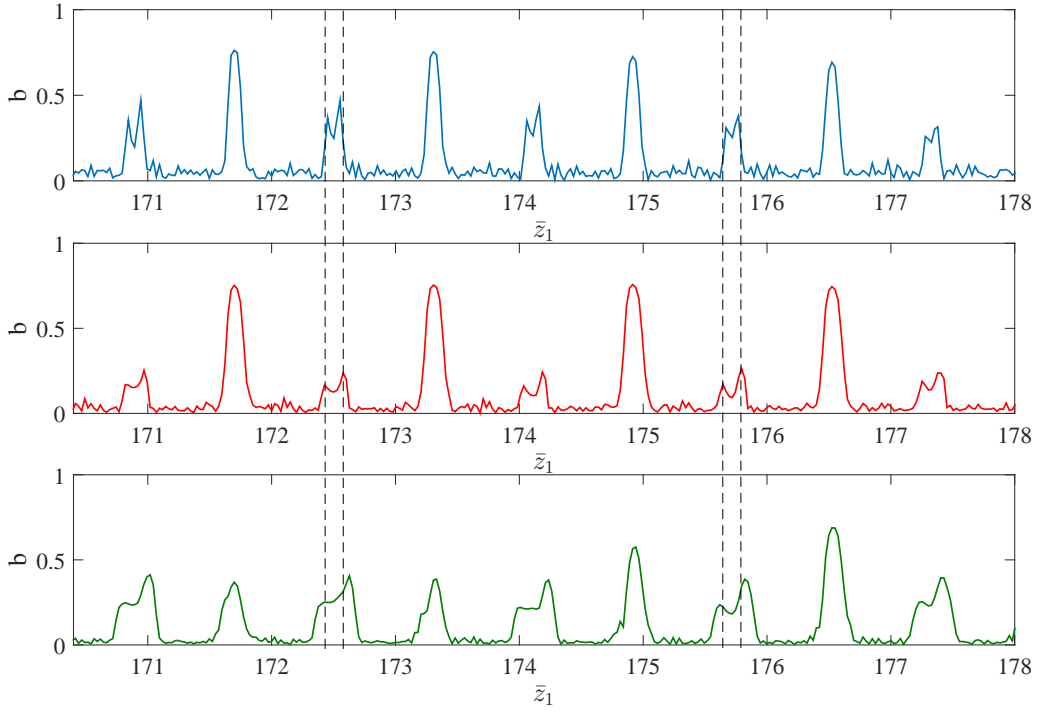
Figure 5.5: Electron beam bunching at the centre of the 25th undulator module for three different values of energy modulation p=±5 (top), ±2.5 (middle, ±1.25 (bottom). The dashed lines mark the longitudinal positions of the bunching peaks for the ±2.5 case. It is seen that increasing the modulation amplitude (p=±5 - top) moves the peaks closer to the centre, while decreasing the modulation amplitude (p=±1.25 - bottom) moves the peaks further apart.

At the minima the regions of the electron beam either side move forwards relative to the local resonance, so do not have the possibility to more optimally match the phase change of the radiation, and so enhance the bunching. The assumption is that the double-peaked bunching profile that occurs at the maxima is detrimental to FEL amplification relative to the behaviour at the minima.

5.4 Alternative modulation methods

5.4.1 Required properties of modulation

It has been shown that a sinusoidal beam energy modulation defines a train of regions at which the FEL interaction is preferentially supported, and can restrict temporal broadening of radiation pulses at these positions. This understanding of the function of the energy modulation, enables the properties of other potential modulation methods to be qualitatively identified. Any alternative method needs to enhance or inhibit the FEL interaction periodically (in $\bar{z}_1$), with the preferentially supported regions being of similar length to l and spaced at s. A more quantitative analysis is now considered.

In Figure 5.6, an example sinusoidal energy modulation is shown together with the calculated energy spread over a $\pi/4$ slippage length (corresponding to $S_e = 8$. The energy spread varies as a smoothed $|\cos\theta|$, with sharp increases in energy spread either side of the minimum energy gradient positions.
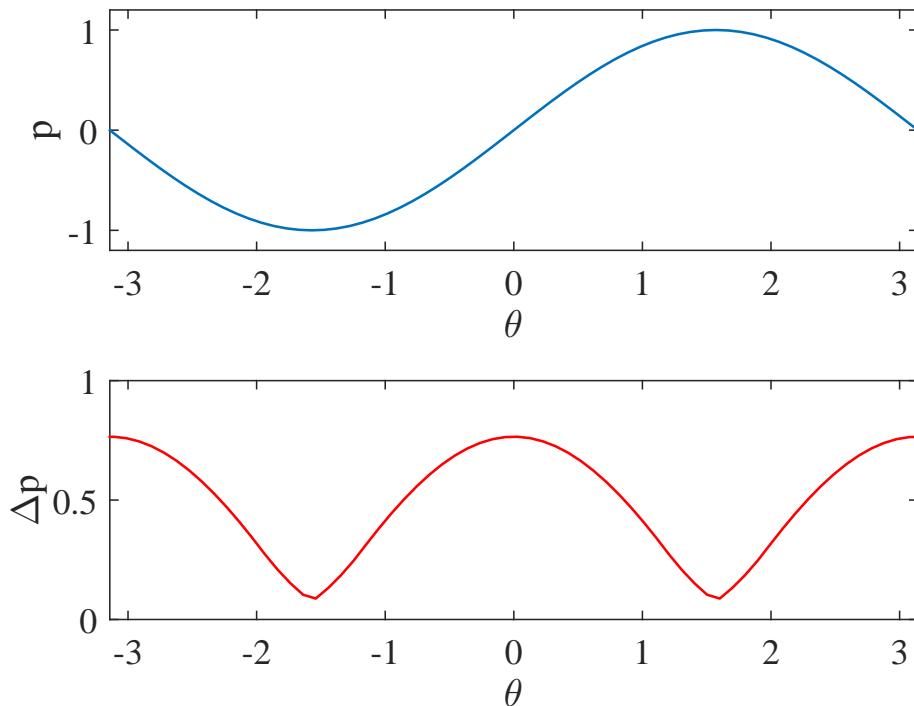
Figure 5.6: Example sinusoidal energy variation and corresponding energy spread over a $\pi/4$ slippage length.

Taking this description a step further, the inverse of the energy spread as a function of longitudinal position is plotted in Figure 5.7. It has been described in Section 5.3.3 that there is an additional process inhibiting growth at the energy maxima relative to the minima, so this section of the curve is dashed, and replaced by a continuation of the low 'quality' region. The resultant curve gives an indication of the 'ideal' properties of the electron bunch modulation in terms of a 'quality factor', Q. The implication is that the ideal form of the quality modulation in the beam is similar to the natural radiation pulse train output of the system.
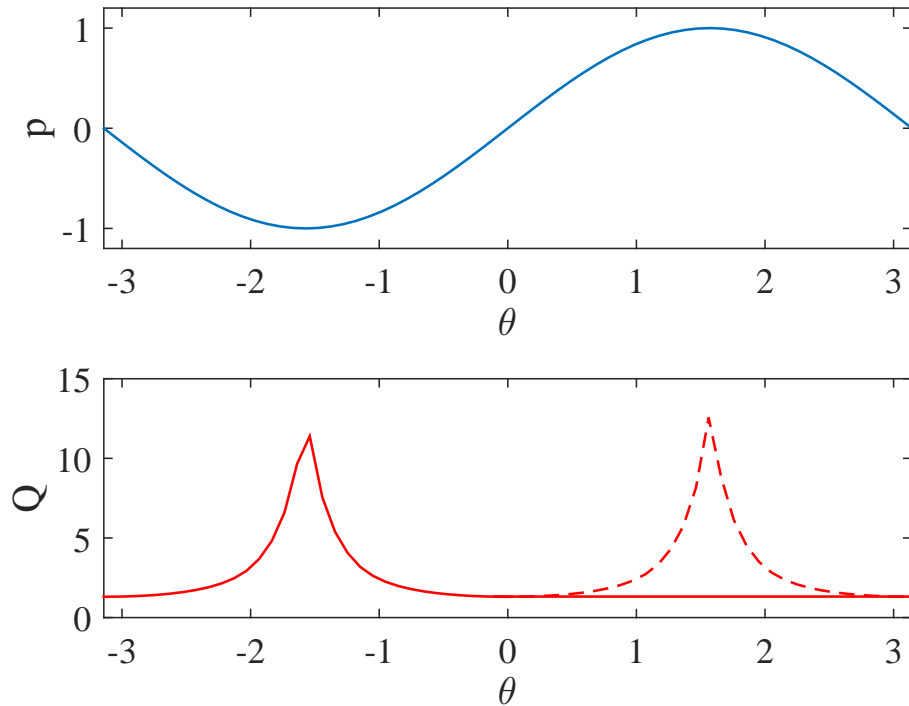
Figure 5.7: Example sinusoidal energy variation and corresponding 'quality' factor $Q = 1/\Delta p$ over a $\pi/4$ slippage length.

5.4.2 Mode-locked FEL with current-modulated beam

The analysis of the previous section showed the form that electron beam modulation should take to generate the mode-locking effect. One method which could potentially deliver the required modulation in electron beam quality is current modulation, as generated in e-SASE [82]. In this section current modulation is investigated as a potential mode-locking technique. This work was carried out in parallel to another group, and was reported in a joint paper [83].

A temporal current variation was introduced to simulations, approximating the form described in Section 5.4.1, as shown in Figure 5.8. Modelling was carried out with parameters similar to those used in Section 4.4.1, using the 1D code.
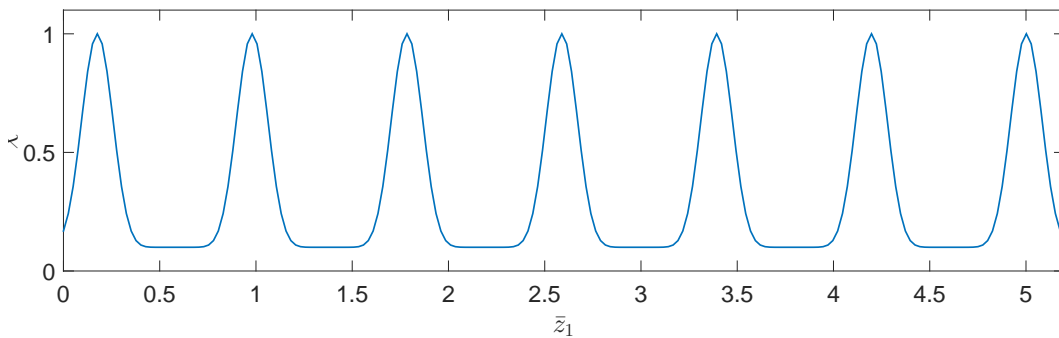
Figure 5.8: Temporal profile of electron beam current used to test current modulation as a method of mode-locking in ML-FEL simulations. The normalised current, χ, is plotted as a function of $\bar{z}_1$.

Figure 5.9 shows the radiation phase and normalised intensity at different stages in the amplification process. A series of short pulses are generated after only one undulator module, as shown in Figure 5.9 (a), however there is no phase correlation from pulse to pulse, and the radiation is at low intensity. Amplification takes place, and it is seen that at saturation (Figure 5.9 (c)), phase correlation has developed over the enhanced coherence length ($S_e \times l_c$).

The output properties are cleaner than the energy modulation case due to the absence of the low intensity pulses which occur at the energy maxima. In practice, an energy modulation leads to a current modulation, so a combination of the two effects may occur. This topic is described further in the next section.
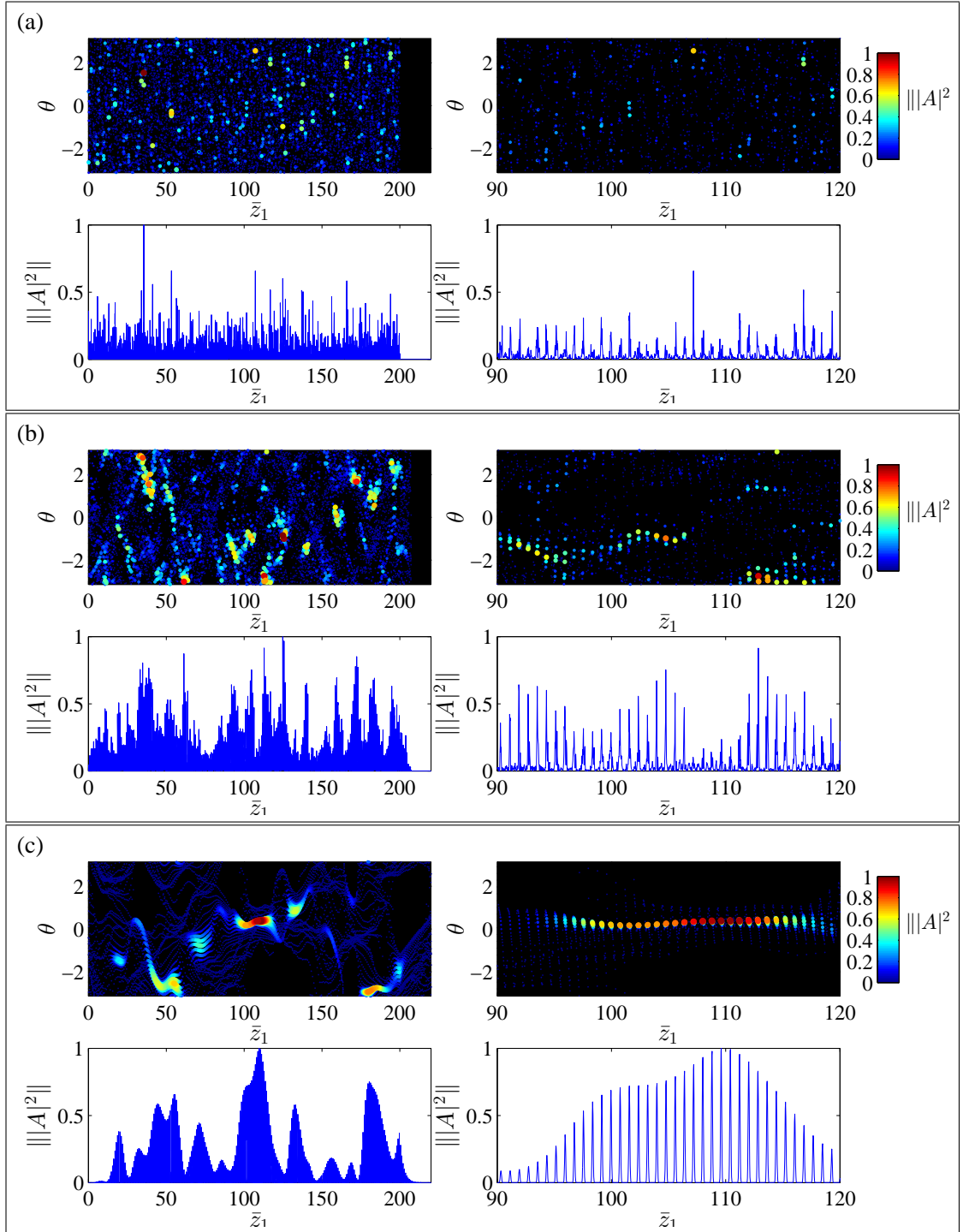
Figure 5.9: Radiation phase (top) and normalised intensity (bottom) for mode-locked amplifier FEL with current modulation after (a) 1, (b) 10, and (c) 50 undulator modules. Plots to the right show an inset of the temporal profile.

5.5 Simulation model limitations for energy modulated beams

The codes used to model the FEL interaction for the work in this thesis (described in Section 2.11) assume that the simulated electrons are confined to their initial localised ponderomotive potentials. It is worth noting here that for some parameters, these approximations may not be valid when simulating cases that utilise energy modulated electron beams, such as the ML-FEL.

On propagation through the undulator-chicane modules, dispersion will cause the applied beam energy modulation to develop into density (current) modulation of the same period, as shown in Figure 5.10. Density modulation due to an initial sinusoidal modulation is possible on the scale of the radiation wavelength but not on the longer scale of the modulation period.

To investigate these effects requires new simulation methods such as [84] that allow for beam current evolution as the interaction progresses. The cases in this thesis work under the assumption that the accumulated current modulation due to dispersive effects upon propagation through the undulator-chicane system is negligible.

A condition for this effect has been derived and shown to be valid for the parameters in this thesis [80].
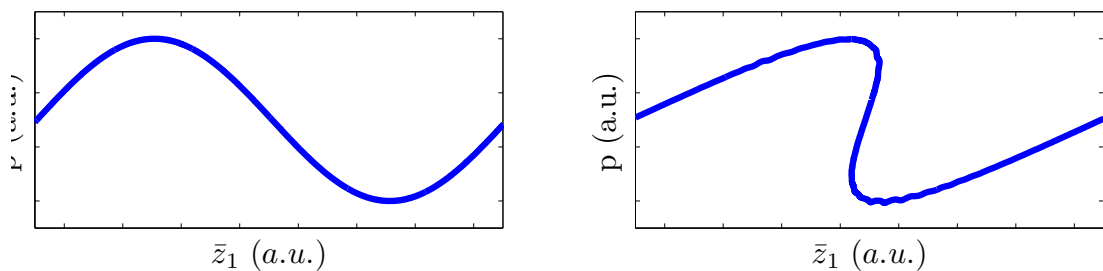
Figure 5.10: Energy modulation evolution in simulation codes. In the code used, electrons are confined to their initial buckets - density modulation (right) due to an initial sinusoidal modulation (left) is possible on the scale of the radiation wavelength but not on the longer scale of the modulation period.

5.6 Conclusions

In this chapter the role of electron beam modulation in the mode-locked amplifier FEL has been investigated in detail, with a number of findings.

The effect of the energy modulation has previously been described as a means of transferring energy to sideband modes [57]. In this chapter a compatible description in the temporal domain has been developed. It has been shown that energy modulation serves to produce a longitudinal variation in the quality of the electron beam for FEL amplification. This longitudinal variation both defines the positions where pulses develop, and constrains pulse broadening that would otherwise occur. Conditions for the required energy modulation properties have been derived. The temporal domain description is developed further in Chapter 6.

The properties of the micro-bunching profile were investigated, and differences in behaviour at the energy maxima and minima were identified. Consequently a theory was developed to explain the difference in amplification rates between the energy maxima and minima.

The required properties of electron beam modulation were established, and it was shown in simulations that a current modulation of the beam has an equivalent effect to energy modulation and hence could be used as an alternative. In some respects the current modulation method may be advantageous, in that the output is cleaner due to the absence of the low intensity pulses which occur at the energy maxima. Having described the required properties of the electron beam modulation it is possible to envisage other possibilities to deliver the mode-locking effect, e.g. to periodically spoil the electron beam emittance.

Chapter 6

Simplified Description of the Mode-Locked Amplifier FEL

6.1 Introduction

In this section a simplified description of the mode-locked amplifier FEL is developed, in order to quantify characteristics of the system such as the growth rate. This problem has been approached previously in the frequency domain by considering the growth rates of the individual modes [85]. Here the problem is addressed with a description in the temporal domain, as outlined in Section 5.2.3. A 'first-order' description is given in Section 6.2, where similarities to the conventional high-igain FEL result are shown. A model to described 'second-order' effects such as pulse broadening is described in Section 6.3.

6.2 First-order description

To illustrate the behaviour of the mode-coupled regime compared to the conventional case, a simple example was considered with the evolution of both systems beginning from a narrow radiation source term of width λ_r. Modelling was carried out with parameters similar to those used in Section 4.4.1 ($S_e = 4$), using the 1D code. The effect of shot noise was excluded. Dispersion in the chicanes was set to zero to exclude the optical klystron effect from altering the gain length.

Figure 6.1 shows the evolution of the longitudinal profiles of the radiation intensity and electron beam micro-bunching as a function of undulator module

number for both cases. The horizontal size of the mode-coupled plots has been reduced by a factor of $S_e = 4$ compared to the conventional case to compare the macroscopic behaviour.
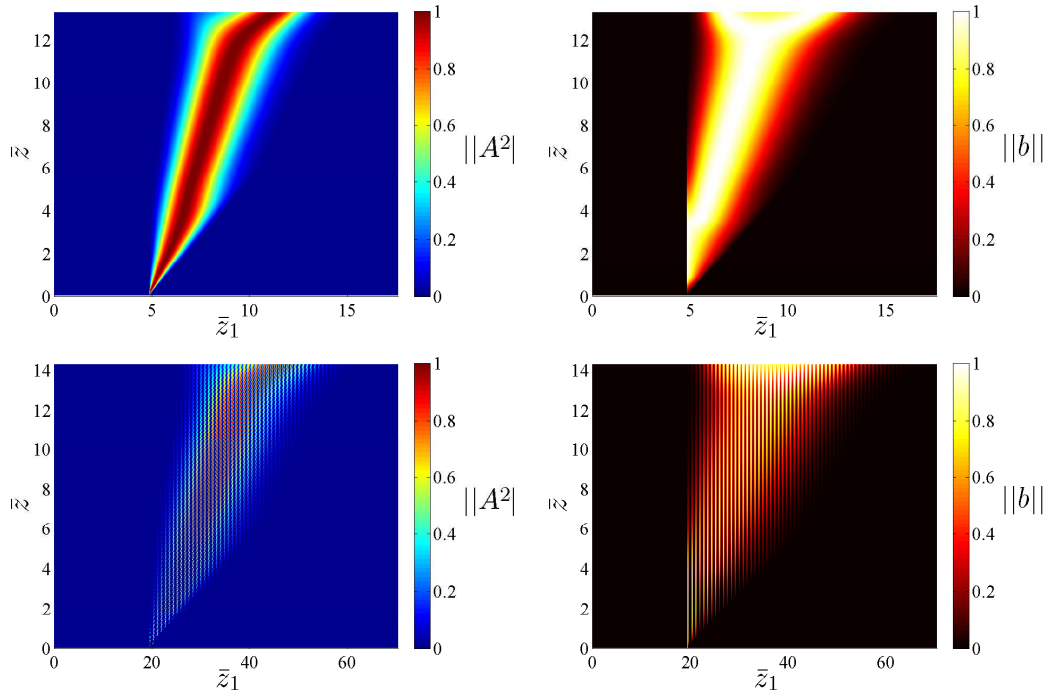
Figure 6.1: Evolution of the longitudinal profiles of the normalised radiation intensity (left) and normalised electron bunching (right) as a function of undulator module number, for the conventional regime (above) and the mode-coupled regime (below) starting from a narrow radiation source term. The horizontal size of the mode-coupled plots has been reduced by a factor of $S_e = 4$ compared to the conventional case to show the similarity in the macroscopic behaviour.

In the mode-coupled case, a train of pulses develops in both the radiation field and the electron beam micro-bunching. This is an example of the similarity between radiation and electron beam properties as discussed in Section 2.10.1.

A key point to note is that the macroscopic properties of the results are extremely similar between the conventional case and the mode-coupled case. The envelope of the pulse train in the mode-coupled case, evolves almost identically to the intensity profile in the conventional case. This supports the earlier assertion in Section 5.2.3 that pulse trains in the mode-locked FEL are equivalent to SASE spikes in the conventional regime. The mode-coupled growth rate is also similar to the conventional case as shown by the similar evolution in $\bar{z}$ in Figure 6.1. Further details on the growth rate are given in Section 6.3.

The similarity of the two regimes outlined in Figure 6.2, which shows a simplified description of the conventional and mode-locked regimes. In the conventional regime the radiation field is shifted forward in z_1 by one radiation wavelength per undulator period. For the mode-locked FEL, the simplified description is that both the radiation field and electron beam are discretised into segments; the radiation and electron beam interact in one module and then the radiation propagates directly ahead into the next electron beam segment. In this case the conventional and mode-locked cases would be identical. The assumption being that the radiation field and electrons outside the interacting segments do not contribute significantly in the interaction.

(a) Conventional FEL amplifier:
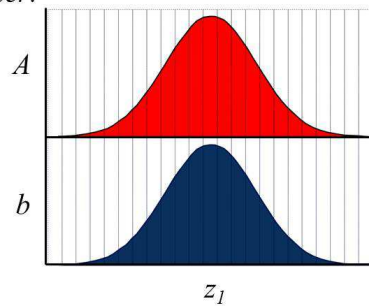
(b) Mode-locked FEL amplifier:
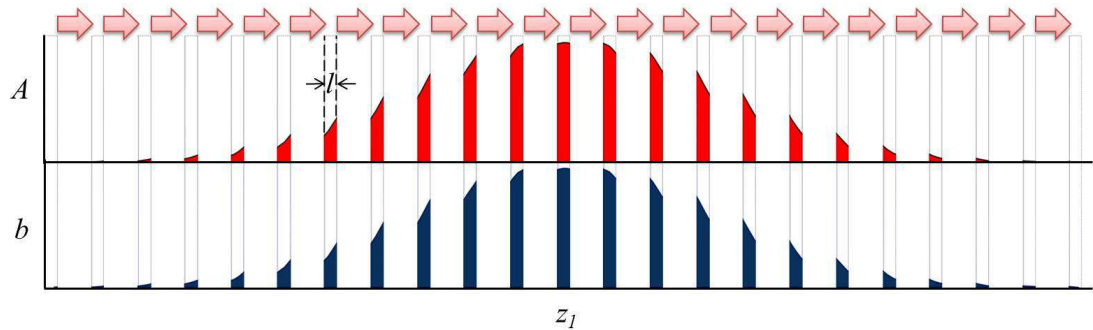
Figure 6.2: Temporal profiles of the radiation field (A), and electron beam micro-bunching (b), in the conventional high-gain FEL amplifier, and the mode-locked/coupled FEL. In the conventional case, longitudinal segments of the radiation field step continuously through the electron bunch. In the mode-locked/coupled case the interacting parts of the field and bunch are segmented, with the radiation segments stepping forward in the chicanes.

The conclusion of this section is that to first order the behaviour of the mode-locked/mode-coupled FEL can be described as being almost exactly equivalent to a conventional high-gain FEL, only differing in whether the interaction is continuous or discretised. It is also noted that in the alternative modal description

of the scheme, the particular modes taking part in the interaction are dependent upon the slippage in the chicanes, $\bar{\delta}$. Changing the value of $\bar{\delta}$ changes the modes that take part in the interaction, and it has been suggested that the total slippage $\bar{s}$ must take integer values. In the temporal description the value of $\bar{s}$ can take non-integer values and the interaction proceeds in the same way.

6.3 Second-order effects

There are some effects that can not be described with the 'first-order' model. Clearly the description of Figure 6.2 is a simplification of the slippage model in the mode-locked FEL. The discretised blocks of radiation field and electron bunch do not remain perfectly aligned with each other throughout amplification. Figure 6.3 shows a more accurate representation of the slippage effect: the radiation and electron blocks are largely kept aligned (as per the 'first-order' model), but there is slippage relative to each other in the undulator sections.
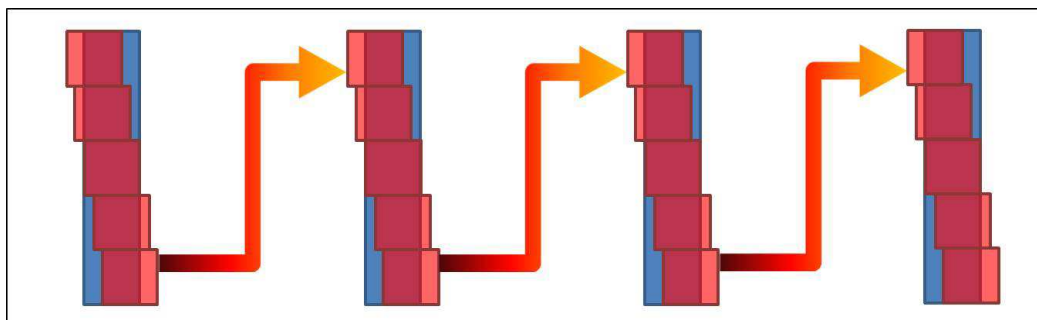
Figure 6.3: A more accurate representation of the slippage effect in the mode-locked FEL: the squares represent blocks of the radiation field (red), and the electron beam bunching (blue). The radiation blocks slip incrementally across the bunching blocks within undulator modules, before shifting ahead to the next bunching block in chicanes.

This gives rise to the following 'second-order' effects:

- Gain variation

- Approximately Gaussian pulse shape

- Pulse broadening/bandwidth narrowing

6.3.1 Simulation - gain variation

The growth rate of the mode-coupled case is now compared against the conventional case. For the 1D simulations shown in Figure 6.1, the maximum radiation intensity with distance through the undulator is plotted in Figure 6.4. The growth rate of the mode-couple case is slightly less than the conventional result.

The gain of the radiation intensity per undulator period is calculated and is also plotted in Figure 6.4 in order to show variations in growth rate within an undulator module. In the centre of undulator modules the growth rate of the mode-coupled case is close to the conventional case, but drops off earlier and later in the modules. This results in the overall lower growth rate seen in the upper plot.
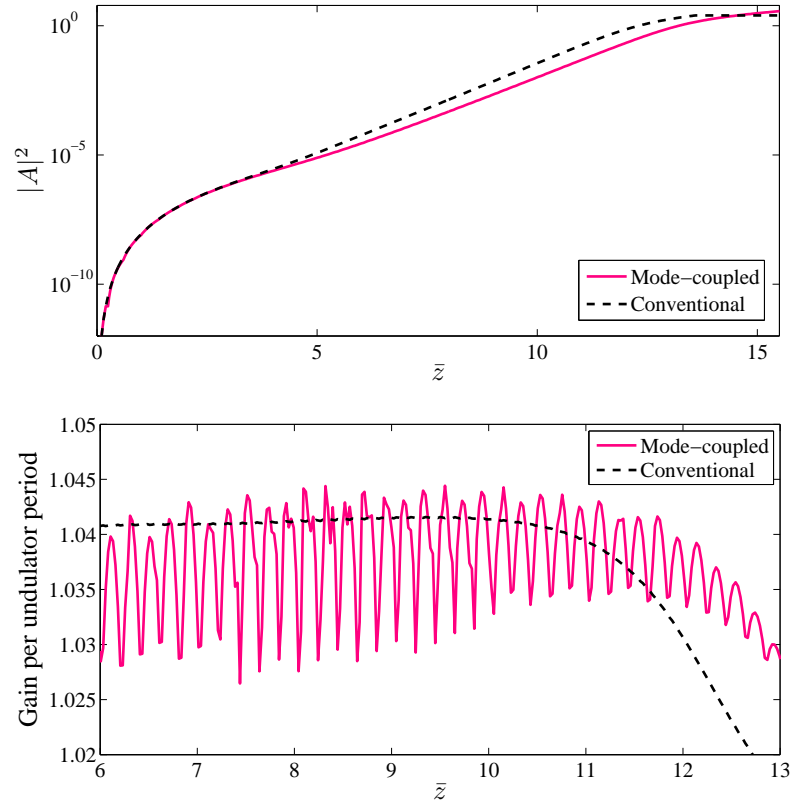
Figure 6.4: 1D simulation results showing the growth of the radiation intensity with distance through the undulator for the mode-coupled and conventional regimes. The variation of the gain of the peak of the radiation intensity with undulator period is also plotted for the two cases. This shows that there is a periodic variation in the gain for the mode-coupled case.

6.3.2   Simulation - pulse broadening

The width of the pulses in the pulse train structure is plotted against distance through the undulator in Figure 6.5 for the 1D simulations of previous sections. There is a continual broadening of the pulse structure in the exponential growth region, as seen in Section 4.4.

The broadening of the pulse structure appears to be a relatively slow process, with the pulses broadening at a rate of approximately 1 radiation wavelength per gain length. This indicates that the 'first-order' approximation that the radiation field and electrons outside the interacting segments do not contribute significantly in the interaction is reasonable. It also suggests that interleaved pulse trains may develop with little interaction between them, as described in Section 5.2.3.
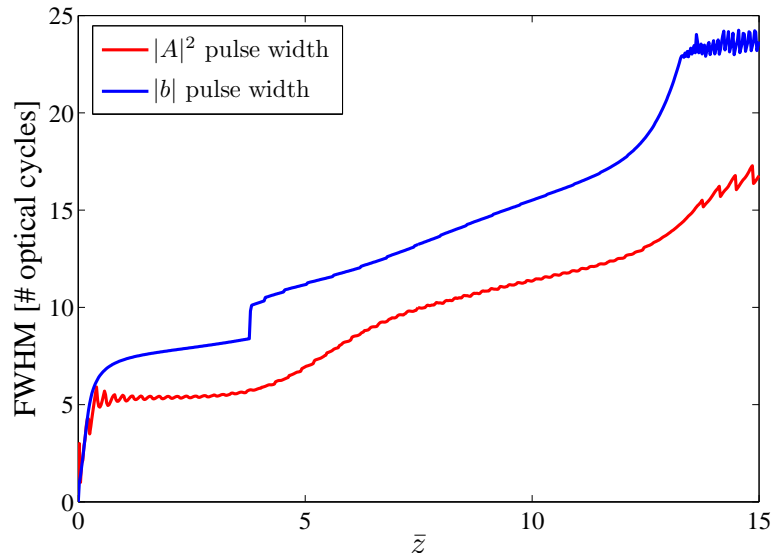
Figure 6.5: The width of the radiation pulses, $|A|^2$, and bunching spikes, b, in the pulse train structure are plotted against distance through the undulator for the results of 1D simulations.

The pulse broadening effect seems to have similarities to effects in conventional lasers. It is stated in [86] that 'the homogeneous laser oscillates on only one longitudinal mode near the center of the atomic transition when no modulation signal is applied. Formation of a stable optical pulse is the result of a delicate balance between the action of the modulator, which broadens the frequency bandwidth and narrows the pulse's duration and the gain medium, whose frequency dependent amplification acts to narrow the pulse's bandwidth and increase its duration'. A similar description could be applied to the mode-locked FEL, where

the slippage of the radiation relative to the electrons acts to broaden the pulses, while the energy modulation acts to narrow them. A simplified description of the pulse slippage effect is developed in the next section.

6.4 Simple model including pulse slippage

A simple model has been developed to describe the evolution of the mode-locked FEL. The model describes an interaction occurring at only the fundamental FEL frequency with no need for separate interactions at different modes. The model describes the growth rate of the radiation intensity and the pulse broadening effect, and the two effects are shown to be intrinsically linked via this description.

The linearised equations in terms of collective variables (with $\delta = 0$) are used (Equations 2.110, 2.111, and 2.112), and longitudinal variation of the parameters is included ($\bar{z}_1$-dependence):

$$\frac{\partial A(\bar{z}, \bar{z}_1)}{\partial \bar{z}} = b(\bar{z}, \bar{z}_1) \tag{6.1}$$

$$\frac{\partial P(\bar{z}, \bar{z}_1)}{\partial \bar{z}} = -A(\bar{z}, \bar{z}_1) \tag{6.2}$$

$$\frac{\partial b(\bar{z}, \bar{z}_1)}{\partial \bar{z}} = -iP(\bar{z}, \bar{z}_1) \tag{6.3}$$

The shifting function (sawtooth wave):

$$f(x) = \frac{1}{2} - \frac{1}{\pi} \sum_{n=1}^{\infty} \sin\left(\frac{n\pi x}{L}\right) \tag{6.4}$$

was used to control the $\bar{z}_1$ slippage of the electron beam terms relative to the radiation field, i.e. the radiation field is incremented forward by one radiation wavelength per undulator period for the number of periods per module, and is periodically reset to its initial value. The system was set up and solved using a differential equation solver in Matlab

The first case investigated had the initial condition of a top-hat function in the intensity temporal profile, representing a discrete segment of radiation field as in Figure 6.2. The initial values of the electron beam parameters were set to zero, $b = P = 0$. Figure 6.6 shows the evolution of $A(\bar{z}, \bar{z}_1)$, $b(\bar{z}, \bar{z}_1)$, and $P(\bar{z}, \bar{z}_1)$ with distance through the undulator. A second case, shown in Figure 6.7, represents the start up from an arbitrary noisy signal.
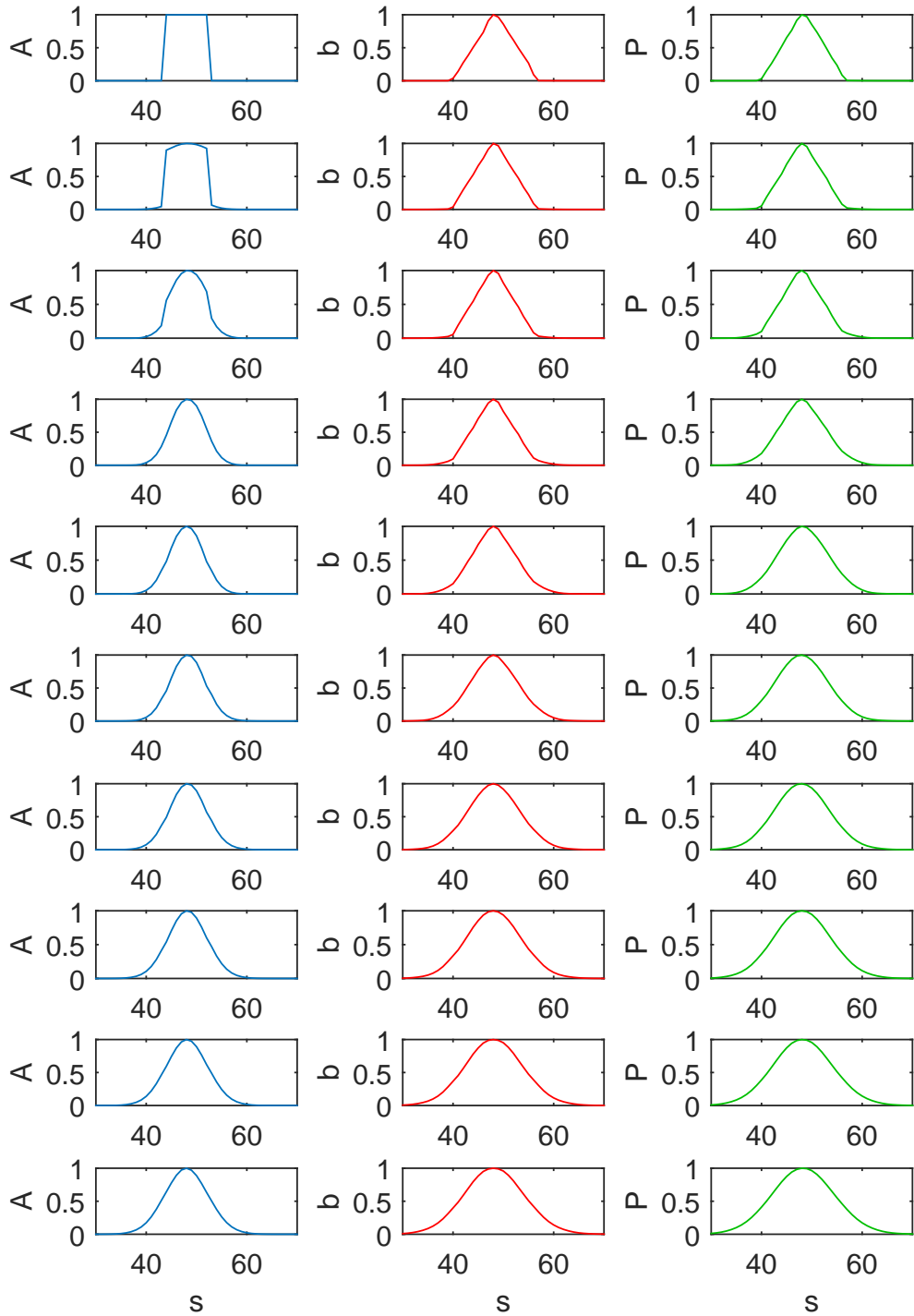
Figure 6.6: Results of periodic shifting during amplification on the temporal profiles of the radiation intensity (left column), micro-bunching (central column), and energy modulation (right column), for a case of start-up from a square radiation profile. The parameters are plotted at intervals of 60 undulator periods, from top to bottom, all plots are normalised to their maximum value.
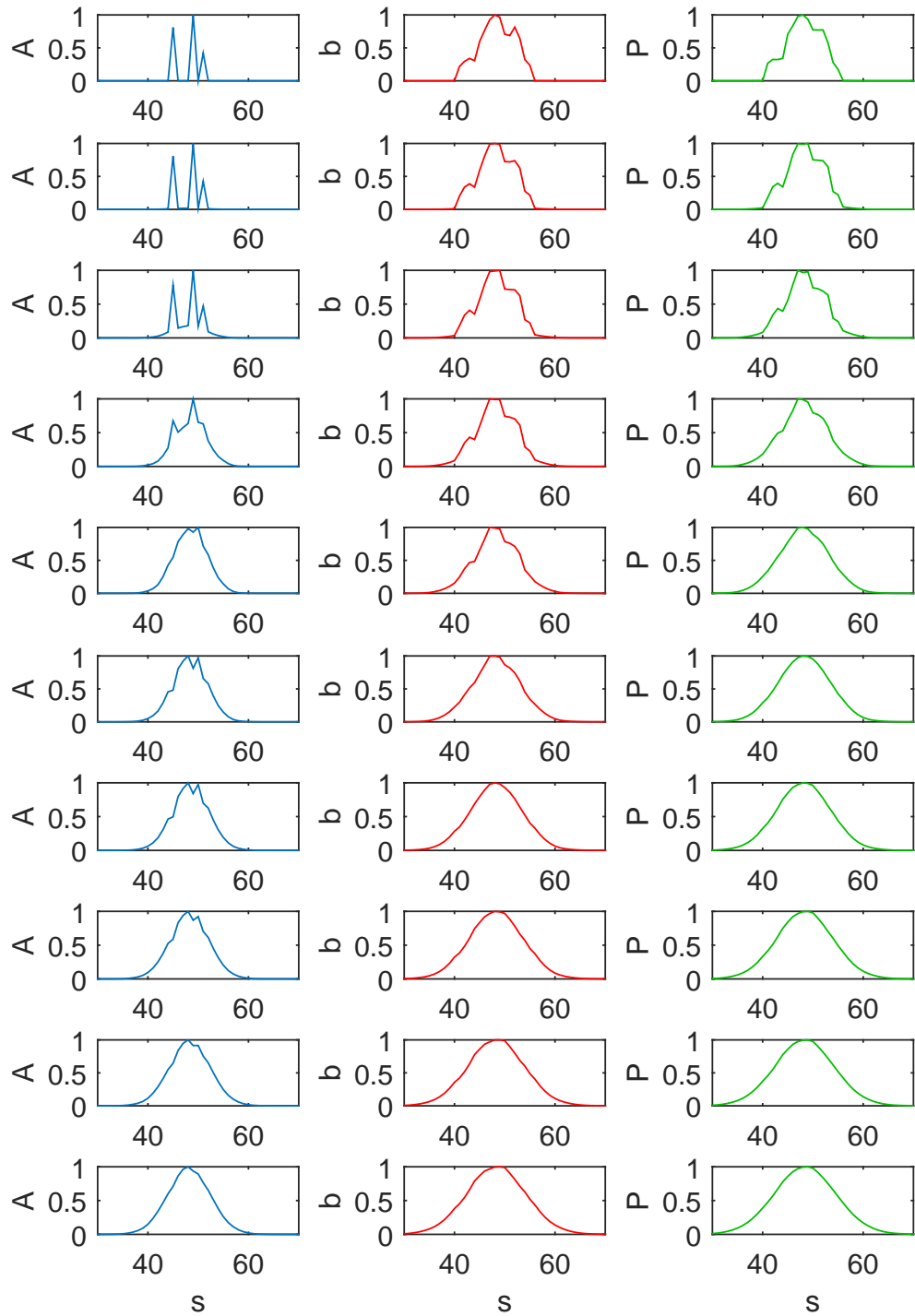
Figure 6.7: Results of periodic shifting during amplification on the temporal profiles of the radiation intensity (left column), micro-bunching (central column), and energy modulation (right column), for a case of start-up from a noisy radiation profile. The parameters are plotted at intervals of 60 undulator periods, from top to bottom, all plots are normalised to their maximum value.

The results of Figure 6.6 and Figure 6.7, indicate that the system quickly evolves to Gaussian pulse shapes regardless of the starting conditions. This is effectively a result of central limit theorem which shows that a Gaussian waveform is produced when an arbitrary shaped pulse is convolved with itself many times [87].

6.4.1 Model - gain variation rate

The implications for the growth rate are now considered. Figure 6.8 shows how the alignment of a radiation pulse and a bunching spike varies with distance through a single undulator. A Gaussian pulse shape is used, following the results of Figure 6.6 and Figure 6.7.
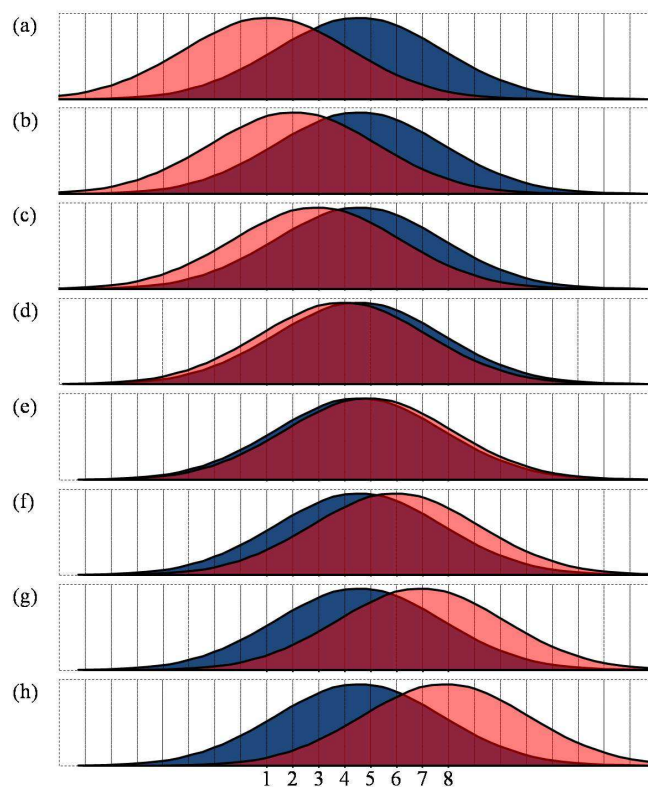
Figure 6.8:   The alignment between the pulses in the radiation (red) and bunching (blue) structures varies with distance through an undulator module (a)→(h). The peak of the radiation field traverses 8 radiation wavelengths (marked by vertical divisions).

Considering the case of moving with the peak of one of the pulses in the radiation field structure, it is straightforward to appreciate why the gain per period varies periodically as shown in Figure 6.4. The radiation growth is dependent

upon the bunching as shown in equation 6.1, and the bunching experienced by the peak of the radiation field varies with distance through the undulator module.

The variation of the gain of the peak of the radiation intensity with undulator period is plotted in Figure 6.9 for the mode-coupled and conventional regimes. This shows a periodic variation in the gain, in good agreement with the simulation results of Figure 6.4.
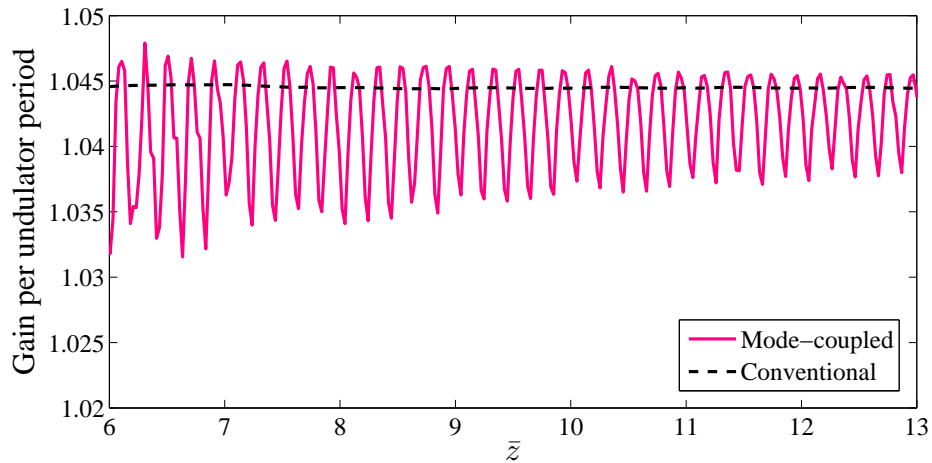
Figure 6.9: Gain per undulator period for the peak of the radiation intensity, as calculated with the simple model, for the mode-coupled and conventional regimes. The periodic variation of the gain for the mode-coupled case is in good agreement with the simulation results of Figure 6.4.

6.4.2 Model - pulse broadening

The pulse broadening effect can also be explained in a similar way to the growth rate variations. The average growth rate of the peak of the radiation field is slightly reduced compared to the conventional growth rate since it experiences parts of the beam with lower bunching. Conversely the average growth rate of the wings of the radiation pulse is slightly increased through experiencing regions of relatively high bunching. The pulses of the bunching structure broaden simultaneously and can be explained in a similar way.

Results from the model showing the width of the pulses plotted against distance through the undulator are given in Figure 6.10. There is a continual broadening of the pulse structure in the exponential growth region which appears in excellent agreement with the simulation results.
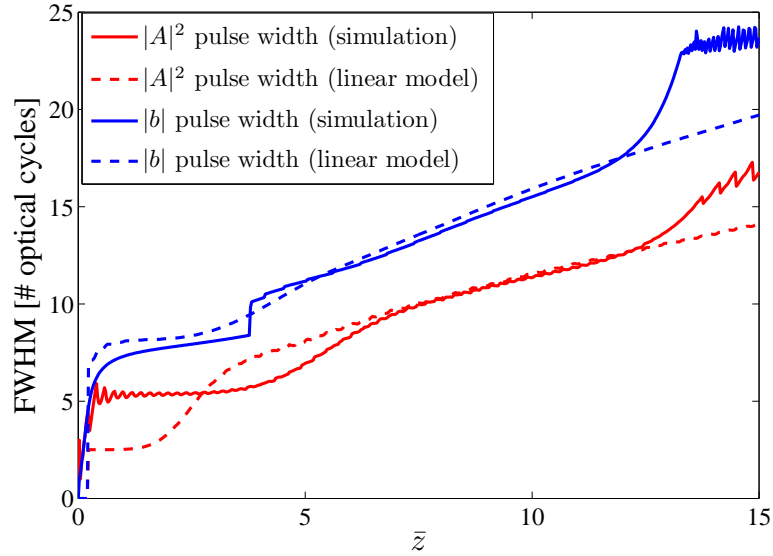
Figure 6.10: Pulse width evolution in the mode-coupled FEL - simulation versus simplified model. Pulse width is plotted against distance through the undulator for both radiation intensity and electron beam micro-bunching. Simulation results are compared to the predictions of the simple model. The results deviate where exponential growth in the simulation saturates at approximately $\bar{z} = 12$.

6.4.3 Relation between growth rate oscillations and pulse duration

It was stated earlier that the pulse width and gain are intrinsically linked in this model. It can be seen in Figure 6.9 that as the pulse width increases, the amplitude of the oscillation in gain decreases. It is straightforward to understand from the arguments of Sections 6.4.1 and 6.4.2 that as the pulse broadens, the gain variation will reduce.

Given sufficient propagation distance the pulse broadening may eventually lead to the pulse train structure washing out entirely and the gain reverting to the conventional FEL case, however the pulse broadening effect is too slow for this to occur for typical parameters. It appears that this effect is occurring in the simulation results of Figure 6.4, supporting the validity of the simple model.

6.4.4 Electron beam modulation

It is straightforward to add a current modulation to the model through introducing a $\chi(\bar{z}_1)$ factor representing current variation, with a Gaussian profile in $\bar{z}_1$. Figure 6.11 show that this can be used to restrict the pulse broadening as would
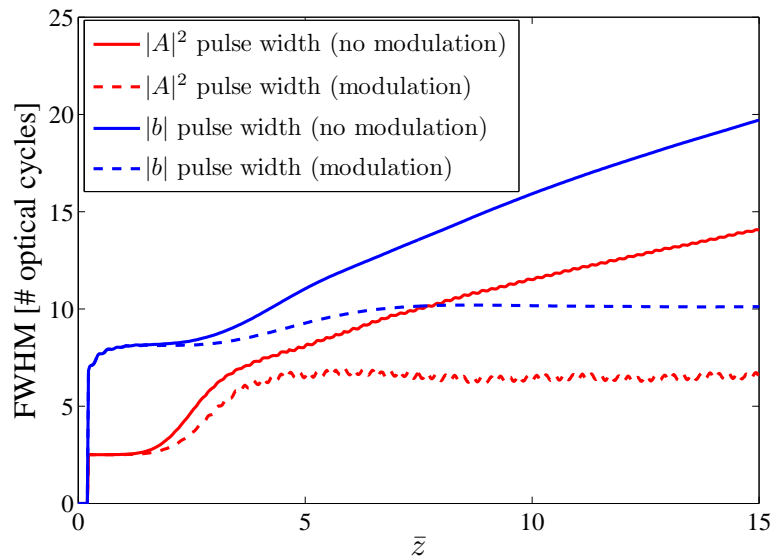
Figure 6.11: The width of the pulses is plotted against distance through the undulator for a case with current modulation. There is now a fixed pulse width.

be expected.

6.5 Conclusions

The results in this chapter indicated that to first order the behaviour of the mode-locked/mode-coupled FEL can be described as being almost exactly equivalent to a conventional high-gain FEL. The only clear difference being that the coherent length of radiation/electron beam involved in the process is continuous in the conventional case, and discretised in the mode-locked/mode-coupled case.

A temporal description of the mode-locked FEL amplifier has been presented and a simple model in terms of collective variables has been developed to describe the system. Results show a good match with simulations indicating that this is a promising approach to describing the system.

Chapter 7

Start-to-End Modelling of the Mode-Locked Amplifier FEL

7.1 Introduction

This chapter describes work carried out to model the mode-locked amplifier FEL scheme [57] in full start-to-end simulations (S2E), in order to show its compatibility with the predicted output from the present generation of accelerator designs.

The mode-locked amplifier scheme is modelled in three-dimensional FEL simulations, using an electron distribution tracked through full start-to-end accelerator simulations of a superconducting re-circulating linac design. It is emphasised that the FEL scheme is independent of the choice of accelerator configuration; the re-circulating linac option is chosen as an example of modern particle accelerator design. S2E modelling includes more complex effects not included in the 'ideal' cases considered so far, such as temporal variations in parameters along the electron bunch. An overview of the method of generation of the electron distribution used in FEL simulations is given in Section 7.2, and three-dimensional modelling of the ML-FEL starting from noise is described in Section 7.3. Some of the content of this chapter has been published in [80].

7.2 Accelerator Modelling

An electron distribution for use in FEL modelling was generated in start-to-end simulations of an accelerator design [88] for the UK New Light Source (NLS)

project [89]. The design comprises of a 200 MeV injector followed by two recirculation passes of a 1 GeV main linac. The photoinjector [90] consists of a normal conducting L-band (1.3 GHz) photocathode gun and a superconducting L-band (1.3 GHz) cavity module, and was simulated using ASTRA [91]. The electron distribution from ASTRA was imported into Elegant [92] for tracking through the accelerator lattice to the FEL. The accelerator design is a two-pass recirculating machine based on nine TESLA type accelerating cryomodules with longitudinal bunch compression carried out in three dedicated bunch compression stages. Following the linac are a beam switchyard, collimation and diagnostic tomography sections. A laser heater is used to mitigate the effects of CSR-induced microbunching. Figure 7.1 shows a schematic layout of the design.
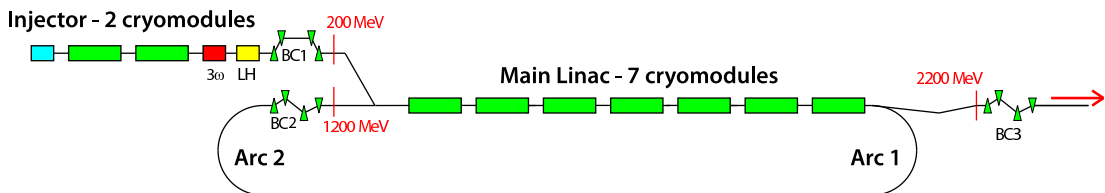
Figure 7.1: Schematic layout of the NLS recirculating accelerator. The 200 MeV injector includes a third harmonic cavity (3ω), laser heater (LH) and bunch compression chicane (BC1). Two passes of a 1 GeV main linac and two further bunch compression stages (BC2 and BC3) follow. Figure reproduced from [89].

The properties of the tracked electron distribution at the entrance to the FEL are given in Figure 7.2. The longitudinal phase space, current profile, slice emittance, and slice energy spread, binned in 1 fs slices, are shown. Peak current of >1 kA is delivered, with some variation over 100 fs. Slice emittances of less than 0.4 mm-mrad are attained. The slice energy spread is below 2×10^{-4} for most of the bunch. A region of duration ~100 fs centred around the peak of the electron bunch current was selected for FEL simulations as indicated in 7.2. The sdds rountine elegant2genesis [93] was used to convert the electron distribution output from Elegant into input for the FEL code Genesis 1.3 [56].

7.3 Mode-locked amplifier method

The resonant wavelength of the FEL was chosen to be 1.24 nm, corresponding to the highest photon energy of the NLS FEL designs [89]. Undulator modules of
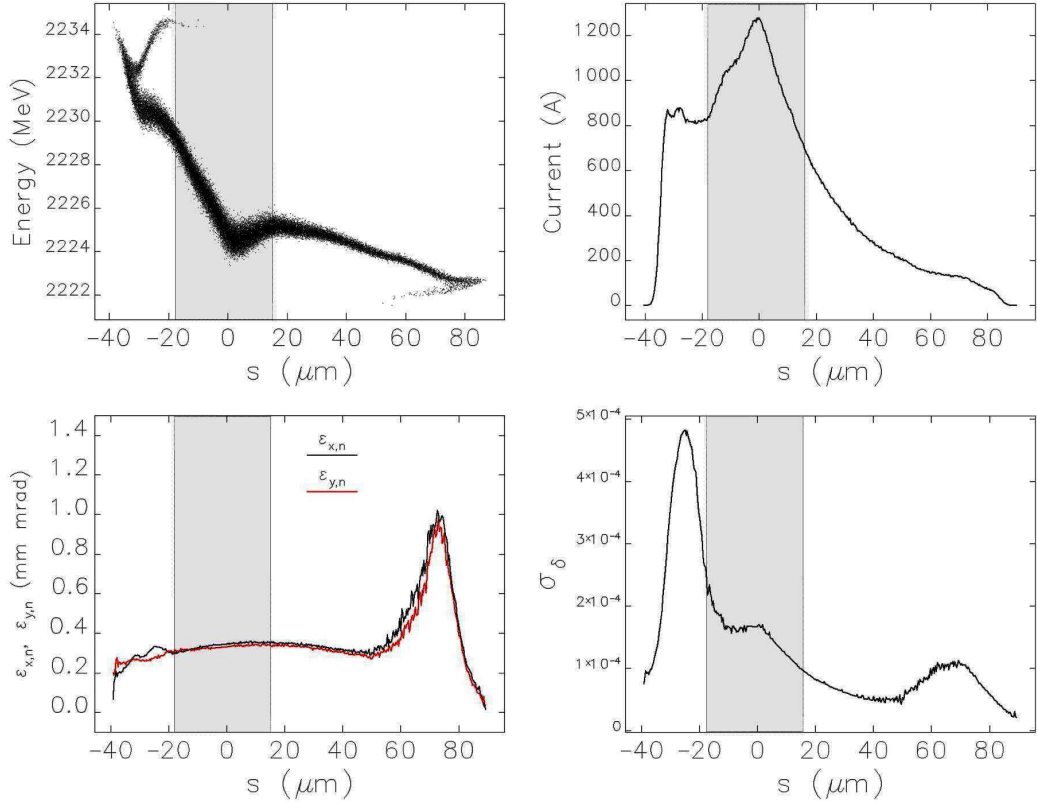
Figure 7.2: Bunch properties on entrance to the FEL in 1 fs slices: Top left - longitudinal phase space, Top right - current profile, Bottom left - slice emittance, Bottom right - slice energy spread. The region selected for FEL simulations is highlighted.

8 periods were chosen (i.e. $l = 8\lambda_r$) and the slippage in the chicanes was set to $\delta = 23\lambda_r$, giving a slippage enhancement factor of $S_e = 3.9$.

7.4 FEL modelling

The FEL modelling method follows that of [57], using the three-dimensional FEL code Genesis 1.3 [56], as described in Section 2.11. In the FEL design, a short modulator section is used to introduce electron energy modulation of period s, matching the total slipppage per undulator-chicane module. A sinusoidal energy modulation was manually added to the electron beam distribution to account for this. The modulation amplitude was varied over a range of values and the optimum value of 0.05% was selected.

The modular undulator-chicane structure was modelled in Genesis 1.3, using

the tracked electron distribution. No seed was used hence the process starts from self-amplification of spontaneous emission (SASE) [43]. The radiation power output close to saturation (145 modules) is shown in Figure 7.3, with details of the initial electron beam energy and current profile. The total undulator length to saturation ($\sim$40 m) and the peak power ($\sim$1 GW), are similar to that of a conventional FEL with the same parameters.

The peak of the radiation power occurs slightly off the peak of the highest current region of the bunch, where both the energy spread and chirp are lower. Due to the increased propagation distance along the bunch, the ML-FEL might be expected to be less tolerant to energy chirp than a conventional high-gain FEL. The envelope of the pulse train retains the SASE noise. Analysis of the radiation phase shows coherence in the pulse train is limited to $\sim S_e \times l_c$. In addition, the variation in energy along the electron bunch leads to a variation in radiation wavelength along the train, which acts to broaden the modal structure of the spectrum.
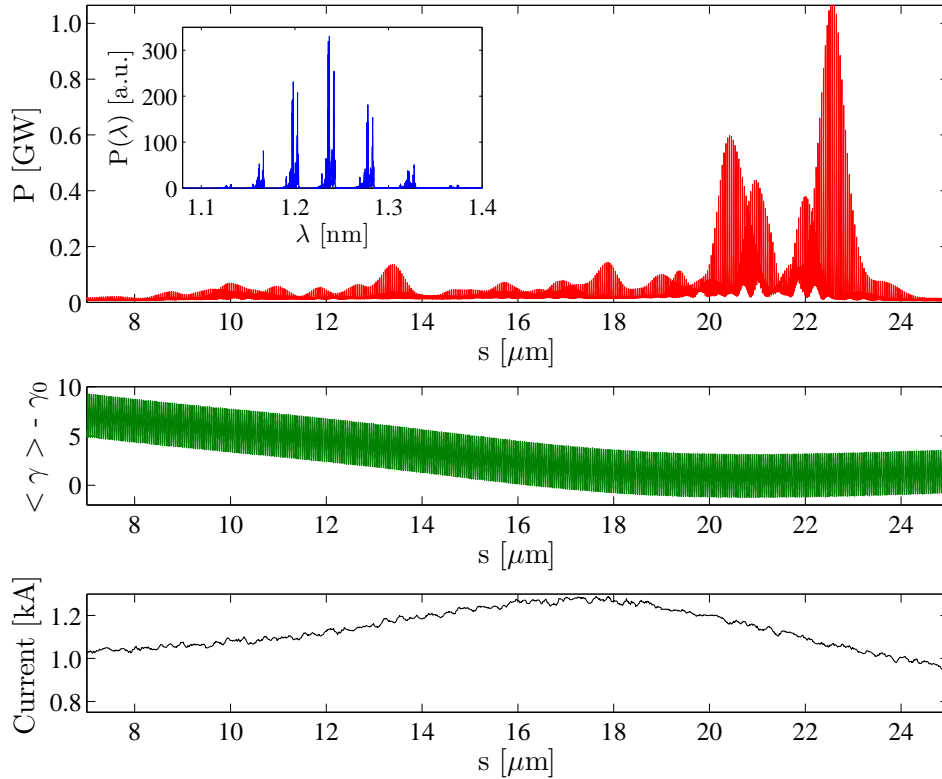
Figure 7.3: Top - radiation power profile output close to saturation (145 modules), and the corresponding radiation spectrum (inset); Middle - initial electron beam energy profile; Bottom - electron beam current profile.

In Figure 7.4, an inset of the radiation power profile is given in order to show the pulse properties, together with the electron beam energy and bunching ($b = \langle e^{i\theta} \rangle$). The pulse duration is $\sim$30 as FWHM; which is approximately 8 optical cycles, corresponding to the number of undulator periods per module.

Figure 7.4 also shows the radiation pulse alignment relative to the electron beam at the centre of the 145th undulator module. In general, the highest intensity radiation pulse trains develop such that they align with the minimum energy positions of the sinusoidal energy modulation. However it is noted that in some regions of the beam, the pulses aligning with the maximum energy positions have higher intensity than those at the minima. This is in contrast to most results with an ideal beam.
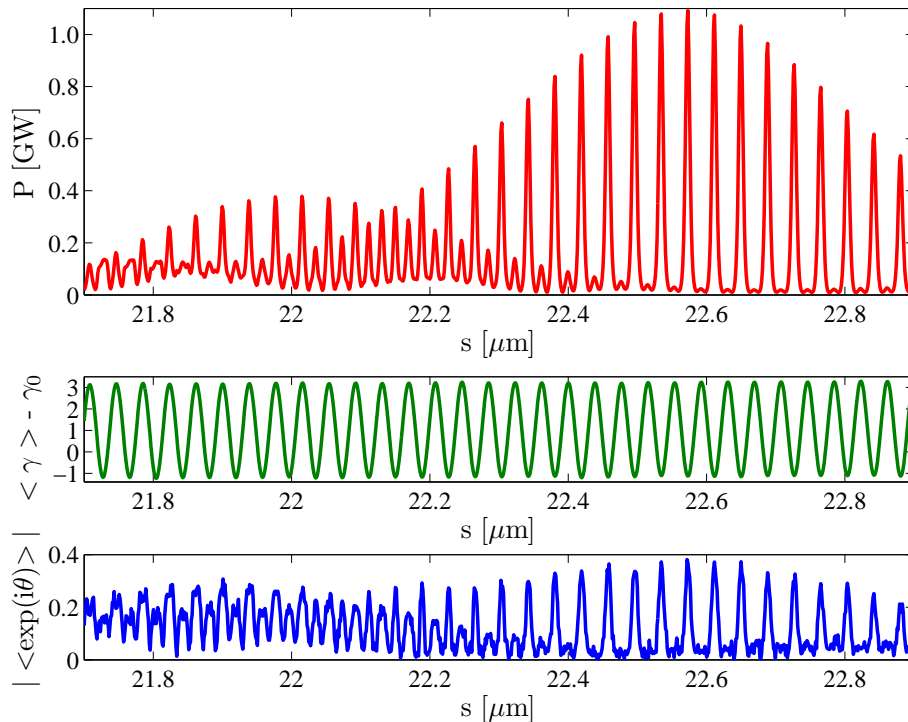
Figure 7.4: Top - radiation power at the centre of the 145th undulator module; Middle - slice-averaged electron beam energy offset from the resonant energy (in terms of electron rest mass energy); Bottom - electron beam bunching at the centre of the 145th undulator module. The radiation pulses align with the positions of minimum energy gradient.

Since two pulses develop per modulation period; the minima and maxima of the energy modulation effectively support two separate sets of modes with the higher electron energy set centred about a shorter wavelength than the lower electron energy set. Due to the energy variation along the bunch, different lon-

gitudinal regions of the beam have a different central wavelength. These effects contribute to broadening of the modes in the radiation spectrum of Figure 7.3. The electron beam bunching is again seen to have a similar pulse train structure to the radiation.

7.5 Conclusions

The mode-locked amplifier scheme has been modelled in three-dimensional FEL simulations using an electron distribution tracked through full start-to-end accelerator simulations of a modern particle accelerator design. The mode-locked scheme is predicted to generate pulses of $\sim$30 as FWHM (approximately 8 optical cycles, corresponding to the number of undulator periods per module), with peak power and saturation length typical of a conventional high-gain FEL with the same parameters ($\sim$1 GW in $\sim$40 m) More realistic effects are included in the start-to-end modelling, compared to the ideal case, such as energy variation along the beam, and current variation. The energy variation along the beam acts to broaden the modal structure of the ML-FEL spectrum, since different longitudinal regions of then beam have different central resonant wavelengths.

Ultimately the mode-locked FEL configuration has been shown to be compatible with predicted output from the present generation of particle accelerators, however, to deliver the few-cycle pulses demonstrated here, very short undulator modules ($\sim$8 periods) would be required. This would require the construction of dedicated undulator lines for this purpose. In the following chapters, an alternative approach is developed which could be added to existing undulator lines.

Chapter 8

Long-Scale Energy Modulation in a Conventional High-Gain FEL

8.1 Introduction

In previous chapters, the cases have been considered of the mode-coupled FEL (consisting of periodic shifting with no energy modulation), and the mode-locked FEL (periodic shifting with energy modulation). For completeness the case was also considered of energy modulation without periodic shifting. It is shown in this chapter and in Chapter 9 that this can also produce very interesting results.

This chapter is essentially concerned with a conventional high-gain amplifier FEL configuration, in which the role of a long-scale (relative to the resonant FEL wavelength) energy modulation is introduced to the electron beam. A method for generating short pulses from this approach is described in Section 8.3. This work was presented in [94].

8.2 Effect of energy modulation

8.2.1 System parameters and modelling method

Simulations have been carried out to assess the effect of an energy modulated electron beam, with long-scale modulation period relative to the resonant FEL wavelength, on a conventional SASE FEL. A resonant FEL wavelength of $\lambda_r =$1.24 nm was chosen for the simulations, and a modulation period of $\approx 30\lambda_r$ was used, since this is a typical value used in mode-locked FEL simulations. Undulator and elec-

tron beam parameters similar to those of the UK New Light Source design [89] were used. The FEL code Genesis 1.3 [56] was used. For simplicity, the beam modulation step was accounted for by applying a sinusoidal energy variation to the electron beam distribution. There was assumed to be no other longitudinal variation in electron beam parameters. The amplitude of the modulation was varied and the effect on FEL behaviour observed.

8.2.2 Amplification rate

In Figure 8.1, the maximum power in the simulated window is plotted against distance through the undulator, for several different values of the initial energy modulation amplitude (0.01 %, 0.05 %, 0.1 % and 0.5 %). For an energy mod-
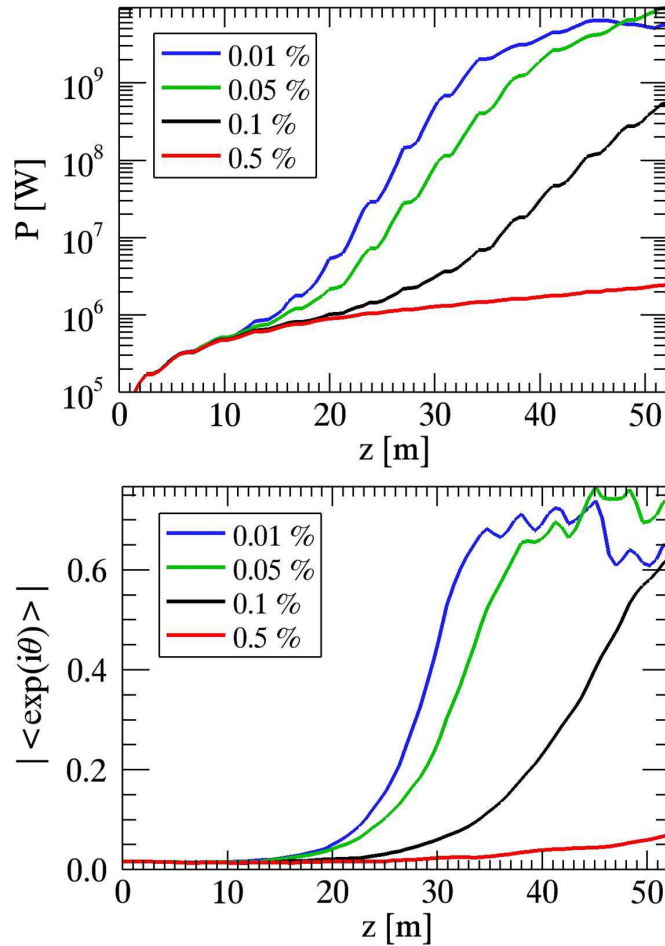
Figure 8.1: Maximum power (top) and maximum bunching (bottom) in the simulated window plotted against distance through the undulator, for different values of initial energy modulation amplitude.

ulation amplitude of 0.01 % the peak power and saturation distance are not significantly different to the case with no energy modulation. As the energy modulation amplitude is increased, the gain length of the FEL is increased. Also shown in Figure 8.1, is the maximum of the bunching ($b = \langle e^{i\theta} \rangle$) in the simulated window plotted against distance through the undulator.

8.2.3 Temporal properties

Figure 8.2 shows the longitudinal profile of the radiation power and that of the electron beam bunching for the different values of initial energy modulation amplitude. For each case the plotted data is near to FEL saturation (the 0.5 % energy modulation case is not shown since saturation was not reached in the simulated undulator distance). For an energy modulation of 0.1 %, there is sig-
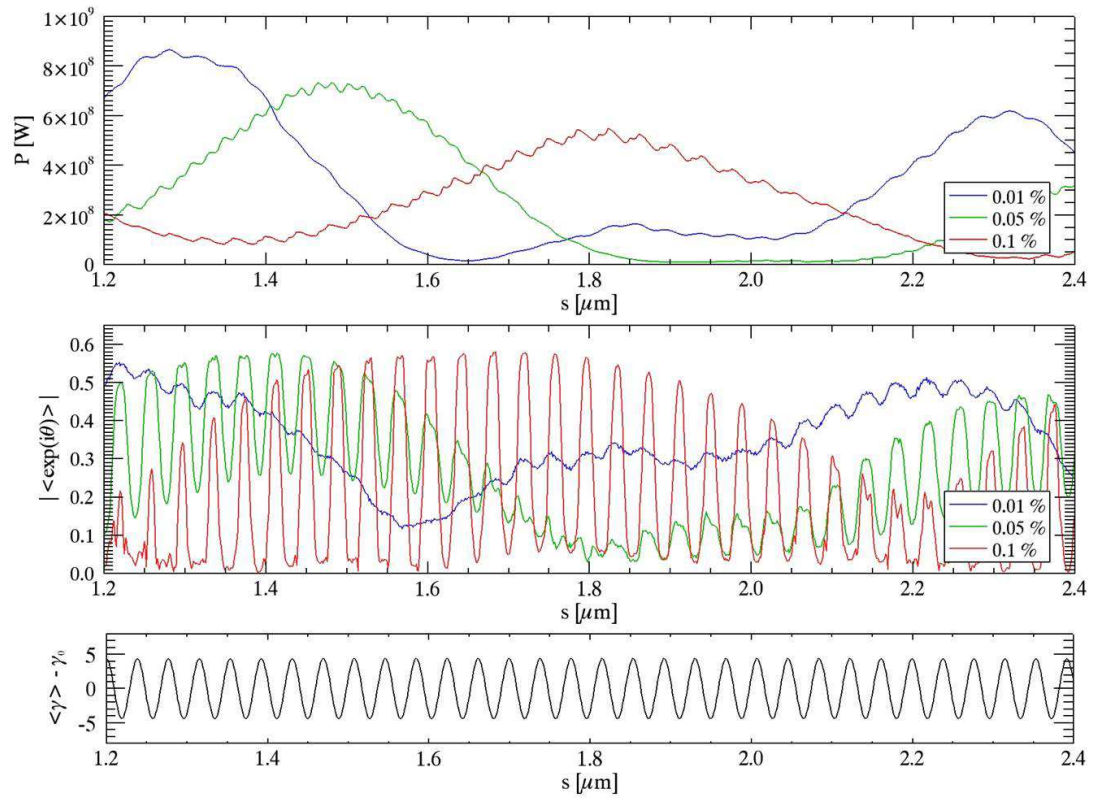
Figure 8.2: Longitudinal profile of the radiation power (top) and that of the electron beam bunching (middle) are shown for different values of the initial energy modulation amplitude. For each case the plotted data is near to FEL saturation. The beam energy at the entrance to the FEL is shown for the 0.1 % energy modulation case (below), to show the position of the bunching peaks relative to the modulation phase.

nificant pulse-train structure observed in the bunching profile. This structure is also evident to a lesser extent at 0.05 % energy modulation, and to a much lesser extent at 0.01 %. The peaks of the bunching profile occur at the positions of minimum electron beam energy. The length of these bunching peaks is only a few optical cycles, indicating that few-cycle structures can be generated in a conventional high-gain FEL.

The radiation profile does not exhibit a similar structure to the bunching profile, even when there is significant structure in the bunching profile. Instead the radiation profile characteristics are similar to typical SASE output with a relatively small undulation on the scale of the bunching structure. This is to be expected since the radiation slips forward relative to the electrons, so that any structure is washed out. This example therefore shows that the 'symmetry' between the temporal profiles of the radiation and electron beam properties - described in Section 2.10.1 can be broken.

8.2.4 Proposed description

The development of the peaks in the temporal profile of the micro-bunching is attributed to a similar mechanism as in the mode-locked FEL - as described in Section 5.3.1. As in the case of the ML-FEL, energy modulation results in two positions of minimum energy gradient, at the minima and maxima of the energy modulation, and regions of higher gradient (chirp) in between. It is noted that the required modulation amplitude to generate the comb structure in the micro-bunching profile is $\sim \rho$. This corresponds to putting the two sets of minimum energy gradient just outside the bandwidth of one another.

The difference compared to the ML-FEL is that the radiation slips continuously through the electron beam, rather than in discrete steps. Consequently there cannot be two resonant interactions interleaved within the same longitudinal region. The two sets of minimum energy gradient are effectively put in competition, with the faster growth rate dominating.

It has been shown for the ML-FEL that the minimum energy positions have higher growth rate, with a theory for this put forward in Section 5.3.3. It is assumed that the same reason applies here. It is noted that the bunching peaks are less sharply defined than for the ML-FEL: this is thought to be because there is not a corresponding radiation pulse train, as shown in Figure 6.2.

8.3 Short pulse generation

8.3.1 Concept

The previous section showed that few-cycle features can be generated in a conventional high-gain FEL, but they occur in the electron beam and not in the radiation profile - it requires a further step to develop this idea into a source of few-cycle radiation pulses. In this section a very simple scheme is proposed to utilise the bunching structure shown in the previous section to deliver radiation output with similar temporal properties but limited power. a method of delivering high power is developed in Chapter 9.

The layout of the proposed scheme is shown in Figure 8.3, including details of the parameters used in simulations. A short modulator section is used to apply an energy modulation to the beam with long-scale period relative to the resonant FEL wavelength. This energy-modulated beam then enters a long conventional FEL amplifier undulator, in which the FEL interaction proceeds to near to saturation. As described in the previous section, a fine structure is generated in the bunching with peaks corresponding to the minimum energy gradient positions. However the radiation temporal profile has only small ripples corresponding to this fine-structure since it slips across both the highly bunched and less bunched regions.

When the bunching is maximised (near saturation) the radiation and electrons are separated (e.g. through used of a chicane) and the electrons are passed through a very short undulator (10 periods) to emit radiation with fine structure corresponding to the bunching.
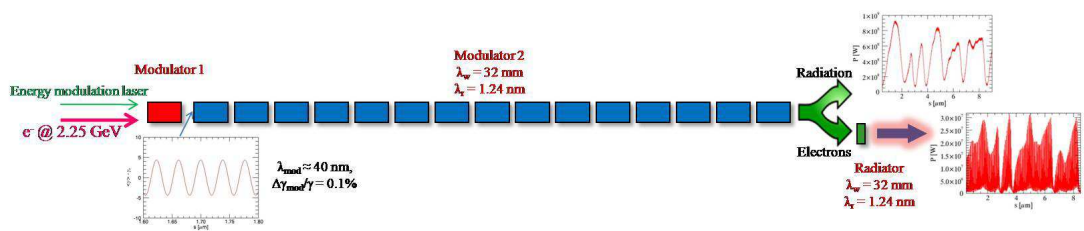
Figure 8.3: Schematic of the simple short pulse generation scheme. A short modulator section ('Modulator 1') is used to apply an energy modulation to the beam with long-scale period relative to the resonant FEL wavelength. The beam then enters a long undulator section ('Modulator 2'), in which the FEL interaction proceeds to near to saturation, generating a fine structure in the bunching but not the radiation profile. The radiation and electrons are then separated and the electrons are passed through a very short undulator (10 periods) to emit radiation with fine structure corresponding to the bunching.

127

It is emphasised that no additional chicane-delay slippage in the main undulator line is required (as applied in [57]).

This method has some similarities to a proposal [78], to manipulate an electron beam to generate significant bunching in a short region of the beam, such that an isolated pulse of significantly less than the coherence length (20 as FWHM at λ_r=1 nm) is generated upon passing through a short (12 period) undulator (see Section 3.2.5). The method proposed in this section differs in using FEL amplification to generate microbunching, and trains of pulses are generated.

8.3.2 Modelling results

Simulations of the scheme shown in Figure 8.3 have been carried out using a 0.1 % amplitude energy modulation. Bunching structure develops as shown in Figure 8.2 with a maximum bunching factor of ≈ 0.6. In the radiator section a pulse train structure develops with $\sim$30 as FWHM radiation pulses at $\sim$30 MW peak power after 10 undulator periods. This corresponds to pulse durations of only ~ 8 optical cycles, however the peak power is a factor of ~ 30 lower power than normal FEL saturation for these parameters.

A short region of the radiation power profile and spectrum at this point are shown in Figure 8.4. The spectrum shows several discrete frequencies. Figure 8.5 shows the radiation phase and power over a longer time window. The envelope of the pulse train shows fluctuations typical of SASE, with phase correlation between radiation pulses over a co-operation length. The output is similar to the SASE ML-FEL case but at lower power.
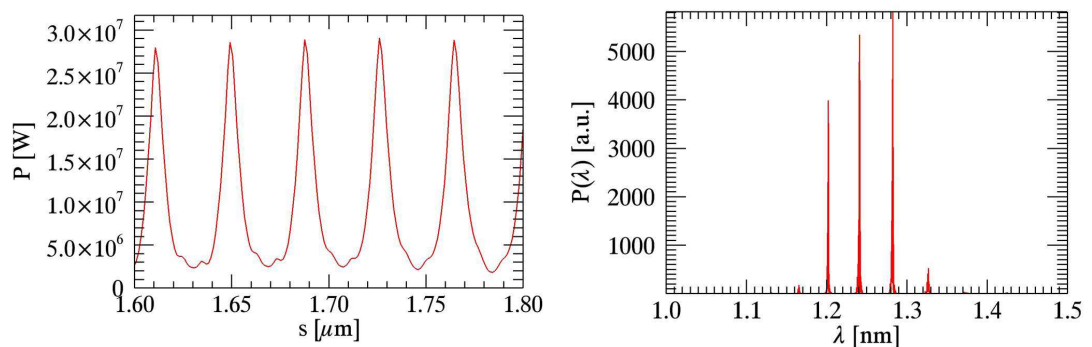
Figure 8.4: Radiation power profile and spectrum in the radiator after 10 undulator periods.

Only a basic optimisation has been carried out to demonstrate the principles
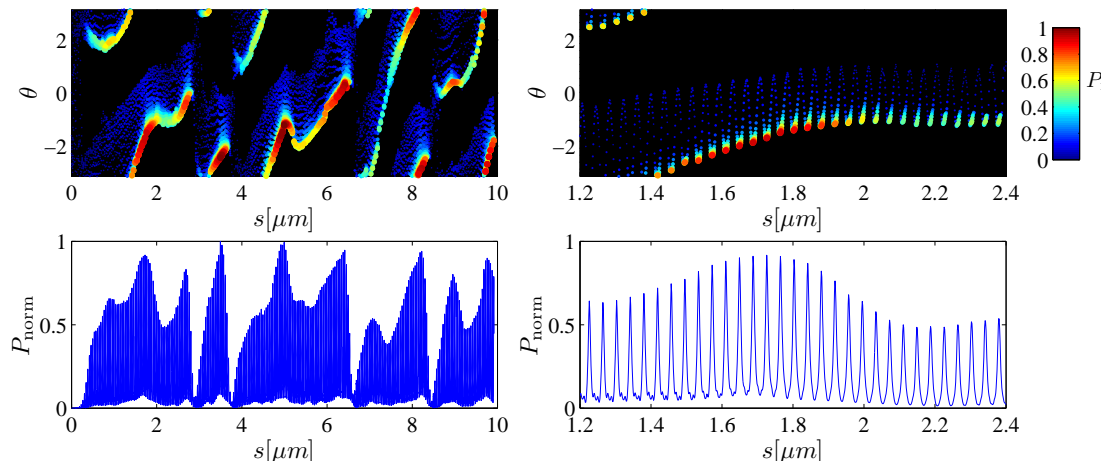
Figure 8.5: Radiation phase (with plot colour correlated to radiation intensity) and normalised power profile in the radiator after 10 undulator periods, for the simulated 30 fs time window (left), and zoomed to show a 4 fs region (right). The phase is continuous on the scale of a co-operation length.

of the scheme, and improved output would be expected with further optimisation, however peak powers are not expected to remain significantly below FEL saturation levels.

8.4 Conclusions

The effect of introducing an energy modulation with long-scale period (relative to the resonant FEL wavelength) in a conventional high-gain FEL has been assessed in simulations. A particularly interesting aspect of the result is that a pronounced comb in the electron bunching of period λ_m is seen to develop for optimised values of the modulation amplitude. This is significant since it shows that the standard high-gain FEL amplification process can support the amplification of extremely short temporal features - down to a few cycles - albeit in the bunching profile rather than the radiation profile. The radiation profile does not exhibit a similar structure to the bunching profile, even when there is significant structure in the bunching. Instead the radiation profile characteristics are similar to typical SASE output with a relatively small undulation on the scale of the bunching structure. This is to be expected since the radiation slips forward relative to the electrons, so that any structure is washed out.

A scheme has been devised to deliver radiation output with similar temporal properties to the mode-locked FEL scheme (i.e. a train of few-cycle radiation

pulses), without the requirement for a bespoke undulator-chicane system, but with reduced peak output power. This scheme could be a precursor to the more complex scheme detailed in Chapter 9.

Chapter 9

Mode-Locked Afterburner FEL

9.1 Introduction

In Chapters 4, 5, and 6, the mode-locked amplifier technique was analysed and developed in several directions. It was shown in Chapter 7 that the technique could be used to generate few-cycle pulses, but to do so requires few-period undulators: a significantly different undulator configuration than other FEL operating modes, and one that is not in place at existing facilities. In Chapter 8 it was shown that short-pulses could be generated with relatively little modification of existing facilities, but at low power.

This chapter details the development of a new concept for few-cycle and high-power pulses - the 'mode-locked afterburner' (ML-AB) - which could be applied relatively straightforwardly as a short extension to existing facilities. The scheme is modelled in 3D simulations for a soft x-ray case and a hard x-ray case, as well as for the parameters of the FEL test facility CLARA [59]. Some of the content of this chapter has been published in [95].

9.2 Mode-locked afterburner concept

As was described in Section 2.8, the FEL process consists of an initial start-up phase, an exponential growth phase and saturation. This means that the majority of the radiation from an high-gain FEL is emitted in the final gain length, typically corresponding to a few metres (at least when tapering is not implemented). It is this key point that is now combined with the results of the previous chapter to give a concept to generate few-cycle and high-power radiation pulses.

9.2.1 Overview and layout

The layout of the mode-locked afterburner method is shown schematically in Figure 9.1. It is proposed to generate trains of few-cycle radiation pulses similar to that of the ML-FEL but by using a short 'afterburner' extension that could relatively easily be added to existing facilities.
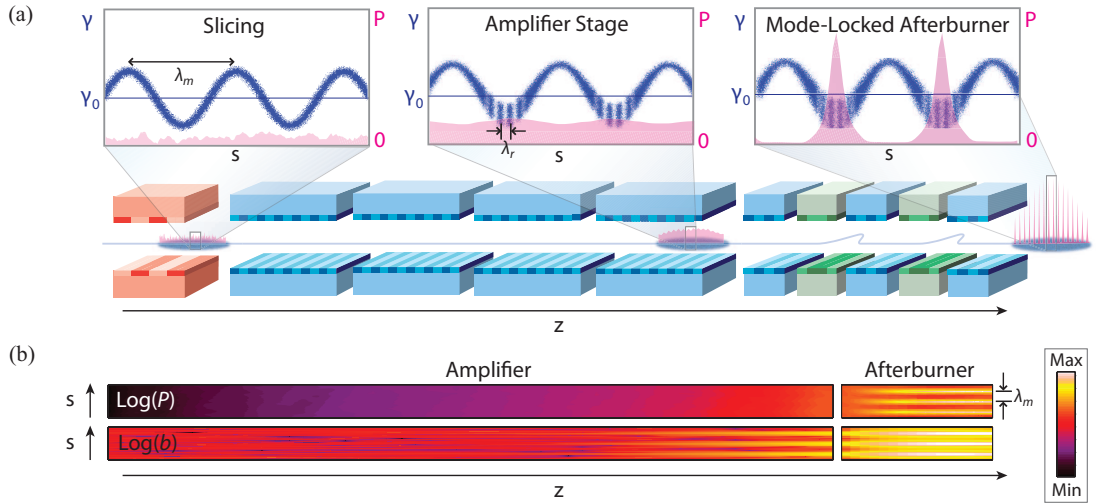
Figure 9.1: (a) Schematic layout of the proposed technique and (b) Example simulation results. An electron beam is sliced (e.g. using an external laser and a short undulator to apply an energy modulation, as shown), such that a comb structure develops in the FEL-induced electron micro-bunching (b) in a long undulator (amplifier stage). Further amplification of the radiation intensity (P) with periodic electron delays (mode-locked afterburner stage) generates a train of few-cycle radiation pulses.

The technique involves preparing an electron beam with periodic regions of high beam quality, each region of length $\ll l_c$, prior to injection into a normal FEL amplifier. Only these high quality regions undergo a strong FEL interaction within the amplifier to generate a periodic comb structure in the FEL-induced micro-bunching. Once the micro-bunching comb is sufficiently well developed, but before any saturation of the FEL process, the electron beam is injected into a 'mode-locked afterburner', which maps the comb structure of the electron micro-bunching into a similar comb of the radiation intensity. The afterburner comprises a series of few-period undulator modules separated by electron delay chicanes similar to that used in the ML-FEL [57]. These undulator-chicane modules maintain an overlap between the comb of bunching electrons and the developing radiation comb, each pulse of length $\ll l_c$, allowing it to grow exponentially in power to

saturation. The pulses are delivered in trains, since amplification occurs over a number of afterburner modules, and would be naturally synchronised to the modulating laser (Figure 9.1).

9.3 Amplifier-stage modelling

9.3.1 Modelling method

Modelling of the method was carried out using the simulation code Genesis 1.3 [56] using the parameters of Table 9.1 in both the soft and hard x-ray.

For the soft x-ray case, with resonant FEL wavelength of λ_r=1.24 nm, the modulation period $\lambda_m = 38.44$nm $(= 31\lambda_r)$ and $\lambda_m \ll l_c$. This is a typical value used in previous mode-locked FEL simulations for few-cycle pulses. This

Table 9.1: Parameters for soft and hard x-ray simulations.

Parameter	Soft x-ray	Hard x-ray
Amplifier stage		
Electron beam energy [GeV]	2.25	8.5
Peak current [kA]	1.1	2.6
ρ-parameter	1.6×10^{-3}	6×10^{-4}
Normalised emittance [mm-mrad]	0.3	0.3
RMS energy spread, σ_γ/γ_0	0.007 %	0.006 %
Undulator period, λ_u [cm]	3.2	1.8
Undulator periods per module	78	277
Resonant wavelength, λ_r [nm]	1.24	0.1
Modulation period, λ_m [nm]	38.44	3
Modulation amplitude, γ_m/γ_0	0.1 %	0.06 %
Extraction point [m]	34.1	36.0
Mode-locked afterburner		
Undulator periods per module	8	8
Chicane delays [nm]	28.52	2.2
No. of undulator-chicane modules	~15	~40

modulation could be achieved using a modulating undulator seeded by current HHG sources [3, 89], or upconversion of a longer wavelength seed. The undulator and electron beam parameters are those of the UK New Light Source design [89]. The electron pulse length was $\gg l_c$ with no other longitudinal variation of beam

parameters.

9.3.2 Optimisation of energy modulation for ML-AB

The performance of the amplifier stage was optimised by varying the relative amplitude, γ_m/γ_0. The growth of the radiation power and electron bunching are plotted for a range of electron energy modulation in Figure 9.2.

Increasing the energy modulation amplitude decreases the region about the extrema able to lase and the mean amplification rate decreases. However, a pronounced comb in the electron bunching of period $\approx \lambda_m$ is seen to develop, as seen in Chapter 8. Since the radiation propagates through the beam, only a relatively small undulation of the radiation power on the scale of λ_m is present. The optimum modulation amplitude was determined to be $\gamma_m/\gamma_0 \approx \rho$, with γ_m/γ_0=0.1 % used for injection into the afterburner. As the modulation amplitude increases the rate of FEL amplication decreases, as would be expected since the beam is being more disrupted.

The extraction point from the amplifier stage was chosen to be 34.1 m, as shown in Figure 9.2. Hence, no increase in the amplifier length from that for normal saturated SASE operation is required.

9.4 Few-cycle bunching to few-cycle radiation pulses

In Chapter 8 it was showed that with a long-scale energy modulation in the electron beam, a conventional high-gain FEL can generate few-cycle features in the micro-bunching structure. The next step is clearly to use this structure in the electron beam to generate few-cycle radiation pulses, and a simple method to do so was developed in Section 8.3, and is now referred to as a single-module afterburner. The mode-locked amplifier, consisting of a series of undulator modules/electron-delay chicanes is modelled in the next section.

To clarify the nomenclature, note that the term 'afterburner' is sometimes used to describe undulators with different period to the main undulator added at the end of the undulator line to generate light of different wavelength to the main output. This is not the case here: both afterburner schemes have the same undulator period as the main line (though changing to harmonics would be an interesting investigation).
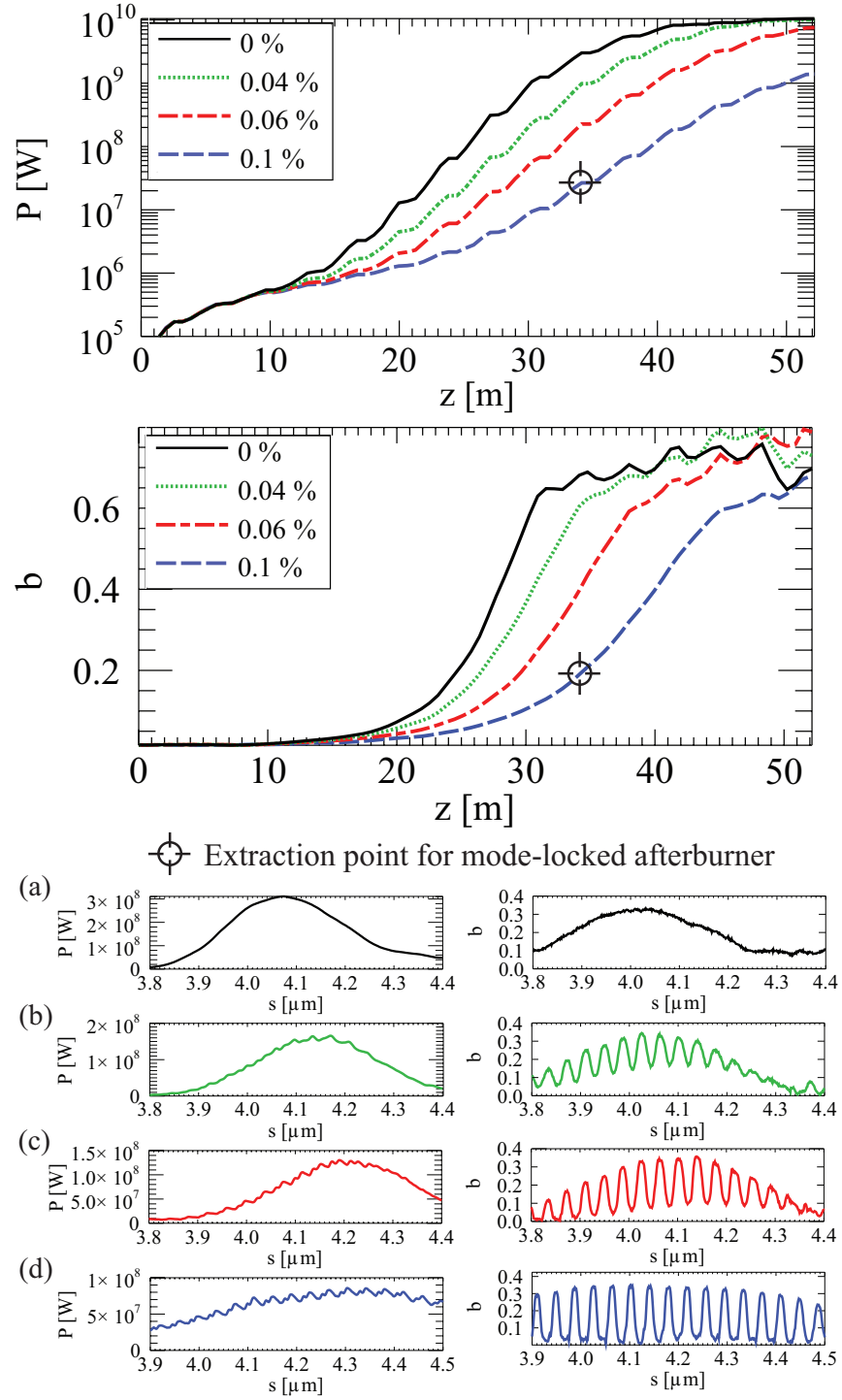
Figure 9.2: Optimisation of the amplifier stage for the soft x-ray case. Maximum radiation power (top) and electron micro-bunching (middle) with distance through the amplifier, for different γ_m/γ_0. Bottom panel: Longitudinal profiles of radiation (left) and bunching (right) for different γ_m/γ_0: (a) 0 %, (b) 0.04 %, (c) 0.06 %, (d) 0.1 %. Each case is at an equivalent level of micro-bunching. A section of length $\sim l_c$ from a longer bunch is shown; l_c increases with increasing γ_m/γ_0.

9.5 Mode-locked afterburner modelling

In this section, the method, shown schematically in Figure 9.1, is optimised to generate trains of few-cycle radiation pulses.

9.5.1 Soft x-ray case

The extraction point from the amplifier stage was chosen to be 34.1 m, as shown in Figure 9.2. Hence, no increase in the amplifier length from that for normal saturated SASE operation is required. Both the electron beam and radiation from the amplifier stage propagate into the afterburner (Figure 9.1). Each afterburner module has 8 undulator periods followed by a chicane that delays the electron beam by 23 resonant wavelengths, so that the total electron delay per module $s = (8 + 23) \times \lambda_r = \lambda_m$. Energy dispersion effects in the chicanes were included, although new chicane designs that reduce dispersive effects may be possible [96].

Figure 9.3 plots the radiation power and spectrum at different positions in the afterburner. A pulse train structure develops rapidly as the radiation and
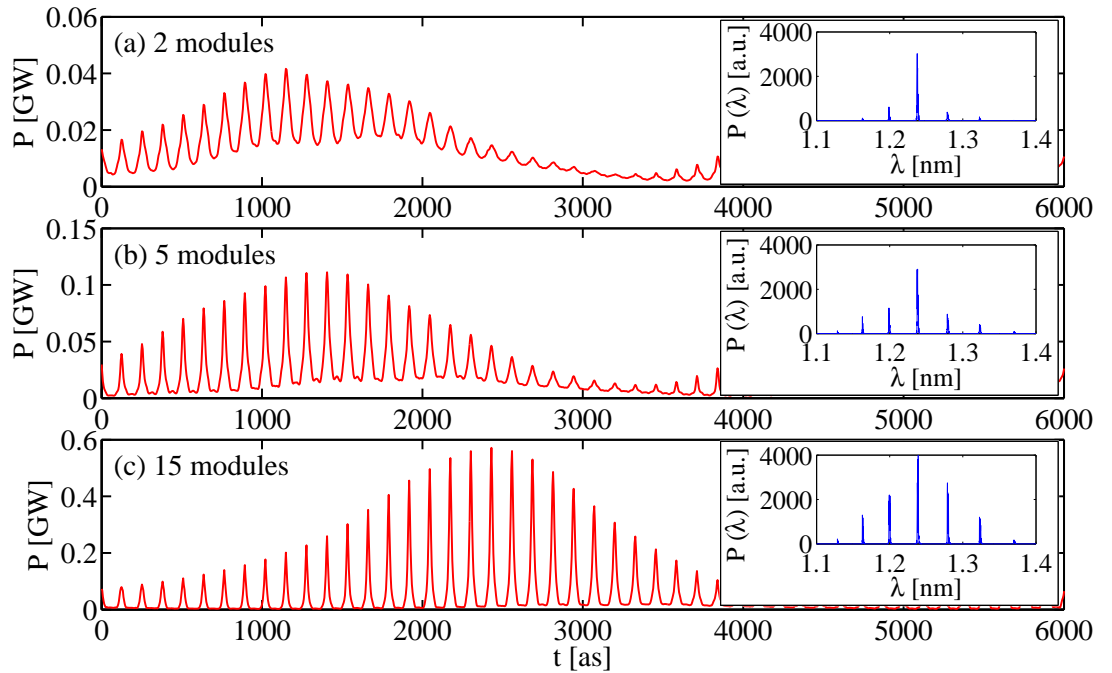
Figure 9.3: Soft x-ray mode-locked afterburner simulation results: Radiation power profile and spectrum after (a) 2, (b) 5 and (c) 15 undulator-chicane modules. The duration of an individual pulse after 15 modules is ∼9 as rms.

bunching combs are regularly re-phased by the chicanes to maintain overlap in the amplifying undulator sections. The growth within the undulator modules of the afterburner is exponential of rate comparable to that in the amplifier stage with no beam energy modulation. The growth in the afterburner is also enhanced by the additional bunching caused by the dispersive chicanes [57].

After 15 afterburner modules the output consists of a train of $\sim$9 as rms radiation pulses separated by $\sim$ 124 as and of $\sim$0.6 GW peak power. The corresponding spectrum is multichromatic with bandwidth envelope increased by $\sim$50 over that of SASE. The pulse train envelope has fluctuations typical of SASE, with phase correlation between individual radiation pulses over a co-operation length. Each afterburner module consists of an undulator module of length 0.26 m and a chicane of length 0.2 m, giving a total length of 6.9 m (excluding diagnostics etc.) for the 15-module afterburner.

9.5.2 Hard x-ray case

A hard x-ray case of resonant FEL wavelength of λ_r=0.1 nm was also simulated, with the aim of demonstrating shorter pulse generation.

A modulation period of λ_m=3 nm was used (λ_m=30$\times\lambda_r$) which may be feasible using HHG sources that are now being developed [11]. Both the undulator and electron beam parameters used are similar to those of the compact SACLA x-ray FEL facility [21, 22], and are detailed in Table 9.1. A reduced peak current is used, typical for a lower electron bunch charge. This allows a slightly reduced, but still realistic, emittance to be assumed to attain a more compact afterburner stage.

As for the soft x-ray case above, the amplifier stage was optimised and a beam energy modulation of γ_m/γ_0=0.06 % chosen. The amplifier section consists of six 277-period undulator modules (36 m). Each afterburner module consists of an undulator module of 8 periods and a chicane with delay of $22\times\lambda_r$. The total electron delay per afterburner module is then equal to λ_m. The total afterburner consists of 40 modules each consisting of an undulator of length 0.144 m and a chicane of length 0.2 m to give 13.8 m in total. Figure 9.4 plots the radiation power and spectrum after 40 undulator-chicane modules.

A pulse train structure of approximately 700 zeptosecond rms duration radiation pulses separated by 10 as and of 1.5 GW peak power is generated. This two
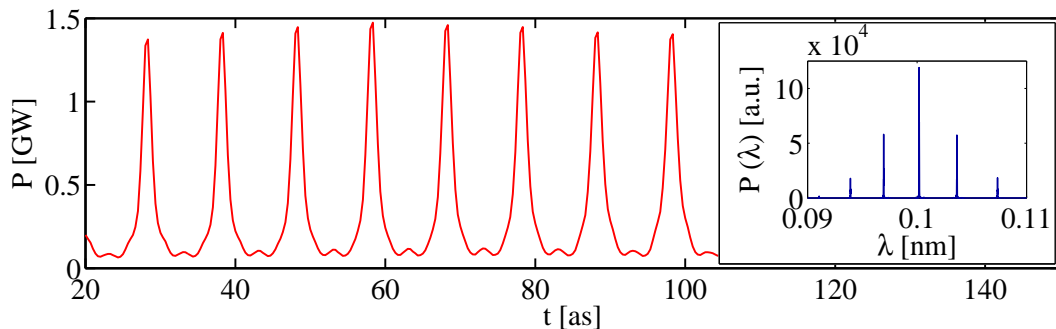
Figure 9.4: Hard x-ray mode-locked afterburner simulation results: Radiation power profile and spectrum after 40 modules. The duration of an individual pulse is ∼700 zs rms.

orders of magnitude shorter than presently available from any light source.

The radiation mode separation is determined by the modulation period of 3 nm corresponding to photon energy difference of ≈ 412 eV. The final spectrum is multichromatic with bandwidth envelope of the modes increased by a factor ∼100 over SASE.

9.6 CLARA test facility example

The mode-locked afterburner concept has also been modelled for the parameters of the UK FEL test facility CLARA [59], which is currently being developed to test advanced FEL concepts.

The undulator modules of CLARA are being designed to be short in terms of number of periods, and with chicanes between modules to enable testing of schemes such as the mode-locked FEL [57], as well as methods for improving the temproral properties [54]. However, for the mode-locked afterburner scheme would the amplifier stage would simply use the main undulator line of CLARA FEL without chicane delays, in order to represent the more standard undulator lines available at user facilities. CLARA has a modulator section that could be used, and short pulses would be generated via the additon of a relatively short afterburner comprising several few-period undulators separated by chicanes.

A case has been considered of CLARA operating at λ_r=100 nm, for which the electron bunch energy would be modulated with period 3 μm using an Optical Parametric Amplifier (OPA) driven by the Ti:sapphire laser. Simulation results using Genesis 1.3 are shown in Figure 9.5 using the following afterburner param-

138

eters: each undulator module has 8 periods and the chicanes comprise four 2.9 cm length, 0.25 T dipoles.

Pulse durations of 700 attoseconds rms are predicted, with peak power reaching ≈20 MW in 10 undulator-chicane modules, such that the total afterburner length is just over 4 m. The spectrum shows clearly separated distinct wavelengths, over a broad bandwidth of ∼13%.
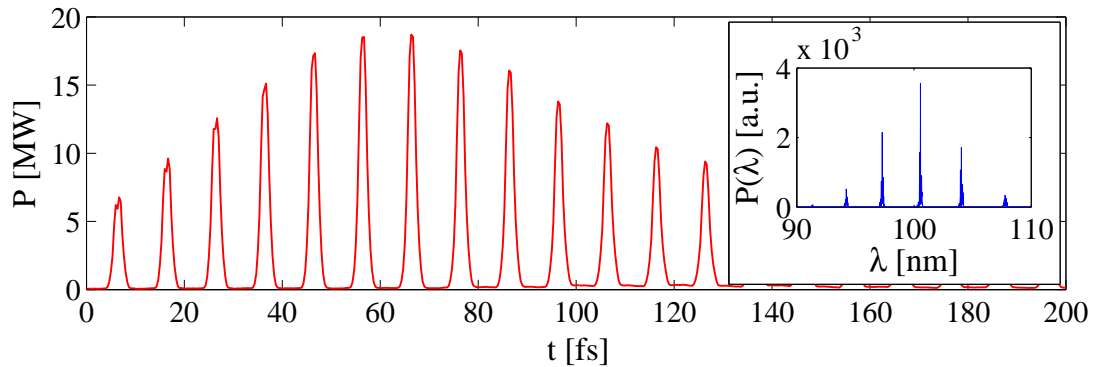
Figure 9.5: CLARA mode-locked afterburner simulation results at 100 nm: Radiation power profile and spectrum after 20 modules. The duration of an individual pulse is ∼700 as rms.

This result shows that by significantly reducing the number of cycles per pulse in the FEL, the mode-locked afterburner could allow attosecond science to be studied even at relatively low energy facilities.

9.7 Conclusions

The mode-locked afterburner examples in this chapter were optimised towards minimising pulse durations using parameters close to those available from current x-ray FEL sources, and test facilities. Using short (8-period) undulator modules in the afterburner, $\sim$5 optical cycles FWHM were attained. The time structure could be modified by changing the number of undulator periods, electron delay lengths, and λ_m, suggesting a development route from present attosecond pulse train experiments [1, 6, 7, 8, 9, 10] to the ultimate capability of the scheme.

Amplification in the afterburner was set to occur just before saturation, allowing a short afterburner to attain high contrast ratio of the pulse train over the amplifier radiation. Further development to maximise the peak power and flexibility of the pulse structure could include investigation of saturation effects in the afterburner (e.g. chicane dispersion, radiation diffraction) and their mitigation through e.g. undulator tapering [41], optimised phase-shifting [97], use of low-dispersion [96] or more compact chicanes. Methods to improve the temporal coherence and stability developed for SASE, may also be applicable.

If the mode-locked afterburner pulse durations were to be scaled to still higher photon energies, e.g to the 50 keV of the proposed x-ray FEL of [98], then pulse durations of 140 zs rms may become feasible. Operation at harmonics of λ_r may be another route to shorter pulse durations. Furthermore, if a relativistic counter-propagating target nuclear beam were used with such pulse trains, as discussed in [99], in addition to the increased doppler-shifted photon energies that the nuclei experience in their boosted frame, the pulse durations may be further reduced towards the timescales of highly ionised heavy elements and nuclear dynamics [19].

The mode-locked afterburner is potentially a relatively simple upgrade to existing x-ray FEL facilities. It offers a flexible route towards the generation of discretely multichromatic output under a broad bandwidth envelope, and so offers few-cycle x-ray pulse trains with GW peak-powers in the temporal domain. This would help facilitate the direct study of the temporal evolution of complex correlated electronic behaviour within atoms, and push capability into the regime of electronic-nuclear dynamics and towards that of the nucleus.

Chapter 10

Conclusions and Future Development

There are a number of conclusions to draw from this work, and a number of steps for potential future development:

Ultra-short pulses:

- **Shortest absolute pulse durations:**
  A key result of the mode-locked FEL and mode-locked afterburner studies is to show the potential of FELs to generate few-cycle pulses at high power: approximately two orders of magnitude shorter than the FEL co-operation length, and, when the mode-locked afterburner is applied at at x-ray wavelength it is predicted to deliver pulse durations down to a single attosecond - and verging into the zeptosecond scale. This is approximately two orders of magnitude shorter than can presently be generated from other sources.

- **Attosecond science at relatively long wavelength FELs:**
  The prospect of reducing FEL pulse durations to a few cycles at any given wavelength also suggests at transformative changes in capability of relatively long wavelength FEL facilities. A test facility such as CLARA [59] operating at relatively low energy (250 MeV: $\sim$30-40 times less than a hard x-ray FEL) and relatively long wavelength (100 nm: $\sim$1000 times longer than hard x-ray), would be on the verge of accessing attosecond science; shorter wavelength FELs would be able to generate attosecond-scale pulses.

- **Pulse trains:**

  An integral feature of the mode-locked amplifier [57], and mode-locked afterburner [95] schemes, is their use of pulse trains to enable high power, few-cycle pulses. Highly significant steps for the future development of this work will be both to demonstrate the methods in experiment, and to identify and bring about experiments requiring such output.

Broad bandwidth envelope, multi-colour:

- The corollary of the ultra-short pulse durations predicted in this thesis, is very broad bandwidth envelope. Since the pulses are delivered in trains, the spectra contain discrete modes, or 'multi-colour' output. The bandwidth envelope is increased by two orders of magnitude compared to conventional SASE output. This could potentially find applications. The spectral features may also be more straightforward to detect in experiments.

Stabilising mode-locked FEL properties/amplifying HHG:

- It has been shown that seeding the mode-coupled/locked FEL with an HHG source has the effect of cleaning up the temporal and spectral properties of the output. This would be expected to improve its utility for experiments.

- The mode-coupled/locked FEL can be considered a promising amplifier for HHG sources: simulations indicated that the radiation can be amplified while retaining a pulse train structure (by two orders of magnitude, given the seed properties of [81]). However, where the bandwidth of the HHG source exceeds that of the single undulator module bandwidth, the bandwidth of the amplified radiation quickly falls to that of the single undulator module bandwidth. By minimising the number of periods per undulator module and using energy modulation, the amplified bandwidth can be maximised.

Insight into the workings of the mode-locked FEL:

- **Temporal description:**

  The results in this thesis indicate that many properties of the the mode-

locked FEL can be described by analogy to the conventional amplifier FEL. The 'natural' unit of both systems seems to be a region of the electron beam/radiation field consisting of total length approximately that of the co-operation length. Conventionally this is a continuous region, but in the mode-locked FEL it is a series of discrete regions. Disregarding increased amplification rates due to the mode-locked optical klystron effect, both systems have very similar growth rates, and macroscopic properties. A simple model in terms of collective variables has been developed to describe the system, and results show a good match to simulations.

- **Role of energy modulation:**
  It has been shown that energy modulation serves to produce a longitudinal variation in the quality of the electron beam for FEL amplification. This longitudinal variation both defines the positions where pulses develop, and constrains pulse broadening that would otherwise occur. Conditions for the required energy modulation properties have been derived. The required properties of electron beam modulation were identified, and using current modulation as an alternative to energy modulation was demonstrated in simulations. Having described the required properties of the electron beam modulation it is possible to envisage other possibilities to deliver the mode-locking effect.

Future developments:

This single-module afterburner scheme detailed in Section 8.3 could potentially act as a precursor to the mode-locked afterburner scheme detailed in Chapter 9. It could be attempted on an existing machine without requiring the construction of a dedicated undulator-chicane system. It would allow principles related to the mode-locked FEL mechanism to be tested, engender the development of appropriate diagnostics and potentially test the utility of the pulse-train structure for experiments. The scheme could potentially be a useful source in its own right.

The mode-locked amplifier [57], and mode-locked afterburner [95] schemes are both considered as promising schemes to be tested at the FEL test facility CLARA [59]. There is potential for an afterburner, once developed and tested on CLARA, to be moved to a shorter wavelength facility to push to shorter

wavelengths, and so to shorter pulse durations.

Bibliography

[1] J. Mauritsson *et al. Phys. Rev. Lett.*, 100:073003, 2008.

[2] P. B. Corkum and F. Krausz. *Nature Physics*, 3:381, 2007.

[3] F. Krausz and M. Ivanov. *Rev. Mod. Phys.*, 81:163, 2009.

[4] Z. Chang *et al. Opt. Lett.*, 37:18, 2012.

[5] J. Levesque and P.B. Corkum. *Can J. Phys.*, 84:1.

[6] P. Johnsson *et al. Phys. Rev. Lett.*, 95:013001, 2005.

[7] T. Remetter *et al. Nature Phys.*, 2:323, 2006.

[8] K. Varjú *et al. J. Phys. B: At. Mol. Opt. Phys.*, 39:3983, 2006.

[9] M. Klaiber, K.Z. Hatsagortsyan, C. Müller and C.H. Keitel. *Optics Lett.*, 33:411, 2008.

[10] K.P. Singh *et al. Phys. Rev. Lett.*, 104:023001, 2010.

[11] T. Popmintchev *et al. Science*, 336:1287, 2012.

[12] C. Hernández-García. *Phys. Rev. Lett.*, 111:033002, 2013.

[13] W.A. Barletta *et al. Nucl. Instrum. Methods Phys. Res. Sect. A*, 618:69, 2010.

[14] B.W.J. McNeil and N.R. Thompson. *Nature Photon.*, 4:814, 2010.

[15] C. Pellegrini. The history of x-ray free-electron lasers. *The European Physical Journal H*, 37:659, 2012.

[16] Z. Huang and K.-J. Kim. Review of x-ray free-electron laser theory. *Phys. Rev. ST Accel. Beams*, 10:034801, 2007.

[17] H.H. Braun. *Proc. 3rd Int. Particle Accelerator Conf., New Orleans, USA*, page 4180, 2012.

[18] S. Kishimoto. *Phys. Rev. Lett.*, 85:1831, 2000.

[19] A.E. Kaplan. *Lasers in Eng.*, 24:3, 2012.

[20] P. Emma *et al. Nature Photonics*, 4:641.

[21] H. Tanaka, T. Shintake *et al. SCSS X-FEL Conceptual Design Report, RIKEN Harima Institute.* 2005.

[22] H. Tanaka *et al. Nature Photonics*, 6:540.

[23] K.-J. Kim and Z. Huang. Synchrotron radiation and free electron laser. *USPAS Lecture Notes*, 2008.

[24] N.R. Thompson. *Improved Temporal Coherence and Short Pulse Generation in Free Electron Lasers.* PhD thesis, University of Strathclyde, 2013.

[25] L.T. Campbell. *The Physics of a 4th Generation Light Source.* PhD thesis, University of Strathclyde, 2011.

[26] S. Reiche. *Numerical Studies for a Single Pass High Gain Free-Electron Laser.* PhD thesis, University of Hamburg, 1999.

[27] H. Motz. Applications of the radiation from fast electron beams. *J. Appl. Phys.*, 22:527, 1951.

[28] G.N. Kulipanov. Ginzburgs invention of undulators and their role in modern synchrotron radiation sources and free electron lasers. *Phys. Usp.*, 50:368, 2007.

[29] H. Motz. Experiments on radiation by fast electron beams. *J. Appl. Phys.*, 24:826, 1953.

[30] R.M. Phillips. The Ubitron, a high-power traveling-wave tube based on a periodic beam 20 interaction in unloaded waveguide. *IRE Trans. Electron Devices*, 7:231, 1960.

[31] J.M.J. Madey. Stimulated emission of bremsstrahlung in a periodic magnetic field. *J. Appl. Phys.*, 42:1906, 1971.

[32] L. Elias *et al.* Observation of stimulated emission of radiation by relativistic electrons in a spatially periodic transverse magnetic field. *Phys. Rev. Lett.*, 36:717, 1976.

[33] D.A.G. Deacon *et al.* First operation of a free-electron laser. *Phys. Rev. Lett.*, 38:892, 1977.

[34] W.B. Colson. One-body electrodynamics in a free electron laser. *Phys. Lett. A*, 64:190, 1977.

[35] F.A. Hopf, P. Meystre, M.O. Scully and W.H. Louisell. Classical theory of a free electron laser. *Phys. Rev. Lett.*, 37:1215, 1976.

[36] N.M. Kroll and W.A. McMullin. Stimulated emission from relativistic electrons passing through a spatially periodic transverse magnetic field. *Phys. Rev. A*, 17:300, 1978.

[37] I.B. Bernstein and J.L. Hirshfield. Amplification on a relativistic electron beam in a spatially periodic transverse magnetic field. *Phys. Rev. A*, 20:1661, 1979.

[38] P. Sprangle and R.A. Smith. Theory of free electron lasers. *Phys. Rev. A*, 21:293, 1980.

[39] A.M. Kondratenko and E.L. Saldin. Generation of coherent radiation by a relativistic electron beam in an undulator. *Part. Accel. 10*, 10:207, 1980.

[40] W.B. Colson. The nonlinear wave equation for higher harmonics in free-electron lasers. *IEEE J. Quant. Electron.*, 17:1417, 1981.

[41] N.M. Kroll, P.L. Morton, and M.N. Rosenbluth. Free-electron lasers with variable parameter wigglers. *IEEE J. Quant. Electron.*, 177:1436, 1981.

[42] R. Bonifacio, F. Casagrande and G. Casati. Cooperative and chaotic transition of a free electron laser hamiltonian model. *Opt. Commun.*, 40:219, 1982.

[43] R. Bonifacio, C. Pellegrini, and L.M. Narducci. Collective instabilities and high-gain regime in a free electron laser. *Opt. Commun.*, 50:373, 1984.

[44] T.J. Orzechowski, B. Anderson, W.M. Fawley, D. Prosnitz, E.T. Scharlemann, S. Yarema, D. Hopkins, A.C. Paul, A.M. Sessler, and J. Wurtele.

Microwave radiation from a high-gain free-electron laser amplifier. *Phys. Rev. Lett.*, 54:889, 1985.

[45] M. Hogan, C. Pellegrini, J. Rosenzweig, G. Travish, A. Varfolomeev, S. Anderson, K. Bishofberger, P. Frigola, A. Murokh, N. Osmanov, S. Reiche, and A. Tremaine. Measurements of high gain and intensity fluctuations in a self-amplified, spontaneous-emission free-electron laser. *Phys. Rev. Lett.*, 80:289, 1998.

[46] W. Ackermann *et al. Nature Photon.*, 1:336.

[47] J.A. Clarke. *The Science and Technology of Undulators and Wigglers*. Oxford University Press, 2004.

[48] R. Palmer. *J. Appl. Phys.*, 43:3014, 1972.

[49] E.D. Courant, C. Pellegrini, and W. Zakowicz. *Phys. Rev. A*, 32:2813, 1985.

[50] M. Xie. Design optimization for an x-ray free electron laser driven by SLAC linac.

[51] R. Bonifacio, F. Casagrande, G. Cerchioni, L. de Salvo Souza, P. Pierini, and N. Piovella. Physics of the high-gain fel and superradiance. *La Rivista del Nuovo Cimento*, 13:1, 1990.

[52] R. Bonifacio, B.W.J. McNeil and P. Pierini. *Phys. Rev. A*, 40:4467, 1989.

[53] R. Bonifacio, L. De Salvo, P. Pierini, N. Piovella, and C. Pellegrini. *Phys. Rev. Lett.*, 73:60, 1994.

[54] B.W.J. McNeil, N.R. Thompson, and D.J. Dunning. Transform-limited x-ray pulse generation from a high-brightness self-amplified spontaneous-emission free-electron laser. *Phys. Rev. Lett.*, 110:134802, 2013.

[55] B.W.J. McNeil, G.R.M. Robb , D. Dunning and N.R. Thompson. FELO: A one-dimensional time-dependent fel oscillator code. *Proc. 28th Int. FEL Conf. Berlin, Germany (2006)*, page 59, 2006.

[56] S. Reiche. *Nucl. Inst. Meth. Phys. Res. A*, 429:243, 1999.

[57] N.R. Thompson and B.W.J. McNeil. *Phys. Rev. Lett.*, 100:203901, 2008.

[58] D.J. Dunning, B.W.J. McNeil, and N.R. Thompson. Towards zeptosecond-scale pulses from free-electron lasers. *Physics Procedia: Proceedings of the workshop 'Physics and Applications of High Brightness Beams: Towards a Fifth Generation Light Source'*, 52:62, 2014.

[59] J.A. Clarke *et al.* CLARA conceptual design report. *Journal of Instrumentation*, 9, 2014.

[60] Y. Ding *et al. Phys.Rev.Lett.*, 102:254801, 2009.

[61] E.L. Saldin, E.A. Schneidmiller and M.V. Yurkov. *Phys. Rev. ST Accel. Beams*, 9:050702, 2006.

[62] A.A. Zholents and M.S. Zolotorev. *New Journal of Physics*, 10:025005, 2008.

[63] P. Emma, Z. Huang, and M. Borland. *Proc. 26th Int. FEL Conf., Trieste*, page 333, 2004.

[64] D. Xiang, Y. Ding and T. Raubenheimer, and J. Wu. *Phys. Rev. ST Accel. Beams*, 15:050707, 2012.

[65] Y. Ding *et al. Phys.Rev.Lett.*, 109:254802, 2012.

[66] L. Giannessi *et al. Phys.Rev.Lett.*, 106:144801, 2011.

[67] G. Marcus *et al. Applied Phys. Lett.*, 101:134102, 2012.

[68] E.L. Saldin, E.A. Schneidmiller and M.V. Yurkov. *Opt. Commun.*, 212:377, 2002.

[69] R. Bonifacio and F. Casagrande. *Nucl. Instrum. Methods Phys. Res. Sect. A*, 239:36, 1985.

[70] L. Giannessi *et al. J. Appl. Phys.*, 98:043110, 2005.

[71] T. Wanatabe *et al. Phys. Rev. Lett.*, 98:034802, 2007.

[72] M. Labat *et al. Phys. Rev. Lett.*, 107:224801, 2011.

[73] L. Giannessi *et al. Phys.Rev.Lett.*, 108:164801, 2012.

[74] L. Giannessi *et al. Phys.Rev.Lett.*, 110:044801, 2013.

[75] R. Colella and A. Luccio. *Opt. Commun.*, 50:41, 1984.

[76] K.-J. Kim, Y. Shvyd'ko, and S. Reiche. *Phys. Rev. Lett.*, 100:244802, 2008.

[77] A.A. Zholents and W.M. Fawley. *Phys. Rev, Lett.*, 92:224801, 2004.

[78] D. Xiang, Z. Huang, and G. Stupakov. *Phys. Rev. ST Accel. Beams*, 12:060701, 2009.

[79] B.W.J. McNeil, N.R. Thompson, D.J. Dunning, and B. Sheehy. High harmonic attosecond pulse train amplification in a free electron laser. *J. Phys. B*, 44:065404, 2011.

[80] D.J. Dunning, B.W.J. McNeil, N.R. Thompson, and P.H. Williams. Start-to-end modelling of a mode-locked optical klystron free electron laser amplifier. *Physics of Plasmas*, 18:073104, 2011.

[81] B.W.J. McNeil, J.A. Clarke, D.J. Dunning, G.J. Hirst, H.L. Owen, N.R. Thompson, B. Sheehy and P.H. Williams. *New Journal of Physics*, 9:82, 2007.

[82] A.A. Zholents. *Phys. Rev. ST Accel. Beams*, 8:040701, 2005.

[83] E. Kur, D.J. Dunning, B.W.J. McNeil, J. Wurtele, and A.A. Zholents. *New J. Phys.*, 13:063012, 2011.

[84] L.T. Campbell and B.W.J. McNeil. Puffin: a three-dimensional, unaveraged free-electron laser simulation code. *Phys. Plasmas*, 19:093119, 2012.

[85] B.W.J. McNeil. 'Linear theory of an FEL with an energy modulated electron beam', (unpublished).

[86] W.H. Lowdermilk. *Laser Handbook Volume 3*. North-Holland, 1979.

[87] S.W. Smith. *Digital signal processing: a practical guide for engineers and scientists*. Newnes, 2003.

[88] P.H. Williams, D. Angal-Kalinin, J.K. Jones, B.D. Muratori, and H.L. Owen. A recirculating linac as a candidate for the UK New Light Source. *Proc. 23ʳᵈ Particle Accelerator Conference, Vancouver, Canada*, 2009.

[89] J.P. Marangos *et al. New Light Source Project: Conceptual Design Report, Science & Technology Facilities Council.* 2010.

[90] J.-H. Han *et al.* *Proc. 31st International Free Electron Laser Conference, Liverpool, UK*, 2009.

[91] K. Floettmann. A space charge tracking algorithm (ASTRA). *DESY*.

[92] M. Borland. elegant: A flexible sdds-compliant code for accelerator simulation. *Advanced Photon Source, LS-287*, 2000.

[93] R. Soliday and M. Borland. elegant2genesis. *Argonne National Laboratory/Advanced Photon Source.*

[94] D.J. Dunning, N.R. Thompson, B.W.J. McNeil. *Proc. 32nd Int. FEL Conf., Malmö, Sweden*, page 636, 2010.

[95] D.J. Dunning, B.W.J. McNeil, and N.R. Thompson. Few-cycle pulse generation in an x-ray free-electron laser. *Phys. Rev. Lett.*, 110:104801, 2013.

[96] J.K. Jones, J.A. Clarke, and N.R.Thompson. *Proceedings of IPAC 2012, New Orleans, USA.*

[97] D. Ratner, A. Chao, and Z. Huang. *Proc. 29th Int. FEL Conf., Novosibirsk.*

[98] B.E. Carlsten *et al.* *Proceedings of 2011 Particle Accelerator Conference, New York, USA.*

[99] T.J. Bürvenich, J. Evers, and C.H. Keitel. *Phys. Rev. Lett.*, 96:142501, 2006.

Publication list

Listed below are the refereed publications, conference papers, and facility design reports that I've contributed to, of relevance to this thesis:

1. *"4GLS Conceptual Design Report"*, CCLRC, UK (2006).
   http://www.4gls.ac.uk

2. *"Issues in High Harmonic Seeding of the 4GLS XUV-FEL"*, B. Sheehy et al. Proc. 28th International Free Electron Laser Conference (FEL 06), Berlin, Germany (2006).

3. *"The Use of HHG at 4GLS"*, B.W.J. McNeil et al. Proc. 28th International Free Electron Laser Conference (FEL 06), Berlin, Germany (2006).

4. *"FELO : A One-Dimensional Time-Dependent FEL Oscillator Code"*, B.W.J. McNeil et al. Proc. 28th International Free Electron Laser Conference (FEL 06), Berlin, Germany (2006).

5. *"First Tolerance Studies for the 4GLS FEL Sources"*, D.J. Dunning et al. Proc. 28th International Free Electron Laser Conference (FEL 06), Berlin, Germany (2006).

6. *"An XUV-FEL amplifier seeded using high harmonic generation"*, B.W.J. McNeil, J.A. Clarke, D.J. Dunning, G.J. Hirst, H.L. Owen, N.R. Thompson, B. Sheehy and P.H. Williams, New J Phys 9 82 (2007).
   doi:10.1088/1367-2630/9/4/082

7. *"A design for the generation of temporally-coherent radiation pulses in the VUV and beyond by a self-seeding high-gain free electron laser amplifier"*, B.W.J. McNeil, N.R. Thompson, D.J. Dunning, J.G. Karssenberg, P.J.M. Van Der Slot, K-J Boller, New J Phys 9 239 (2007)
   doi:10.1088/1367-2630/9/7/239

8. *"Short wavelength regenerative amplifier free electron lasers"*, D.J. Dunning, B.W.J. McNeil, N.R. Thompson, FEL Frontiers 2007 - Proceedings of the International Workshop on Frontiers in FEL Physics and Related Topics, pp 167 , Elba Island-La Biodola, Tuscany (Italy), Nucl. Instrum. Meth. A 593 (1-2) 116-119 (2008).
   doi:10.1016/j.nima.2008.04.045

9. *"Retention of attosecond pulse structure in an HHG seeded FEL Amplifier"*, B.W.J. McNeil, N.R. Thompson, D.J. Dunning, B. Sheehy, Proc. 30th International Free Electron Laser Conference (FEL 08), Gyeongju, Korea, 24-29 Aug 2008.

10. *"Study of an HHG-seeded harmonic cascade FEL for the UK's New Light Source"*, N.R. Thompson, D.J. Dunning, B.W.J. McNeil, R. Bartolini, Proc. 31st International Free Electron Laser Conference (FEL 09), Liverpool, UK (2009).

11. *"Start-to-end simulations of SASE and HHG-seeded mode-locked FEL"*, D.J. Dunning, N.R. Thompson, P.H. Williams, B.W.J. McNeil, Proc. 31st International Free Electron Laser Conference (FEL 09), Liverpool, UK (2009).

12. *"Long-scale modulation of electron beam energy in free electron lasers"*, D.J. Dunning, N.R. Thompson, B.W.J. McNeil, Proc. 32nd International Free Electron Laser Conference (FEL 10), Malmo, Sweden (2010).

13. *"Design of the recirculating Linac option for the UK New Light Source"*, P.H. Williams, D. Angal-Kalinin, J.K. Jones, D. Dunning, N.R. Thompson, R. Bartolini, I.P. Martin, J. Rowland, 1st International Particle Accelerator Conference (IPAC 10), Kyoto, Japan (2010).

14. *"Improved temporal coherence in SASE FELs"*, N.R. Thompson, D.J. Dunning and B.W.J. McNeil, Proc. 1st International Particle Accelerator Conference (IPAC 10), Kyoto, Japan (2010).

15. *"Optimisation of an HHG-seeded harmonic cascade FEL design for the NLS project"*, D.J. Dunning, N.R. Thompson, B.W.J. McNeil, R. Bartolini, Z. Huang, H. Geng, 1st International Particle Accelerator Conference (IPAC 10), Kyoto, Japan (2010).

16. *"New Light Source: Conceptual Design Report"*, J.P. Marangos *et al.*, Science & Technology Facilities Council (2010).
    http://www.newlightsource.org/

17. *"Recirculating linac free-electron laser driver"*, P.H. Williams, D. Angal-Kalinin, D.J. Dunning, J.K. Jones, N.R. Thompson, Phys Rev Special Topics 14 (5) 050704 (2011).
    doi:10.1103/PhysRevSTAB.14.050704

18. *"Considerations for a Light Source Test Facility at Daresbury Laboratory"*, N.R. Thompson, J.A. Clarke, D.J. Dunning, J.W. McKenzie, Proc. 33rd International Free Electron Laser Conference (FEL2011), Shanghai, China (2011).

19. *"High harmonic attosecond pulse train amplification in a free electron laser"*, B.W.J. McNeil, N.R. Thompson, D.J. Dunning, B. Sheehy, J Phys B 44 (6) 065404 (2011)
    doi:10.1088/0953-4075/44/6/065404

20. *"A wide bandwidth free-electron laser with mode locking using current modulation"*, E. Kur, D.J. Dunning, B.W.J. McNeil, J. Wurtele, A.A. Zholents, New J Phys 13 (6) 063012 (2011).
    doi:10.1088/1367-2630/13/6/063012

21. *"Start-to-end modelling of a mode-locked optical klystron free electron laser amplifier"*, D.J. Dunning, B.W.J. McNeil, N.R. Thompson, P.H. Williams, Physics of Plasmas 18 (7) 073104 (2011).
    doi:10.1063/1.3605027

22. *"Design study of an HHG-seeded harmonic cascade free-electron laser"*, D.J. Dunning, N.R. Thompson, B.W.J. McNeil, Journal of Modern Optics 58 (16) 1362-1373 (2011).
    doi:10.1080/09500340.2011.586475

23. *"FEL considerations for CLARA: a UK test facility for future light sources"*, D.J. Dunning et al. Proc. ICFA Workshop on Future Light Sources (FLS2012), Newport News, USA (2012).

24. *"Few-Cycle Pulse Generation in an X-Ray Free-Electron Laser"*, D.J. Dunning, B.W.J. McNeil, N.R. Thompson, Physical Review Letters, 110, 104801

(2013).
doi:10.1103/PhysRevLett.110.104801

25. *"Transform-Limited X-Ray Pulse Generation from a High-Brightness Self-Amplified Spontaneous-Emission Free-Electron Laser"*, B.W.J. McNeil, N.R. Thompson, D.J. Dunning, Physical Review Letters, 110, 134802 (2013).
doi:10.1103/PhysRevLett.110.134802

26. *"The Conceptual Design of CLARA, A Novel FEL Test Facility for Ultra-short Pulse Generation"*, J.A. Clarke et al. Proc. International Particle Accelerator Conference (IPAC13), Shanghai, China (2013).

27. *"Towards zeptosecond-scale pulses from free-electron lasers"*, D.J. Dunning et al. Proc. High Brightness Electron Beams Workshop (HBEB13), San Juan, Puerto Rico (2013).

28. *"The Conceptual Design of CLARA, A Novel FEL Test Facility for Ultra-short Pulse Generation"*, J.A. Clarke *et al.*, Science & Technology Facilities Council (2013). J A Clarke et al. 2014 JINST 9 T05001

Presentations

Listed below are presentations that I've given on the topics in this thesis:

Invited Talks

- 'Towards Zeptosecond-Scale Pulses from X-Ray Free-Electron Lasers'
  Physics and Applications of High Brightness Beams: Towards a Fifth Generation Light Source (HBEB 2013)
  San Juan, Puerto Rico, March 25-28, 2013
  http://pbpl.physics.ucla.edu/HBEB2013/

- 'Towards Zeptosecond-Scale Pulses from X-Ray Free-Electron Lasers'
  35$^{\text{th}}$ International Free-Electron Laser Conference (FEL 2013)
  Manhattan, USA, August 26-30, 2013
  http://www.c-ad.bnl.gov/fel2013/

Contributed talks

- 'FEL Considerations for CLARA: a UK Test Facility for Future Light Sources'
  ICFA Workshop on Future Light Sources (FLS 2012)
  Thomas Jefferson National Accelerator Facility, March 5-9, 2012
  https://www.jlab.org/conferences/FLS2012

- 'Towards Zeptosecond-Scale Pulses from X-Ray Free-Electron Lasers'
  IoP Particle Accelerators and Beams Group Annual Meeting
  The Cockcroft Institute, Warrington, UK, 10$^{\text{th}}$ April 2013

Other:

In addition to presenting in poster sessions for the conference papers listed in the previous section, I also attended the ATTO2013 conference and presented topics of this thesis in a poster session:

- 'Few-cycle pulse trains from x-ray free-electron lasers'
  4th International Conference on Attosecond Physics (ATTO2013)
  Institut Pasteur, Paris, July 8-12, 2013
  http://atto2013.celia.u-bordeaux1.fr/

High harmonic attosecond pulse train amplification in a free electron laser

B W J McNeil[1]**, N R Thompson**[1,2]**, D J Dunning**[1,2] **and B Sheehy**[3]

[1] SUPA, Department of Physics, University of Strathclyde, Glasgow G4 0NG, UK
[2] ASTeC and Cockcroft Institute, STFC Daresbury Laboratory, Warrington WA4 4AD, UK
[3] Collider Accelerator Department, Brookhaven National Laboratory, Upton, NY 11973, USA

E-mail: b.w.j.mcneil@strath.ac.uk

Abstract

It is shown using three-dimensional simulations that the temporal structure of an attosecond pulse train, such as that generated via high harmonic generation in noble gases, may be retained in a free electron laser amplifier through to saturation using a mode-locked optical klystron configuration. At wavelengths of $\sim$12 nm, a train of attosecond pulses of widths $\sim$300 as with peak powers in excess of 1 GW are predicted.

(Some figures in this article are in colour only in the electronic version)

1. Introduction

Attosecond pulses from high harmonic generation in noble gases can been used to great effect in capturing and controlling ultra-fast events in atomic and molecular physics [1, 2]. While many techniques require single attosecond pulses, methods that utilize trains of attosecond pulses, as generated in the normal mode of operation of an HH source, have also been employed to both capture and control electronic processes within atoms and molecules [3–8].

High-gain free-electron lasers (FELs) operating at similar wavelengths typically have longer pulse durations but offer peak powers several orders of magnitude greater than the HH sources. If a FEL is seeded by and amplifies an HH source, the initial HH power, P_0, is exponentially amplified as a function of distance through the FEL interaction region as $P(z) \approx P_0 \exp(z/\sqrt{3}l_g)$ where $l_g = \lambda_u/4\pi\rho$ is the nominal gain-length, ρ is the FEL scaling parameter that determines the FEL coupling strength and efficiency and λ_u is the period of the undulator [9]. However, due to the relative propagation of the radiation pulses through the amplifying electron bunch, such amplification of the HH source tends to 'wash out' the HH attosecond pulse train structure [10].

Several techniques have been proposed to achieve attosecond pulse durations in FELs (see e.g. [11–15]). The widths of the light pulses generated are limited by the coherence length of the FEL interaction $l_c = \lambda_r/4\pi\rho$, where λ_r is the resonant FEL wavelength [9], and pulse widths tend to have durations $l_c/c \gtrsim 2$ fs at the $\sim$12 nm wavelengths considered here.

An alternative method, that applies the concepts from mode-locked cavity lasers in FEL *amplifiers*, has also been proposed [16] that may generate a *train* of pulses with durations not restricted by the FEL coherence length l_c. In this technique, a series of spatiotemporal shifts are introduced between the radiation and the co-propagating electron bunch that define a set of axial radiation modes. The spatiotemporal shifts are achieved by delaying the electron bunch using magnetic chicanes inserted between undulator modules. Introducing a modulation of the electron beam properties at the mode spacing periodically suppresses or enhances the FEL interaction at different longitudinal positions along the beam, so that a train of equally spaced pulses develop aligned with the regions of strongest FEL interaction. In the frequency domain, this is equivalent to the modes developing sidebands that overlap neighbouring modes, allowing mode-locking to occur and is analogous with mode-locking in conventional cavity lasers [17].

The spectrum generated by the XUV mode-coupled SASE system of [16] has a modal structure with mode-spacing $\Delta\omega$ similar to the spacing of harmonics in an HH source. Equivalently, the temporal structure of the two systems form an attosecond pulse train. By matching the spectral/temporal structures of a mode-coupled FEL amplifier to an HH seed, it may therefore be possible to amplify the HH seed to saturation while retaining its attosecond train structure. Furthermore,
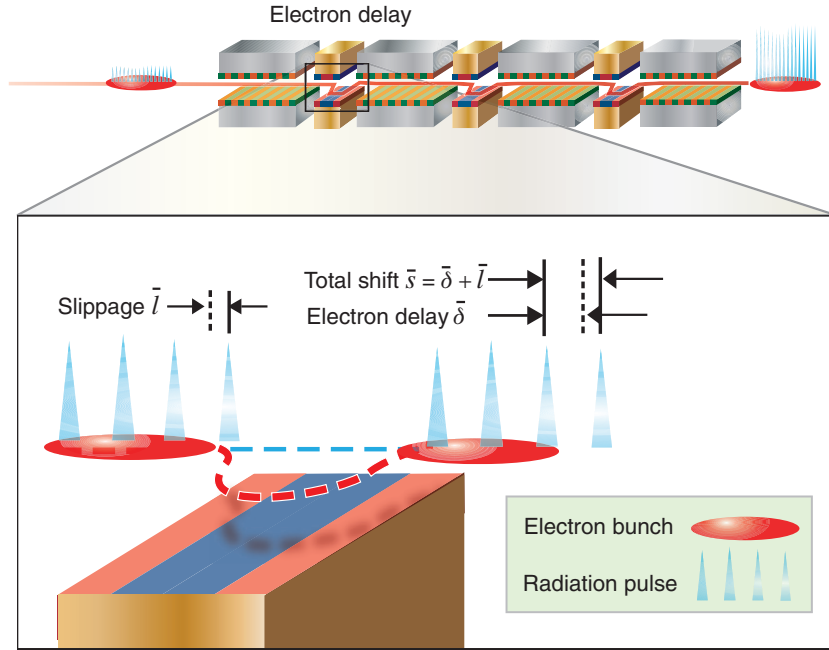
Figure 1. Schematic of the mode-coupled amplifier FEL interaction operating with an HH seed. The inset shows details of the electron delay.

it should be possible to achieve this without the need for introducing a modulation at the mode spacing as the HH attosecond seed already comprises a pulse train structure. In this paper it is demonstrated via 1D and 3D numerical simulations that this is the case.

2. Mode generation in an amplifier

The spatio-temporal shifts that generate the equally spaced modal structure in the amplifier spectrum are achieved by periodically delaying the electron bunch using magnetic chicanes between undulator modules [16], as shown schematically in figure 1.

The notation used here follows that of [16]. The total propagation distance of a radiation wavefront ahead of the electron bunch per module in units of the cooperation length l_c is $\bar{s} = s/l_c = \bar{l} + \bar{\delta}$, where $\bar{l}$ is the similarly scaled slippage occurring in the undulator and $\bar{\delta}$ is that within the chicane. The scaled FEL radiation frequency is defined as $\bar{\omega} = (\omega - \omega_r)/2\rho\omega_r$ where ω_r is the resonant FEL frequency. The slippage enhancement factor is defined as $S_e = \bar{s}/\bar{l}$. In [16], a solution is obtained for the one-dimensional wave equation describing the field evolution of a small, constant electron source term for a series of N undulator–chicane modules. For $S_e > 1$ the spectrum takes the form of a sinc-function envelope (the single undulator module spectrum) modulated by a frequency comb centred at the scaled resonant frequency $\bar{\omega}$, with mode separation $\Delta\bar{\omega} = 2\pi/\bar{s}$ corresponding to $\Delta\omega = 2\pi/T_s$, where $T_s = s/c = \bar{s}l_c/c$ is the time taken for radiation to travel the slippage length. The number of modes under the central peak of the spectrum is shown to be $N_0 = 2S_e - 1$.

The delay provided by a four-dipole chicane is of the order of its R_{56}. The HH pulses are separated by one half the drive laser wavelength, i.e. ∼400 nm, so the R_{56} of the slippage enhancing chicanes are of this order. By comparison, a bunch compression chicane used prior to electron injection into the FEL has an R_{56} typically of several cm, and the slippage enhancing chicanes placed between the undulator modules are seen to be weaker by several orders of magnitude. Any CSR disruption caused by these chicanes can therefore be assumed to be negligibly small.

3. Amplification of an HH seed

The temporal profile of the HH seed is a comb of attosecond pulses separated by half the wavelength of the drive laser λ_d and modulated by the drive laser power envelope. The spectral and temporal structure of the radiation generated by the undulator–chicane system is matched to that of the HH seed by setting $\bar{s} = \bar{\lambda}_d/2$, where $\bar{\lambda}_d = \lambda_d/l_c$ is the scaled drive laser wavelength.

For a typical FEL parameter of $\rho = 2 \times 10^{-3}$, similar to that for an FEL operating in the XUV, then for undulator modules of eight periods, $\bar{l} = 0.201$. The value of the scaled slippage generated by the chicanes is chosen to be $\bar{\delta} = 0.616$ so that $\bar{s} = \bar{\lambda}_d/2$, matching the undulator–chicane system to the spectral and temporal structure of the HH seed. This gives a slippage enhancement factor of $S_e = 4.0625$.

The HH seed was modelled in a similar way to that described in [10] with a FEL resonant wavelength chosen to be the 65th harmonic of the drive laser wavelength of $\lambda_d = 805$ nm (e.g. Ti:sapphire), i.e. $\lambda_r = \lambda_d/65$. The HH field was constructed by first summing over a weighted harmonic series
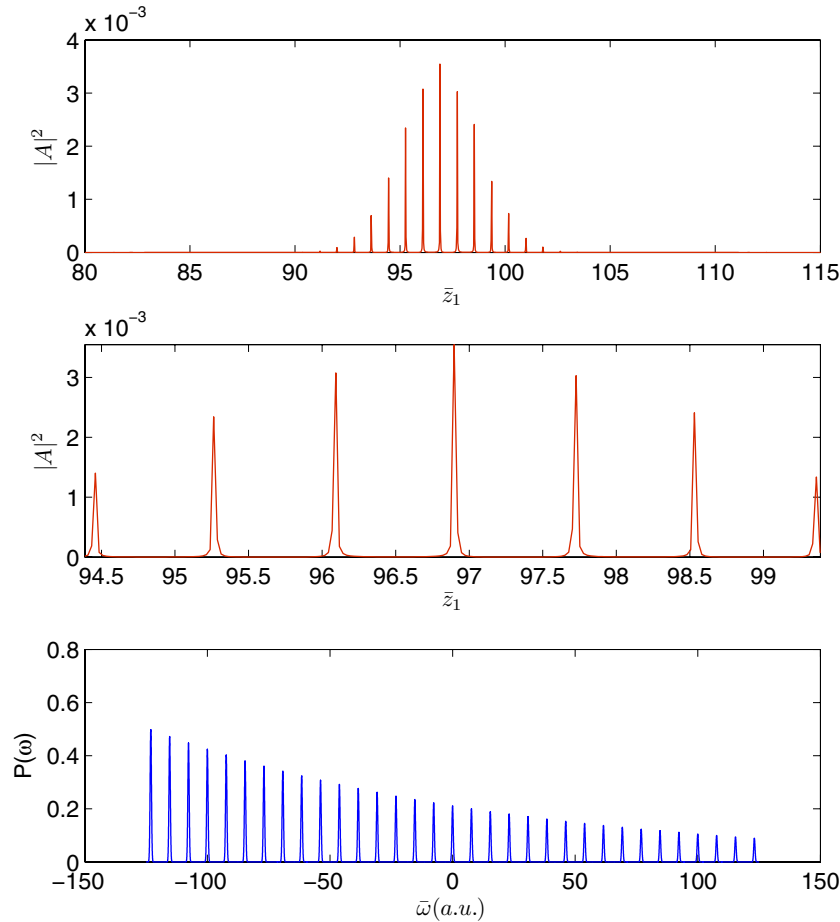
Figure 2. Scaled longitudinal intensity profile top and middle (detail) as a function of the scaled distance within the pulse $\bar{z}_1$ measured in cooperation lengths, and scaled spectral power distribution for the HH seed (bottom).

modulated by an envelope determined by the Gaussian drive laser centred at $t = t_0$ and of width $\sigma_d \approx 3$ fs:

$$E_{\text{HH}} \propto \exp\left(-\frac{(t-t_0)^2}{2\sigma_d^2}\right) \sum_h \mathcal{E}_h \, e^{-i(\omega_h(t-t_0)+\phi_h)} \qquad (1)$$

where $h = 1, 3, 5, \ldots$, $\omega_h = h\omega_d$ are the odd harmonics of the drive laser frequency and ϕ_h and $\mathcal{E}_h$ represent the phases and amplitudes of individual harmonic components, respectively.

In a typical HH spectrum, the harmonic yield drops quickly over the first few harmonic orders, then much more slowly over a 'plateau region', up to a wavelength and intensity-dependent cutoff order, beyond which the yield drops precipitously. Both the amplitude of particular harmonics and their relative phases are sensitive functions of the experimental conditions. We consider here a somewhat idealized HH source while retaining its essential features. The field amplitude dependence is assumed to be of the form

$$\mathcal{E}_h = \left(\frac{\eta_p^{h_m/h_p}}{\eta_m}\right)^{\frac{h_p}{h_m-h_p}} \exp\left(-\frac{\ln(\eta_p/\eta_m)}{h_m-h_p}h\right) \qquad (2)$$

where $h_m = 95$ is the maximum harmonic, $h_p = 11$ is the harmonic where the plateau region begins, $\eta_p = 5 \times 10^{-6}$ is the harmonic yield efficiency of the HH process at the beginning of the plateau and $\eta_m = 5 \times 10^{-7}$ is that at the maximum

harmonic. We choose this form to approximate the slow decline in harmonic yield of one to two orders of magnitude between the beginning of the plateau and the cutoff that has been observed in experiments [18]. A different smoothly falling function or small variations of individual harmonic amplitudes from this dependence do not significantly alter the attosecond character of the seed.

Most numerical FEL simulation codes, like those used in this paper, average both the electron motion and the radiation field locally within the pulses over a radiation wavelength. The Nyquist theorem then limits the bandwidth of frequencies that can be properly modelled to $\omega_r/2 < \omega_r < 3\omega_r/2$ [10] which, for the resonant harmonic $h = 65$ considered here, corresponds to an harmonic range $33 < h < 95$, all of which fall within the harmonic plateau region. We include only these harmonic orders in the simulation.

The attosecond character of the seed is sensitive to variations in the relative phases, ϕ_h, of the harmonics [19]; when these phases vary, the pulse train can have more structure than that of the 'clean' pulse train of figure 2, in which it was assumed $\phi_h = 0$ for all harmonic orders. While we use the phase-locked seed of figure 2 in our simulations below for clarity, we have also varied these phases and run the simulations using a more structured seed and

3
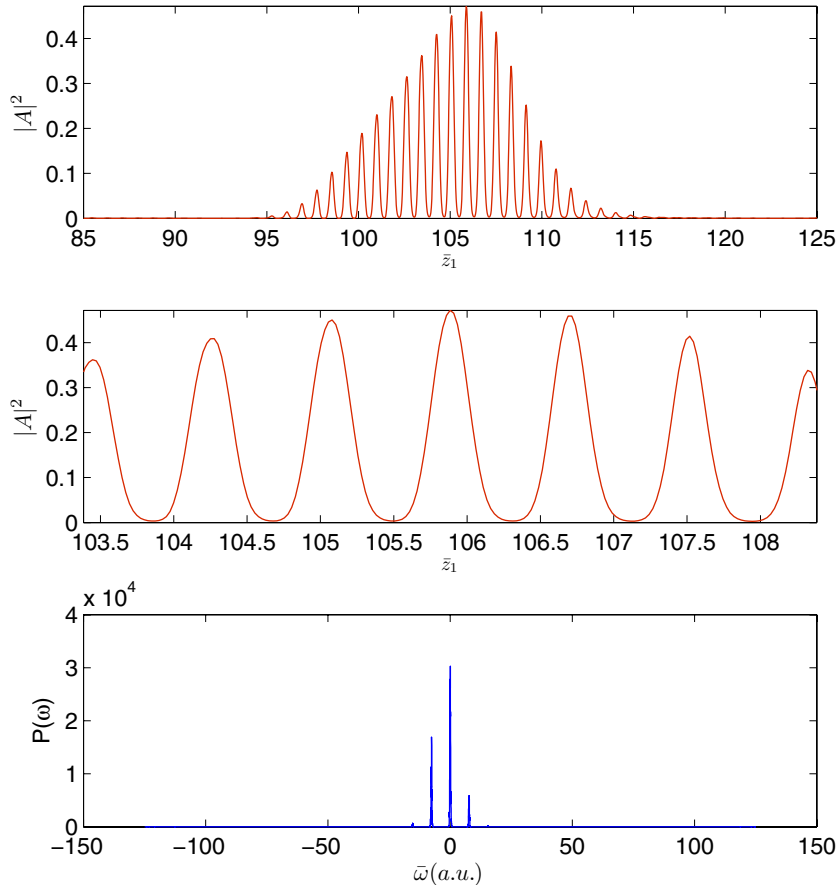
Figure 3. Scaled longitudinal intensity profile (top and middle) and scaled spectral power distribution of the amplified HH radiation for $\bar{l} = 0.201$ ($S_e = 4.0625$), after 22 undulator–chicane modules.

find, unsurprisingly, that the amplified output also has more structure, although a well-defined pulse train is retained.

The system is modelled using a 1D code similar to that described in [20]. The HH seed is injected into the amplifying undulator–chicane modules with a cold electron beam. Note that no energy modulation of the electron beam was used. This is different from the mode-locked SASE case of [16] which starts up from noise and requires a beam energy modulation at the mode spacing $\Delta\bar{\omega}$ to generate an isolated train of equally spaced pulses. Here, the HH seed is modelled as a set of in-phase modes; hence, it consists of a train of equally spaced pulses in the temporal domain. It will be seen that while this temporal structure is retained, a broadening of the individual pulses occurs. The pulse durations attained are in agreement with the scaling observed in [16] for the pulse width, $\tau_p \propto 1/\sqrt{N_0}$, where N_0 is the number of amplified modes.

After 22 undulator–chicane modules, the amplified scaled radiation power and spectrum are as shown in figure 3. It is seen that the HH seed is amplified and the comb of temporal spikes is retained, but with increased pulse widths as discussed. This number of modules corresponds to a scaled FEL interaction length of $22 \times \bar{l} \approx 4.4$. This is just prior to saturation where scaled powers of $|A|^2 \approx 1$ are achieved. However, the temporal structure of the pulses begins to break up at saturation. (Note that the dispersive strength of the

chicanes $D = R_{56}/2l_c \approx 10\bar{\delta}/6$ reduces the gain length as discussed in [16].)

4. Optimizing the system

In [16] it is demonstrated that the pulse widths in mode-locked SASE simulations are proportional to $1/\sqrt{N_0}$; this is in agreement with an analogous relation from mode-locked conventional cavity lasers.

The maximum bandwidth of the amplified radiation spectrum is that of the single undulator module spectrum, with the minimum number of optical cycles per pulse approximately equal to the number of undulator periods per module. In order to attain narrower amplified HH pulses, the bandwidth of the system (and hence the number of modes amplified) is increased by reducing the number of undulator periods per module. To reduce $\bar{l}$ while continuing to satisfy the condition $\bar{s} = \bar{\lambda}_d/2$, the value of $\bar{\delta}$ is increased to keep $\bar{s}$ constant. The system is simulated for a case with the number of undulator periods per module set to 4. The corresponding value of the slippage enhancement factor is $S_e = 8.125$.

The spectral power distributions for the two cases $S_e = 4.0625$ and $S_e = 8.125$ are shown in figures 3 and 4, respectively. It is seen that the width of the spectral envelope of the amplified radiation is increased with the reduced undulator module length $\bar{l}$. The number of modes, N_0, under the
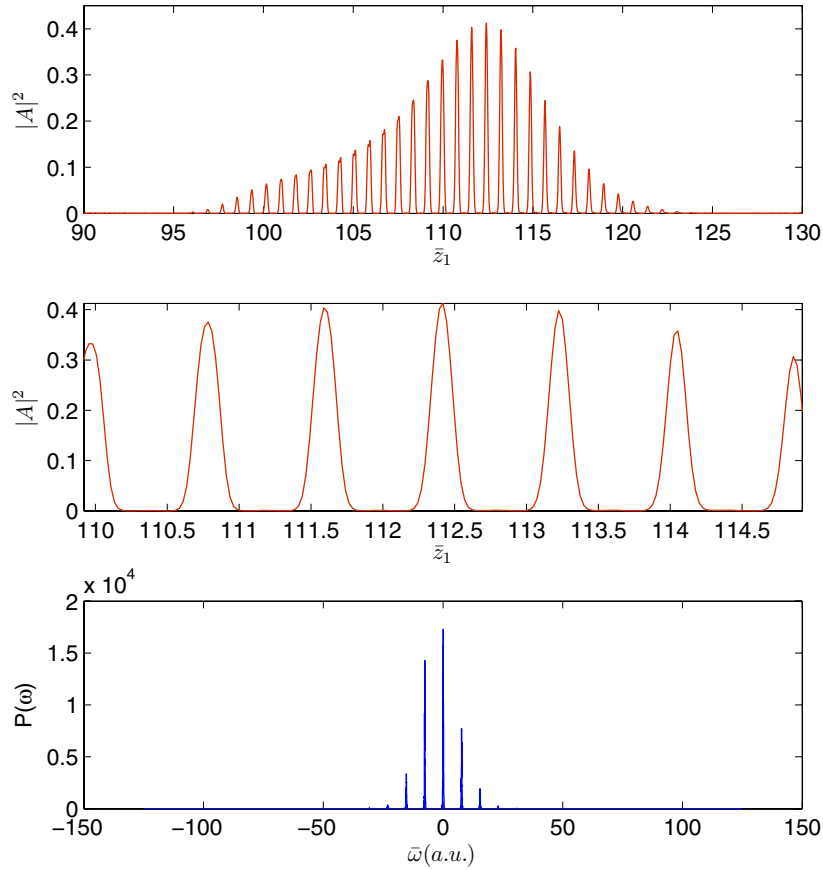
Figure 4. Scaled longitudinal intensity profile (top and middle) and scaled spectral power distribution of the amplified HH radiation for $\bar{l} = 0.101$ ($S_e = 8.125$), after 34 undulator–chicane modules.

central peak of the spectrum increases, narrowing the temporal duration of the pulses. The variations of the peak intensity and pulse width with scaled distance through the undulator are plotted in figure 5 for the two cases $S_e = 4.0625$ ($\bar{l} = 0.201$) and $S_e = 8.125$ ($\bar{l} = 0.101$). For both cases, there is an initial rapid broadening since only the modal content that falls under the envelope of the single undulator spectrum is amplified. The pulse durations continue to increase more slowly during further amplification. This slow pulse broadening effect is attributed to slippage in the undulators. For $S_e = 8.125$, 34 undulator–chicane modules are required to produce the same amplification of the 22-module $S_e = 4.0625$ case. This corresponds to a reduction in the total undulator length from 4.4 to 3.4, which can be attributed to more effective seeding since a broader spectral range of the seed is amplified, and reduced gain length due to an increased number of chicanes.

For larger values of S_e, the broadening of the modal sinc-function envelope becomes restricted by the Nyquist limit.

5. Energy spread

The effects of energy spread on the interaction have been investigated using the 1D model by introducing a relative Gaussian energy spread of width $\sigma_\gamma/\gamma = \rho/10 = 0.02\%$ for the case $S_e = 8.125$. The results close to saturation are plotted in figure 6, which is the equivalent of figure 4. While the
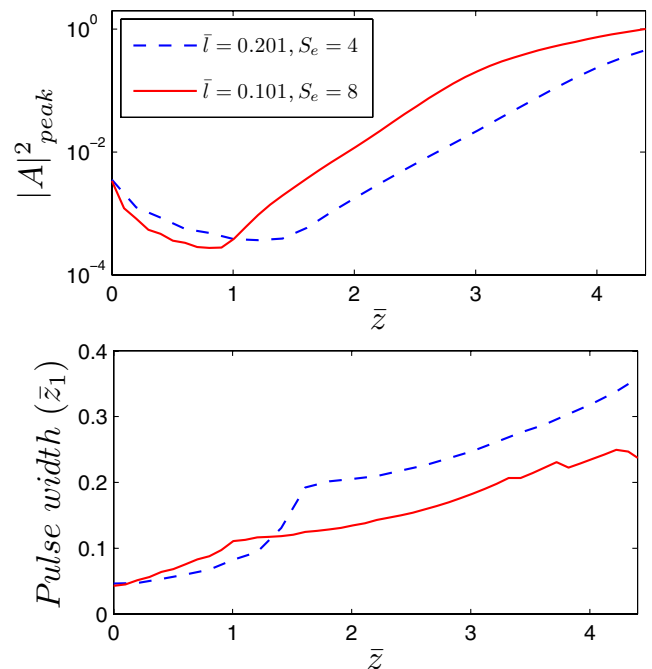
Figure 5. Scaled peak intensity (top) and pulse width in units of l_c (bottom) plotted against the scaled interaction length, $\bar{z}$ [16], for the two cases $S_e = 4.0625$ ($\bar{l} = 0.201$) and $S_e = 8.125$ ($\bar{l} = 0.101$). It is seen that by reducing the number of undulator periods per module, both the pulse duration and the gain length are reduced.
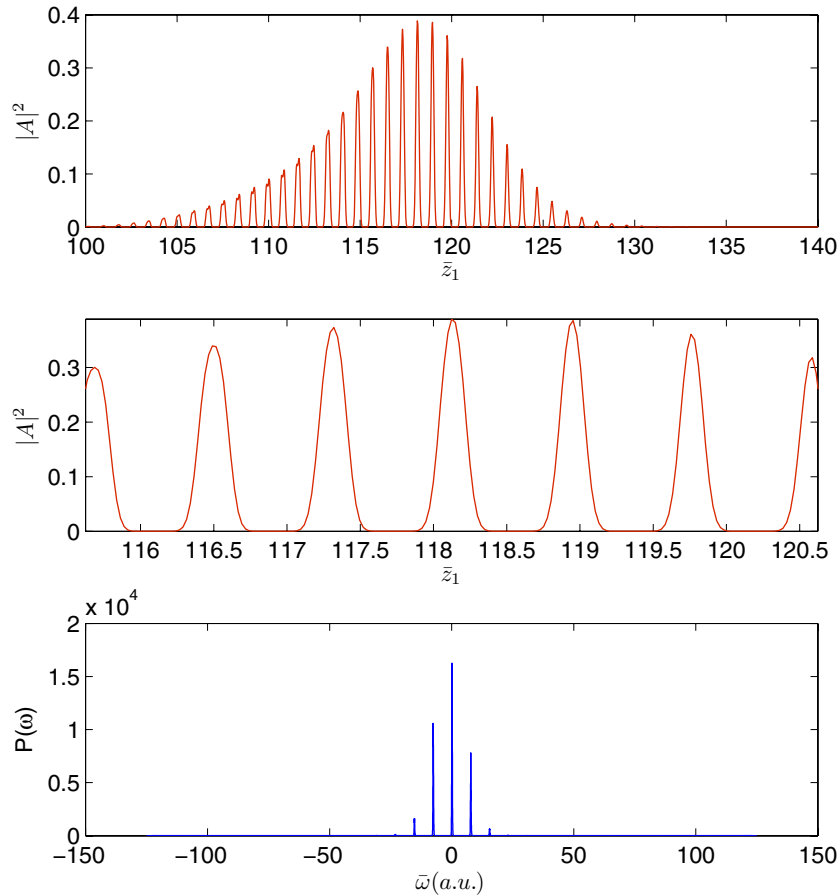
Figure 6. Scaled longitudinal intensity profile (top and middle) and scaled spectral power distribution of the amplified HH radiation for $\bar{l} = 0.101$ ($S_e = 8.125$) and an initial energy spread $\sigma_\gamma/\gamma = 0.02\%$, after 42 undulator–chicane modules.

cold beam case took 34 undulator–chicane modules, the case here took 42 modules. Note that the temporal and spectral structure of the radiation power remains largely unaffected by the energy spread. Larger energy spreads have also been simulated with the main effect being that a larger number of modules are required to achieve saturation.

6. Results of 3D simulations

The system has also been modelled using the three-dimensional FEL simulation code Genesis 1.3 [21]. The main results of the 1D simulations are reproduced using the 3D code and show amplification of an HH seed pulse retaining its pulse train structure. The Genesis simulation code models both the radiation field and the electron beam in 3D and requires careful matching of the electron beam to the undulator/chicane lattice structure which additionally contains an electron beam quadrupole focussing lattice to maintain a good electron–radiation field coupling through the long structure. The focussing lattice was optimized for normal FEL interaction in the absence of the chicane fields and it was found that this set-up also worked well when the chicanes were included to generate the radiation modes matched to the HH seed.

Similar parameters as for the XUV mode-coupled FEL amplifier of [16] were used (i.e. without electron beam

modulation) including an energy spread of width $\sigma_\gamma/\gamma = 0.01\%$. The seed power and spectrum show the attosecond pulse train structure and frequency comb, as seen in figure 7. The peak power of the seed is 3 MW in an envelope of $\sigma_d \approx 25$ fs. (This peak power is a reasonable estimate of what can be expected from HH sources in the present to near future [22] and can be reduced by an order of magnitude while still retaining a good amplified pulse train structure that dominates competing SASE. Methods that enhance HH yields by orders of magnitude have been demonstrated [23, 24], although the impact of these methods on the attosecond character of the source has not been investigated.) It was assumed that the wavelength of the Ti:sapphire drive laser was $\lambda_d = 780$ nm and the FEL was then tuned to be resonant with the 63rd harmonic of the drive laser with $\lambda_r = 12.4$ nm. The repetition rate of the seed pulses is the same as that of the drive laser which could be expected to rise from the current 10s of Hz to ~1 kHz in the next few years [22].

Each undulator module had four periods of 3.1 cm and each chicane had a delay of 28 radiation wavelengths corresponding to a slippage enhancement $S_e = 8$. These parameters for the undulator–chicane modules then match the mode spacing of the HH seed. The amplified seed approaching saturation, after 47 modules, is plotted in figure 8 and the pulse temporal and spectral properties agree well with the equivalent

J. Phys. B: At. Mol. Opt. Phys. **44** (2011) 065404

B W J McNeil *et al*
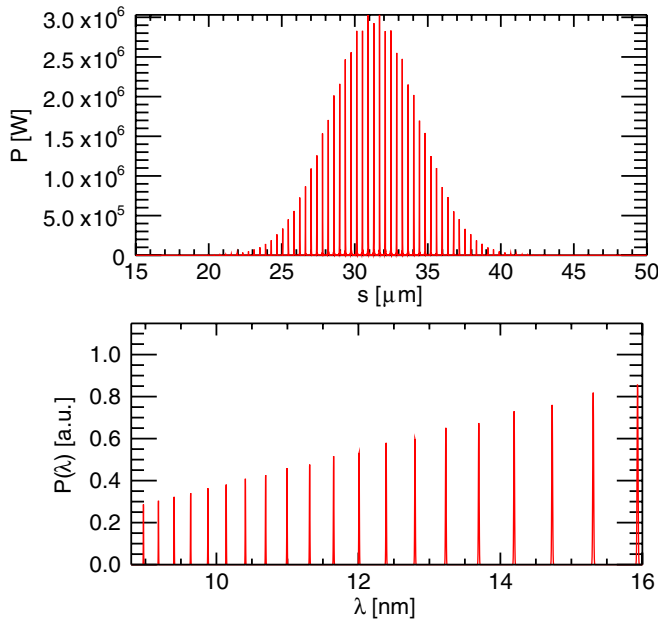
Figure 7. Longitudinal intensity profile (top) and spectral power distribution (bottom) of the HH seed in 3D simulations.

one-dimensional $S_e = 8.125$ case of figure 6. The FWHM length of each pulse in the amplified train is 300 as. Further 3D simulations (not shown) with $S_e = 4$ agreed well with the $S_e = 4.0625$ case of figure 3. As may be expected from an amplifier seeded using a source of good temporal coherence with power well above noise level, the temporal coherence length of the amplified output is found, though not shown here, to be retained with little reduction.

7. Conclusions

It was shown, using 1D and 3D simulations, that the attosecond structure of the HH seed can be amplified to saturation using a mode-locked optical klystron FEL amplifier configuration of [16] to increase the peak power by a factor ~300. No pre-conditioning of the electron beam (e.g. energy or current modulation) was required. The only requirement is for an undulator–chicane modular structure, the radiation spectrum of which matches an HH seed source.

The maximum bandwidth of the amplified radiation is critical to achieving the minimum pulse durations (maximum mode number) from the system, and is set by the single undulator module spectrum. Reducing the number of undulator periods per module therefore appears to be the most effective route to achieving the shortest possible pulse durations. The introduction of a modulation to the electron bunch at the mode spacing may well restrict the slow pulse broadening effect observed and so allow shorter pulse durations than those reported here. This will be investigated in future work. The behaviour of the MLOK system when modelled in a code allowing a greater spectral bandwidth, and so shorter pulse lengths, such as that of [25], will also be investigated.
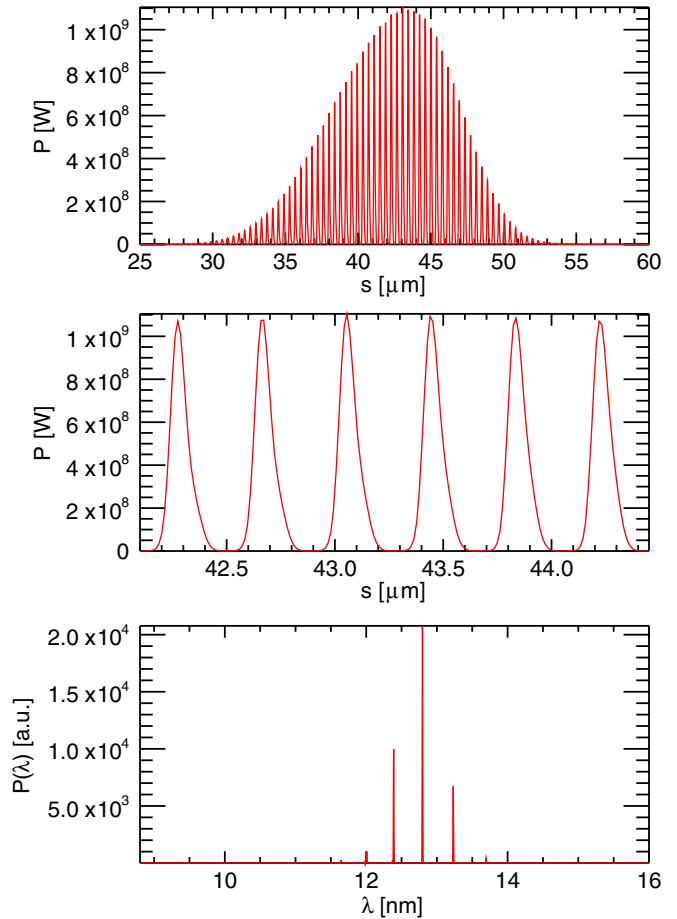
Figure 8. Longitudinal intensity profile (top and middle) and spectral power distribution (bottom) of the amplified HH radiation in 3D simulations, with $S_e = 8$. The agreement with the equivalent 1D simulations shown in figure 6 is very good.

References

[1] Corkum P B and Krausz F 2007 *Nat. Phys.* **3** 381
[2] Krausz F and Ivanov M 2009 *Rev. Mod. Phys.* **81** 163
[3] Johnsson P *et al* 2005 *Phys. Rev. Lett.* **95** 013001
[4] Remetter T *et al* 2006 *Nat. Phys.* **2** 323–6
[5] Varjú K *et al* 2006 *J. Phys. B: At. Mol. Opt. Phys.* **39** 3983–91
[6] Mauritsson J, Johnsson P, Mansten E, Swoboda M, Ruchon T, L'Huillier A and Schafer K J 2008 *Phys. Rev. Lett.* **100** 073003
[7] Klaiber M, Hatsagortsyan K Z, Müller C and Keitel C H 2008 *Opt. Lett.* **33** 411–3
[8] Singh K P *et al* 2010 *Phys. Rev. Lett.* **104** 023001
[9] Bonifacio R, Pellegrini C and Narducci L 1984 *Opt. Commun.* **50** 373
[10] McNeil B W J, Clarke J A, Dunning D J, Hirst G J, Owen H L, Thompson N R, Sheehy B and Williams P H 2007 *New J. Phys.* **9** 82
[11] Xiang D, Huang Z and Stupakov G 2009 *Phys. Rev. ST Accel. Beams* **12** 060701 and references [6–15] therein

[12] Ding Y *et al* 2009 *Phys. Rev. ST Accel. Beams* **12** 060703
[13] Penn G and Zholents A 2009 *Proc. 31st Int. Free Electron
     Laser Conf. (Liverpool, UK) MOPC73,* p 176
     (http://accelconf.web.cern.ch/AccelConf/FEL2009/papers/
     mopc73.pdf)
[14] Ding Y *et al* 2009 *Phys. Rev. Lett.* **102** 254801
[15] McNeil B W J and Thompson N R 2010 *Proc. 32nd Int. Free
     Electron Laser Conf. (Malmo, Sweden)* THOB4
[16] Thompson N R and McNeil B W J 2008 *Phys. Rev. Lett.*
     100 203901
[17] Siegman A E 1986 *Lasers* (Sausalito, CA: University Science
     Books) chapter 27
[18] L'Huillier A and Balcou Ph 1993 *Phys. Rev. Lett.* **70** 774

[19] Antoine P, L'Huillier A and Lewenstein M 1996 *Phys. Rev.
     Lett.* **77** 1234
[20] McNeil B W J, Robb G R M, Dunning D and Thompson N R
     2006 *Proc. 28th Int. FEL Conf. (Berlin, Germany)
     MOPPHO11,* p 59 (http://accelconf.web.cern.ch/
     AccelConf/f06/PAPERS/MOPPH011.PDF)
[21] Reiche S 1999 *Nucl. Instrum. Methods Phys. Res.* A **429** 243
[22] Marangos J *et al* 2010 *NLS Project: Conceptual Design Report*
     Section 10.2 available at http://www.newlightsource.org
[23] Jong Kim I *et al* 2005 *Phys. Rev. Lett.* **94** 243901
[24] Takahashi E J *et al* 2007 *Phys. Rev. Lett.* **99** 053904
[25] McNeil B W J and Robb G R M 2002 *Phys. Rev.* E
     65 046503

Start-to-end modelling of a mode-locked optical klystron free electron laser amplifier

D. J. Dunning,[1,2,a)] B. W. J. Mc Neil,[1,b)] N. R. Thompson,[1,2,c)] and P. H. Williams[2,d)]
[1]*University of Strathclyde (SUPA), Glasgow G4 0NG, United Kingdom*
[2]*ASTeC, Daresbury Laboratory, Warrington WA4 4AD, United Kingdom*

A free electron laser (FEL) in a mode-locked optical klystron (MLOK) configuration is modelled using start-to-end simulations that simulate realistic electron beam acceleration and transport before input into a full three-dimensional FEL simulation code. These simulations demonstrate that the MLOK scheme is compatible with the present generation of radiofrequency accelerator designs. A train of few-optical cycle pulses is predicted with peak powers similar to those of the equivalent conventional FEL amplifier. The role of electron beam energy modulation in these results is explained and the limitations of some simulation codes discussed. It is shown how seeding the FEL interaction using a High Harmonic seed laser can improve the coherence properties of the output. © *2011 American Institute of Physics*. [doi:10.1063/1.3605027]

I. INTRODUCTION

The successful commissioning of the Linac Coherent Light Source (LCLS) x-ray free electron laser amplifier[1] has introduced a new era of short wavelength free electron laser (FEL) facilities[2] enabling unprecedented high brightness spatial resolution at the atomic scale ~ 1 Å. In such FELs, a relativistic electron beam is injected into a magnetic undulator which causes the electrons to oscillate transversely to their direction of propagation along an undulator axis of period λ_u. The interaction of these undulating electrons with the radiation they emit results in a collective instability which bunches the electrons at a resonant wavelength λ_r, causing them to emit coherently at that wavelength.[2] An initially small light signal of power P_0 is exponentially amplified along the z axis of the undulator as $P(z) \approx P_0/9 \exp(\sqrt{3}z/l_g)$ until saturation when the electrons begin to de-bunch. The nominal gain length of the collective instability $l_g = \lambda_u/4\pi\rho$, determines the rate of amplification of both the electron bunching and the radiation power and also the efficiency of the amplifier via ρ, the FEL parameter.[3] Within the electron pulse, a radiation wavefront will propagate ahead of the copropagating electrons by one cooperation length $l_c = \lambda_r/4\pi\rho$ in one gain length through the undulator.[4] Thus, the cooperation length also determines the coherence length l_{coh} of the radiation field with $l_{coh} \approx l_c$. At short x-ray wavelengths, there are presently no external seed fields available for amplification and the FEL amplifier starts from noise. When the electron pulse lengths l_b are long with respect to the cooperation length, $l_b \gg l_c$, many autonomous regions evolve from the noise that are uncorrelated in phase giving a "spikey" output with poor longitudinal (temporal) coherence. Each spike is of width $\sim l_c$

with spike separation of $\sim 2\pi l_c$.[5] For shorter electron pulses $l_b \lesssim 2\pi l_c$, it is possible to have a single spike output of width $\sim l_c$. Thus, the cooperation length sets an approximate lower limit for the radiation pulse duration for unmodified FEL amplifier operation. Several schemes have been proposed to generate such short isolated radiation pulses from an FEL amplifier (see e.g., Refs. 6–8 and references therein), all with output pulse durations $\gtrsim l_c/c$, which in the x-ray gives typical minimum pulse durations ≈ 200 as. Other methods are, therefore, required to achieve shorter durations towards the atomic unit of time of 24 as, which would allow interrogation and possible control of events at both the spatial and temporal resolution of the atom.[9,10]

Two methods have been suggested that may achieve this goal. In Ref. 11, a modified echo enhanced harmonic generation scheme uses laser induced electron beam modulation and magnetic chicane dispersion to generate a single 20 as full width at half-maximum (FWHM) pulse of peak power 180 MW at wavelength of 1 nm. The second method is that of the mode locked optical klystron,[12–14] which uses a method with similarities to mode generation and locking in conventional cavity oscillator lasers. Initial simulations predict that a MLOK FEL can generate a train of 23 as (FWHM) pulses, separated by 150 as, with peak powers of ~ 5 GW at a wavelength of 1.5 Å.

In a normal FEL amplifier, a resonant radiation wavefront propagates, or "slips," one resonant wavelength λ_r over an electron in one undulator period.[2] In the MLOK, additional slippage is introduced between the electrons and radiation by a periodic series of chicanes that delays the electrons. The FEL interaction then occurs in a periodic series of undulator-chicane modules. This creates radiation modes centred about the resonant wavelength and separated in frequency by $\Delta\omega = 2\pi c/s$ where s is the total relative slippage between electrons and radiation in one undulator-chicane module. Despite operating as an amplifier, the MLOK method is similar to the process of mode-locking in conventional cavity

a)Electronic mail: david.dunning@stfc.ac.uk.
b)Electronic mail: b.w.j.mcneil@strath.ac.uk.
c)Electronic mail: neil.thompson@stfc.ac.uk.
d)Electronic mail: peter.williams@stfc.ac.uk.

18, 073104-1
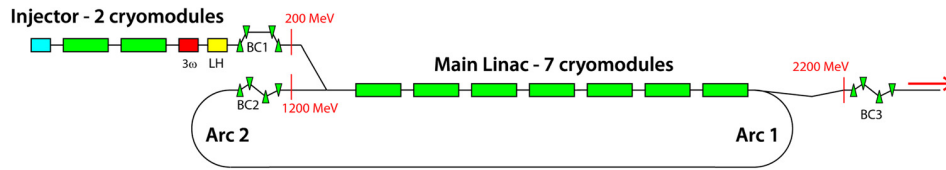
FIG. 1. (Color online) Schematic layout of the NLS recirculating accelerator. The 200 MeV injector includes a third harmonic cavity (3ω), laser heater (LH), and bunch compression chicane (BC1). Two passes of a 1 GeV main linac and two further bunch compression stages (BC2 and BC3) follow.

oscillator lasers, where the slippage distance s is equivalent to the round-trip cavity length of the conventional laser. Locking between modes is achieved, again in a manner similar to conventional lasers, by introducing a modulation at the mode spacing $\Delta\omega$. This, essentially optical method, results in the generation of a train of short pulses of duration $\ll l_c/c$, uniformly spaced at the modulation period.

In this paper, the MLOK method is modelled using a realistic electron beam generated by a full start-to-end simulation to demonstrate its compatibility with the predicted output from present generation accelerator designs for ~ 1 nm FEL output wavelength. The role of energy modulation of the electron beam to lock the modes is described in more detail than previously, in particular by considering the amplification of a high harmonic seed source. Amplification of a high harmonic (HH) source has previously been investigated using simulations in the absence of any beam energy modulation[14] where a slow broadening of the individual radiation pulses was observed in simulations as the interaction progressed through the MLOK system. Some electron beam dispersive effects that are not included in the simulation model are identified, and the potential effects and benefits discussed.

II. START-TO-END MODELLING

The MLOK method is modelled in full three-dimensional FEL simulations using an electron distribution tracked through full start-to-end accelerator simulations of a superconducting re-circulating linac design. It is emphasised that the MLOK method is independent of the choice of accelerator configuration: the aim here is to demonstrate that the MLOK FEL is compatible with present accelerator designs. An overview of the method of generation of the electron distribution used in the simulations is given, and full three-dimensional modelling of a MLOK FEL starting from noise is presented.

A. Accelerator modelling

An electron distribution for use in FEL modelling was generated in start-to-end simulations of an accelerator design[15] for the UK New Light Source (NLS) project. The design comprises of a 200 MeV injector followed by two recirculation passes of a 1 GeV main linac. The photoinjector[16] consists of a normal conducting L-band (1.3 GHz) photocathode gun and a superconducting L-band (1.3 GHz) cavity module and was simulated, for these lower energies, by using the simulation code ASTRA.[17] The electron distribution generated by ASTRA was imported into the Elegant[18] code for tracking through the accelerator lattice to the FEL

entrance. The accelerator design is a two-pass recirculating machine based on nine TESLA-type accelerating cryomodules with longitudinal bunch compression carried out in three dedicated bunch compression stages. Following the linac are a beam switchyard, collimation, and diagnostic tomography sections. A laser heater is used to mitigate the effects of Coherent Synchrotron Radiation-induced microbunching. Figure 1 shows a schematic layout of the design.

The properties of the tracked electron distribution at the entrance to the FEL are given in Figure 2. The longitudinal phase space, current profile, slice emittance, and slice energy spread, binned in 1 fs slices, are shown. Peak current of >1 kA is achieved, but with some variation over 100 fs. Slice emittances of less than 0.4 mm-mrad are attained. The slice energy spread is below 2×10^{-4} for most of the bunch. A region of duration ~ 100 fs centred around the peak of the electron bunch current was selected from this distribution for FEL simulations. The routine elegant2genesis[19] was used to convert the electron distribution output from Elegant into an input distribution for the three dimensional FEL simulation code Genesis 1.3.[20]

B. The mode locked optical klystron FEL amplifier

The MLOK FEL amplifier[12,14] uses similarities from mode-locking in conventional lasers to generate a train of short, uniformly spaced pulses, with individual pulse lengths significantly less than the cooperation length, l_c. An equally spaced modal structure is generated in the spectrum by periodically delaying the electron bunch using magnetic chicanes inserted between the undulator modules. The total relative slippage of the radiation through the electron bunch per undulator-chicane module is $s = l + \delta$, where $l = N_u \lambda_r$ is the slippage occurring in the undulator module of N_u periods and δ that within the chicane. The slippage enhancement factor is defined as $S_e = s/l$. For $S_e > 1$, the spectrum takes the form of a frequency comb modulated by the sinc-function envelope of the single undulator module spectrum centered at the resonant FEL frequency, ω_r. The mode separation of the frequency comb is $\Delta\omega = 2\pi/T_s$, where $T_s = s/c$ is the time taken for radiation to propagate the slippage length. This mode spacing, therefore, determines the number of modes falling under the central envelope of the single undulator module spectrum, $N_0 = 2S_e - 1$.

In Ref. 12, the introduction of a sinusoidal modulation of the electron beam energy, of frequency equal to the mode spacing, causes the equally spaced modes to develop sidebands that overlap with neighbouring modes allowing mode-locking to occur. This phase matches the modes to generate a temporal train of uniformly spaced short pulses. The effect
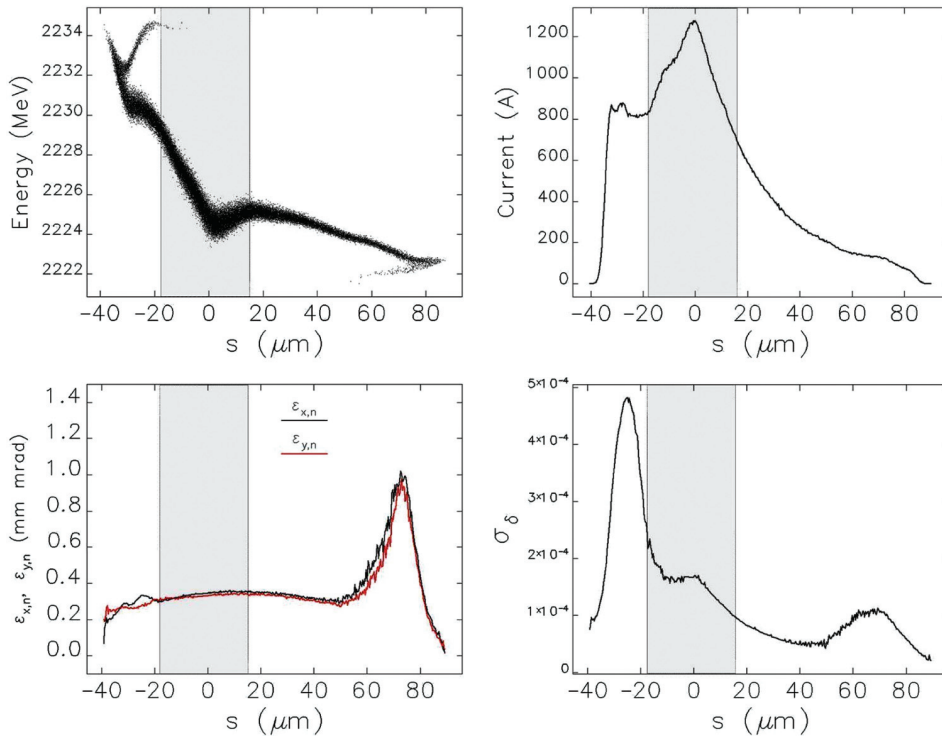
FIG. 2. (Color online) Bunch properties in 1 fs bins on entrance to the modulator prior to entry to the MLOK FEL: Top left—longitudinal phase space, Top right—current profile, Bottom left—slice emittance, and Bottom right—slice energy spread. The region selected for FEL simulations is highlighted.

of this energy modulation is considered in more detail in the following work.

The exemplar system used here has a resonant FEL wavelength of $\lambda_r = 1.24$ nm, corresponding to the highest photon energy of the designs for the NLS FEL proposal.[21] Undulator modules of $N_u = 8$ periods were chosen so that $l = 8\lambda_r$, and the relative electron beam/radiation slippage induced by the dispersive effects of each chicane placed between the undulator modules was set to $\delta = 23\lambda_r$, giving a slippage enhancement factor of $S_e = 3.9$.

C. Modelling the MLOK FEL interaction

The three-dimensional FEL code Genesis 1.3 (Ref. 20) was used to model the FEL interactions. A short modulator section was used to introduce a sinusoidal electron energy modulation in the tracked electron distribution of Fig. 2, of scaled amplitude γ_m about the mean energy $\gamma_0 \approx 4356$ and of period s to match the total slippage per undulator-chicane module. The modulation amplitude was varied over a range of values and a value of $\gamma_m/\gamma_0 = 0.02\%$ was chosen. The modulation amplitude that optimised the generation of the narrowest pulses was $\gamma_m/\gamma_0 \approx 0.05\%$, however, as discussed in Sec. IV, the effects of larger energy modulations may not be modelled sufficiently well by the current state of the art computer simulation codes like Genesis 1.3. Details of the effects of varying the modulation amplitude are presented and discussed in Sec. III.

The modular undulator-chicane structure was also modelled using Genesis 1.3, using the energy modulated tracked electron distribution. No seed was used so that the amplification process started from self-amplification of spontaneous

emission (SASE).[3] The radiation output power close to saturation after 120 undulator-chicane modules is shown in Fig. 3 and includes details of the initial electron beam energy and current profile. The total undulator length to saturation is ∼33 m and yields peak powers of ∼1 GW similar to the results for a FEL amplifier operating in SASE mode using the same parameters. The peak of the radiation power occurs in the high current, low energy chirp section of the electron bunch. The pulse train retains the effects of SASE noise but
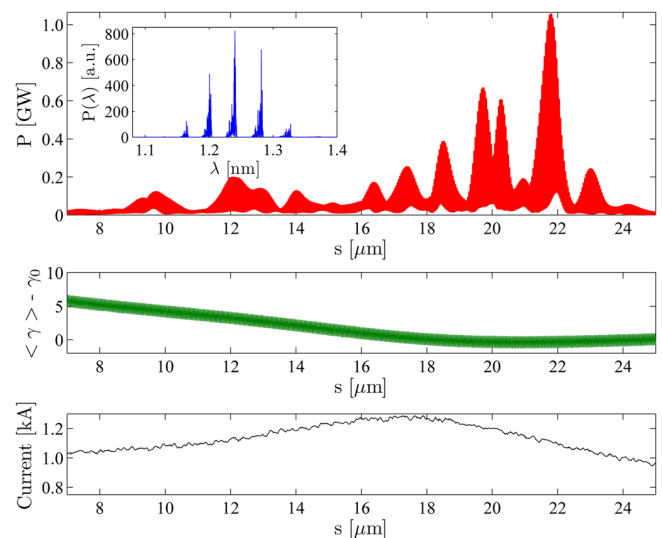
FIG. 3. (Color online) Top—radiation pulse output power close to saturation (120 modules) and the corresponding radiation spectrum (inset); Middle—the initial energy modulated electron beam energy; and Bottom—electron beam current profile.
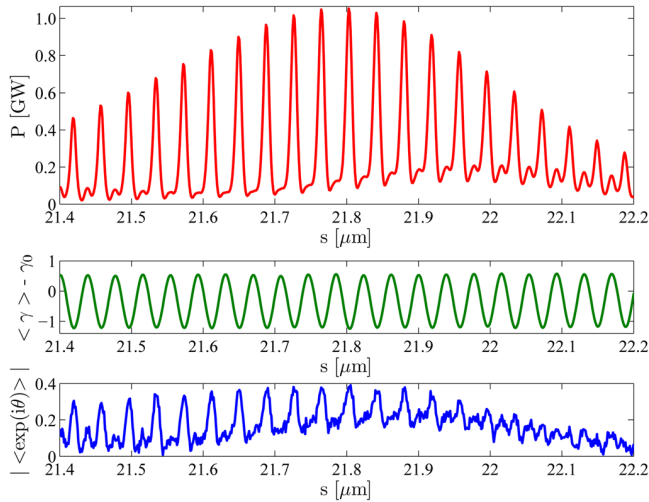
FIG. 4. (Color online) Top—radiation power at the centre of the 120th undulator module; Middle—slice-averaged electron beam energy offset from the resonant energy (in terms of electron rest mass energy); Bottom—electron beam bunching at the centre of the 120th undulator module. The radiation pulses align with the positions of minimum energy gradient.

with a longer envelope modulation. This longer modulation occurs as the cooperation length is increased by the slippage enhancement factor: $S_e \times l_c$.[12] Analysis of the radiation phase also shows that the coherence in the pulse train is extended by the same factor so that the coherence length $l_{coh} \sim S_e \times l_c$. The energy chirp along the electron bunch results in a corresponding chirp in resonant radiation wavelength along the pulse train.

Fig. 4 shows a more detailed plot of the radiation power profile at the centre of the 120th undulator module, together with the electron beam energy and the modulus of the complex bunching parameter, $b = \langle e^{i\theta} \rangle$. The individual pulses within the train have durations ~30 as FWHM, with the number of optical cycles corresponding to approximately the number of undulator periods per module. The radiation pulse alignment relative to the modulated electron beam can also be observed. The radiation pulse trains align with either the minimum or maximum of the sinusoidal energy modulation. It is intuitively reasonable that these regions of minimum energy gradient appear to preferentially support the FEL interaction, allowing the radiation pulses to develop. Two pulses at the minima and maxima of the energy modulation, therefore, develop per modulation period, and two separate sets of modes develop with the maxima of the energy beam modulation supporting a set of shorter wavelength modes than those of the modulation minima by a factor $\Delta\lambda/\lambda \approx 4\gamma_m/\gamma_0$. These are observed in the spectrum inset of Fig. 3 as a splitting of the spectrum at each of the main mode wavelengths, although other effects will be present which will cause further structure in the spectrum due to the energy chirp of the beam. The electron beam bunching parameter is also observed to have a similar pulse train structure as that of the radiation.

III. ROLE OF ENERGY MODULATION

In Sec. II C, the amplitude of the energy modulation was chosen by performing simulations with different modulation amplitudes and selecting the optimum for pulse train generation. Radiation pulse trains were shown to develop at the positions of minimum beam energy gradient at the extrema of the energy modulation. Here, the role of energy modulation in the mode-locked amplifier is considered further. To avoid noise in the temporal properties associated with SASE, a MLOK FEL amplifier simulation was seeded using a model developed to describe an attosecond pulse train from a high harmonic source.[14]

Previous studies[14] have shown that the pulse train structure of an HH source can be retained during amplification to saturation in the mode-locked FEL without modulation of the electron beam. However, the radiation pulses broaden as the FEL interaction progresses. Here, it is shown that an electron beam energy modulation can restrict this pulse broadening effect, and a novel method for seeding the mode-locked configuration is proposed which requires no phase matching between the seed and modulated beam.

A. Modelling method

Simulations were carried out assuming a uniform electron beam current using a 1-D code similar to that described in Ref. 22. The notation follows that of Ref. 12, with the scaled units of Refs. 3 and 4 being used. In these units, $\bar{z}_1$ is the local distance measured within the electron beam in units of the cooperation length, l_c. The relative propagation, or "slippage," of a radiation wavefront with respect to the electron bunch per undulator-chicane module in these units is $\bar{s} = \bar{l} + \bar{\delta}$, where $\bar{l}$ is the slippage in the undulator ($\bar{l} = N_u\lambda_r/l_c$) and $\bar{\delta}$ is that within the chicane. The scaled resonant FEL frequency is $\bar{\omega} = (\omega - \omega_r)/2\rho\omega_r$ and the slippage enhancement factor is $S_e = \bar{s}/\bar{l}$.

The temporal profile of the HH seed is given by a comb of attosecond pulses separated by half the wavelength of the drive laser, λ_d. The HH seed was modelled in a similar way to that described in Refs. 14 and 23 with the resonant FEL wavelength chosen to be the 65th harmonic of the drive laser, i.e., $\lambda_r = \lambda_d/65$. For a typical drive laser wavelength of $\lambda_d = 805$ nm (e.g., Ti:Sapphire), the 65th harmonic is 12.4 nm. The temporal and modal structure used to model the seed is shown in Fig. 5.

With a FEL parameter of $\rho = 2 \times 10^{-3}$ (typical for an FEL operating in the extreme ultraviolet (XUV) and with 8 periods per undulator module, the scaled undulator slippage is $\bar{l} = 0.201$. The spectral and temporal structure of the radiation generated by the undulator-chicane system was matched to the HH seed by setting the scaled chicane slippage to be $\bar{\delta} = 0.616$ so that $\bar{s} = \bar{\lambda}_d/2$, where $\bar{\lambda}_d = \lambda_d/l_c$ is the scaled drive laser wavelength, giving a slippage enhancement factor of $S_e \approx 4.1$.

B. Beam modulation and seed phase-matching

An electron beam energy modulation was introduced of period $\bar{\lambda}_d/2$ equal to both the slippage in an undulator-chicane module and the HH seed pulse train spacing. Figure 6 shows a schematic of two different initial phases of the HH seed with respect to the beam energy modulation phase. The subsequent slippage of a radiation wavefront relative to the
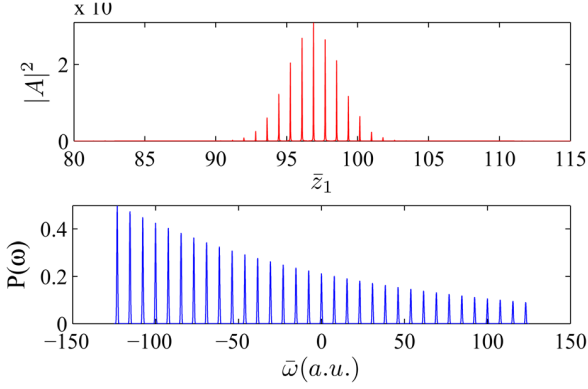
FIG. 5. (Color online) Scaled longitudinal intensity profile (top) and spectral power distribution (bottom) for the HH seed.

FIG. 7. (Color online) Peak radiation intensity after 40 modules against initial longitudinal position of the seed pulses (top) relative to the electron beam energy modulation (bottom), for varying energy modulation amplitude. The initial alignment of the seed becomes more critical as the energy modulation amplitude increases. The optimum initial alignment of the peak powers of the seed was found to be half of the undulator slippage behind the positions of zero energy gradient.

electron beam due to that occurring in the undulators and chicanes are also shown. It is clear that the FEL interaction in the undulators will differ for the two initial phases due to the different electron energy chirps experienced by the radiation pulses.

The initial phase $\bar{z}_{10}$ of a peak of the HH seed pulse with respect to the beam energy modulation was varied over one modulation period and the scaled power of the radiation recorded for fixed undulator length $\bar{l}$. The results are plotted in Fig. 7 for a range of energy modulation amplitudes. For zero energy modulation, there is clearly no dependence on the initial phase $\bar{z}_{10}$ of the seed. As the amplitude increases, the initial phase alignment of the seed becomes more significant. The optimum amplification of the seed was seen to occur with seed pulses phased $\bar{l}/2$ behind the maxima and minima of the energy modulated electron beam at the beginning of each undulator as shown in Fig. 6(b). This

corresponds to the optimum radiation peak powers being coincident with the zero energy gradient of the electron beam at the middle of each undulator module and concurs with the results of the start-to-end simulations of Sec. III C where the amplification started from noise.

For larger beam energy modulation amplitudes, it may be expected that those regions of the beam that have sufficiently large energy gradients, such as Fig. 6(a), will not support FEL lasing. Assuming an energy modulation of the form

$$\gamma = \gamma_0 + \gamma_m \cos(\Delta\bar{\omega}\bar{z}_1), \qquad (1)$$

then a radiation wavefront propagating about the maximum of the beam energy gradient will experience a beam energy range of $\Delta\gamma \approx \gamma_m \Delta\bar{\omega}\bar{l}$ in one undulator module. If this range is sufficiently large that $\Delta\gamma/\gamma_0 > \rho$, then the FEL interaction will be suppressed.[3] Hence, for a beam modulation period defined by the radiation mode spacing, $\Delta\bar{\omega} = 2\pi/\bar{s}$, then, for beam energy modulation amplitudes,

$$\gamma_m/\gamma_0 > \rho S_e/2\pi, \qquad (2)$$

the radiation peak powers will start to become confined to grow about to the extrema of the beam energy modulation where the energy gradients are smallest. For the above parameters used here, this corresponds to $\gamma_m/\gamma_0 > 0.13\%$. The effect can be seen from Fig. 7 where radiation output is suppressed with increasing beam energy modulation amplitude for pulses that are phased to evolve in the regions of high energy gradient about $\bar{z}_{10} \approx 0.3$ and 0.7.

The optimal longitudinal phase alignment of the seed of $\bar{z}_{10} = 0.51$ from Fig. 7 was used in the simulations and the energy modulation amplitude varied. The scaled pulse width $\bar{l}_r$ and the peak scaled radiation power $|A|^2_{peak}$ are plotted as a function of the interaction distance through the undulator $\bar{z}$, in Figure 8. With zero energy modulation, the radiation pulses are seen to broaden in agreement with previous studies.[14] An energy modulation amplitude of 0.1%–0.2% is

FIG. 6. (Color online) Alignment of the HH seed pulses relative to the electron beam energy modulation at the start of an undulator module for two cases (a) $\bar{l}/2$ behind the central energy of the modulation and (b) $\bar{l}/2$ behind the minima of the energy modulation. Here, $p = (\gamma - \gamma_0)/\rho\gamma_0$ is the scaled electron beam energy.
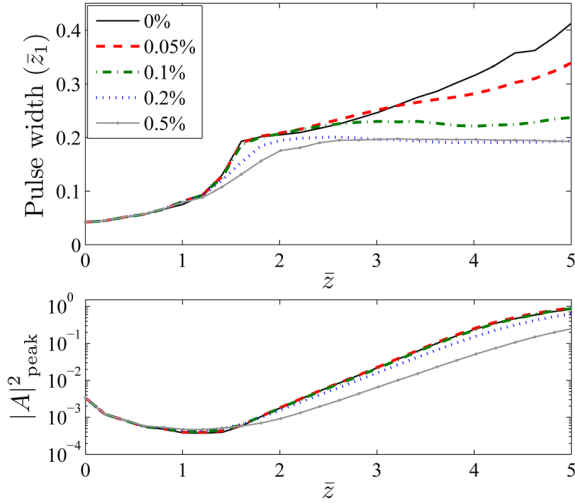
FIG. 8. (Color online) Scaled radiation pulse width $\bar{l}_r$ (top) and peak intensity $|A|^2_{peak}$ (bottom) plotted as a function of scaled distance, $\bar{z}$, through the undulator for different energy modulation amplitudes. The optimal initial seed alignment is used ($\bar{z}_{1_0} \approx 0.51$ in Fig. 7). An energy modulation amplitude of $\gamma_m/\gamma_0 \approx 0.2\%$ is sufficient to restrict pulse broadening. Increasing the modulation amplitude further does not reduce the pulse width but does reduce the growth rate.

seen to be sufficient to restrict the pulse broadening effects in accord with condition (2). Increasing the modulation amplitude above this value does not reduce the output pulse width further, which has a lower limit determined by the relative slippage in one undulator module, to give $\bar{l}_r \approx \bar{l} = 0.2$. Increased beam energy modulation amplitude does however decrease the radiation growth in accord with the condition (2).

A condition for the upper limit of the energy modulation that accommodates the dual criteria of allowing sufficient growth rate while minimising the pulse duration may be obtained by considering the beam energy range a radiation pulse interacts with when propagating $\pm \bar{l}/2$ about the extrema of the modulated beam. By expanding $\cos(x) \approx 1 - x^2/2$ in the modulation term of Eq. (1), and letting $\Delta\bar{z}_1 = \bar{l}/2$, then setting the energy range to the upper limit of ρ, the condition for the upper limit of the energy modulation is obtained

$$\gamma_m/\gamma_0 < 2\rho S_e^2/\pi^2. \tag{3}$$

For the parameters used above, this corresponds to a beam energy modulation of $\gamma_m/\gamma0 < 0.68\%$.

The conditions (2,3) may be combined to give the range of electron beam energy modulation that allow the pinning of the radiation pulses to the beam modulation extrema while allowing for a satisfactory radiation growth rate

$$\frac{S_e}{2\pi} < \frac{\gamma_m}{\rho\gamma_0} < \frac{2S_e^2}{\pi^2}. \tag{4}$$

The difference in gain between the maxima and minima of the energy modulations is noted with the minima (positive energy curvature) giving slightly greater gain, however further analysis is required to fully understand this effect.

While in the HH seeded MLOK FEL, the seed pulses are optimally amplified when aligned to the positions of minimum beam energy gradient at the extrema of the modulation. In the SASE mode, when the system starts from noise, the extrema now define the positions about which the radiation pulses preferentially grow as observed in the start-to-end simulations of Sec. III A. This pinning of the radiation pulses to these well defined phases, in both the seeded and SASE cases, is of significant benefit where the phasing of the output pulses to an external signal is important e.g., pump-probe type experiments.

C. Filtered seed

The Sec. III B showed that use of an HH seed allows control of the envelope and relative phases of the radiation pulse train over lengths significantly greater than the cooperation length, and that pulse broadening effects[14] could be reduced by seeding an energy modulated beam. However, phase-matching of the HH seed pulse train to the correct phase of the electron beam energy modulation was necessary to achieve optimum output. It is now shown that it is possible to seed the MLOK FEL with an HH source that is filtered to remove all harmonics except the resonant harmonic of the central mode. As this filtering removes the attosecond pulse train structure of the seed, no phase-matching of seed and energy modulated beam is required at the start of the interaction. However, the temporal coherence of the seed is retained during amplification and the mode-locked pulse train structure grows as the interaction proceeds.

The HH seed field of Fig. 5 was filtered to preserve only the central resonant mode, $\bar{\omega} = 0$, removing the attosecond structure so that the seed retains the simple Gaussian envelope of the HH drive laser. A beam energy modulation amplitude of $\gamma_m/\gamma_0 = 0.2\%$ was used in these simulations. The minimum of the modulated beam energy, with the larger growth rate, was chosen to be resonant with the seed. Other parameters are similar to those used in Sec. III B and results of the simulations are shown in Fig. 9. While the interaction was seeded at the central mode frequency only, the mode frequencies quickly develop, lock, and were amplified to generate a pulse train which retains the good temporal coherence properties of the seed. At saturation similar pulse widths and powers to those of Fig. 8 of Sec. III B were obtained.

IV. SIMULATION MODEL LIMITATIONS AND POTENTIAL FUTURE DEVELOPMENT

Most computational codes that model the FEL interaction, like those used in the results presented above, assume that the simulation electrons are confined to their initial localised ponderomotive potentials and that the FEL interaction is averaged over an undulator period. For some parameters, these approximations may not be valid when simulating FEL interactions that utilise energy modulated electron beams, such as the MLOK.

For a sufficiently large energy modulation amplitude of the electron beam, longitudinal electron transport on scales greater than the resonant radiation wavelength cannot be modelled easily using simulation codes such as those used in
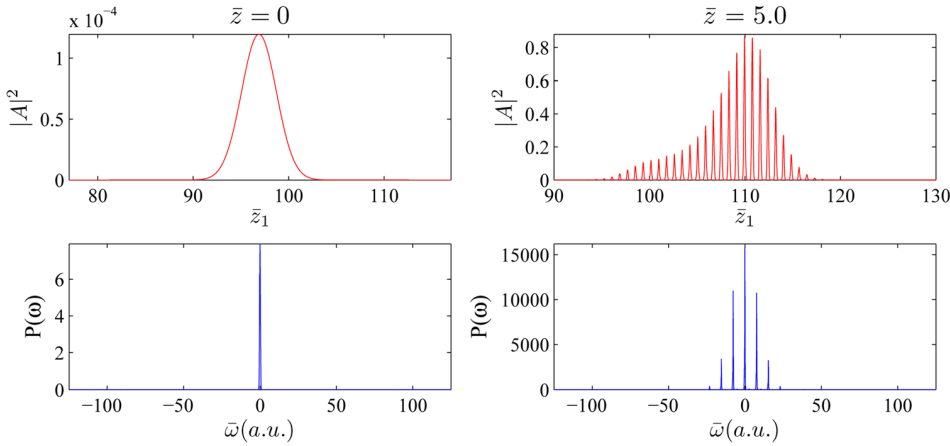
FIG. 9. (Color online) Simulation results for the MLOK FEL with a filtered, single mode, HH seed. The left plots show the initial scaled power (top) and scaled spectral power (bottom) of the seed at $\bar{z} = 0$. The right plots show the equivalent close to saturation at $\bar{z} = 5$.

this paper. On propagation through the undulator-chicane modules, dispersion will cause beam energy modulation, with a period of the radiation mode spacing, to develop into a density (current) modulation of the same period. While this current modulation will not affect the creation of the radiation modes, which is essentially an optical process, the current modulation can by itself couple and lock the radiation modes to generate a train of short pulses.[24] This effect may, therefore, be beneficial to the mode-locking process. However, to investigate these effects will require new simulation methods that allow for beam current evolution as the interaction progresses. In order for such dispersive effects to be small, as required by the simulation codes used in this paper, the growth rate of the current modulation should be significantly smaller than the FEL interaction in a gain length l_g, and a condition that describes this is now derived.

From Ref. 12, the effect of chicane dispersion on the scaled position of the jth electron with scaled energy $p_j = (\gamma_j - \gamma_0)/\rho\gamma_0$ is given by

$$\bar{z}_{1j} \rightarrow \bar{z}_{1j} + 2\rho D p_j,$$

where $D = R_{56}/2l_c \approx 10\bar{\delta}/6$ is the scaled dispersive strength of a single chicane. The dispersive effects can act to enhance the FEL electron bunching process at the radiation wavelength so reducing the gain and saturation lengths in what has been called a distributed optical klystron.[25–27] However, these dispersive effects will also have an effect on a beam with energy modulation of period greater than the radiation wavelength, such as that employed to couple the modes in the MLOK FEL. In this case, the dispersive bunching would maximise for an approximate propagation in $\bar{z}_1$ of $\bar{s}/4$ by the maximum and $-\bar{s}/4$ by the minimum of energy modulation. The effects of such bunching may be considered negligible if it is much less than the modulation period in a FEL saturation length, which may be written as the condition

$$2\rho N_{sat} D p_m \ll \frac{\bar{s}}{4}$$

where $N_{sat} = \bar{z}_{sat}/\bar{l}$ is the number of undulator chicane modules in saturation length $\bar{z}_{sat}$ and $p_m = \gamma_m/\rho\gamma_0$ is the scaled

beam energy modulation amplitude. The definition of the slippage enhancement factor $S_e = \bar{s}/\bar{l}$ and the relation above for the scaled dispersive strength D, may be used to obtain

$$\frac{\gamma_m}{\gamma_0} \ll \frac{3}{40N_{sat}} \frac{S_e}{S_e - 1}.$$

In the start-to-end simulations, using the tracked electron beam of Sec. II, this inequality is satisfied by a factor of approximately four, while for the simulations of Sec. III, it is satisfied by a factor of approximately two for the $\gamma_m/\gamma_0 = 0.2\%$ modulation amplitude case. Some effects due to dispersion on the energy modulated beam may, therefore, be expected. Such effects, as now discussed, may in fact be beneficial to radiation generation.

Modulation of the electron beam energy, and the current modulation that results, can also be a significant source of coherent spontaneous emission (CSE), another process not modelled by averaged codes.[28] Initial studies[29] indicate that this is the case and that the increased frequency content able to be to be modelled (due to a larger Nyquist frequency) introduces further, shorter duration, pulse structure. This may occur without any collective high-gain FEL interaction, i.e., relying on CSE only, and the MLOK may be able to generate pulse trains from beams that may not be able to operate as an FEL e.g., due to deleterious beam quality effects. This may open up new opportunities for light sources and will be the subject of future research.

V. CONCLUSIONS

The MLOK FEL configuration has been shown to be compatible with the predicted output from the present generation of accelerators by using so-called start to end numerical simulations. The role of electron beam energy modulation has been described and explains the relative phasing of the radiation pulse evolution with respect to the beam energy modulation. A relatively simple method of seeding the MLOK FEL with a filtered HH source was shown to control the envelope and phase of the mode-locked pulse train. Such control would assist in the phasing of the short pulse train

with respect to a pump field in pump-probe type experiments. The limitations of present, averaged, FEL simulation codes were considered and a criteria for the validity of these codes derived when energy modulated beams are employed. Finally, the use of coherent spontaneous emission in a MLOK configuration was discussed. Such systems may offer a new method of generating short pulse trains of coherent, high power radiation without the need to rely upon the FEL interaction.

[1]P. Emma, R. Akre, J. Arthur, R. Bionta, C. Bostedt, J. Bozek, A. Brachmann, P. Bucksbaum, R. Coffee, F.-J. Decker, Y. Ding, D. Dowell, S. Edstrom, A. Fisher, J. Frisch, S. Gilevich, J. Hastings, G. Hays, Ph. Hering, Z. Huang, R. Iverson, H. Loos, M. Messerschmidt, A. Miahnahri, S. Moeller, H.-D. Nuhn, G. Pile, D. Ratner, J. Rzepiela, D. Schultz, T. Smith, P. Stefan, H. Tompkins, J. Turner, J. Welch, W. White, J. Wu, G. Yocky, and J. Galayda, Nature Photon. **4**, 641 (2010).

[2]B. W. J. McNeil and N. R. Thompson, Nature Photon. **4**, 814 (2010).

[3]R. Bonifacio, C. Pellegrini, and L. Narducci, Opt. Commun. **50**, 373 (1984).

[4]R. Bonifacio, B. W. J. McNeil, and P. Pierini, Phys. Rev. A **40**, 4467 (1989).

[5]R. Bonifacio, L. de Salvo, P. Pierini, N. Piovella, and C. Pellegrini, Phys. Rev. Lett. **73**, 70 (1994).

[6]E. L. Saldin, E. A. Schneidmiller, and M. V. Yurkov, Phys. Rev. ST Accel. Beams **9**, 050702 (2006).

[7]A. A. Zholents and M. S. Zolotorev, New J. Phys. **10**, 025005 (2008).

[8]P. Emma, Z. Huang, and M. Borland, in *Proceedings of the 26th International FEL Conference* (Trieste, 2004), p. 333. Available from Joint Accelerator Conferences online at http://www.jacow.org.

[9]P. B. Corkum and F. Krausz, Nat. Phys. **3**, 381 (2007).

[10]F. Krausz and M. Ivanov, Rev. Mod. Phys. **81**, 163 (2009).

[11]D. Xiang, Z. Huang, and G. Stupakov, Phys. Rev. ST. Accel. Beams **12**, 060701 (2009).

[12]N. R. Thompson and B. W. J. McNeil, Phys. Rev. Lett. **100**, 203901 (2008).

[13]B. W. J. McNeil and N. R. Thompson, "Mode locked optical klystron configuration in an FEL cavity resonator, THOB4," in *Proceedings of the 32nd International FEL Conference* (Malmö, Sweden, 2010), pp. 558–561.

[14]B. W. J. McNeil, N. R. Thompson, D. J. Dunning, and B. Sheehy, J. Phys. B **44**, 065404 (2011).

[15]P. H. Williams, B. D. Muratori, S. L. Smith, J. Rowland, D. Angal-Kalinin, J. K. Jones, H. L. Owen, R. Bartolini, and I. P. Martin, "A recirculating linac as a candidate for the UK New Light Source, WE5RF," in *23rd Particle Accelerator Conference* (Vancouver, Canada, 2009). Available from Joint Accelerator Conferences online at http://www.jacow.org.

[16]J.-H. Han, H. Huang, and S. Pande, "Technical design of the baseline gun for the NLS project, TUPC44," in *Proceedings of the 31st International FEL Conference* (Liverpool, UK, 2009), pp. 340–343.

[17]K. Floettmann, *ASTRA Users Manual*, available at http://www.desy.de/~mpyflo/Astra_dokumentation/ (Deutsches Elektronen-Synchrotron, Hamburg, Germany).

[18]M. Borland, *User's Manual for elegant*, available at http://www.aps.anl.gov/Accelerator_Systems_Division/Accelerator_Operations_Physics/manuals/elegant_latest/elegant.html (Argonne National Laboratory, Argonne, USA).

[19]R. Soliday and M. Borland, *elegant2genesis*, available at http://www.aps.anl.gov/Accelerator_Systems_Division/Operations_Analysis/manuals/SDDStoolkit/node32.html (Argonne National Laboratory, Argonne, USA).

[20]S. Reiche, Nucl. Instrum. Methods Phys. Res. A **429**, 243 (1999).

[21]*NLS Project: Conceptual Design Report*, edited by J. Marangos and R. Walker (2010), available at http://www.newlightsource.org (Science and Technology Facilities Council, UK).

[22]B. W. J. McNeil, G. R. M. Robb, D. Dunning, and N. R. Thompson, "FELO: A one-dimensional time-dependent FEL oscillator code, MOPPH011," in *Proceedings of the 28th International FEL Conference* (Berlin, Germany, 2006), pp. 59–62. Available from Joint Accelerator Conferences online at http://www.jacow.org.

[23]B. W. J. McNeil, J. A. Clarke, D. J. Dunning, G. J. Hirst, H. L. Owen, N. R. Thompson, B. Sheehy, and P. H. Williams, New J. Phys. **9**, 82 (2007).

[24]E. Kur, D. J. Dunning, B. W. J. McNeil, J. Wurtele, and A. A. Zholents, "A wide bandwidth free-electron laser with mode locking using current modulation," New J. Phys. **13**, 063012 (2011).

[25]V. N. Litvinenko, Nucl. Instrum. Methods Phys. Res. A **304**, 463 (1991).

[26]G. R. Neil and H. P. Freund, Nucl. Instrum. Methods Phys. Res. A **475**, 381 (2001).

[27]Y. Ding, P. Emma, Z. Huang, and V. Kumar, Phys. Rev. ST Accel. Beams **9**, 070702 (2006).

[28]B. W. J. McNeil, M. W. Poole, and G. R. M. Robb, Phys. Rev. ST Accel. Beams **6**, 070701 (2003).

[29]D. Dunning, B. McNeil, N. Thompson, and B. Sheehy, Workshop on high-harmonic seeding for present and future short wavelength Free-Electron Lasers (FELs), Frascati, Italy, 2008, available at http://www.elettra.trieste.it/FERMI/index.php?n=Main.SeedingWS.

PHYSICAL REVIEW LETTERS

Few-Cycle Pulse Generation in an X-Ray Free-Electron Laser

D. J. Dunning,[1,2,*] B. W. J. McNeil,[2,†] and N. R. Thompson[1,2,‡]

[1]*ASTeC, STFC Daresbury Laboratory and Cockcroft Institute, Warrington WA4 4AD, United Kingdom*
[2]*Department of Physics, SUPA, University of Strathclyde, Glasgow G4 0NG, United Kingdom*

A method is proposed to generate trains of few-cycle x-ray pulses from a free-electron laser (FEL) amplifier via a compact "afterburner" extension consisting of several few-period undulator sections separated by electron chicane delays. Simulations show that in the hard x ray (wavelength ~0.1 nm; photon energy ~10 keV) and with peak powers approaching normal FEL saturation (GW) levels, root mean square pulse durations of 700 zs may be obtained. This is approximately two orders of magnitude shorter than that possible for normal FEL amplifier operation. The spectrum is discretely multichromatic with a bandwidth envelope increased by approximately 2 orders of magnitude over unseeded FEL amplifier operation. Such a source would significantly enhance research opportunity in atomic dynamics and push capability toward nuclear dynamics.

PACS numbers: 41.60.Cr

Pulses of light, tens to hundreds of attoseconds in duration, have enabled the exploration and control of processes that occur at atomic time scales [1,2]. A common source of such pulses results from high harmonic generation (HHG) in a laser driven gas [3] from which isolated pulses may be generated or, more commonly, a periodic train of pulses that can act as an ultrafast strobe. This fast stroboscopic property has been successfully applied to a range of experiments to image and control electron wave packet behavior in atoms [4,5]. Reducing pulse durations toward 1 as, and beyond into the zeptosecond regime, with high (GW) peak powers may extend opportunities to directly resolve electronic behavior within inner shells of atoms, the imaging and possible control of electronic-nuclear interactions such as nuclear excitation by electron transition or capture (NEET/NEEC) [6], and move toward the resolution of nuclear dynamics [7]. However, this will require a sufficient flux of photons with energies in the hard x ray ($\gtrsim 10$ keV) that are not available from HHG sources.

The recently realized x-ray free-electron laser (FEL), which can generate the higher photon energies at multi-GW powers, would offer this enhanced temporal resolution if few-cycle, hard x-ray radiation pulses could be generated. The FEL is currently a unique source for scientific experiments, with facilities such as FLASH [8], LCLS [9], SACLA [10] and FERMI@elettra [11] in operation, and others in development [12], including proposals for a very hard x-ray source of coherent 50 keV photons [13]. The normal x-ray FEL operating mode is via a high-gain amplifier generating self-amplified spontaneous emission (SASE) [14], which has noisy temporal and spectral properties [15], although new methods are being introduced to improve on this [12]. The characteristic minimum pulse duration for such high-gain amplifier FELs is determined by the FEL bandwidth [15,16], which for present x-ray FELs corresponds to durations $\gtrsim 100$ as. In this Letter a

new operating method is proposed that, via a relatively simple upgrade, would allow existing x-ray FELs to generate trains of high-power (GW), few-cycle pulses into the zeptosecond regime—at least 2 orders of magnitude shorter than currently achievable. The corresponding spectrum is discretely multichromatic within a broad bandwidth envelope. Potential applications of such sources are the stroboscopic interrogation of matter [4] with intensities enhanced by orders of magnitude compared with current sources, while the multiple narrow frequency modes may be exploited in applications such as resonant inelastic x-ray scattering [17]. High energy photon pulses of zeptosecond duration begin to make feasible access to the temporal behavior of the nucleus, in what has been coined nuclear quantum optics [18].

In a high-gain FEL amplifier, a relativistic electron beam propagates through a long undulator, allowing a resonant, cooperative interaction with a copropagating radiation field of resonant wavelength $\lambda_r = \lambda_u(1 + \bar{a}_u^2)/2\gamma_0^2$ [12], where λ_u is the undulator period, $\bar{a}_u$ is the rms undulator parameter, and γ_0 is the mean electron energy in units of the electron rest mass energy. The cooperative instability results in an exponential amplification of both the resonant radiation intensity and the electron microbunching, $b = \langle e^{-i\theta_j} \rangle$ [14], where θ_j is the ponderomotive phase [12] of the jth electron. In the one-dimensional limit, the length scale of the exponential gain is determined by the gain length $l_g = \lambda_u/4\pi\rho$, where ρ is the FEL coupling parameter [14]. A resonant radiation wave front propagates ahead of the electrons at a rate of λ_r per λ_u. This relative propagation, or "slippage" in one gain length l_g is called the "cooperation length," $l_c = \lambda_r/4\pi\rho$ [19], which determines the phase coherence length and bandwidth of the interaction.

Several methods have been proposed to generate short radiation pulses by "slicing" short regions of high beam

104801-1

quality from within a longer electron pulse [20–23], with the shortest pulses generated at LCLS to date of $\gtrsim 1$ fs duration [24]. However, the FEL bandwidth restricts the minimum pulse length from such schemes to $\gtrsim l_c$ [15,16], with typical value $l_c \sim 200\lambda_r$ corresponding to ~ 100 as for x-ray FELs. By inserting electron delays between modules within the long undulator, the phase coherence length of the interaction can be discretized, increasing the bandwidth. The mode-locked FEL amplifier (ML-FEL) proposal [25] uses this to generate a train of pulses with lengths $\ll l_c$ and peak powers approaching FEL saturation. The number of optical cycles per pulse is approximately the number of undulator periods per module, so could potentially deliver few-cycle pulses. However, this would require significantly modifying existing FELs, which typically have several hundred periods per module.

In this Letter, a method, shown schematically in Fig. 1, is proposed to generate trains of few-cycle radiation pulses similar to that of the ML-FEL but by using a short "afterburner" extension that could relatively easily be added to existing facilities. The technique involves preparing an electron beam with periodic regions of high beam quality, each region of length $\ll l_c$, prior to injection into a normal FEL amplifier. Only these high quality regions undergo a strong FEL interaction within the amplifier to generate a periodic comb structure in the FEL-induced microbunching. Once the microbunching comb is sufficiently well developed, but before any saturation of the FEL process, the electron beam is injected into a "mode-locked afterburner," which maps the comb structure of the electron microbunching into a similar comb of the radiation intensity. The afterburner comprises a series of few-period undulator modules separated by electron delay chicanes similar to that used in the ML-FEL [25]. These undulator-chicane modules maintain an overlap between the comb of

bunching electrons and the developing radiation comb, each pulse of length $\ll l_c$, allowing it to grow exponentially in power to saturation. The pulses are delivered in trains since amplification occurs over a number of afterburner modules, and would be naturally synchronized to the modulating laser (Fig. 1).

Several methods could be used to generate the periodically bunched electron beam prior to the afterburner, including energy modulation [20,26], emittance spoiling [22], and current enhancement [27,28]. Here, electron beam energy modulation is used as illustrated in Fig. 1. For a sufficiently large sinusoidal energy modulation of the form $\gamma(t) = \gamma_0 + \gamma_m \cos(\omega_m t)$, where ω_m is the modulation frequency, those regions of the beam about the mean energy γ_0 will be "spoiled" due to the larger energy gradients, whereas about the extrema, $\gamma \approx \gamma_0 \pm \gamma_m$, a higher beam quality exists due to smaller energy gradients. Only these latter regions may be expected to experience a strong FEL interaction within the amplifier to generate the comb structure in the electron bunching parameter. In fact, strong microbunching develops only at the minima of the energy modulation. It is noted from FEL linear theory [14] that there is an asymmetry about the resonant frequency for the rate of exponential gain with a critical radiation frequency below which no exponential instability exists. It may be intuitively expected that electrons about the minima will experience radiation fields generated by higher energy electrons, and so greater than their resonant frequency. Due to this gain asymmetry favoring higher frequencies these lower energy regions of the modulated beam may be expected to dominate any FEL interaction in the amplifier. This is what is observed in simulations here and in other work [26] and has also been confirmed in a more complete linear theory for an energy modulated beam [29].
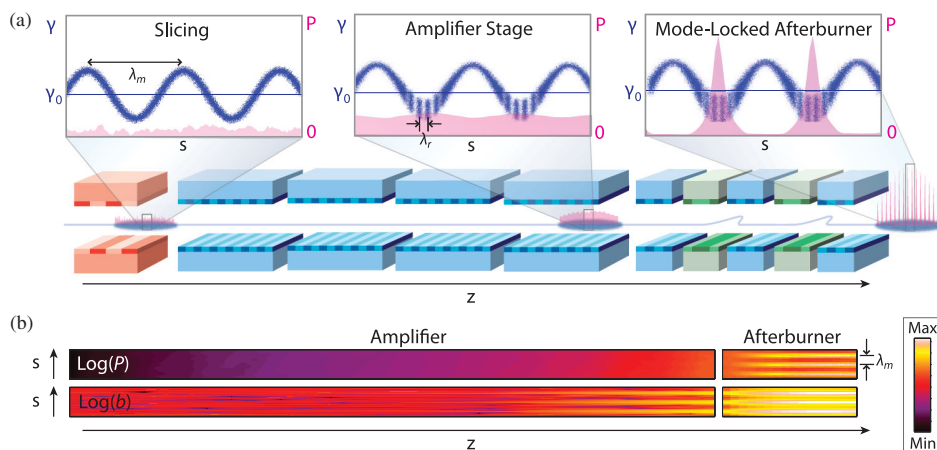
FIG. 1 (color).   (a) Schematic layout of the proposed technique and (b) Example simulation results. An electron beam is sliced (e.g., using an external laser and a short undulator to apply an energy modulation, as shown), such that a comb structure develops in the FEL-induced electron microbunching (b) in a long undulator (amplifier stage). Further amplification of the radiation intensity (P) with periodic electron delays (mode-locked afterburner stage) generates a train of few-cycle radiation pulses.

Simulations of the method were carried out using the simulation code GENESIS 1.3 [30] using the parameters of Table I in both the soft and hard x ray. For the soft x-ray case, with resonant FEL wavelength of $\lambda_r = 1.24$ nm, the modulation period $\lambda_m = 38.44$ nm ($= 31\lambda_r$) and $\lambda_m \ll l_c$. This modulation could be achieved using a modulating undulator seeded by current HHG sources [2,31]. The undulator and electron beam parameters are those of the UK New Light Source design [31]. The electron pulse length was $\gg l_c$ with no other longitudinal variation of beam parameters. The performance of the amplifier stage was optimized by varying the relative amplitude, γ_m/γ_0. The growth of the radiation power and electron bunching are plotted for a range of electron energy modulation in Fig. 2. Increasing the energy modulation amplitude decreases the region about the extrema able to lase and the mean amplification rate decreases. However, a pronounced comb in the electron bunching of period $\approx \lambda_m$ is seen to develop. Because the radiation propagates through the beam, only a relatively small undulation of the radiation power on the scale of λ_m is present. The optimum modulation amplitude was determined to be $\gamma_m/\gamma_0 \approx \rho$, with $\gamma_m/\gamma_0 = 0.1\%$ used for injection into the afterburner. The extraction point from the amplifier stage was chosen to be 34.1 m, as shown in Fig. 2. Hence, no increase in the amplifier length from that for normal saturated SASE operation is required. Both the electron beam and radiation from the amplifier stage propagate into the afterburner (Fig. 1). Each afterburner module has eight undulator periods followed by a chicane that delays the electron beam by 23 resonant wavelengths, so that the total electron delay per module $s = (8 + 23) \times \lambda_r = \lambda_m$. Energy dispersion effects in the chicanes were included, although new chicane designs that reduce dispersive effects may be possible [32]. Figure 3 plots the

radiation power and spectrum at different positions in the afterburner. A pulse train structure develops rapidly as the radiation and bunching combs are regularly rephased by the chicanes to maintain overlap in the amplifying undulator sections. The growth within the undulator modules of the afterburner is exponential of rate comparable to that in the amplifier stage with no beam energy modulation. The growth in the afterburner is also enhanced by the additional bunching caused by the dispersive chicanes [25]. After 15 afterburner modules the output consists of a train of ~9 as rms radiation pulses separated by ~124 as and of ~0.6 GW peak power. The corresponding spectrum is multichromatic with bandwidth envelope increased by ~50 over that of SASE. The pulse train envelope has fluctuations typical of SASE, with phase correlation between individual radiation pulses over a cooperation length. Each afterburner module consists of an undulator

TABLE I. Parameters for soft and hard x-ray simulations.

Parameter	Soft x ray	Hard x ray
Amplifier stage		
Electron beam energy [GeV]	2.25	8.5
Peak current [kA]	1.1	2.6
ρ parameter	1.6×10^{-3}	6×10^{-4}
Normalized emittance [mm-mrad]	0.3	0.3
rms energy spread, σ_γ/γ_0	0.007%	0.006%
Undulator period, λ_u [cm]	3.2	1.8
Undulator periods per module	78	277
Resonant wavelength, λ_r [nm]	1.24	0.1
Modulation period, λ_m [nm]	38.44	3
Modulation amplitude, γ_m/γ_0	0.1%	0.06%
Extraction point [m]	34.1	36.0
Mode-locked afterburner		
Undulator periods per module	8	8
Chicane delays [nm]	28.52	2.2
No. of undulator-chicane modules	~15	~40

FIG. 2 (color online). Optimization of the amplifier stage for the soft x-ray case. Maximum radiation power (top) and electron microbunching (middle) with distance through the amplifier, for different γ_m/γ_0. Bottom panel: Longitudinal profiles of radiation (left) and bunching (right) for different γ_m/γ_0: (a) 0%, (b) 0.04%, (c) 0.06%, (d) 0.1%. Each case is at an equivalent level of microbunching. A section of length $\sim l_c$ from a longer bunch is shown; l_c increases with increasing γ_m/γ_0.
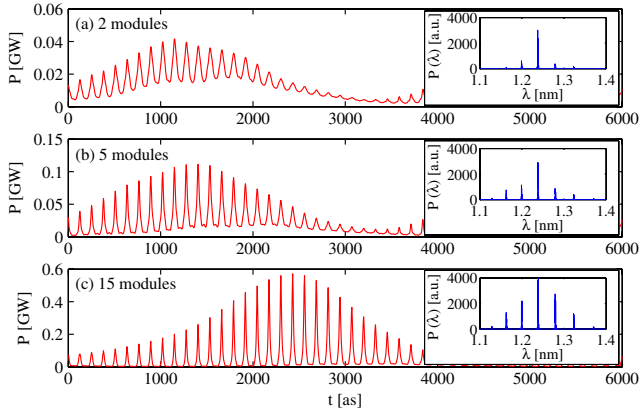
FIG. 3 (color online).   Soft x-ray mode-locked afterburner
simulation results: Radiation power profile and spectrum after
(a) 2, (b) 5, and (c) 15 undulator-chicane modules. The duration
of an individual pulse after 15 modules is $\sim$9 as rms.

FIG. 4 (color online).   Hard x-ray mode-locked afterburner
simulation results: Radiation power profile and spectrum after
40 modules. The duration of an individual pulse is $\sim$700 zs rms.

module of length 0.26 m and a chicane of length 0.2 m,
giving a total length of 6.9 m (excluding diagnostics, etc.)
for the 15-module afterburner.

A hard x-ray case of resonant FEL wavelength of $\lambda_r =$
0.1 nm was also simulated, with the aim of demonstrating
shorter pulse generation. A modulation period of $\lambda_m =$
3 nm was used ($\lambda_m = 30 \times \lambda_r$), which may be feasible
using HHG sources that are now being developed [33].
Both the undulator and electron beam parameters used are
similar to those of the compact SACLA x-ray FEL facility
[10] and are detailed in Table I. A reduced peak current is
used, typical for a lower electron bunch charge. This allows
a slightly reduced, but still realistic, emittance to be
assumed to attain a more compact afterburner stage. As
for the soft x-ray case above, the amplifier stage was
optimized and a beam energy modulation of $\gamma_m/\gamma_0 =$
0.06% chosen. The amplifier section consists of six 277-
period undulator modules (36 m). Each afterburner module
consists of an undulator module of eight periods and a
chicane with delay of $22 \times \lambda_r$. The total electron delay per
afterburner module is then equal to λ_m. The total after-
burner consists of 40 modules, each consisting of an undu-
lator of length 0.144 m and a chicane of length 0.2 m to
give 13.8 m in total. Figure 4 plots the radiation power and
spectrum after 40 undulator-chicane modules. A pulse train
structure of approximately 700 zs rms duration radiation
pulses separated by 10 as and of 1.5 GW peak power is
generated. The radiation mode separation is determined by
the modulation period of 3 nm corresponding to photon
energy difference of $\approx$ 412 eV. The final spectrum is
multichromatic with the bandwidth envelope of the modes
increased by a factor $\sim$100 over SASE.

Both examples in this Letter were optimized toward
minimizing pulse durations using parameters close to those
available from current x-ray FEL sources. Using short
(8-period) undulator modules in the afterburner, $\sim$5 optical
cycles FWHM were attained. However, the time structure
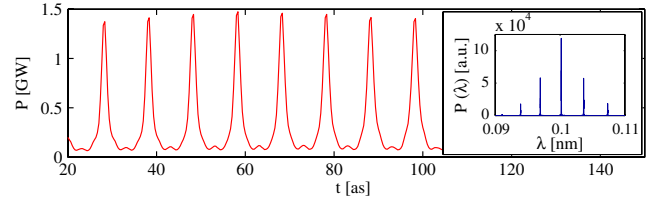
could be modified by changing the number of undulator
periods, electron delay lengths, and λ_m, suggesting a devel-
opment route from the present attosecond pulse train
experiments [4,5] to the ultimate capability of the scheme.
Amplification in the afterburner was set to occur just
before saturation, allowing a short afterburner to attain a
high contrast ratio of the pulse train over the amplifier
radiation. Further development to maximize the peak
power and flexibility of the pulse structure could include
an investigation of saturation effects in the afterburner
(e.g., chicane dispersion, radiation diffraction) and their
mitigation through, e.g., undulator tapering [34], optimized
phase-shifting [35], use of low-dispersion [32] or more
compact chicanes. Methods to improve the temporal co-
herence and stability developed for SASE may also be
applicable. A potential proof-of-principle experiment
would be to use a single-module afterburner [36]. This
is similar to other proposals [37,38] to attain pulse lengths
$\ll l_c$, but at relatively low power, since they operate via
coherent spontaneous emission in a single short undulator
rather than exponential amplification.

If the above results are scaled to higher photon energies,
e.g., to the 50 keV of the proposed x-ray FEL of Ref. [13],
then pulse durations of 140 zs rms may become feasible.
Operation at harmonics of λ_r may be another route to
shorter pulse durations. Furthermore, if a relativistic
counter-propagating target nuclear beam were used with
such pulse trains, as discussed in Ref. [18], in addition to
the increased Doppler-shifted photon energies that the
nuclei experience in their boosted frame, the pulse dura-
tions may be further reduced toward the time scales of
highly ionized heavy elements and nuclear dynamics [7].

The mode-locked afterburner is potentially a relatively
simple upgrade to existing x-ray FEL facilities. It offers a
flexible route toward the generation of discretely multi-
chromatic output under a broad bandwidth envelope, and
so offers few-cycle x-ray pulse trains with GW peak
powers in the temporal domain. This would help facilitate
the direct study of the temporal evolution of complex
correlated electronic behavior within atoms and push ca-
pability into the regime of electronic-nuclear dynamics and
toward that of the nucleus.

*david.dunning@stfc.ac.uk
†b.w.j.mcneil@strath.ac.uk
‡neil.thompson@stfc.ac.uk

[1] P. B. Corkum and F. Krausz, Nat. Phys. **3**, 381 (2007).

[2] F. Krausz and M. Ivanov, Rev. Mod. Phys. **81**, 163 (2009).

[3] A. McPherson, G. Gibson, H. Jara, U. Johann, T. S. Luk, I. A. McIntyre, K. Boyer, and C. K. Rhodes, J. Opt. Soc. Am. B **4**, 595 (1987).

[4] J. Mauritsson, P. Johnsson, E. Mansten, M. Swoboda, T. Ruchon, A. L'Huillier, and K. Schafer, Phys. Rev. Lett. **100**, 073003 (2008).

[5] P. Johnsson *et al.*, Phys. Rev. Lett. **95**, 013001 (2005); T. Remetter *et al.*, Nat. Phys. **2**, 323 (2006); K. Varjú *et al.*, J. Phys. B **39**, 3983 (2006); M. Klaiber, K. Z. Hatsagortsyan, C. Müller, and C. H. Keitel, Opt. Lett. **33**, 411 (2008); K. P. Singh *et al.*, Phys. Rev. Lett. **104**, 023001 (2010).

[6] S. Kishimoto, Y. Yoda, M. Seto, Y. Kobayashi, S. Kitao, R. Haruki, T. Kawauchi, K. Fukutani, and T. Okano, Phys. Rev. Lett. **85**, 1831 (2000).

[7] A. E. Kaplan, Lasers Eng. **24**, 3 (2012).

[8] W. Ackermann *et al.*, Nat. Photonics **1**, 336 (2007).

[9] P. Emma *et al.*, Nat. Photonics **4**, 641 (2010).

[10] H. Tanaka, T. Shintake *et al.*, in *SCSS X-FEL Conceptual Design Report* (RIKEN Harima Institute, Japan, 2005). H. Tanaka *et al.*, Nat. Photonics **6**, 540 (2012).

[11] C. J. Bocchetta *et al.*, Report No. ST/F-TN-07/12, 2007.

[12] B. W. J. McNeil and N. R. Thompson, Nat. Photonics **4**, 814 (2010).

[13] B. E. Carlsten *et al.*, in *Proceedings of 2011 Particle Accelerator Conference, New York, 2011* (JACoW, New York, 2011), p. 799.

[14] R. Bonifacio, L. M. Narducci, and C. Pellegrini, Opt. Commun. **50**, 373 (1984).

[15] R. Bonifacio, L. De Salvo, P. Pierini, N. Piovella, and C. Pellegrini, Phys. Rev. Lett. **73**, 70 (1994).

[16] E. L. Saldin, E. A. Schneidmiller, and M. V. Yurkov, Opt. Commun. **212**, 377 (2002).

[17] L. J. P. Ament, M. van Veenendaal, T. P. Devereaux, J. P. Hill, and J. van den Brink, Rev. Mod. Phys. **83**, 705 (2011).

[18] T. J. Bürvenich, J. Evers, and C. H. Keitel, Phys. Rev. Lett. **96**, 142501 (2006).

[19] R. Bonifacio, B. W. J. McNeil, and P. Pierini, Phys. Rev. A **40**, 4467 (1989).

[20] E. L. Saldin, E. A. Schneidmiller, and M. V. Yurkov, Phys. Rev. ST Accel. Beams **9**, 050702 (2006).

[21] A. A. Zholents and M. S. Zolotorev, New J. Phys. **10**, 025005 (2008).

[22] P. Emma, Z. Huang, and M. Borland, in *Proceedings of the 26th International Free Electron Laser Conference, Trieste, 2004* (JACoW, Trieste, 2004), p. 333.

[23] D. Xiang, Y. Ding, T. Raubenheimer, and J. Wu, Phys. Rev. ST Accel. Beams **15**, 050707 (2012).

[24] Y. Ding *et al.*, Phys. Rev. Lett. **102**, 254801 (2009).

[25] N. R. Thompson and B. W. J. McNeil, Phys. Rev. Lett. **100**, 203901 (2008).

[26] D. J. Dunning, B. W. J. McNeil, N. R. Thompson, and P. H. Williams, Phys. Plasmas **18**, 073104 (2011).

[27] A. A. Zholents, Phys. Rev. ST Accel. Beams **8**, 040701 (2005).

[28] E. Kur, D. J. Dunning, B. W. J. McNeil, J. Wurtele, and A. A. Zholents, New J. Phys. **13**, 063012 (2011).

[29] B. W. J. McNeil, "Linear Theory of an FEL with an Energy Modulated Electron Beam," (unpublished).

[30] S. Reiche, Nucl. Instrum. Methods Phys. Res., Sect. A **429**, 243 (1999).

[31] J. P. Marangos *et al.*, in *New Light Source Project: Conceptual Design Report* (Science and Technology Facilities Council, UK, 2010).

[32] J. K. Jones, J. A. Clarke, and N. R. Thompson, in *Proceedings of IPAC 2012, New Orleans* (JACoW, New Orleans, 2012), p. 1759.

[33] T. Popmintchev *et al.*, Science **336**, 1287 (2012).

[34] N. M. Kroll, P. L. Morton, and M. N. Rosenbluth, IEEE J. Quantum Electron. **17**, 1436 (1981).

[35] D. Ratner, A. Chao, and Z. Huang, in *Proceedings of the 29th International FEL Conference, Novosibirsk, 2007* (JACoW, Novosibirsk, 2007), p. 69.

[36] D. J. Dunning, N. R. Thompson, and B. W. J. McNeil, in *Proceedings of the 32nd International FEL Conference, Malmö, 2010* (JACoW, Malmö, 2010), p. 636.

[37] A. A. Zholents and W. M. Fawley, Phys. Rev. Lett. **92**, 224801 (2004).

[38] D. Xiang, Z. Huang, and G. Stupakov, Phys. Rev. ST Accel. Beams **12**, 060701 (2009).

Physics and Applications of High Brightness Beams Workshop, HBEB 2013

Towards zeptosecond-scale pulses from x-ray free-electron lasers

David J. Dunning[a,b,*], Brian W.J. McNeil[b], Neil R. Thompson[a,b]

[a]*ASTeC, STFC Daresbury Laboratory and Cockcroft Institute, Warrington, WA4 4AD, United Kingdom*
[b]*Department of Physics, SUPA, University of Strathclyde, Glasgow G4 0NG, United Kingdom*

Abstract

The aim of the workshop was to consider what developments might be achievable in the next generation of light sources. One area of particular interest is the generation of ultra-short pulses of light. High harmonic generation (HHG) sources are now capable of reaching pulse durations in the range of tens to hundreds of attoseconds, thereby facilitating the study of electron dynamics. Here we consider the potential of free-electron lasers (FELs) to contribute to this field. First we make the case for FELs in general as a particularly promising source of ultra-short pulses, and summarise some of the relevant proposals. Different classes of ultra-short pulse techniques are identified—each with respective merits and potentially better suited to different types of application. Particular focus is given to highlighting a recent proposal by the authors to generate trains of few-cycle pulses from amplifier FELs, which if applied at hard x-ray wavelengths could generate pulses at the single attosecond scale, or even shorter—into the zeptosecond scale.

Keywords: free-electron laser; FEL; short-pulse; attosecond; zeptosecond

1. Introduction

The motivation for generating short pulses of light is to study and influence ultra-fast dynamic processes. To do this, radiation pulses on a shorter scale than the dynamics involved are required. The timescales of different processes have been described by Krausz and Ivanov (1): Atomic motion on molecular scales occurs at femtosecond (10^{-15} s) to picosecond (10^{-12} s) scales, electron motion in outer shells of atoms takes place on tens to hundreds of attoseconds, and electron motion in inner shells of atoms is expected to occur around the scale of a single attosecond (10^{-18} s). At faster scales still are nuclear dynamics, which are predicted to occur at zeptosecond (10^{-21} s) time scales .

The record for the shortest pulse of light has seen a progression from approximately 10 ps in the 1960s to around 67 attoseconds generated recently by Chang et al. (2)—a development of approximately five orders of magnitude in five decades. As noted by Corkum et al. (3; 4), it is particularly relevant to consider the way in which this frontier progressed. The duration of a pulse of light is its wavelength, λ_r multiplied by the number of optical cycles, N, divided by the speed of light. Initially progress was made in conventional lasers operating at approximately a fixed wavelength ($\lambda_r \approx 600$ nm), by reducing the number of optical cycles. This continued until, in the mid 1980s, pulses of only a few

---

* Corresponding author. Tel.: +44-1925-603739.
  E-mail address: david.dunning@stfc.ac.uk

cycles could be generated (corresponding to a few fs), then could proceed little more. It took a transformative step—high harmonic generation (HHG) (1; 3; 4), for progress to continue by (in very simple terms) reducing the wavelength of the generated light. X-ray free-electron lasers (FELs) (reviewed in several recent papers (5; 6; 7)) presently surpass HHG sources in terms of shortest wavelength by approximately two orders of magnitude, and it is this property which suggests FELs as a candidate for progressing to still shorter radiation pulses than are available today.

2. Short-pulse potential of free-electron lasers

The free-electron laser in fact has two particular advantages which give it potential for pushing the frontier of short pulse generation. The first, as described in the previous section, is short wavelength. Recent new FEL facilities (LCLS (8) commissioned in 2009, and SACLA (9) commissioned in 2011) have extended FEL operation down to approximately 0.1 nm. Assuming that pulses of only a few optical cycles could be attained, this would correspond to pulse durations of approximately a single attosecond—approximately two orders of magnitude shorter than present HHG sources, and four orders of magnitude beyond conventional lasers.

Of course x-ray sources other than FELs have been available for many years, however the peak powers are insufficient to deliver a significant number of photons within an attosecond timescale. It is the high peak power of the free-electron laser (exceeding synchrotrons - the next highest intensity source of x-rays - by approximately 9 orders of magnitude) which gives it potential to push the frontier of ultra-short pulse generation. A hard x-ray FEL typically generates approximately 20 GW peak power, corresponding to 10^{25} photons/second. For a pulse duration of a single attosecond this would correspond to 10^7 photons per pulse. The challenge for reaching the very shortest pulses from FELs - as described in the following sections - will be to minimise the number of cycles per pulse.

3. Standard operating mode of a hard x-ray FEL - SASE

Present hard x-ray FELs normally operate in the high-gain amplifier mode generating self-amplified spontaneous emission (SASE) (as described by Bonifacio et al. (10)), which has noisy temporal and spectral properties (11). A relativistic electron bunch is injected into a long undulator (an alternating polarity magnetic field with period λ_u) which causes the electrons to oscillate transversely and so emit radiation. The electrons' transverse oscillation allows a resonant, co-operative interaction with the co-propagating radiation field of resonant wavelength $\lambda_r = \lambda_u(1 + \bar{a}_u^2)/2\gamma_0^2$ (6), where $\bar{a}_u$ is the rms undulator parameter and γ_0 is the mean electron energy in units of the electron rest mass energy. The co-operative instability results in an exponential amplification of both the resonant radiation intensity and the electron micro-bunching, $b = \langle e^{-i\theta_j} \rangle$ (10), where θ_j is the ponderomotive phase (6) of the jth electron. In the one-dimensional limit, the length-scale of the exponential gain is determined by the gain length $l_g = \lambda_u/4\pi\rho$, where ρ is the FEL coupling parameter (10) (typically $\rho \approx 10^{-4} - 10^{-3}$ for x-ray FELs). The exponential growth saturates when a fraction approximately equal to ρ of the electron beam power is extracted into radiation power. In the undulator, a resonant radiation wavefront propagates ahead through the electron bunch at a rate of one radiation wavelength, λ_r per undulator period, λ_u. This relative propagation, or 'slippage' in one gain length l_g is called the 'co-operation length', $l_c = \lambda_r/4\pi\rho$ (12), which determines the phase coherence length. The electron bunch is relatively long, at least in the context of this paper, with a few-fs bunch corresponding to $\approx 10^4 \times \lambda_r$ at 0.1 nm. The total duration of the radiation emission is similar to that of the electron bunch length (e.g. a few fs), however it consists of sharp spikes on the much shorter scale of the co-operation length, typically a few hundred radiation wavelengths, corresponding to approximately 100 as for hard x-ray FELs, as shown in Figure 1 (a).

3.1. Slicing a single SASE spike

Since each SASE spike acts independently it has been proposed by a number of groups (e.g. 11; 13; 14; 15; 16) that only one spike can be made to occur, either by reducing the bunch length or by slicing the electron beam quality. Experimental progress has been made for a few of these methods, including reducing the electron bunch length (17), and by slicing part of the beam via emittance spoiling (15; 18). A short-pulse technique using chirped electron beams and a tapered undulator has been demonstrated at visible wavelengths (19; 20) and could be extended to x-ray.

A number of proposals (e.g. by Saldin et al. (13)) suggest using a few-cycle conventional laser pulse to pick out part of the electron beam, as shown in Figure 1 (b), which has the advantage of generating a radiation pulse synchronised to the external source. Picking out one SASE spike for present hard x-ray FEL parameters corresponds to a few hundred optical cycles or ≈100 as, which would be close to the frontier presently set by HHG, and at shorter wavelength and higher photon flux (methods are predicted to reach normal SASE saturation power levels or even higher). This technique therefore has exceptional potential, however in terms of shortest pulse duration there is still potential for a further two orders of magnitude reduction by reducing the number of cycles per pulse. Possible methods of doing this are considered in the following sections.
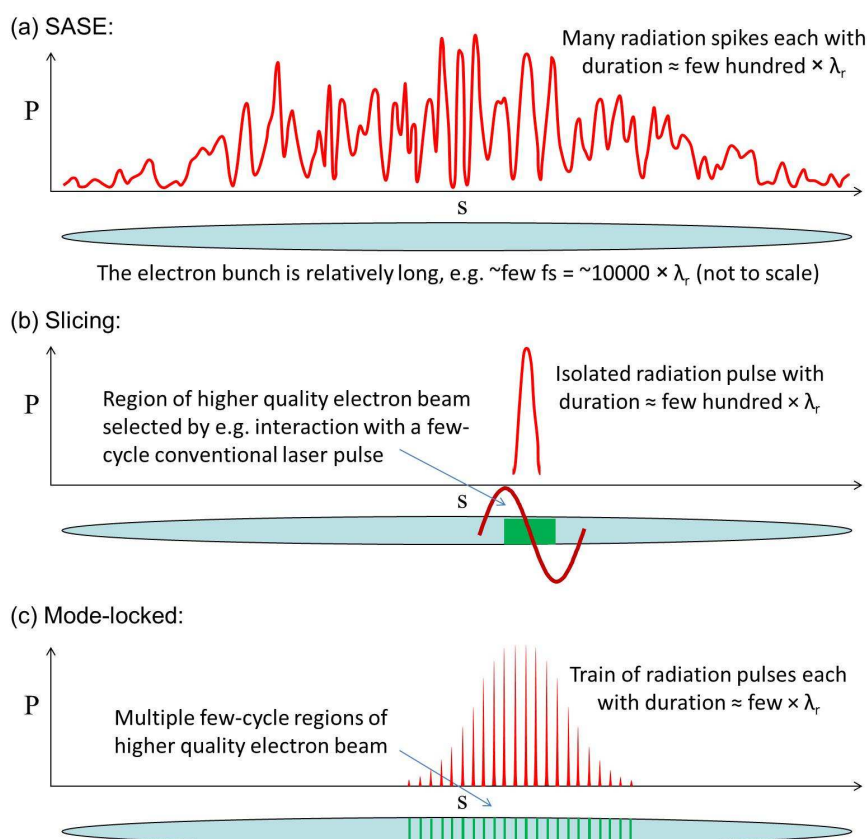
Fig. 1. Figure to illustrate different concepts for FEL operation (not to scale): (a) Typical hard x-ray SASE FEL output consists of a number of radiation spikes, each of length $\approx l_c$ (a few hundred optical cycles); (b) Example of proposals to 'slice' the electron bunch such that a single pulse of length $\approx l_c$ (a few hundred optical cycles) is generated; (c) The mode-locked FEL concepts work by slicing the electron bunch into regions $\ll l_c$, and periodically shifting the radiation to generate a pulse train with pulses on a similarly short scale.

4. Issues in generating few-cycle pulses from FEL amplifiers

Exponential amplification of the radiation power in an FEL amplifier requires a sustained interaction between the radiation field and the electron bunch. This presents a difficulty for generating few-cycle radiation pulses from FELs, since the slippage of the radiation relative to the electrons means that a few-cycle radiation pulse can only interact with a fixed point in the electron beam for a few undulator periods before slipping ahead of it. For example if we were to use one of the methods described in the previous section but were to slice a high quality section of the electron beam much shorter than one SASE spike (e.g. a few cycles) then the rapid slippage of the generated radiation ahead of the high quality region would significantly inhibit FEL amplification (11; 21). Future increases in electron beam

brightness may reduce the FEL co-operation length and so enable reducing pulse durations from this method to some extent.

Another route forward may be the superradiant regime in a seeded FEL amplifier, which has been addressed in theory (22; 23), and in experiment, with short pulses generation observed in both direct seeding (24; 25) and harmonic cascade (26; 27) configurations. In such techniques a short section of an electron bunch is seeded such that it reaches saturation before the rest of the bunch (which starts up from noise). Beyond saturation the FEL interaction proceeds into the superradiant regime in which the radiation intensity continues to increase (though quadratically with distance through the undulator, z, rather than exponentially), and the pulse length reduces as $z^{-1/2}$. Compared to the exponential regime, where the 'centre-of-mass' of a radiation spike is kept close to the electron longitudinal velocity due to amplification, in this mode the radiation pulse propagates closer to the speed of light, so forward relative to the electrons. Consequently it propagates into 'fresh' electrons, provided the rest of the bunch starting from noise has not reached saturation. This technique has been demonstrated at longer wavelengths (24; 25; 26; 27), however its scalability to hard x-ray wavelengths still requires significant development. Few-cycle pulses have been attained via superradiance in FEL oscillators, but FEL oscillators operating at x-ray wavelengths are still under development (28), and present ideas for suitable mirror cavities have very narrow bandwidth which would seem incompatible with the broad-band operation required for few-cycle pulses.

An alternative might be to disregard FEL amplification to establish microbunching, and instead use an external source (though this itself may be a FEL) to induce microbunching (or a single sharp current spike) over a region only a few cycles in length and then make it radiate in an undulator, as shown in Figure 2. There are several proposals to do this, such as by Zholents and Fawley (29) or by Xiang et al. (30), though again the slippage has a limiting effect. If the number of undulator periods in the radiator is greater than the number of cycles in the microbunched region, then the slippage effect dominates and lengthens the pulse. The undulator must therefore be similarly short - also a few periods - otherwise slippage of the radiation relative to the electrons broadens the pulse. As a consequence proposals for this type of technique predict relatively low power compared to FEL saturation, however the power could potentially be increased by future improvements in electron beam brightness. Requiring the microbunching to be imposed by an external source may also present difficulties in scaling such techniques to the shortest wavelengths of FELs in some cases.
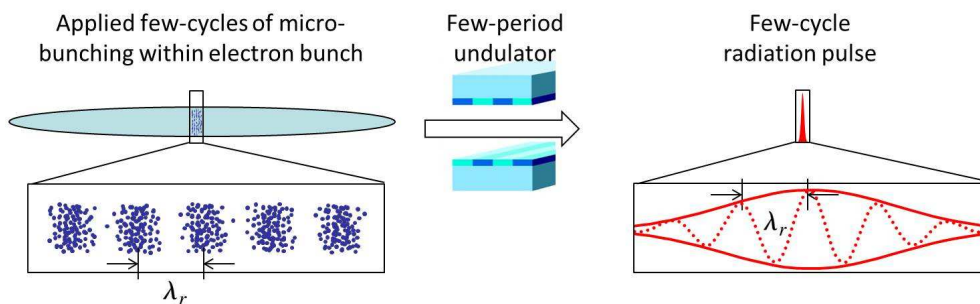
Fig. 2. Figure to illustrate a concept to generate an isolated few-cycle pulse from an electron bunch. Instead of using the FEL interaction, an external source is used to induce microbunching over a region only a few cycles in length, followed by a few-period undulator to emit a few-cycle pulse.

5. Few-cycle pulses via pulse-train operation

We noted in the previous section that the slippage of the radiation ahead of the electrons seems to imply a trade-off between maximising the emitted power (requiring a long interaction), and minimising the pulse duration (requiring a short interaction). However the mode-locked FEL amplifier concept proposed by Thompson and McNeil (31) circumvents this by dividing the long FEL interaction into a series of short interactions separated by a longitudinal re-alignment of the radiation and electron beam. Such re-alignment can be achieved via magnetic chicanes to delay the electron beam relative to the radiation, as shown in Figure 3.

In this case the radiation always propagates ahead relative to the electrons, which is not advantageous for amplifying an isolated ultra-short pulse. However, it allows a *train* of ultra-short pulses to be amplified. If we consider

one pulse in the train, it interacts with the electron beam for several undulator periods, increasing the intensity of the radiation and increasing the microbunching of the electron beam over that region. It then is shifted forward relative to the electrons, to interact with the region of the electron beam previously aligned with the radiation pulse preceding it in the train. This allows a series of short interactions, thereby allowing the pulse duration to be minimised while at the same time maximising the power.
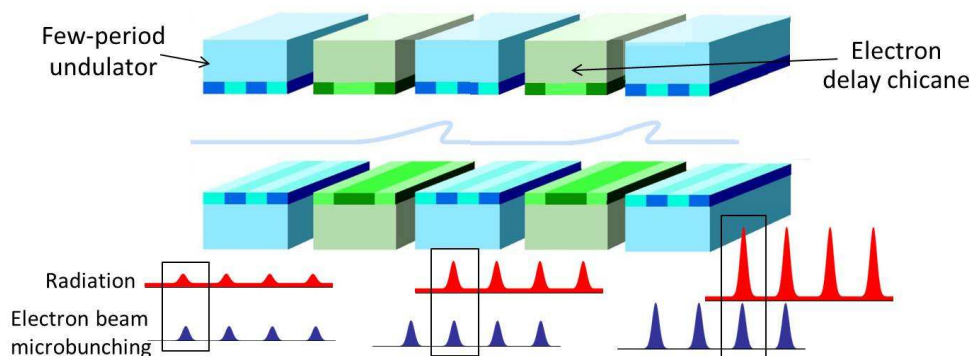
Fig. 3. Schematic layout of a section of the undulator used in the mode-locked FEL amplifier and mode-locked afterburner techniques. Chicanes are used to periodically delay the electrons to keep the developing radiation spikes overlapped with regions of high microbunching.

Though such a technique would allow an external pulse train source (such as that available from HHG) to be amplified (32), such sources are not available at hard x-ray wavelengths so the FEL starts up from noise. In this case multiple interleaved pulse trains may be supported, and a comb structure variation must be applied to the electron beam properties (31; 33; 34) to select a single clean pulse train structure, as shown in Figure 1 (c). The minimum number of optical cycles per pulse from this method is approximately the number of undulator periods per section, so it could potentially deliver few-cycle pulses. However, this would require significantly modifying existing FELs, which are typically divided into modules of several hundred periods.

5.1. Mode-locked afterburner

A new method has recently been developed by the authors (35) that would allow existing x-ray FEL facilities to generate trains of few-cycle radiation pulses via the addition of only a relatively short 'afterburner' extension that could relatively easily be added to existing facilities. The technique involves preparing an electron beam with periodic regions of high beam quality, each region of length $\ll l_c$, prior to injection into a normal FEL amplifier. This can be achieved for example via electron beam energy modulation, where the extrema have less energy spread and are able to lase more easily. Alternatively a current or emittance modulation could be used. Slippage occurring in the amplifier washes out any short-scale structure in the radiation, however only the high quality regions of the electron beam undergo a strong FEL interaction such that a periodic comb structure is generated in the FEL-induced micro-bunching.

Once the micro-bunching comb is sufficiently well developed, but before FEL saturation, the electron beam is injected into a 'mode-locked afterburner', which maps the comb structure of the electron micro-bunching into a similar comb of the radiation intensity. The afterburner comprises a series of few-period undulator modules separated by electron delay chicanes similar to that used in the mode-locked amplifier FEL (31), as shown in Figure 3. These undulator-chicane modules maintain an overlap between the comb of bunching electrons and the developing radiation comb, each pulse of length $\ll l_c$, allowing it to grow exponentially in power towards FEL saturation power levels ($\gtrsim$GW). The pulses are delivered in trains, since amplification occurs over a number of afterburner modules, and would be naturally synchronised to the modulating laser. Alternatively a single short undulator could be used with the advantage of increased simplicity but with lower power (36).

Because this method requires no modification of the main undulator we are free to choose the parameters of the afterburner for minimum pulse duration i.e. short (few-period) undulators. Modelling of the concept at hard x-ray wavelengths, and with 8-period undulators in the afterburner predicts pulse durations of only five optical cycles

FWHM, corresponding to 700 zeptoseconds RMS pulse duration (35). It is also relevant to note that the corresponding spectral properties, which are multi-chromatic within a very broad ($\approx 10\%$) bandwidth envelope, may also be useful for some applications. If the above results are scaled to higher photon energies, e.g to the 50 keV of the proposed x-ray FEL of (37), then pulse durations of 140 zs rms may become feasible (35).

6. Conclusion

There is much potential for generating ultra-short pulses from FELs, and a number of ideas have been proposed. The concepts can be loosely grouped into several categories, each of which has respective merits. Slicing a single SASE spike is predicted to generate isolated pulses with durations of several hundred radiation wavelengths, and high peak power. Using an external source to impart microbunching over a few-cycle region of the beam is predicted to give shorter pulses but relatively low power. A recent proposal by the authors is predicted to generate few-cycle pulses with high powers by generating the pulses in a train, which if applied at hard x-ray wavelengths may allow pulses at the single attosecond scale, or even shorter—into the zeptosecond scale. We anticipate significant development in this field and look forward to future progress.

References

[1] F. Krausz and M. Ivanov, Rev. Mod. Phys. **81**, 163 (2009).
[2] Z. Chang *et al.*, Opt. Lett. **37**, 18 (2012).
[3] J. Levesque and P.B. Corkum, Can J. Phys. **84**, 1-18 (2006).
[4] P.B. Corkum and F. Krausz, Nature Phys. **3**, 381 (2007).
[5] W.A. Barletta *et al.*, Nucl. Instrum. Methods Phys. Res. Sect. A **618**, 69 (2010).
[6] B.W.J. McNeil and N.R. Thompson, Nature Photon. **4**, 814 (2010).
[7] H.H. Braun, Proc. 3rd Int. Particle Accelerator Conf., New Orleans, USA, 4180 (2012).
[8] P. Emma *et al.*, Nature Photon. **4**, 641 - 647 (2010).
[9] H. Tanaka, T. Shintake *et al.*, SCSS X-FEL Conceptual Design Report, RIKEN Harima Institute (2005),
        H. Tanaka *et al.*, Nature Photon. **6**, 540-544 (2012).
[10] R. Bonifacio, L.M. Narducci and C. Pellegrini, Opt. Commun. **50**, 373 (1984).
[11] R. Bonifacio, L. De Salvo, P. Pierini, N. Piovella and C. Pellegrini, Phys. Rev. Lett. **73**, 70 (1994).
[12] R. Bonifacio, B.W.J. McNeil and P. Pierini, Phys. Rev. A **40**, 4467 (1989).
[13] E.L. Saldin, E.A. Schneidmiller and M.V. Yurkov, Phys. Rev. ST Accel. Beams **9**, 050702 (2006).
[14] A.A. Zholents and M.S. Zolotorev, New Journal of Physics **10**, 025005 (2008).
[15] P. Emma, Z. Huang and M. Borland, Proc. 26th Int. FEL Conf., Trieste, 333 (2004).
[16] D. Xiang, Y. Ding and T. Raubenheimer and J. Wu, Phys. Rev. ST Accel. Beams **15**, 050707 (2012).
[17] Y. Ding *et al.*, Phys. Rev. Lett. 102, 254801 (2009).
[18] Y. Ding *et al.*, Phys. Rev. Lett. 109, 254802 (2012).
[19] L. Giannessi *et al.*, Phys. Rev. Lett. 106 144801 (2011).
[20] G. Marcus *et al.*, Applied Phys. Lett. 101, 134102 (2012).
[21] E.L. Saldin, E.A. Schneidmiller and M.V. Yurkov, Opt. Commun. **212**, 377 (2002).
[22] R. Bonifacio and F. Casagrande, Nucl. Instrum. Methods Phys. Res. Sect. A **239**, 36 (1985).
[23] L. Giannessi *et al.*, J. Appl. Phys. **98**, 043110 (2005).
[24] T. Wanatabe *et al.*, Phys. Rev. Lett. **98**, 034802 (2007).
[25] M. Labat *et al.*, Phys. Rev. Lett. 107, 224801 (2011).
[26] L. Giannessi *et al.*, Phys.Rev.Lett. 108 164801 (2012).
[27] L. Giannessi *et al.*, PRL 110, 044801 (2013).
[28] R. Colella, A. Luccio, Opt. Commun. **50**, 41 (1984).
        K.-J. Kim, Y. Shvyd'ko, S. Reiche, Phys. Rev. Lett. **100**, 244802 (2008).
[29] A.A. Zholents, W.M. Fawley, Phys. Rev, Lett. **92**, 224801 (2004).
[30] D. Xiang, Z. Huang and G. Stupakov, Phys. Rev. ST Accel. Beams **12**, 060701 (2009).
[31] N.R. Thompson and B.W.J. McNeil, Phys. Rev. Lett. **100**, 203901 (2008).
[32] B.W.J. McNeil, N.R. Thompson, D.J. Dunning, B. Sheehy, J. Phys. B **44** (6) 065404 (2011).
[33] D.J. Dunning, B.W.J. McNeil, N.R. Thompson and P.H. Williams, Physics of Plasmas, **18**, 073104, (2011).
[34] E. Kur, D.J. Dunning, B.W.J. McNeil, J. Wurtele and A.A. Zholents, New J. Phys. **13** 063012 (2011).
[35] D.J. Dunning, B.W.J. McNeil and N.R. Thompson, Phys. Rev. Lett. **110**, 104801 (2013).
[36] D.J. Dunning, N.R. Thompson, B.W.J. McNeil, Proc. 32nd Int. FEL Conf., Malmö, Sweden, 636 (2010).
[37] B.E. Carlsten *et al.*, Proc. of 2011 Particle Accelerator Conf., New York, USA, 799-801 (2011).